EXPERIMENTS ON THIN AIRFOILS SPANNING A TRANSONIC SHEAR FLOW

Thesis by

Raymond Robert Cosner

In Partial Fulfillment of the Requirements

for the Degree of

Doctor of Philosophy

California Institute of Technology

Pasadena, California

1976

(Submitted September 18, 1975)

ACKNOWLEDGMENTS

Without the constant guidance and enthusiasm of the staffs of the School of Aeronautics and the Jet Propulsion Center of the California Institute of Technology, this project would not have been completed. Doctors E. E. Zukoski and W. D. Rannie, by their constant interest and availability, were indispensible in the planning and execution of the experiments, as well as in consideration of the philosophical concepts that arose in the course of the work. Doctor T. Kubota was similarly willing to share his time and knowledge with me in the development of the theoretical calculation of Chapter IV. Several important discussions were held with Dr. A. Roshko concerning the transonic shear layer. I must gratefully acknowledge the support of a Daniel and Florence Guggenheim Fellowship and several research assistantships during the course of my work.

Financial support for this research project came from the National Aeronautics and Space Administration as a part of a series of studies of the performance of transonic axial-flow compressors. The wind tunnel used in these experiments was designed by Dr. E. E. Zukoski and Mr. J. P. Dolait.

A note of appreciation is due Sam Roman and Paul Baloga, who through their experience guided me to the solution of several troublesome practical problems. Thanks are also due George Lundgren and the other members of the Aeronautics Shop, whose suggestions and careful execution of my drawings in the fabrication of parts required were of great assistance.

The method by which the airfoils described in Chapter V were cast was developed by Dr. D. Collins of the Jet Propulsion Laboratory. Several discussions with him were important to the successful result.

Special thanks are due Roberta Duffy and Virginia Conner, whose skill in typing this thesis is evident.

ABSTRACT

A wind tunnel was built at the California Institute of Technology to provide two uniform coflowing streams at Mach numbers of 0.6 and 1.4 with a plane mixing layer in between. Preliminary studies were made of this free shear layer, indicating a region of self-similar behavior and general agreement in growth rate with previous studies.

A program of experimental and theoretical work was completed in which wedges were installed in the supersonic stream to create shock waves incident on the shear layer. Similar studies were performed with wedges in the subsonic stream. Good agreement was found between the analytic first-order theory and experiment in showing that the upstream propagation of pressure disturbances ahead of their source in the uniform subsonic stream is limited to about 0.6 subsonic layer thicknesses.

The problem of an airfoil in spanwise-varying transonic shear was studied experimentally with the goal of understanding the interactions in the shear region between the supersonic and subsonic streams, especially in terms of deviations from quasi-two-dimensional behavior. The effect of modest angle of attack was also examined.

TABLE OF CONTENTS

Table of Contents (continued)

Table of Contents (continued)

LIST OF TABLES

LIST OF FIGURES

List of Figures (continued)

List of Figures (continued)

List of Figures (continued)

List of Figures (continued)

List of Figures (continued)

List of Figures (continued)

LIST OF SYMBOLS

Symbols Introduced in Chapter I

c	airfoil chord
c_a	axial velocity
M_t	rotor tip relative Mach number
r	radius from rotor axis
t	airfoil thickness
w_r	air relative velocity over rotor blade
Ω	rotor angular velocity

Symbols Introduced in Chapter II

M	Mach number
x	tunnel-based coordinate
y	" " "
z	" " "

Subscripts:

1	supersonic stream
2	subsonic stream

Symbols Introduced in Chapter III

A	shear layer aspect ratio (section 3.2); flow area (elsewhere)
b	tunnel test section width
$f(M_1')$	function describing the effect of compressibility on the shear layer spreading rate (Fig. 3.7 and eq. 3.2)
H	stream-tube height (Fig. 3.10)
M_1'	supersonic stream Mach number relative to the subsonic stream
P	static pressure

Symbols Introduced in Chapter III (cont'd.)

t shear layer and boundary layer thickness (Fig. 3.10)

U unperturbed velocity

δ_s shear layer maximum-slope thickness: $\delta_s = \dfrac{U_1 - U_2}{\left(\frac{dU}{dy}\right)_{max}}$

η similarity variable, y/x

ρ static density

Superscripts:

$*$ choked condition

Subscripts:

n integer index (non-negative)

t stagnation quantity

Symbols Introduced in Chapter IV

a local speed of sound

A_n defined in eq. (4.47)

B_n defined in eq. (4.64)

$C_{ij}(k)$ Fourier coefficients, eq. (4.14)

$f(k)$ function defined in eq. (4.21)

F choking function, eq. (4.31); also, the hypergeometric function

$g(k)$ function defined in eq. (4.51)

h stream-tube height

$H(x)$ unit step function

i $\sqrt{-1}$

I_{mn} integrals defined in eqs. (4.26) and (4.55)

$\mathcal{I}_{mn}$ integrand of integral I_{mn}

Symbols Introduced in Chapter IV (cont'd.)

j	integer that identifies pole locations
J	cutoff value of j for summing the actual series (p. 87)
k	Fourier variable
n	non-negative integer
$q(k)$	function defined in eq. (4.22)
r	reflection coefficient, eq. (4.2); also, Mach number parameter, eq. (4.29)
R_n, R_{mn}	residue at a pole
S	series defined in eq. (4.65)
S_{mn}	location function defined in eqs. (4.27) and (4.56)
t	wedge thickness
u	x-component of velocity
v	y-component of velocity
V_w	distribution of wall inclination angle
α	parameter identified in eq. (4.65)
β	$\sqrt{\|M^2 - 1\|}$
γ	ratio of specific heats
δ_o	flow deflection angle of incident shock wave
δ_1	flow deflection angle of reflected expansion fan
ϵ	perturbation expansion parameter
θ	parameter employed in Ref. 18, defined on p. 108
θ_i, θ_r	parameters defined in eq. (4.40)
ξ	parameter defined in eq. (4.41)
φ	first-order velocity perturbation potential
φ', φ''	velocity perturbation potential expansion functions, eq. (4.7a)

Symbols Introduced in Chapter IV (cont'd.)

Φ exact velocity perturbation potential

ω z-component of vorticity, eq. (4.4)

Superscripts:

(j) jth pole of series

' perturbation quantity; also, differentiation with respect to k

~ Fourier transform of a function

* $f(ix) = f^{*}(x)$

$\wedge$ a function under the asymptotic substitution

Subscripts:

o unperturbed state

$,x$ $\frac{\partial}{\partial x}$

$,y$ $\frac{\partial}{\partial y}$

m, n, ν non-negative integral indices

w condition at the subsonic wall

Symbols Introduced in Chapter V

D shock standoff distance

h airfoil bluntness height

q dynamic pressure

R shock radius of curvature on the airfoil plane

s parameter introduced in eq. (5.7)

y' lateral distance of blunt leading edge pressure effect

α angle of attack

δ shock wave flow deflection angle

δ_o airfoil leading edge deflection angle

Symbols Introduced in Chapter V (cont'd.)

$\delta_{.99}$ perceptible boundary layer thickness, $U/U_\infty = 0.99$

Δ asymptotic detached shock wave translation distance, section 5.4.1.2; also, shear layer displacement distance, elsewhere

ϵ defined in eq. (5.1)

θ_o asymptotic shock wave angle

Subscripts:

g geometric condition, not dependent on flow

i induced flow due to angle of attack

LE leading edge

$\mathcal{C}_L$ airfoil centerline

∞ far upstream

Symbols Introduced in Appendix B

C_D strut drag coefficient based on chord

$\dot{m}$ mass flow rate

Subscripts:

i condition at compressor intake

Symbols Introduced in Appendix D

A_n Fourier coefficient, eq. (D.13)

B function introduced in eq. (D.14)

C_{mn}, D_{mn} Fourier coefficients, eq. (D.11)

Y_n separation function defined in eq. (D.4)

Z_n separation function defined in eq. (D.3)

ϵ wall inclination boundary condition

λ_n eigenvalue

Symbols Introduced in Appendix D (cont'd.)

Superscripts:

$'$	perturbation quantity or differentiation with respect to k

Subscripts:

m, n	integers that identify separate eigenvalues and eigenfunctions

Symbols Introduced in Appendix F

$a_2(\lambda)$, $b_2(\lambda)$	Fourier coefficients defined in eq. (F.5)
F_3, F_4	functions defined in eq. (F.10)
n	non-negative integer
S	variable defined in eq. (F.6)
β	reciprocal scale distance associated with the boundary condition
ϵ	wall deflection angle
θ	parameter defined in eq. (F.3)
λ	Fourier variable
ξ	spatial variable defined in eq. (F.7)

I. INTRODUCTION

1.1 Transonic Axial-Flow Compressors

Throughout the history of manned flight, the contintually-increasing demands placed on flight vehicle power plants has stimulated a large amount of research in airbreathing propulsion systems. During the last three decades, the turbojet engine and its evolutionary derivatives have gained considerable popularity. This gain has been accompanied by increasing interest in one of its primary components, the axial-flow compressor.

An axial-flow compressor is built up from one or more stages, each consisting of a set of rotor blades and a set of stator blades spaced at equal intervals circumferentially around the annular flow area. As is shown in Figure 1.1, the rotor blades are fixed to the hub which rotates at several thousand RPM, while the stator blades are fixed to the cylindrical casing and remain stationary. The detailed design of the rotor and stator blades will not be discussed here (see Reference 1 for a thorough discussion). It will suffice to say that a stage may consist of, say, sixty blades of each type equally spaced around the hub. The blades are twisted and they vary in cross section from root to tip. The purpose of the rotor blade is to do work on the fluid, raising the static pressure and increasing the kinetic energy of the fluid, while the stator blades serve to remove the fluid rotation introduced by the rotor by turning the flow back to more or less its original direction and in addition transform some of the velocity head into additional pressure rise. The pressure ratio of a transonic stage can exceed 1.8.

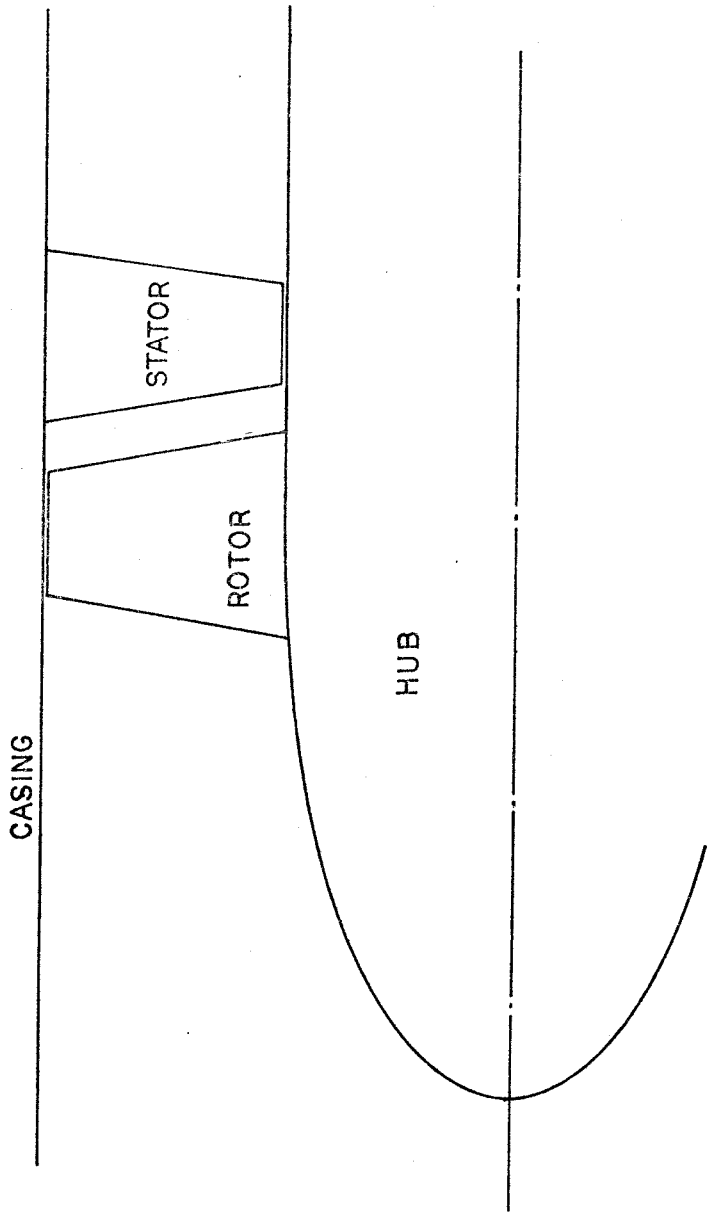

Figure 1.1: Compressor Stage Layout

Assume that ahead of the rotor the flow is axial of magnitude c_a. At a given radius r from the centerline of the rotor the velocity of the blade is Ωr, where Ω is the rotation speed in radians per second. The air velocity relative to the blade is then

$$w_r = \sqrt{c_a^2 + (\Omega r)^2} \quad . \tag{1.1}$$

For many years, the tacit assumption was made by compressor designers that all air velocities relative to both the rotor and stator blades should be subsonic, as the presence of supersonic velocities must entail a large performance and efficiency penalty due to compressibility effects and shock losses. Thus, most compressor research was devoted to the subsonic rotor, in which the air velocity relative to the rotor blade is subsonic everywhere. A comprehensive discussion of subsonic compressor stages is provided in Reference 1.

The majority of the design methods are based on a combination of theoretical and experimental results of two-dimensional flow through cascades with blade sections tested as a two-dimensional airfoil in a uniform flow with properties appropriate to the specific radius. A series of blade cross sections are calculated for several radial locations at a prescribed design flow pattern, and a final form of the blade is faired in from the calculated sections. Such a procedure is referred to as blade element theory, and is essentially the procedure by which compressor blades are designed today. Its drawback lies in an inadequate treatment of radial flow effects, and it succeeds because at subsonic speeds (i.e., a maximum relative Mach number less than about 0.7 to 0.75) these secondary effects

are in fact quite small. Various early tests confirmed that a serious drop in performance occurred at transonic speeds [2] where the flow becomes more complicated.

In addition to the subsonic rotor, attention has been given (ca. 1950) to the supersonic rotor, in which the relative air velocities over the rotor blades are supersonic everywhere. Certainly by the very nature of supersonic flow the spanwise effects have a limited region of influence. Shock losses can be minimized by using blades that are quite thin and have their maximum thickness well aft of the leading edge to keep the leading angle as small as possible. A low camber angle is also desirable. The merits of this design are that with the inherently higher throughflow velocity the same mass flow can be passed with a lesser frontal area, thus reducing the drag of the engine. In addition, because of the higher relative speeds, the entire compression process is more energetic. Thus, an individual stage can be expected to have a higher pressure ratio, permitting a reduction in the total number of stages and thus the overall weight and complexity of the engine.

Of course, for a compressor to operate at supersonic speeds it must first accelerate through transonic speeds, where spanwise effects are known to dominate [3]. A linearized analytic calculation for non-lifting transonic rotor blades (blades in which the relative air velocity is subsonic at the hub and supersonic at the tip) was developed by McCune in 1958 [4, 5] showing as expected the deficiencies of blade element theory. Later work by Okurounmu and McCune [6, 7] has extended the theory to lifting blades. These ad-

vances have shown on a mathematical basis that the actual flow deviates strongly from the predictions of blade element (quasi-two-dimensional) calculations, even in the case of uniform loading per unit span of the blade, over the entire transonic blade.

Uncertainty over the behavior of a compressor in the transonic region, coupled with a belief that deviations from expected performance would be unfavorable, led to serious doubts about whether the supersonic compressor could be started and what its off-design performance would be. However, in actual tests it was found that the transonic performance was the best of all! (See Reference 2 for a discussion of this. The work of this reference is not the first in the field, but is the best documented of the early studies.)

Of course, the next step in this research program (early 1950's) was to construct a compressor stage explicitly designed for transonic operation. The rotor was the pioneering portion of the project; the stator was designed to be wholly subsonic and to use existing knowledge only. The results were extremely encouraging, showing no loss of efficiency until the rotor tip relative Mach number was in the upper end of the transonic range (M_t = 1.1). The pressure ratio of 1.47 and adiabatic efficiency of over 90 per cent were both better than the anticipated values, and the pressure ratio was considerably better than for existing subsonic compressors. While new losses due to shocks were present, the level of work input was also higher and the overall efficiency did not suffer.

Naturally, these results stimulated a program of research into transonic compressors to gain a better understanding of the

processes at work. The goal was to assemble a large body of data similar to that on subsonic compressors which culminated in the preparation of Reference 1. The double circular arc airfoil was chosen as a reference based on preliminary studies. This program continued to bear out the high initial promise of the transonic compressor. Test rotors showed pressure ratios of 1.9 to 2.0 with adiabatic efficiencies of 87 to 92 per cent (both of these parameters would be reduced with the addition of a stator to form a complete stage). Production engines appear feasible with single-stage compression ratios above 1.5, compared with 1.18 for a subsonic stage [8].

Unfortunately, transonic compressors are often quite sensitive to inlet flow distortion, and small errors in design and fabrication have a very significant effect. Excellent dimensional reliability is demanded. (The discussion of the preceding several pages was drawn largely from References 2 and 9.)

After 1957, the research interest in transonic compressors was markedly reduced, as it was felt that a reasonable amount of information had been gathered. However, this interest has been reviving lately. The National Aeronautics and Space Administration's Lewis Research Center is directing several research projects in the field.

The design of a transonic compressor blade still largely follows the tenets of blade element theory in lieu of any other practical technique. An additional complication is the presence of shock waves in the system. Development of a smooth shock system, minimizing

disruptive effects, requires an iterative design procedure [10]. Spanwise effects over a blade are still not well understood, and consequently represent a major potential source of problems.

1.2 Non-Rotating Studies

Thus far, studies of rotating systems have not resulted in a good understanding of the characteristics of the flow field. With this in mind, the Lewis Research Center of the National Aeronautics and Space Administration has contracted with the California Institute of Technology to study a relevant non-rotating flowfield.

The assumption has been made in this study that to some substantial extent the effects due to compressibility observed in a transonic rotor can be distinguished from those due to rotation, and hence treated separately.

To meet the goal of simulating in some way the Mach number effects in a non-rotating system, a wind tunnel producing a transonic shear flow was designed by Zukoski and Dolait [11] at Caltech. The notable feature of this tunnel is that the test section flow consists of two parallel streams of design Mach numbers 1.4 and 0.7, with a plane shear (mixing) layer in between. This Mach number distribution may be compared to that of a currently-studied transonic rotor in Figure 1.2. It should be emphasized that this facility is not intended to duplicate the flow over a transonic rotor blade neglecting rotational effects. Rather, the purpose is to permit the study of a flow field in which some of the gross features are similar to those over an actual blade, with an eye toward gaining understanding of the

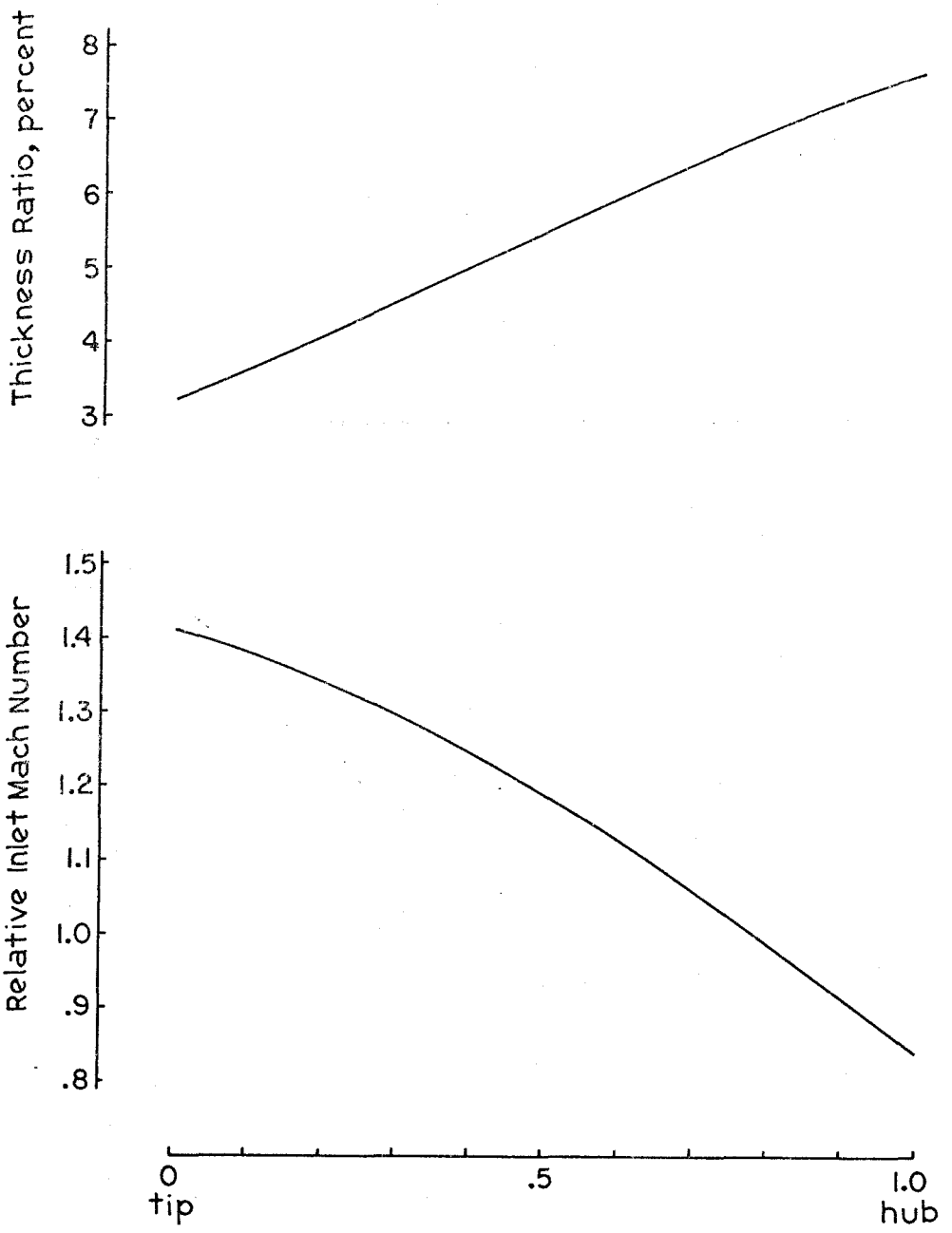

Figure 1.2: Transonic Rotor Data (from Ref. 12, November 1973)

basic fluid dynamic mechanisms involved.

The mixing between the supersonic and subsonic streams at constant static pressure of itself is an interesting problem which is discussed in Chapter III. However, in the context of the larger study, the shear layer can better be regarded as a region where, in the presence of a perturbation to either stream (such as a model placed within the test section), a complex interaction occurs between the two streams.

The project had two objectives: to study the way in which the disturbance from a model modifies the inviscid supersonic flow upstream of the model (the disturbance wave must first enter the subsonic stream to propagate upstream, then re-enter the supersonic flow); and to examine the flow field adjacent to and downstream of a representative airfoil placed within a flow in which the freestream Mach number varies along its span.

Chapter II of this thesis describes the design and operation of the Transonic Shear Flow Wind Tunnel. The flow within the tunnel when no models are present is discussed in Chapter III. This includes consideration of the shear layer, the inhomogeneous structure of the unperturbed flow, and the blockage and choking effects relevant to the tunnel.

Chapter IV discusses the two-dimensional "wedge" problem of a thin plate attached to either the supersonic (top) or subsonic (bottom) wall of the tunnel across the full width. This plate, with its inclined leading and trailing edges (hence the label "wedge"), permitted the study of a relatively simple system in which the disturbance

source was well defined. In addition, it was felt that a general study of the reflection of shock waves off the transonic shear layer would be of interest. This problem, with some simplifying assumptions, was modeled in a first-order analytic calculation evaluated on the computer. Reasonable agreement was found between theory and experiment.

The main portion of the project is described in Chapter V. Attention centers on the case of a 6% - thick biconvex airfoil in the center of the tunnel with the freestream Mach number varying from 0.6 to 1.4 along its span. The flow field is considered in detail through experimental data from the airfoil in both a non-lifting configuration and at modest angles of attack. More abbreviated discussions are presented of the similar cases of a pitot strut ($t/c = 20\%$, diamond section) passing spanwise through the flow.

In Chapter VI the results of these studies are summarized and recommendations for future work involving this facility are presented. Suggestions for improving the operation of the tunnel are also noted.

II. THE TRANSONIC SHEAR FLOW WIND TUNNEL

2.1 Design

The Transonic Shear Flow Wind Tunnel, also known as the Bisonic Wind Tunnel, was designed by E. E. Zukoski and J. P. Dolait [11] as a part of Dolait's work toward the degree of Aeronautical Engineer at the California Institute of Technology. Briefly, the objective was to provide two parallel-flowing streams of air at ambient total temperature and equal static pressures, one stream being supersonic and the other subsonic. The design goals for this tunnel were $M_1 = 1.4$ and $M_2 = 0.7$ (throughout this report, except where specifically stated otherwise, the subscript "1" identifies the supersonic stream and "2" the subsonic stream). In actual practice, the measured values are $M_1 = 1.400 \pm .015$ and $M_2 = .590 \pm .035$. The large deviation of M_2 from the design goal will be discussed later.

The Transonic Shear Flow Wind Tunnel (TSFWT) is driven by the first and second stages of the GALCIT Hypersonic Wind Tunnel compressor plant, with a power consumption of about 140 kw. The total mass flow rate of air is designed to be 1.69 pounds per second. A schematic diagram of the entire air system is presented in Figure 2.1. A more detailed drawing of the installation in the wind tunnel room in the basement of the Guggenheim Building is presented in Figure 2.2, which is to accompany the following description.

The six-inch feedline from the compressor room passes up through the floor into the tunnel room, and immediately encounters a hand-operated valve. This valve is employed in an on-off manner only, for tunnel startup and shutdown, and is not used for flow meter-

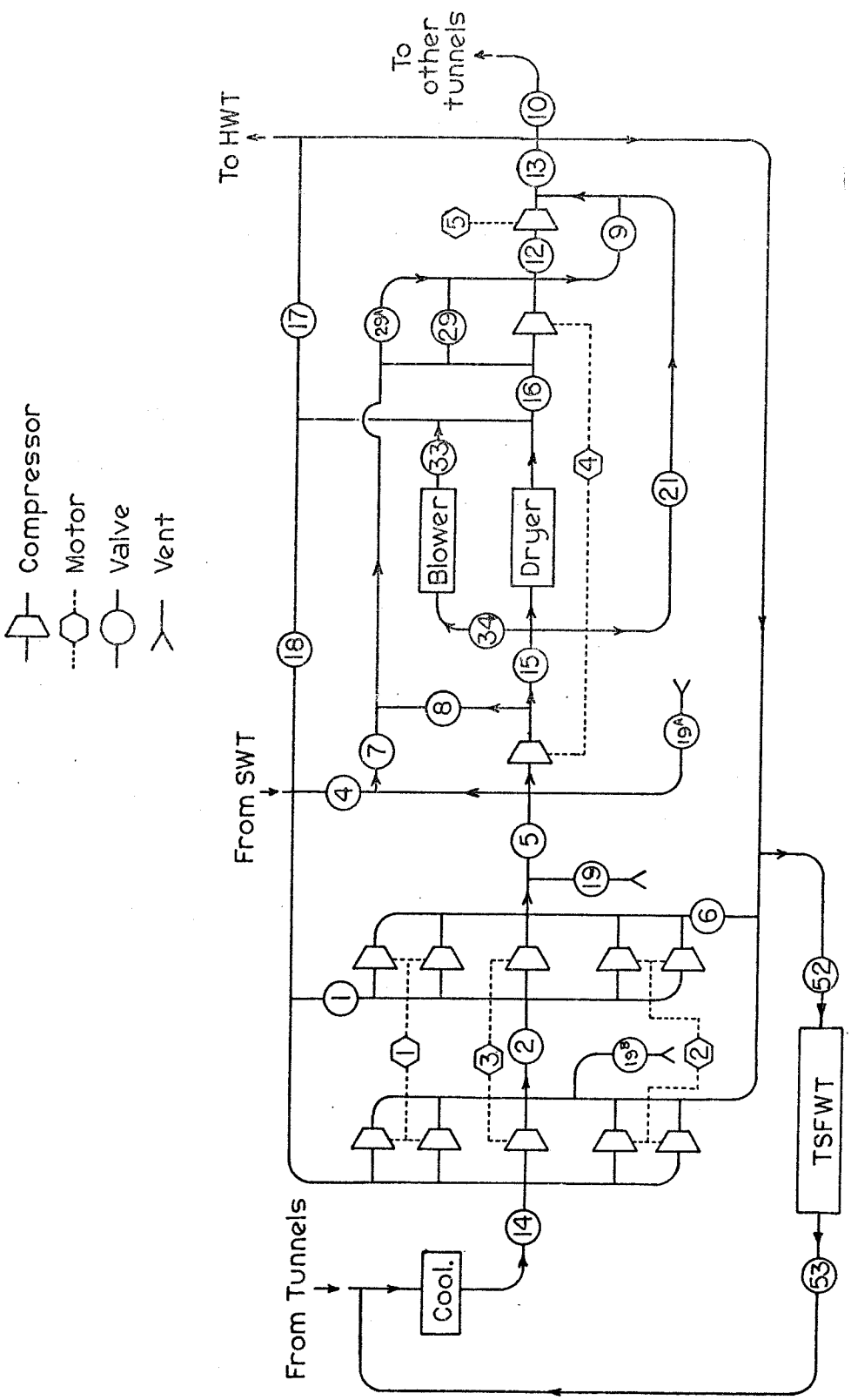

Figure 2.1: Transonic Shear Flow Wind Tunnel Air System

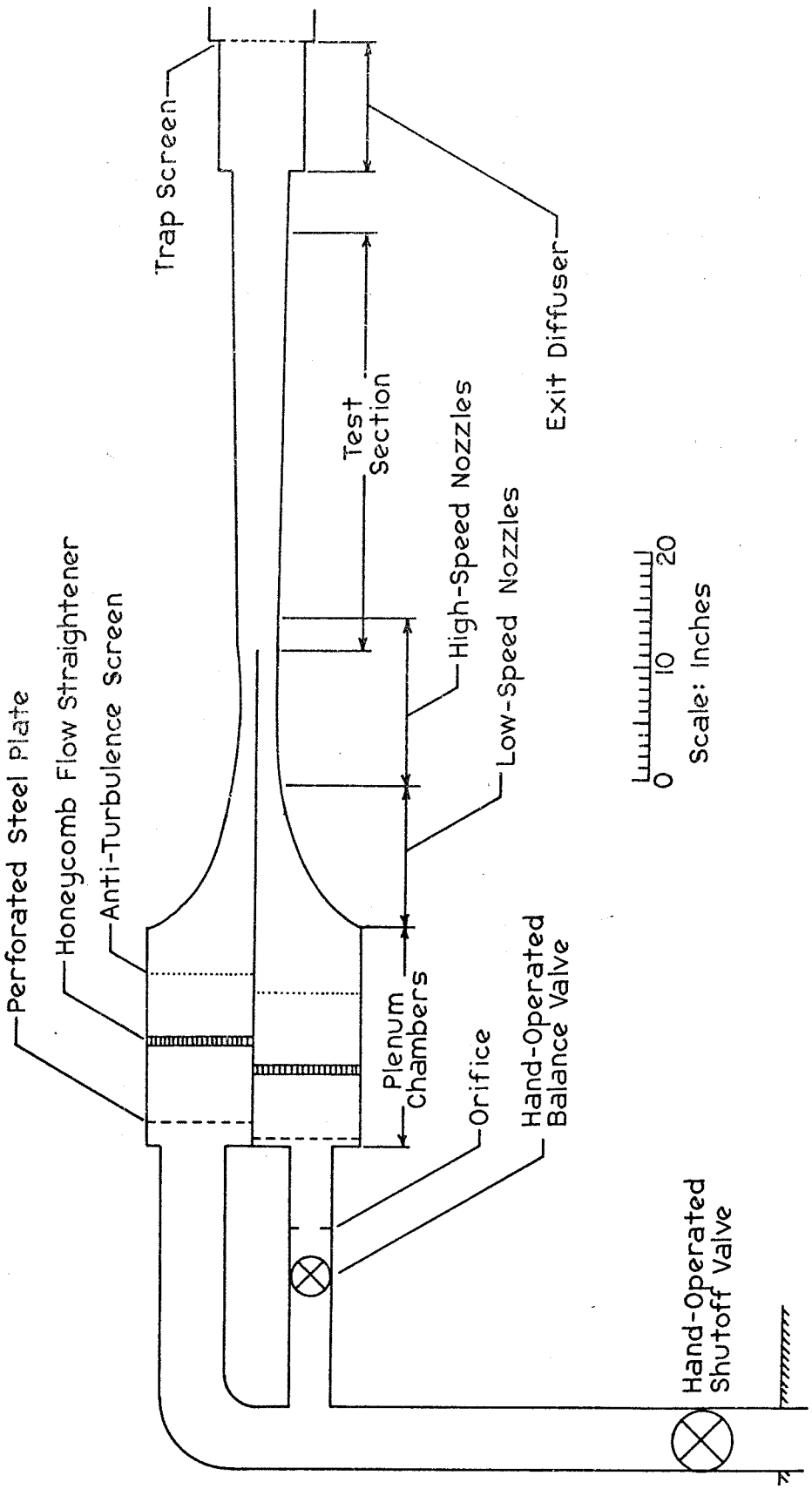

Figure 2.2: Transonic Shear Flow Wind Tunnel Installation

ing. The main feedline branches into two lines, eventually destined for the supersonic and subsonic nozzles (also referred to as the upper and lower nozzles, feedlines, etc., respectively, in reference to their installed positions). The upper feedline runs directly into the upper plenum chamber, while the lower feedline first passes through a hand-operated valve (used for flow regulation) and a fixed orifice of 3.01 inches inside diameter (used to cause the necessary loss of total pressure for equal static pressures at different Mach numbers) and then delivers its air to the lower plenum chamber.

Upon entering the plenum chamber, the jet of high-speed air is broken up by a perforated steel plate, and then passes through a honeycomb grid and a fine mesh screen in order to reduce the turbulence level. Depending on the number of wind tunnel runs since the brass screen was last cleaned, the loss of total pressure through the plenum chamber ranges from .05 psi to 1.0 psi (when the loss reaches 1.0 psi, cleaning is considered mandatory).

Upon leaving the plenum chambers, the air goes through two identical nozzles which accelerate it to Mach 0.5, and then through a converging-diverging nozzle (upper stream) or a converging nozzle (lower stream) which provide the final test section flow. At the nozzle exits, the streams should have the same static pressure and Mach numbers 1.4 and 0.7. The valve in the lower feedline is adjusted as necessary to control the total pressure in the subsonic stream. The splitter plate separating the upper and lower flows is 1/4 inch thick in the plenum chambers and low-speed nozzles, and 1/16 inch thick in the high-speed nozzles, ending with a 3° taper;

the trailing edge is at the nozzle exit plane and is blunted .005 inch.

The test section is 50.00 mm (1.969 inch) wide, and is 100 mm high (50 mm for each stream) at the nozzle exit plane, expanding slowly by means of adjustable top and bottom walls from 100 mm high at the nozzle exits to 100 mm to 120 mm high at the downstream end of the test section. The test section is 1 meter long (about 40 inches) with its upstream end being at the nozzle exit plane. Two types of sidewalls are available, both running the full length of the test section: steel, to permit pressure measurements or model attachment as necessary; and glass, to permit the use of schlieren system, shadowgraph, or other optical measurement techniques. Pressures are read out electronically using transducers. Flow properties important to the operation of the tunnel, such as supply pressure, plenum pressure, accuracy of balancing the exit pressure of the two nozzles, and pressure loss through the upper plenum chamber, are continually monitored through a set of pressure gauges. A telephone links the wind tunnel with the adjacent control room where the operation of the compressor plant is controlled and monitored.

The tunnel-based coordinate system used for recording data is depicted in Figure 2.3. A traversing strut, capable of making static or pitot pressure measurements in the $z = 0$ plane (wind tunnel centerline) versus y for several values of x, has been used to survey the shear layer. In addition, because the cross-section of the strut is approximately that of a double-wedge airfoil, qualitative observations of the flow with the strut installed were used in conjunction with the airfoil studies.

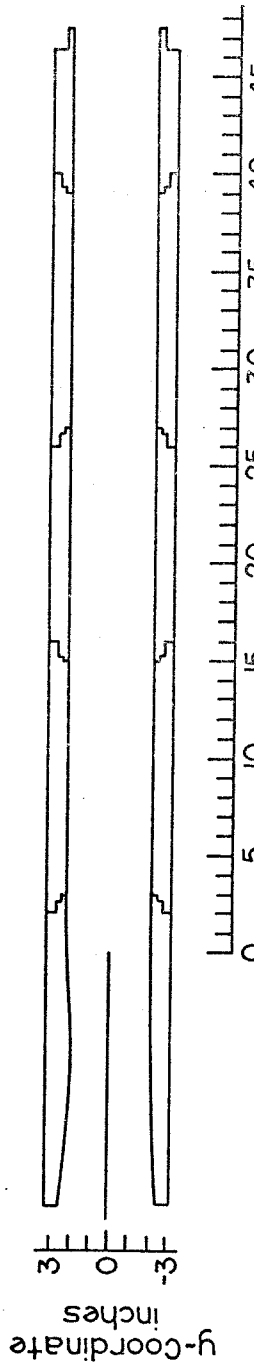

Figure 2.3: Test Section and Coordinate System (z-coordinate conforms to a right-hand system)

A schlieren system is attached to the tunnel and has given useful qualitative results on Polaroid film, though admittedly the system quality is rather poor. Static pressure taps have been installed in the walls in large number. These taps, through banks of toggle valves and hand-operated Scanivalves, can be interrogated individually and read by means of the pressure transducer.

On leaving the test section, the air enters the eight-inch diameter exit diffuser, where the supersonic stream shocks down to subsonic velocity and the two flows mix thoroughly. A 1/4-inch mesh copper screen is installed at the downstream end of the exit diffuser to trap any free objects that might otherwise be swept into the compressors. From the screen, the exit line returns to the compressor plant in the Guggenheim sub-basement, on the floor immediately below the wind tunnel.

The test section sidewalls are readily removable, as are two of the three sections forming the top and bottom walls of the test section. These parts, known as the first and second removable sections, span the distance from x = 3 inches (i.e., 3 inches downstream of the plane of the nozzle exits and the splitter plate trailing edge) to x = 15 inches and from x = 27 inches to x = 39 inches, respectively. The center section, from x = 15 inches to x = 27 inches, is also removable, though with somewhat more difficulty. Figure 2.3 is a section view of the tunnel cut on the z = 0 plane to show the arrangement of the top and bottom wall sections, and Figure 2.4 is a cut through a representative plane of x = const., showing the arrangement of the sidewalls, top and bottom walls, and their supporting structure.

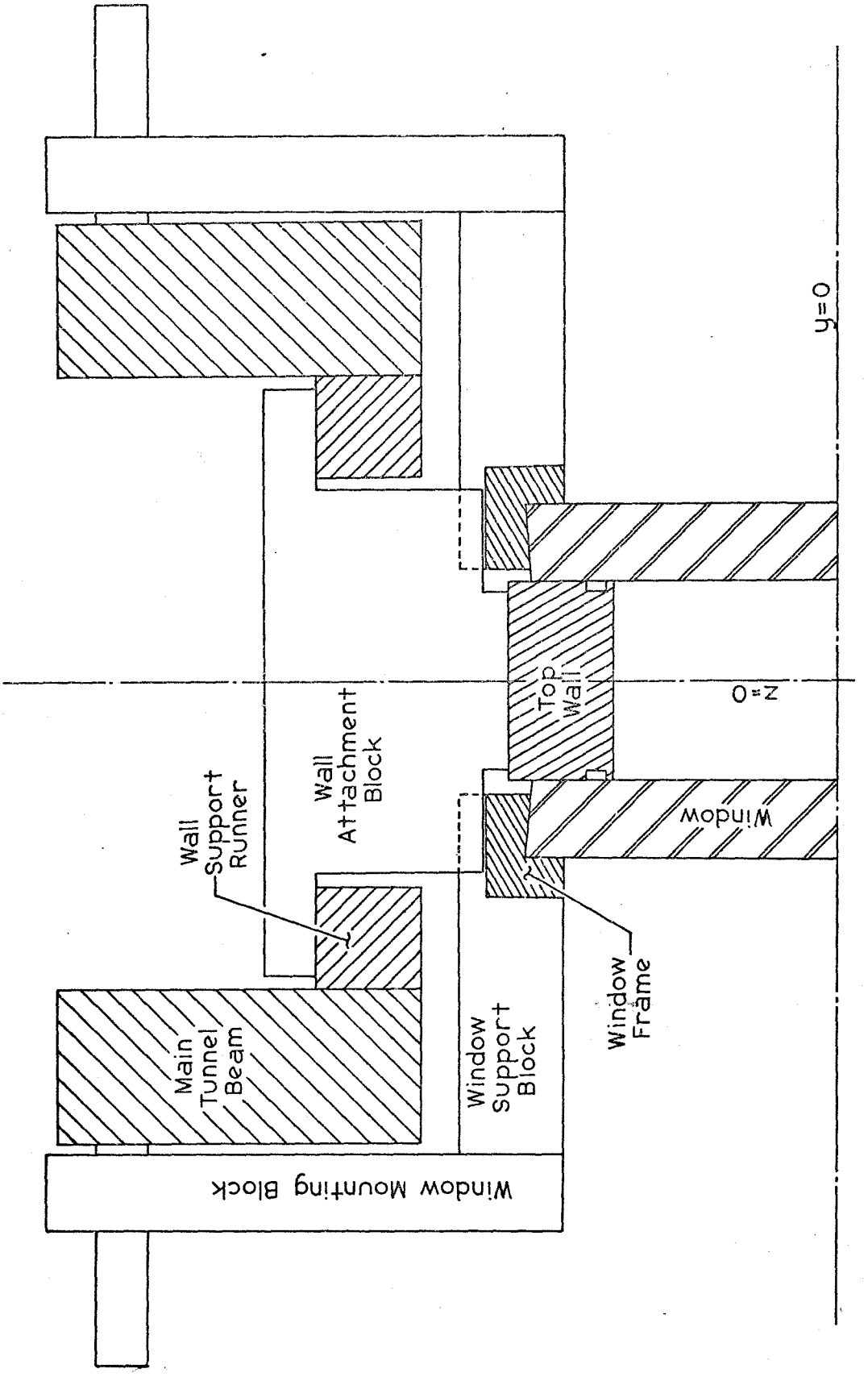

Figure 2.4: Vertical Cross-Section of Wind Tunnel

2.2 Operation

Table A. 1 (Appendix A) lists all runs of the Transonic Shear Flow Wind Tunnel through the completion of this project. The first run was on 19 March 1973, and Runs 1 through 25 were mainly concerned with the shakedown of the wind tunnel and the evolution of operating procedures, although data from Runs 14 through 21 have also been used in this report. Some runs after Run 26 yielded no data; these are noted in Table A.1. The normal operating procedures are given in Appendix A, which is largely taken from an operation and maintenance handbook prepared by the author.

The usual data returned from the tunnel are wall static pressures. Holes of 1/16-inch diameter were drilled into the wall from the outside of the tunnel, almost to the inner face. A drill of .020- to .030-inch diameter was used to complete the tap to the inner surface, and burrs were removed with a fine stone. A brass tube was force-fit into the 1/16-inch hole and sealed with epoxy so that about an inch protruded from the wall. To promote sealing, an epoxy ring was painted around the outside of the tube near the open end, and a vinyl plastic tube was slipped over this after the epoxy had hardened. The plastic line is run into either a bank of toggle valves or one of several 24-pole, single-throw Scanivalves, which can be switched by hand as desired to interrogate an individual pressure tap. Response times, depending on the length of the line to a specific tap, range up to a couple of seconds. As no attempt has been made to measure time-varying phenomena in the test section, this response is considered quite satisfactory.

Readings are made to an accuracy of 0.1 per cent by the Statham pressure transducer, which is driven by a standard power supply built previously at Caltech, and read by a digital voltmeter. Occasionally, readings accurate to 0.5 per cent are made using an x-y plotter.

Before a run, the air in the circuit is dried out overnight to lower its dewpoint to the neighborhood of -60° F. The air supply is at ambient total temperature (about 80° F) and is delivered from the compressors at approximately ambient total pressure (14.3 psia at Pasadena's altitude) though various flow losses reduce the total pressure to about 12.0 to 12.5 psia by the time the air reaches the plenum chambers immediately upstream of the nozzles. These flow losses turned out to be about twice what was expected during the design phase, and are considered responsible for the under-performance of the subsonic nozzle. With an unanticipated loss of total head, the velocity in the lower plenum chamber is less than intended, and consequently the Mach number at the exit of the subsonic nozzle is less than designed.

III. EMPTY WIND TUNNEL DATA

3.1 General Discussion

Once assembly of the Transonic Shear Flow Wind Tunnel was complete, the immediate goal was to gain familiarity and confidence in the tunnel and to develop the proper operating procedures. These procedures are described in Appendix A. This task began with the first run on 19 March 1973 and was completed with Run 24 on 5 September 1973.

The compilation of research data used for this report commenced with Run 26 on 10 October 1973 (Run 25 on 8 October 1973 was intended to provide research data but was aborted). The general goal of the empty-tunnel runs was to assemble a body of reference data concerning the nominal flow to be expected, so that comparisons could later be made to see the effect of various models on the overall flow field.

First, the strut mentioned in the previous section was used to survey the shear layer by means of a pitot probe at four stations, varying from $x = 4.19$ inches to $x = 28.18$ inches. Shadowgraph studies of the shear layer were also performed. The results of these experiments will be described in the next section.

The other phase of the empty-tunnel runs was to determine the schlieren and wall-pressure measurements that would be found when no model was present in the tunnel. Several runs were performed in the process of locating and stopping numerous troublesome leaks before any valid data were obtained. Also, it was determined that certain leaks were inherent in the design and consequently could only be

minimized, rather than completely stopped. This was especially noticeable in the seals at the upstream and downstream ends of the windows. No reliable method of completely suppressing leaks at these positions was ever found, though judicious use of electrical tape and grease was definitely helpful. Once it was felt that the best practical procedures had been found, the studies of the empty-tunnel flow proceeded quickly. This portion of the results is described in Section 3.3.

Several additional relevant studies were performed which, while they were generally computational rather than experimental in their basis, provide additional interesting detail concerning the fluid mechanics evident in the wind tunnel. These data, which discuss such questions as the range of application of linearized theory, considerations of the generalized choking condition for a non-uniform stream, and the effect of subcritical blockage, are discussed in Section 3.4.

3.2 Shear Layer

The first data taken in the Transonic Shear Flow Wind Tunnel were pitot pressure surveys through the shear layer in the center of the tunnel at four streamwise positions (pitot strut centerlines at $x = 5.75$ inches, 12.25 inches, 21.00 inches, and 29.75 inches). These raw pitot pressure profiles were measured with an open-ended 1/32 inch O. D. tube aligned with the flow, attached to a strut passing vertically across the tunnel. The strut cross-section is a double-wedge with a flat in the center at the point of maximum thickness,

1/16 inch. This causes a tunnel blockage of 3.18 per cent. A hollow tube runs down inside the strut, connected to the pitot tube at one end and a pressure transducer at the other. The pitot tube projects $1\frac{1}{2}$ to 2 inches ahead of the strut centerline. The strut can be moved vertically (i.e., along its axis) by a traversing mechanism mounted outside the wind tunnel. This mechanism permits traverses at rates as slow as .0005 in./sec., and via a potentiometer permits position readout accurate to .001 inches. The transducer output versus vertical position (y-coordinate) for the four streamwise (x-coordinate) positions is presented in Figure 3.1.

The static pressure was measured at the top and bottom walls in the immediate vicinity of the pitot measuring plane. Generally, these pressures were the same to the measuring accuracy of the system (0.01 psia, 0.3 per cent), but where they differed slightly it was assumed that the subsonic wall pressure was valid all across the subsonic stream (a good assumption, as it turned out) and that in the supersonic stream the static pressure varied linearly from the subsonic wall pressure at $y = 0$ (approximately the sonic line) to the supersonic wall pressure. Figure 3.2 shows sidewall pressure measurements for an empty-tunnel run which indicates the accuracy of these assumptions. The error in the assumed static pressure distribution is generally negligible in the subsonic stream and of the order of one per cent in the supersonic stream. From these data, the Mach number profiles of Figure 3.3 were calculated and distributions of velocity were found. These curves should be accurate to 0.3 per cent in the subsonic stream and 1.3 per cent in the supersonic stream.

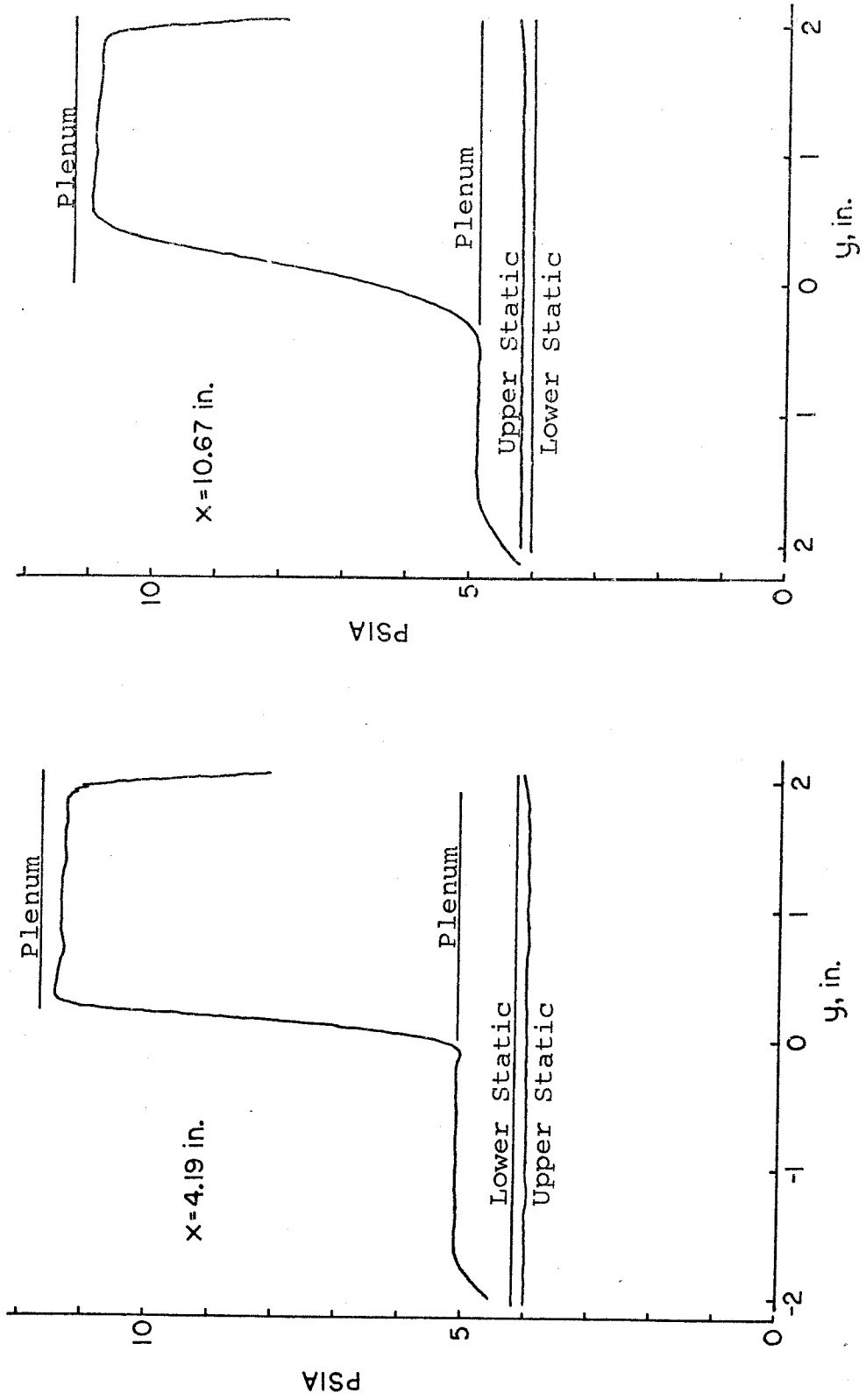

Figure 3.1: Pitot Transducer Output

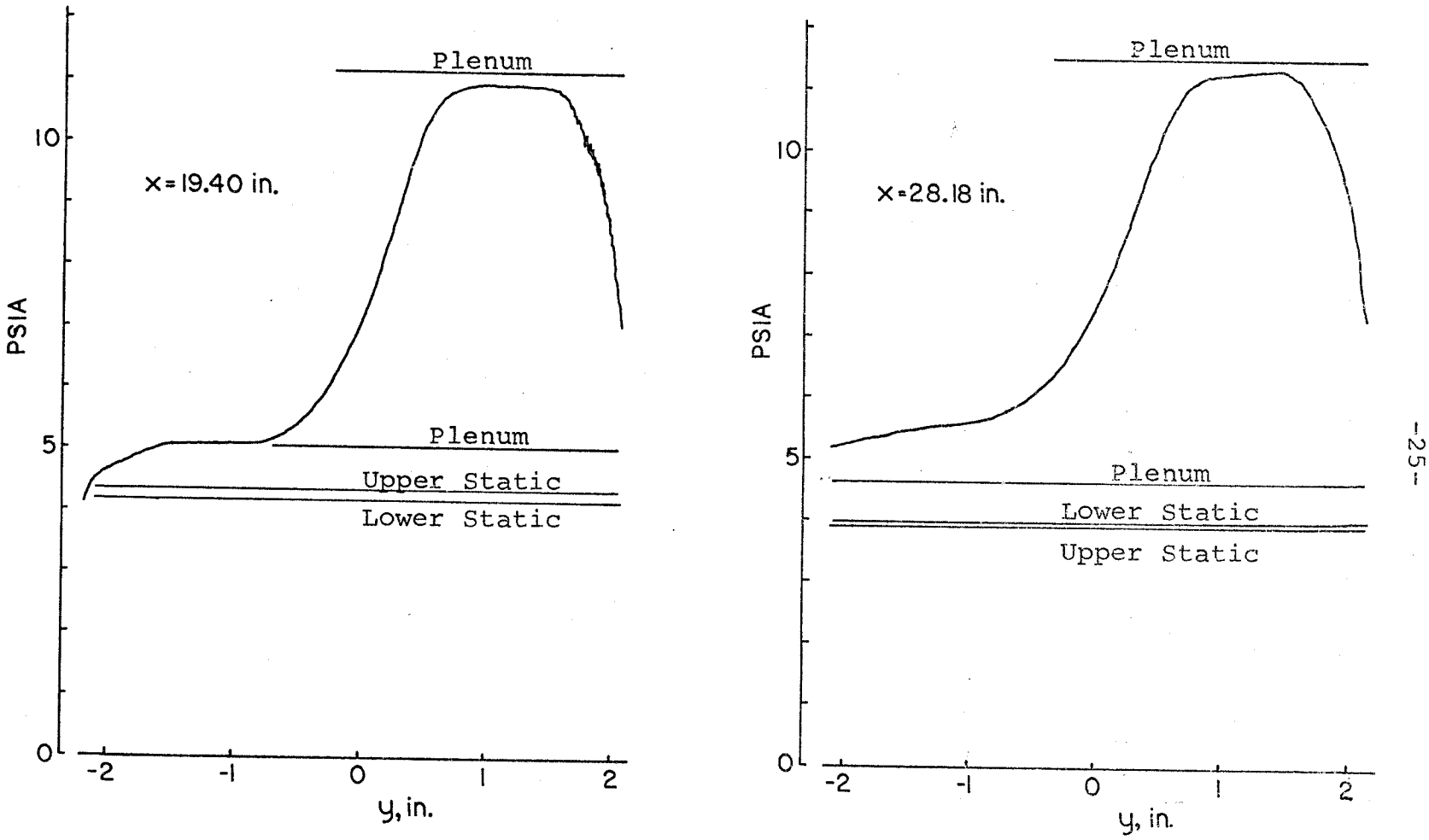

Figure 3.1, cont'd.: Pitot Transducer Output

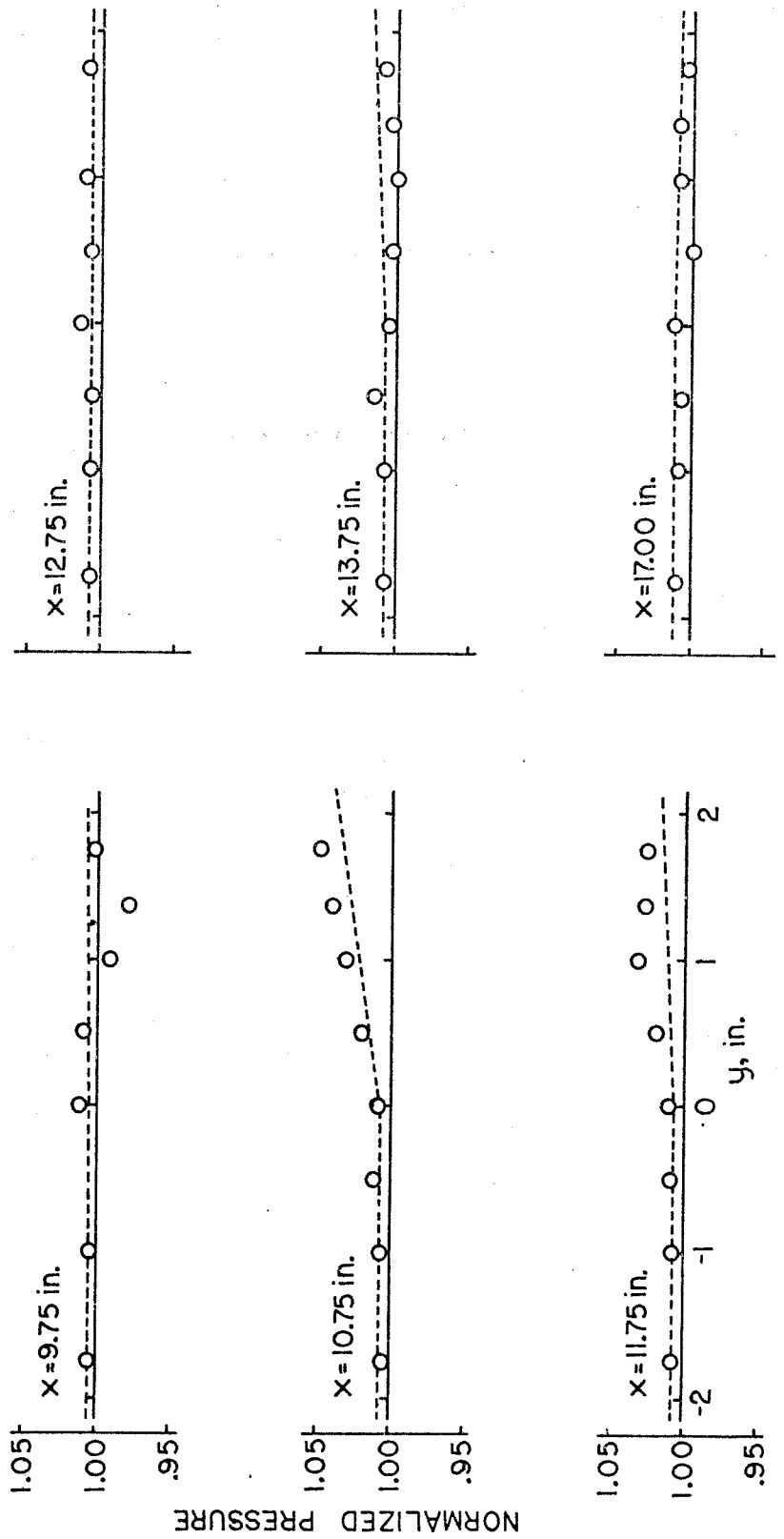

Figure 3.2: Empty-Tunnel Sidewall Pressure (Comparing measured and assumed static pressure profiles, Run 94)

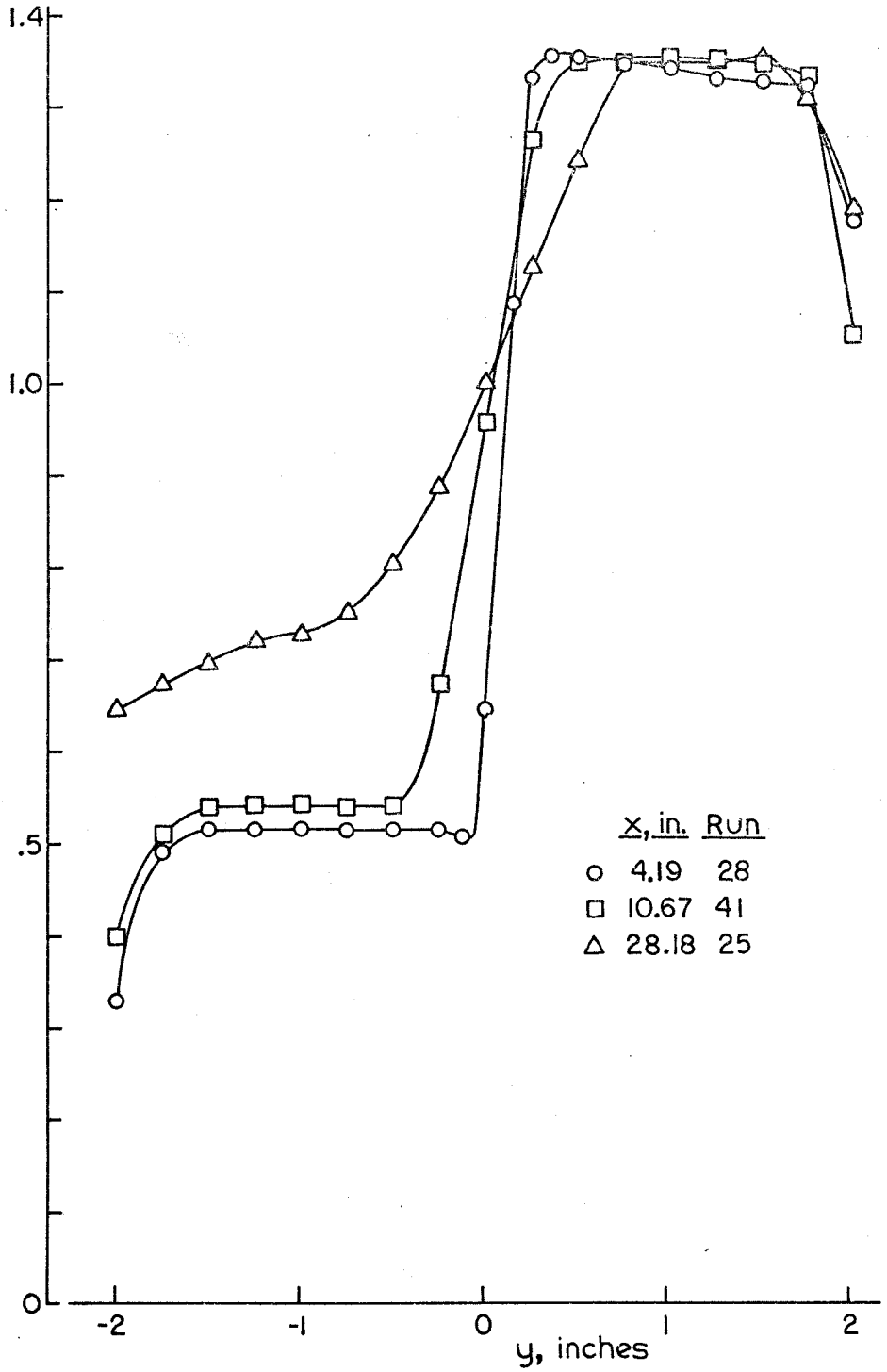

Figure 3.3: Mach Number Profiles

By offsetting the pitot probe from the centerline of the tunnel toward a sidewall, the two-dimensionality of the unperturbed flow at x = 17.85 inches, somewhat downstream of the point where models are installed, is verified (see Figure 3.4).

Next, an attempt was made to check for similarity in the velocity distribution by plotting the profiles against the usual similarity parameter. The results are shown in Figure 3.5. The maximum-slope velocity thickness, δ_s, was also calculated and is presented in Figure 3.6. These figures taken together suggest the shear layer exhibits similarity for x less than 14 inches, growing at a rate of

$$\frac{d\delta_s}{dx} = .062 ,$$

and then changes to a mean growth rate of

$$\frac{d\delta_s}{dx} = .029 .$$

Presumably this change in $(d\delta_s/dx)$ reflects the point at which the shear layer and boundary layer begin to interfere with each other; however, the figure previously mentioned in support of two-dimensional flow at x = 17.85 inches shows that this interference must be quite minor for some distance beyond x = 14 inches. In making comparisons to the results of other shear layer experiments, it seems valid to talk about the first region of shear layer growth only, where the effects of interference presumably are inconsequential.

For $M_1 = 1.4$ and $M_2 = 0.6$, the velocity ratio becomes $(U_2/U_1) = 0.489$, and the density ratio is $(\rho_2/\rho_1) = 0.770$ under the assumption that the total temperature is the same in each stream. Brown and Roshko [13] give a best-fit line for low Mach number shear

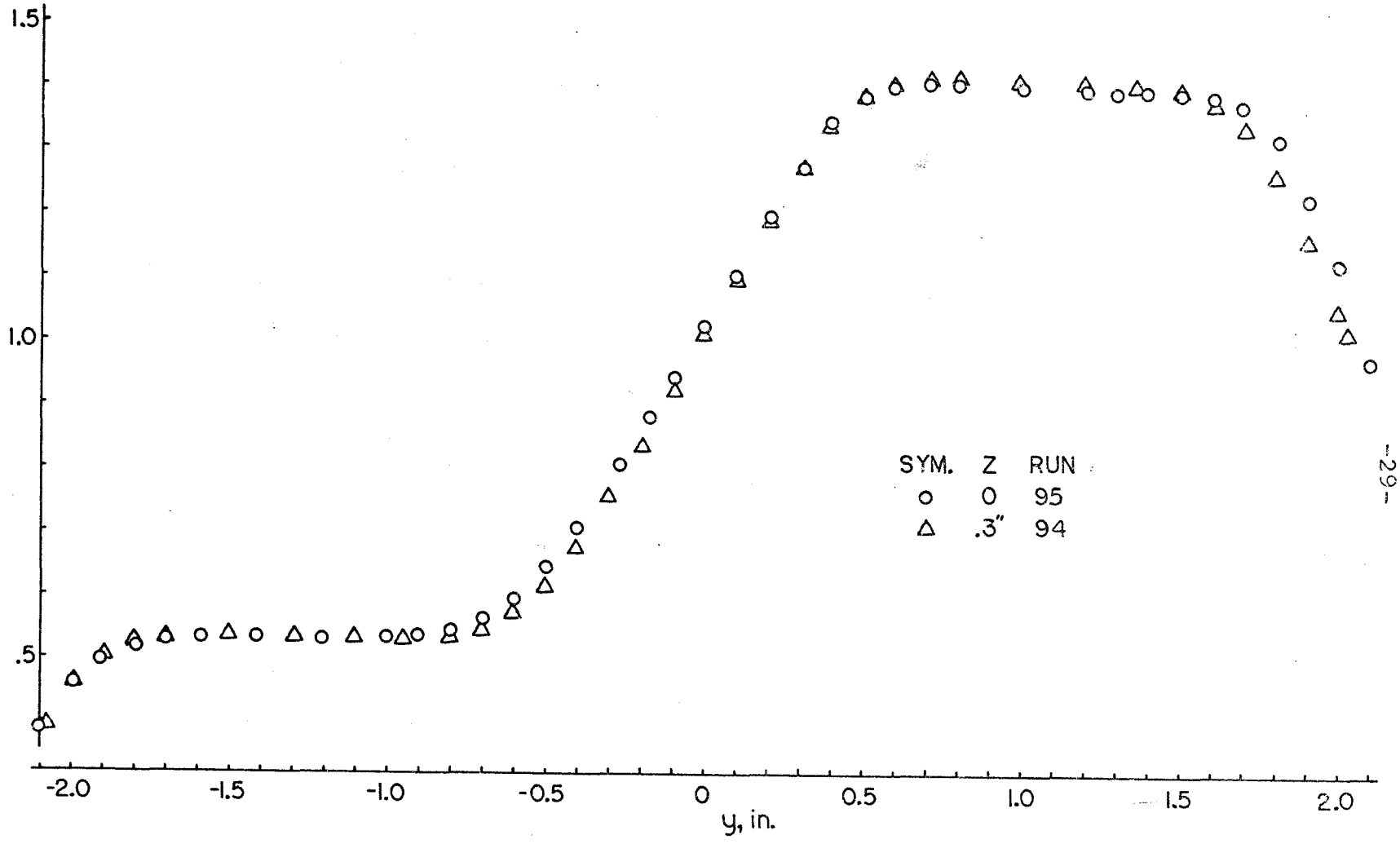

Figure 3.4: Mach Number Distribution at x = 17.85 inches on z = 0 (centerline) and z = 0.3 inch

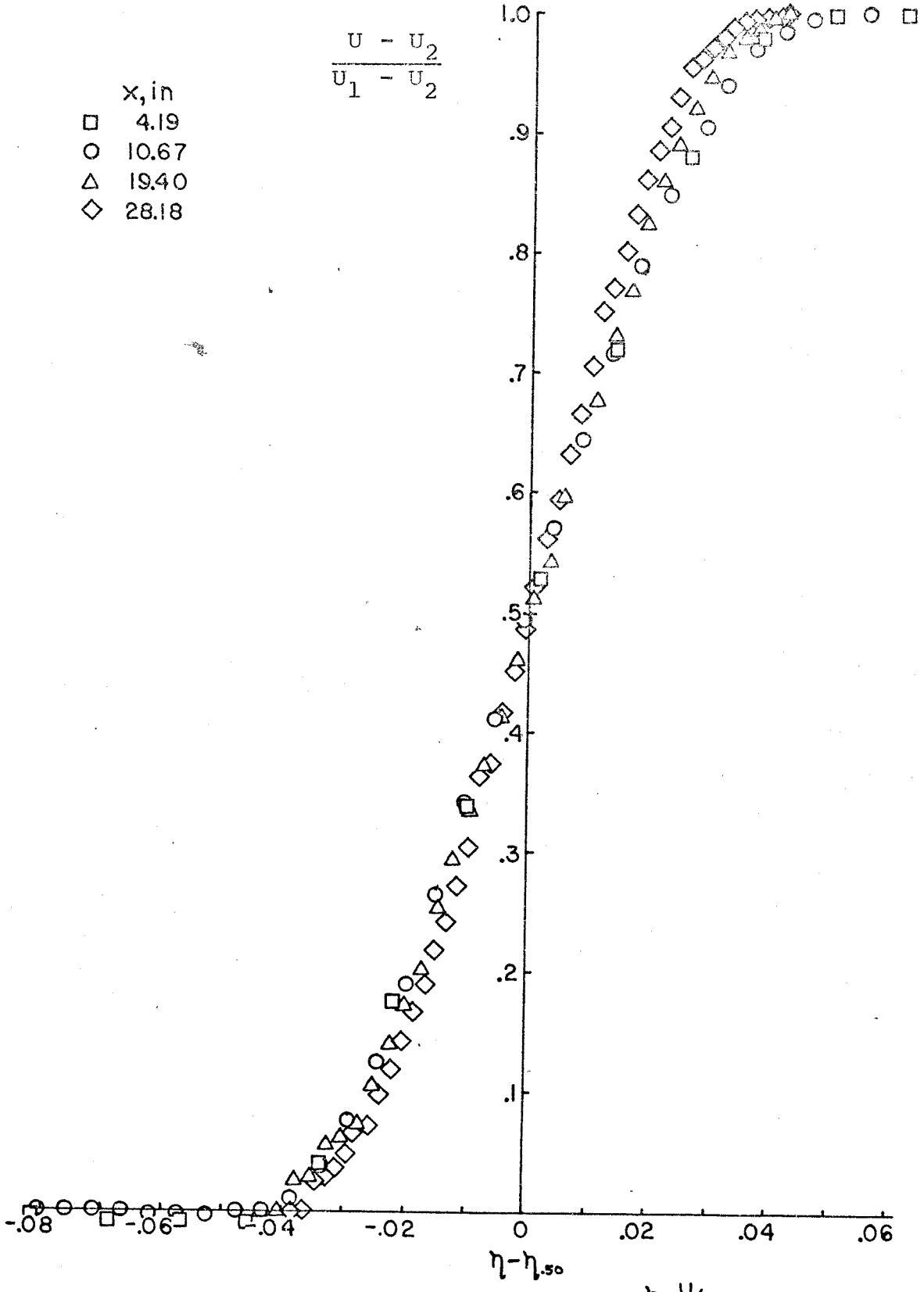

Figure 3.5: Similarity Velocity Profiles

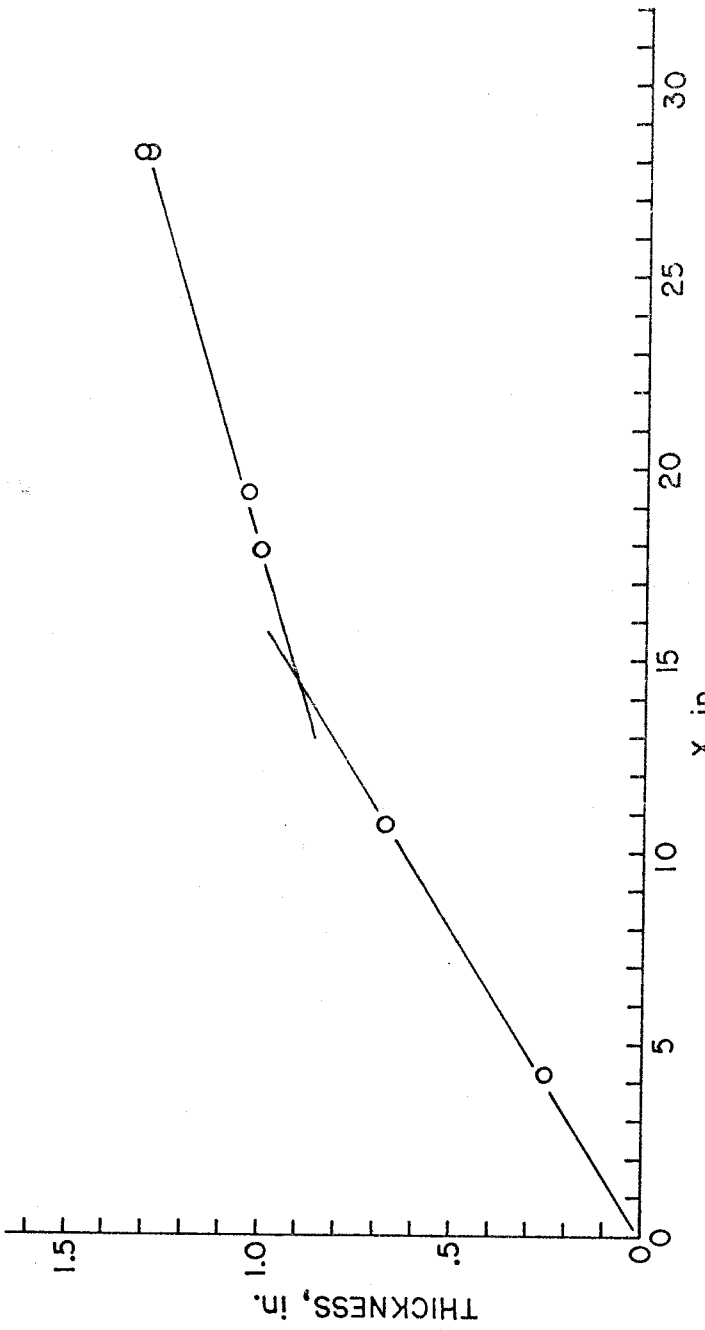

Figure 3.6: Shear Layer Thickness Distribution (Calculated by maximum-slope method based on Mach number)

layer data:

$$\frac{d\delta_s}{dx} = 0.181 \frac{1 - U_2/U_1}{1 + U_2/U_1} \qquad (3.1)$$

with RMS deviation of .015 in the coefficient. For the case in question here, this expression reduces to

$$\frac{d\delta_s}{dx} = .062 \pm .005 \ ,$$

which agrees well with the measurement in the initial growth region.

While the shear layer is transonic to an observer in a stationary reference frame, to an observer moving with the low-speed flow, the high-speed flow appears subsonic (at a Mach number of 0.716). Maydew and Reed [14] conclude for compressible axisymmetric jets into still air that as long as the jet core is subsonic relative to the surrounding fluid, the Mach number has no perceptible effect on the spreading rate. This can also be seen in Brown and Roskho (Figure 15, Reference 13) which shows that for a subsonic relative Mach number, the spreading rate for a compressible flow is the same as for incompressible flow at the same density ratio across the shear layer.

The graph of Figure 3.7, based on the reference just cited, estimates the effect of compressibility (as measured by M_1', the Mach number of the high-speed side relative to the low-speed side) on the shear layer spreading rate. This effect will be measured by the function $f(M_1')$. The effect of density ratio and velocity ratio from the same reference can be combined with the compressibility effect to give a modified form of eq. (3.1):

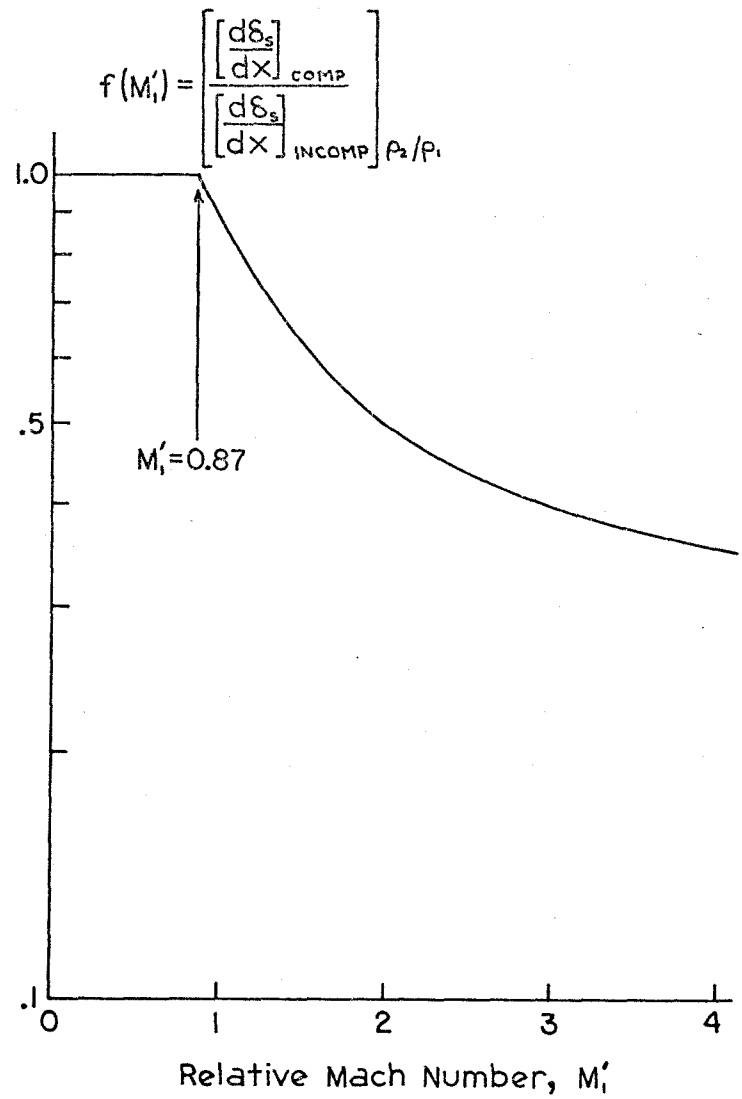

Figure 3.7: Effect of Compressibility on Shear Layer Spreading Rate (Based on Reference 13)

$$\frac{d\delta_s}{dx} = 0.181\left(\frac{\rho_2}{\rho_1}\right)^{0.153} f(M_1') \frac{1 - U_2/U_1}{1 + U_2/U_1} \qquad (3.2)$$

again with RMS deviation of ±.015 in the coefficient. This new relation reduces to a nearly identical result:

$$\frac{d\delta_s}{dx} = .060 \pm .005 \ ,$$

which now embraces the compressible-flow data cited by Brown and Roshko. It should be noted that eq. (3.2) has only been fitted to data in which the entire flow has the same total temperature.

The preceding discussion is valid only if the mixing layer is planar. In a wind tunnel, this means the thickness of the shear layer must be considerably less than the width of the tunnel (b) so that the main characteristics of the shear layer are not affected by its finite width. In other words, the aspect ratio $A = b/\delta_s$ must be considerably greater than one. A breakdown in this assumption as δ_s increases and A decreases is seen in Figure 3.6 in the range from x = 11 inches (A = 2.9) to x = 18 inches (A = 2.0). Presumably this change is more gradual than the straight lines which have been fitted to the data in the figure.

It should also be noted that Maydew and Reed [14] and Siriex and Solignac [15] conclude that up to low supersonic Mach numbers (say, M_1' less than 2), compressibility has little effect on the shape of the velocity profile. This effect, not included in eq. (3.2), sets a limit on M_1' for validity of this expression, and results in an overprediction of the spreading rate for higher relative Mach numbers.

3.3 Empty-Tunnel Measurements

At the first complete run of the wind tunnel, it became apparent that the flow without any model present would still have a certain inhomogeneous structure and would not conform to the ideal of uniform, constant-pressure flow. Thus, an early task was to gain an understanding of the empty-tunnel flow field in order to distinguish later which observed effects were inherent in the tunnel and which were due to a specific experiment. It was hoped that in the process of making these measurements, a high level of repeatability would be demonstrated.

Two phenomena are consistently present in the empty tunnel: a shock system originating at the trailing edge of the splitter plate ($x = 0$) which causes certain slight periodic pressure disturbances on the subsonic wall for the first 12 to 15 inches of the test section; and a constant-rate drop of static pressure throughout the remainder of the test section. If the windows or sidewalls were installed with even a slight offset (say, 0.005 inch) they likewise set up a shock system persisting downstream through several cycles of reflection off the walls. These phenomena will be discussed individually.

First consider the shock system which is created at the trailing edge of the splitter plate. The initial shock and its first reflection show up very clearly on schlieren photographs and on supersonic wall and sidewall pressures. On reflection into the supersonic stream off the wall, the wave becomes sufficiently diffuse due to the wall boundary layer that it is barely visible in schlieren photographs, and it becomes completely invisible after the next reflection off the

shear layer. However, its continued presence can be noted in supersonic wall pressure measurements through several complete cycles of reflection off the wall and the shear layer (see Figure 3.8a).

Primarily, this shock is created by the geometry of the splitter plate trailing edge. The splitter is smooth to the trailing edge on the supersonic side, but is tapered upward at a 3^{o} angle on the subsonic side, and ends with a blunt edge where its thickness is approximately 0.005 inch. The trailing edge was blunted slightly as a safety precaution in view of the work to be performed manually in the test section close to the splitter plate between runs.

Two characteristics of the shock are significant. First, the shock is fully formed no more than 1/8 inch downstream of the trailing edge. This makes it seem unlikely that it might result from a coalescence of small-amplitude compression waves, which in turn cases doubt on the possibility that it is created in some way by the boundary-layer wake flow downstream of the splitter. In addition, no related expansion fan is visible in the schlieren system, as would be expected in a supersonic wake collapse. Second, measurements of both the shock angle and the wall pressure rise after reflection, together with the computed Mach number at the nozzle exit, indicate the shock has a deflection angle of 0.8^{o} to 1.0^{o}.

The primary mechanism responsible for the creation of this shock seems to be the 3^{o} up-angle imparted to the subsonic stream in the immediate vicinity of the trailing edge due to the taper of the splitter plate. Estimates of shock strength can be made by balancing the net momentum vectors of both streams before and after the shock.

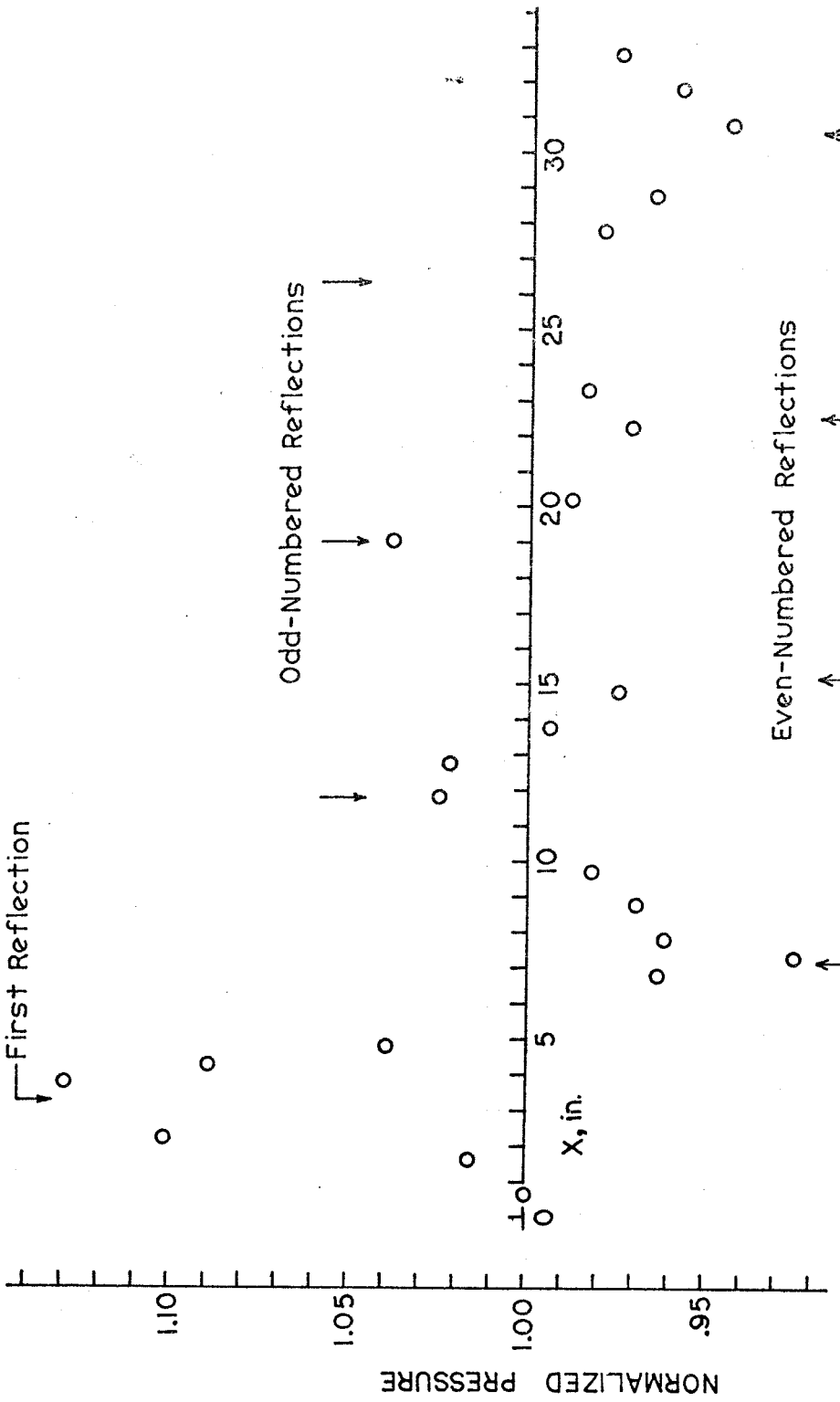

Figure 3.8a: Empty-Tunnel Supersonic Wall Pressure (Run 53), identifying reflections of the splitter plate wave off the supersonic wall

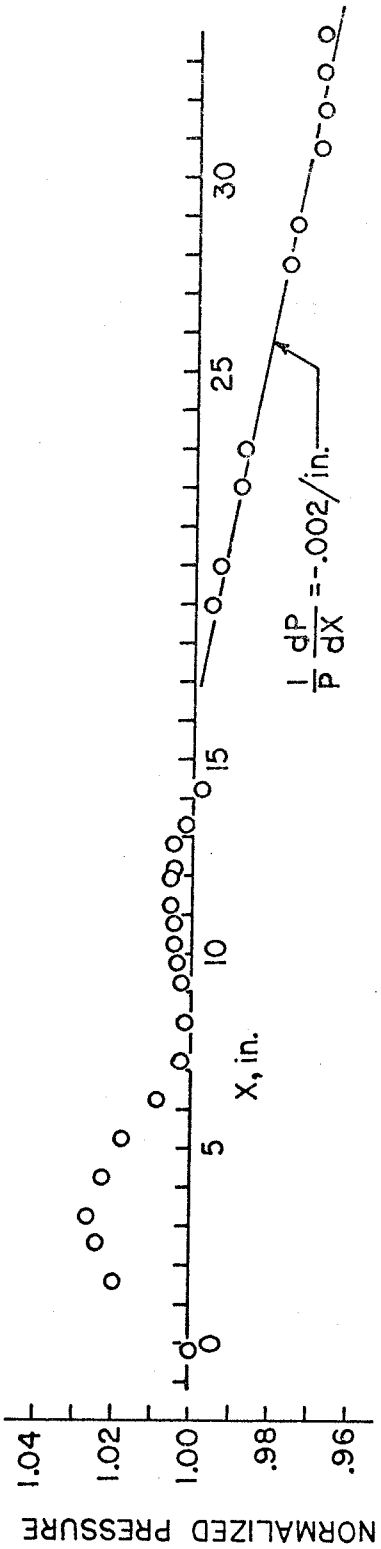

Figure 3.8b: Empty-Tunnel Subsonic Wall Pressure (Run 53)

This balance indicates that a flow deflection of 0.67° would be produced. This result is close enough to the calculated value to be consistent with the model. In addition, there is the effect of unequal mass entrainment in the splitter plate wake from the supersonic and subsonic streams, though this must have a relatively small influence. Eggers [16], Ikawa [17], and other investigators report that the rate of entrainment of mass decreases somewhat as Mach number increases. This is related to the observation of the previous section, that the spreading rate (related to the entrainment rate) of a shear layer decreases for increasing Mach number. Thus, the larger portion of the mass needed to fill in the wake from the splitter plate must be supplied by the subsonic stream, increasing the local up-angle of the subsonic stream immediately downstream of the trailing edge, and consequently increasing slightly the shock wave deflection angle.

The subsonic stream soon reaches equilibrium after its flow area has increased sufficiently to cause a pressure rise equivalent to that due to the shock. The shock wave, after reflecting off the supersonic wall, returns to the interface and reflects as an expansion fan at about x = 4 inches. The reader is referred to Chapter IV for a consideration of the mechanisms by which a shock reflects off the shear layer. Considering that the supersonic wave changes sign at each reflection from the shear layer, the entire pattern should repeat at intervals of about 8 or 9 inches, with a considerably reduced amplitude at the subsonic wall on successive cycles, due to attenuation at each reflection. In fact, these wave disturbances are not distinguishable on the subsonic wall after about 15 inches (i.e., two

wave cycles). The disturbances on the supersonic wall are more persistent.

The second phenomenon in the empty tunnel consistently present is a constant-rate decrease of subsonic wall static pressure (and, necessarily, overall mean test section pressure, though the effect is most apparent near the subsonic wall). This decrease starts at x = 15 inches (see Figure 3.8b) and has the slope

$$\frac{1}{p}\frac{dp}{dx} = -0.002/\text{inch.}$$

It may be recalled that the wind tunnel design allowed the top and bottom walls of the test section to be movable. When the tunnel was assembled, the walls were set at their maximum divergence. Apparently, this design-limited divergence was inadequate to cope with the combined effects of the spreading shear layer and the thickening boundary layers on all the walls. In any event, the one-dimensional analyses of the following section will show that to raise the test-section static pressure, the top and bottom walls should be diverged still further (about 4 mm, or .16 inch, at the downstream end of the test section). Unfortunately, the remedy of this deficiency would have required total disassembly and recalibration of the wind tunnel. The expense in time and money was not considered justifiable.

The pressure decrease rate was very repeatable between runs; the value quoted is accurate to 0.0003/inch. The splitter shock system was less repeatable, by far. The magnitude of the first pressure rise on the supersonic wall seemed to fall randomly anywhere between 0.08 and 0.14 (in terms of pressures normalized by the nozzle exit

static pressure). Qualitatively, the structure remained the same, but this annoying lack of repeatability, together with other effects mentioned in the following section, made quantitative comparisons of supersonic wall data very difficult.

Another source of non-repeatable pressure fluctuations which, however, could be suppressed with diligent effort, was due to the design of the interface in the $x = 0$ plane between the window (or steel sidewall) and the steel sideplates of the high-speed nozzles.

The windows fit against the upstream and downstream ends of the window cavity as plugs, with the ends cut at a 45° angle. This required a careful, iterative adjustment plus a certain amount of good luck to adjust the size of the opening just right so that the window butts up flat against the top and bottom walls all along the span of the test section, and with a thin gasket in place forms an airtight seal at the bevel at each end without applying too much stress at the ends (one window was broken in this manner). The difficulty under these circumstances of getting the installed, tightened-down window coplanar with the nozzle sidewalls without an air leak when the tunnel circuit was evacuated often resulted in a mismatch, which set up a long-persisting shock system that reflected from side to side down the length of the test section, impairing the usefulness of the data. Window effects were not noticeable, however, in data taken within the subsonic layer.

Redesign of the windows was considered in order to replace the bevelled-plug installation with some other geometry, such as a straight-sided plug with O-rings, but it was found eventually that

careful adjustment could control the problem and the redesigning efforts were not pursued.

3.4 Blockage and Choking Effects

In general, a gas flow is said to be "choked" at a particular station if the mass flow rate at that station cannot be increased by any changes downstream of the station. Thus, when the flow is choked, the maximum possible mass flow is passing through the area in question.

For one-dimensional flow, this corresponds to a "throat," or section of minimum area, at which the Mach number is one. It can readily be shown that the mass flow per unit area for specified upstream conditions is maximum at the sonic speed; so at a throat, the flow passage area determines the net mass flow for the entire system. From another point of view, the choking area for a specified flow is the minimum area through which the flow can pass consistent with the specified upstream conditions. The choking area of a specified inviscid, isentropic, one-dimensional flow is uniquely determined by the upstream flow properties. In a two-dimensional, inviscid, isentropic stream, however, the choking area depends additionally on the streamline curvature in the vicinity of the minimum-area section. Departures from one-dimensional flow will tend to reduce the choking mass flow rate. Effects such as boundary layers also tend to lower the choking mass flow.

The basic concepts just described are relevant to the consideration of choking for the two-stream system under consideration

here, although other effects must be considered as well. Consider the idealized model of an inviscid, irrotational, isentropic flow composed of two uniform streams flowing through a duct, separated by a shear (or vorticity) layer of zero thickness. The upstream flow properties are specified and remain constant for all perturbations of the flow in the region of interest. If the walls are gradually constricted, slowly enough that at a particular section the Mach number remains uniform across each separate stream and the pressure is uniform across the combined flow, then the situation is analogous to that described earlier as "one-dimensional" flow; that term will be employed in the two-stream case as well.

This two-stream, one-dimensional flow of course has some minimum area for changes of geometry consistent with the specified upstream flow; this is the choking area. In this case, however, neither stream is at sonic speed; stream 1 is still supersonic, and stream 2 is still subsonic. The necessary condition for choking is that the overall flow area be a minimum consistent with the upstream constraints, e.g. that the equation

$$\frac{dA_1}{dp} + \frac{dA_2}{dp} = 0 \tag{3.3}$$

or the relation

$$A_1 \frac{(M_1^2 - 1)}{M_1^2} = A_2 \frac{(1 - M_2^2)}{M_2^2} \tag{3.4}$$

be satisfied.

Since p, M_1, and M_2 are monotonically related to each other (total pressure is constant in each stream), either Mach number could

have been used instead of pressure in eq. (3.3) and eq. (3.4) would still have been obtained. Figure 3.9 presents choking margin (percentage reduction in overall flow area to cause choking) versus M_1 and M_2 for the two-stream system in which the streams have equal areas in the upstream condition. From this figure, one can readily see that the choking margin depends much more strongly on M_2 than on M_1. For $M_1 = 1.4$, the system is choked at $M_2 = 0.8195$ when upstream the condition is A_1 equal to A_2 and $M_2 = 0.6$. Tables 3-1a and 3-1b present computer-calculated choking-area ratios and normalized choking pressure for various values of the initial area ratio A_2/A_1, M_1, and M_2. Table 3-2 presents stream Mach numbers, pressure, and stream and net flow area for the case where initially the flow met the conditions $A_1 = A_2$, $M_1 = 1.4$, and $M_2 = 0.6$, which is approximately the experimental case that was investigated.

To determine the magnitude of the effect of the shear layer on the choking, a similar analysis was performed in which the shear layer was given finite thickness (comparable to the experimental case at the primary station of interest) and broken into 100 isentropic streams of equal area with a linear distribution of Mach number. The results of this are also presented in Figure 3.9. Although there is a consistent reduction of the choking margin due to the thickness of the shear layer, the reduction is relatively small. Thus, the errors introduced into the choking margin calculations by assuming the shear layer to have zero thickness are slight.

A decrease in flow area of greater magnitude than the choking margin would presumably have a large effect. It was assumed that

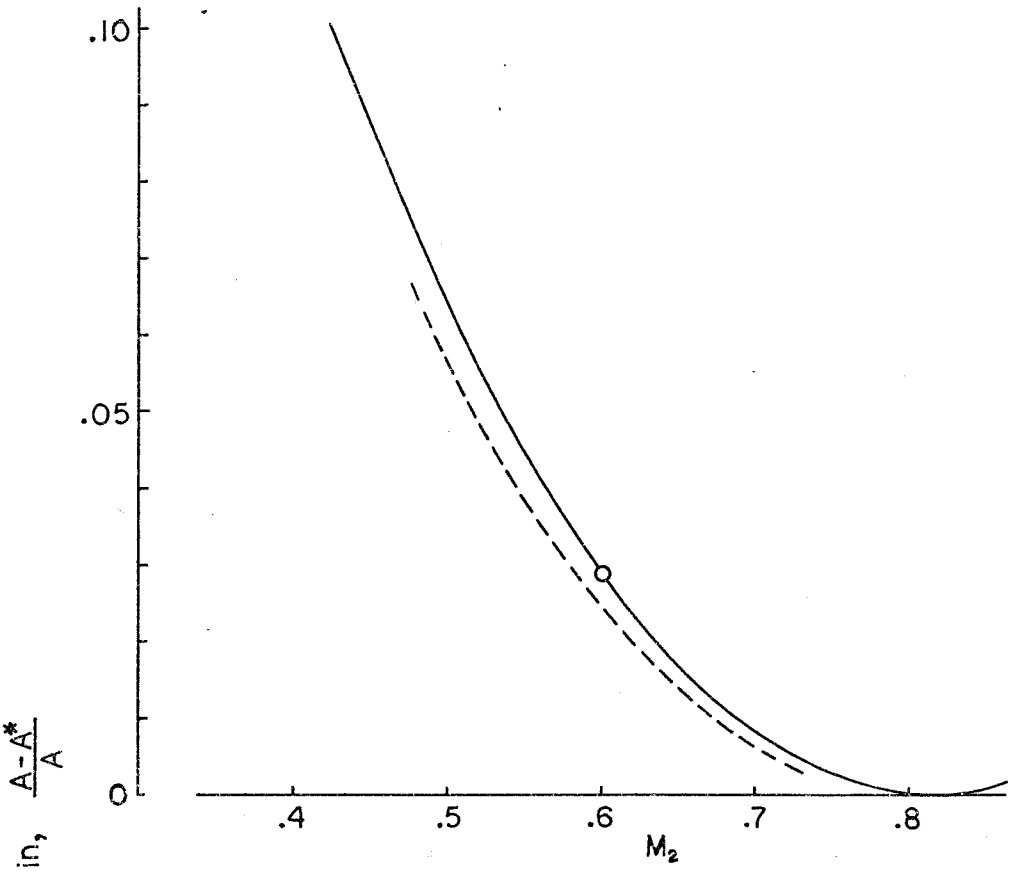

A. M_1 = 1.4: Solid line for shear layer of zero thickness; dashed line for 100-strip isentropic shear layer 0.62 inch thick

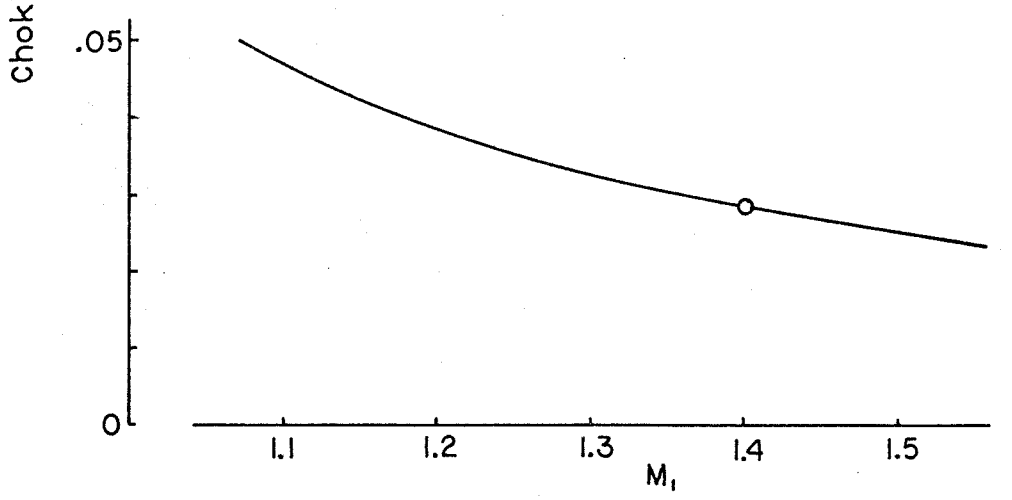

B. M_2 = 0.6: Shear Layer of Zero Thickness

Figure 3.9: Effect of M_1, M_2, and Finite Shear Layer Thickness on Choking Margin

INITIAL AREA RATIO (SUB/SUPER) = 0.90

M1	M2					
	0.45	0.50	0.55	0.60	0.65	0.70
1.05			0.9694	0.9678	0.9704	0.9788
1.10		0.9685	0.9572	0.9625	0.9724	0.9822
1.15	0.9456	0.9434	0.9519	0.9638	0.9755	0.9852
1.20	0.9262	0.9382	0.9526	0.9665	0.9784	0.9877
1.25	0.9213	0.9384	0.9548	0.9692	0.9810	0.9898
1.30	0.9211	0.9402	0.9573	0.9717	0.9831	0.9915
1.35	0.9224	0.9424	0.9597	0.9739	0.9850	0.9928
1.40	0.9243	0.9446	0.9619	0.9758	0.9865	0.9940
1.45	0.9262	0.9467	0.9638	0.9775	0.9878	0.9949
1.50	0.9281	0.9485	0.9655	0.9790	0.9890	0.9957

INITIAL AREA RATIO (SUB/SUPER) = 1.00

M1	M2					
	0.45	0.50	0.55	0.60	0.65	0.70
1.05				0.9685	0.9683	0.9765
1.10		0.9782	0.9571	0.9597	0.9694	0.9797
1.15	0.9514	0.9422	0.9482	0.9599	0.9722	0.9828
1.20	0.9234	0.9335	0.9476	0.9622	0.9750	0.9853
1.25	0.9154	0.9323	0.9494	0.9648	0.9776	0.9874
1.30	0.9137	0.9335	0.9516	0.9672	0.9798	0.9892
1.35	0.9143	0.9354	0.9539	0.9694	0.9817	0.9907
1.40	0.9158	0.9375	0.9561	0.9714	0.9833	0.9919
1.45	0.9176	0.9394	0.9580	0.9731	0.9847	0.9930
1.50	0.9194	0.9413	0.9597	0.9746	0.9859	0.9938

INITIAL AREA RATIO (SUB/SUPER) = 1.10

M1	M2					
	0.45	0.50	0.55	0.60	0.65	0.70
1.05				0.9702	0.9667	0.9745
1.10		0.9913	0.9584	0.9575	0.9667	0.9775
1.15	0.9604	0.9425	0.9453	0.9564	0.9691	0.9804
1.20	0.9222	0.9298	0.9433	0.9582	0.9718	0.9830
1.25	0.9105	0.9270	0.9444	0.9606	0.9744	0.9852
1.30	0.9072	0.9274	0.9464	0.9630	0.9766	0.9870
1.35	0.9070	0.9289	0.9485	0.9652	0.9785	0.9885
1.40	0.9081	0.9308	0.9506	0.9671	0.9802	0.9898
1.45	0.9096	0.9327	0.9525	0.9689	0.9817	0.9909
1.50	0.9113	0.9345	0.9543	0.9704	0.9829	0.9919

Table 3.1a: Choking Area Ratio

INITIAL AREA RATIO (SUB/SUPER) = 0.90

M1	M2					
	0.45	0.50	0.55	0.60	0.65	0.70
1.05	0.1483	0.3923	0.5689	0.6882	0.7694	0.8264
1.10	0.4513	0.5822	0.6811	0.7549	0.8104	0.8537
1.15	0.5944	0.6752	0.7406	0.7932	0.8361	0.8727
1.20	0.6713	0.7279	0.7764	0.8177	0.8539	0.8872
1.25	0.7176	0.7610	0.7998	0.8348	0.8673	0.8990
1.30	0.7480	0.7833	0.8163	0.8475	0.8779	0.9089
1.35	0.7690	0.7993	0.8285	0.8574	0.8867	0.9175
1.40	0.7844	0.8113	0.8381	0.8655	0.8942	0.9250
1.45	0.7962	0.8206	0.8458	0.8723	0.9006	0.9316
1.50	0.8054	0.8281	0.8522	0.8781	0.9063	0.9374

INITIAL AREA RATIO (SUB/SUPER) = 1.00

M1	M2					
	0.45	0.50	0.55	0.60	0.65	0.70
1.05	0.0770	0.3304	0.5277	0.6613	0.7515	0.8142
1.10	0.3948	0.5414	0.6521	0.7342	0.7954	0.8424
1.15	0.5550	0.6452	0.7180	0.7760	0.8227	0.8619
1.20	0.6411	0.7040	0.7574	0.8025	0.8414	0.8764
1.25	0.6930	0.7407	0.7831	0.8208	0.8552	0.8881
1.30	0.7268	0.7654	0.8010	0.8342	0.8660	0.8978
1.35	0.7502	0.7829	0.8142	0.8445	0.8748	0.9061
1.40	0.7673	0.7960	0.8244	0.8529	0.8822	0.9133
1.45	0.7802	0.8061	0.8325	0.8598	0.8886	0.9197
1.50	0.7902	0.8142	0.8392	0.8657	0.8942	0.9254

INITIAL AREA RATIO (SUB/SUPER) = 1.10

M1	M2					
	0.45	0.50	0.55	0.60	0.65	0.70
1.05	0.0276	0.2721	0.4883	0.6357	0.7347	0.8028
1.10	0.3410	0.5023	0.6244	0.7147	0.7814	0.8321
1.15	0.5171	0.6165	0.6965	0.7598	0.8103	0.8520
1.20	0.6123	0.6812	0.7394	0.7883	0.8299	0.8667
1.25	0.6695	0.7215	0.7674	0.8078	0.8441	0.8783
1.30	0.7068	0.7485	0.7867	0.8219	0.8551	0.8878
1.35	0.7325	0.7677	0.8009	0.8328	0.8641	0.8960
1.40	0.7512	0.7818	0.8118	0.8414	0.8715	0.9030
1.45	0.7652	0.7927	0.8203	0.8485	0.8778	0.9092
1.50	0.7761	0.8014	0.8273	0.8545	0.8833	0.9146

Table 3.1b: Choking Pressure

M1	M2	P	A1	A2	A
1.3200	0.4387	1.1176	0.4821	0.6217	1.1038
1.3300	0.4613	1.1023	0.4841	0.5982	1.0823
1.3400	0.4831	1.0873	0.4862	0.5780	1.0642
1.3500	0.5041	1.0723	0.4884	0.5605	1.0489
1.3600	0.5244	1.0576	0.4906	0.5453	1.0359
1.3700	0.5441	1.0429	0.4929	0.5319	1.0248
1.3800	0.5632	1.0285	0.4952	0.5200	1.0152
1.3900	0.5818	1.0142	0.4976	0.5094	1.0070
1.4000	0.6000	1.0000	0.5000	0.5000	1.0000
1.4100	0.6178	0.9860	0.5025	0.4915	0.9940
1.4200	0.6352	0.9721	0.5050	0.4839	0.9889
1.4300	0.6522	0.9585	0.5076	0.4770	0.9847
1.4400	0.6689	0.9449	0.5103	0.4708	0.9811
1.4500	0.6854	0.9315	0.5130	0.4652	0.9782
1.4600	0.7015	0.9183	0.5158	0.4600	0.9758
1.4700	0.7174	0.9052	0.5186	0.4554	0.9740
1.4800	0.7331	0.8923	0.5215	0.4512	0.9727
1.4900	0.7485	0.8795	0.5245	0.4474	0.9719
1.5000	0.7638	0.8669	0.5275	0.4440	0.9714
1.5100	0.7788	0.8544	0.5305	0.4408	0.9714
1.5200	0.7936	0.8421	0.5336	0.4380	0.9717
1.5300	0.8083	0.8299	0.5368	0.4355	0.9723
1.5400	0.8228	0.8178	0.5401	0.4332	0.9733
1.5500	0.8371	0.8059	0.5433	0.4312	0.9745
1.5600	0.8513	0.7942	0.5467	0.4293	0.9760
1.5700	0.8654	0.7826	0.5501	0.4277	0.9778
1.5800	0.8793	0.7712	0.5536	0.4263	0.9799
1.5900	0.8930	0.7599	0.5571	0.4251	0.9822
1.6000	0.9067	0.7487	0.5607	0.4240	0.9847
1.6100	0.9202	0.7377	0.5643	0.4231	0.9875
1.6200	0.9336	0.7268	0.5680	0.4224	0.9904
1.6300	0.9469	0.7161	0.5718	0.4218	0.9936
1.6400	0.9601	0.7055	0.5756	0.4214	0.9970
1.6500	0.9732	0.6950	0.5795	0.4211	1.0006

Table 3.2: One-Dimensional Variation of Flow Properties about Reference Case

such an occurrence would entail a shock somewhere in the supersonic nozzle so that the flow would be wholly subsonic. Certainly, the nozzle exit pressures in each stream would no longer be equal; the static pressure throughout the system upstream of the constriction would rise. Whether this would happen discontinuously or simply be occasioned by the onset of a continuous pressure rise as the minimum area is reduced is open to question. However, the new operating point would depend on the entire system, especially on the operating line of the compressor plant.

Disturbances of relatively short span in the streamwise direction may have blockage ratios greater than the choking limit without any problems of this sort arising. This is because in transonic shear flow the one-dimensional choking margin is related to a minimum area reduction necessary to choke the tunnel if the constriction is maintained over an axial distance of several duct heights so the two streams can reach relative equilibrium. If the perturbation is not maintained for this distance, then the effect of the interaction between the two streams is lessened, and their response tends to be more independent of each other.

For example, a uniform stream at Mach 1.4 has a choking margin of 11.5 percent, and for a stream at Mach 0.6 the margin is 18.8 percent. Thus, for a disturbance of sufficiently short span that the stream interactions do not have a significant effect, each stream can withstand a blockage very close to these individual limits (say, a 10 percent blockage of each stream). As this 10 percent blockage takes on a larger streamwise extent, the flow approaches a choked condition

due to the supersonic and subsonic streams reaching equilibrium with each other. Eventually, if the blockage is maintained, the tunnel will choke and the conditions at the source of the flow must change.

The reason why the equilibrium choking margin is much less for the combined flow than for either stream considered separately is that the value of dA/dp is of different sign in subsonic and supersonic streams. A given minute change of pressure (reversing for the purpose of illustration the usual cause-and-effect sequence) causes offsetting changes of area in each stream at equilibrium, and the net area change is less than the change in either of the separate streams.

The equilibrium choking margin is modified considerably by the presence of boundary layers on the walls, and by the finite thickness of the shear layer. The effect of the thickness of these layers is illustrated in Figure 3.10. Growth of the boundary layers on the walls, particularly on the subsonic wall, accounts for the increased choking margin. Regions of flow which were at Mach number 0.6 (in the model without boundary layers) have been replaced by flows at lower Mach numbers where $\frac{dA}{dp}$ is much greater. A measure of the choking margin, employed in Eq. (3.3), is

$$\frac{dA}{dp} = \sum_n \frac{dA_n}{dp} \quad .$$

The flow is choked when $\frac{dA}{dp} = 0$. The unperturbed flow is characterized by a positive $\frac{dA}{dp}$, so the changes introduced by the subsonic boundary layer increase the magnitude of $\frac{dA}{dp}$ and move the flow farther from a choked condition. By contrast, it has already been seen (cf. Figure 3.9) that the effect of finite shear layer thickness is to decrease

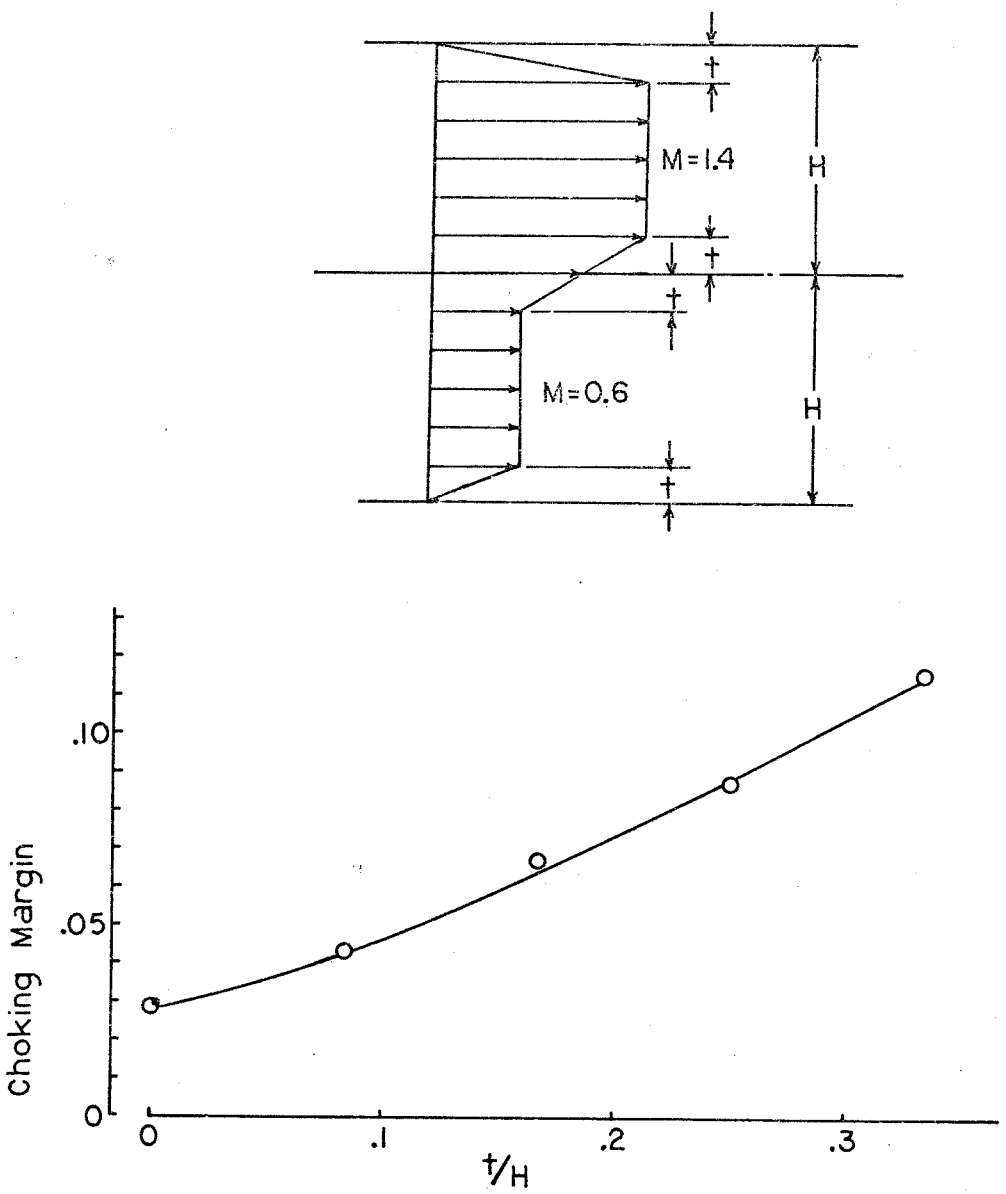

Figure 3.10: Effect of Shear Layer and Boundary Layer Thickness on Choking Margin

slightly the choking margin. The supersonic boundary layer has relatively little effect since within that region there are strips where $\frac{dA}{dp}$ is positive and others where it is negative. These have a largely offsetting effect.

Thus far, all of the discussions of choking margin have been based on theoretical grounds. Figure 3.11 presents the one-dimensional choking margin based on experimentally-measured Mach number distributions (those shown in Figures 3.3 and 3.4). This shows a reduction of the choking margin in the streamwise direction. The combined flow has many qualitative aspects of uniform subsonic flow, since $\frac{dA}{dp}$ is positive. The gradual drop in static pressure through the test section, illustrated in Figure 3.8b, confirms that this subsonic-like flow is tending toward a choked condition in the streamwise direction. It has been seen that this condition is due to the wall divergence limitation of the wind tunnel design: a greater wall divergence (which is not possible) would correct the losses in static pressure and in choking margin. In the context of the preceding discussion, Figure 3.11 indicates that the subsequent changes in choking margin from a given state are due to the spreading shear layer (which tends to reduce the margin) and that the shear layer grows at a much faster rate than the subsonic boundary layer. This difference in growth rate can be seen in Figures 3.1 and 3.3.

The response to area changes of less than the one-dimensional choking limit remains to be considered. This has relevance in determining the effect of model blockage on the flow. The mechanism for this study was a partial span strut (bearing a pitot tube, which is

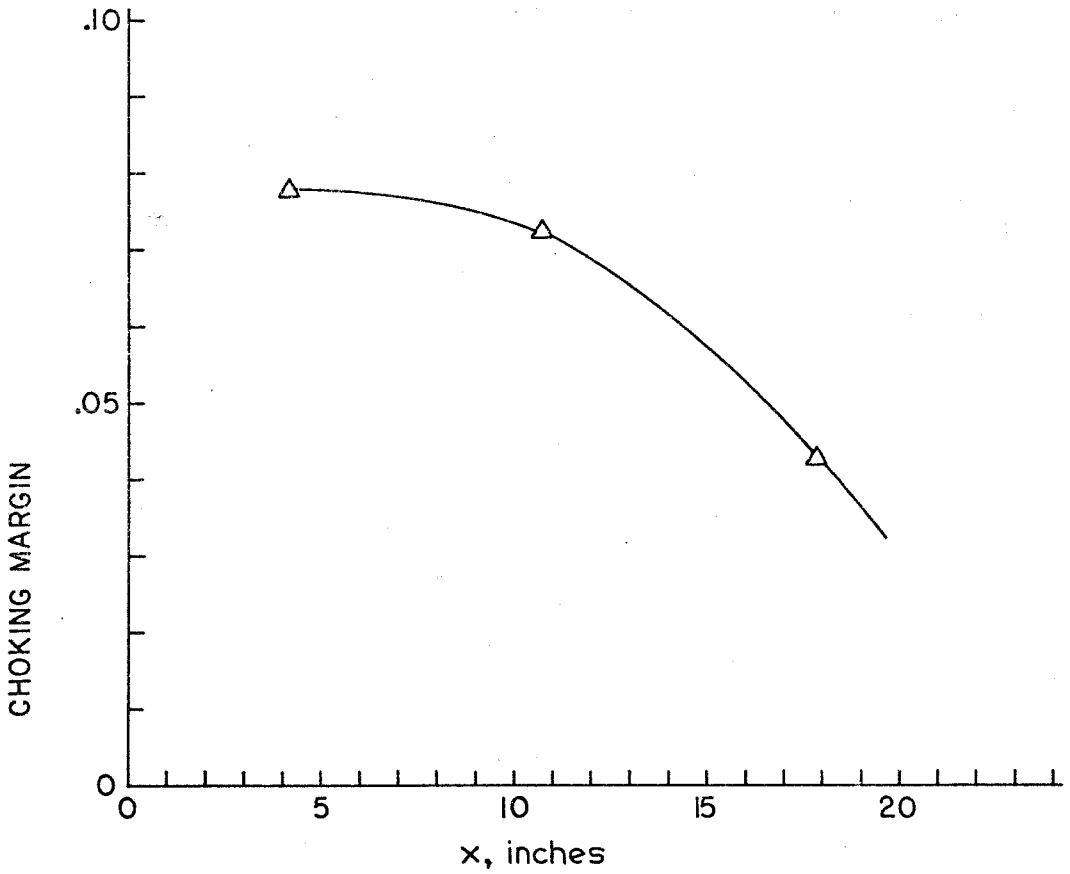

Figure 3.11: Empty-Tunnel Choking Margin

incidental to this discussion) which traversed in the vertical plane in the center of the tunnel. The strut could be mounted in either the top or the bottom wall and could be retracted to within 1/16-inch of the wall. When extended fully, it reached through both streams to the other wall. The cross section of the strut was a diamond of chord 5/16 inch and maximum thickness 1/16 inch. Fully extended, it blocked about 3.04 percent of the flow passage area (recall that this is greater blockage than the one-dimensional choking margin of 2.86 percent).

In the blockage experiments, the strut was mounted through the subsonic wall so as to minimize its disturbance to the flow when fully retracted, and it was mounted with its centerline at the 29.75-inch access port (the farthest-downstream position available) in order to obtain the most information possible on the upstream influence of flow blockage. Several taps were selected in both the subsonic and supersonic walls, and the pressure at the wall was measured versus strut extension. Percentage pressure deviations, compared to local readings when the strut was fully retracted, were plotted for a number of wall taps. Some of these data are presented in Figure 3.12.

An examination of the figure reveals that the disturbance, whose source is at x = 29.75 inches, seems to have undimished strength throughout the test section and into the subsonic plenum chamber. The mean flow loss of total pressure can be shown to be negligible when the strut is confined to the subsonic stream, but quickly becomes important as the strut enters the supersonic stream. The figure shows that the trend of wall pressure can be related to

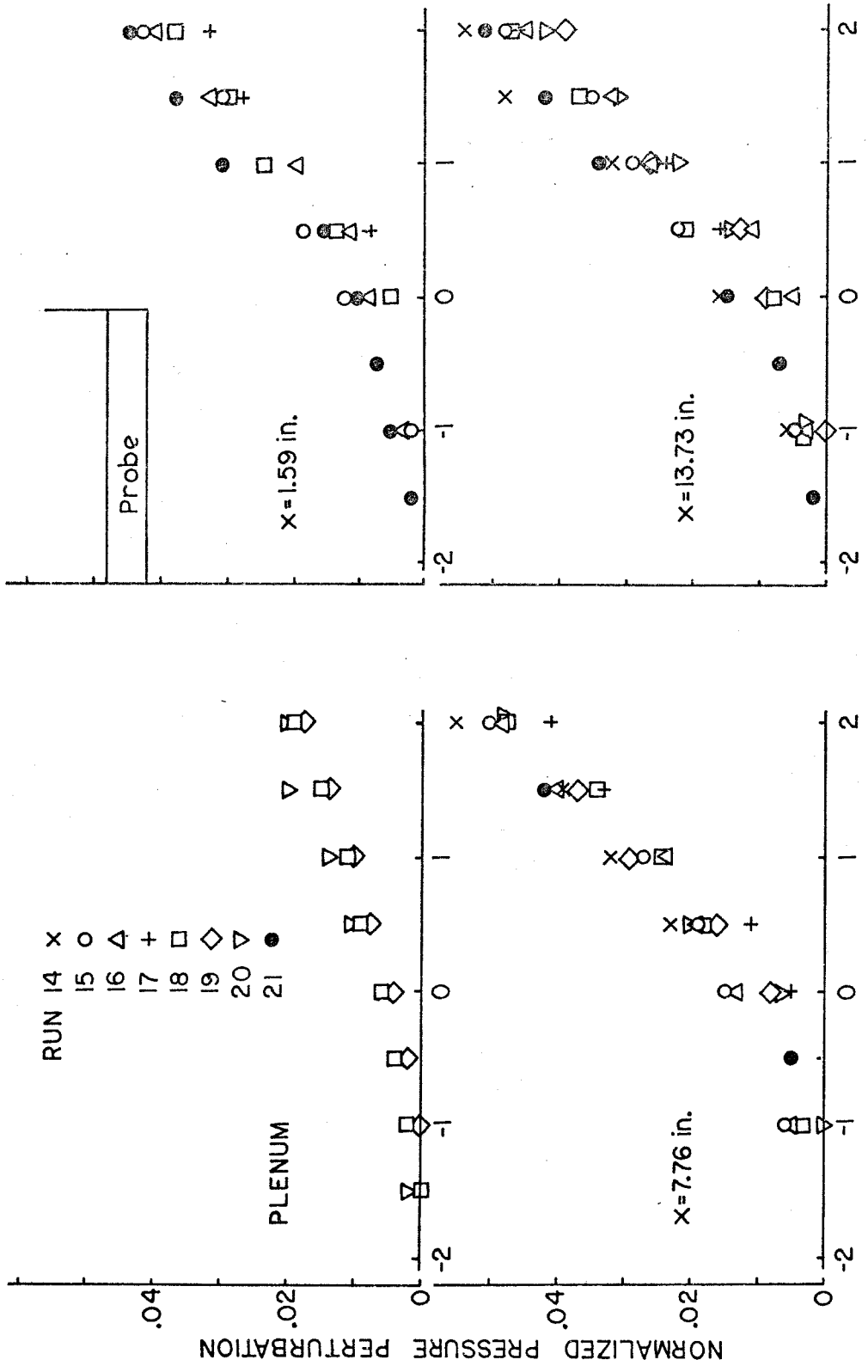

Figure 3.12: Subsonic Stream Variable Blockage Effects

this mean loss. This realization, and the fact that the pressure in the subsonic plenum chamber is also dependent on the strut extension, means that there is an interaction between the compressor plant and the test section model of sufficient strength to affect the test section flow a few percent. This tunnel/plant interaction is discussed further in Appendix C.

Pressure variations due to the interaction are both larger and more irregular on the supersonic wall than on the subsonic wall. This is because the initial strength of the splitter plate shock and its subsequent propagation characteristics are sensitive to the nozzle exit conditions M_1, M_2, P_{t1}, and P_{t2}. Of these, P_{t2}, and through it M_2, the splitter plate shock system, and all supersonic wall pressures, are seen to be fairly sensitive to the tunnel/plant interaction. Thus, a regular procedure could not be devised through which pressure variations in the supersonic stream seen on the walls could be corrected by reference to the unperturbed flow condition.

IV. WEDGE STUDIES

4.1 Discussion

A substantial portion of the experiments performed as a part of this project was concerned with the effects of a thin finite wedge attached to either the supersonic (top) wall or the subsonic (bottom) wall. It was hoped that these comparatively simple experiments would give a degree of insight into the performance of the wind tunnel, the approximately two-dimensional interaction of weak shock waves with a transonic shear layer, and the effect of a change of overall flow area on the two-stream flow field. In addition, we hoped to obtain some information concerning the extent to which the inviscid flow would be modified in the region upstream of some obstructing object.

Two wedges were constructed for these studies, each of which had different angles at the leading and trailing edges so that by flipping the piece end-for-end it would do double duty. The length of both wedge pieces was fifteen inches from leading edge to trailing edge. As the nominal height of a stream tube is 2.15 inches, the effects due to the leading and trailing edges are separated by 6 or 7 stream-heights. Each wedge piece had 13 static pressure taps and was secured to the top or bottom wall with 16 screws of size 1-64. Sealing around the static taps in the wedge, which were aligned with existing static taps in the wall, was accomplished by putting a generous layer of machine oil on the mating surface before the wedge was attached to the wall. On the whole, this procedure worked well, though occasionally data were lost due to an inadequate seal.

The two wedge pieces will be referred to as the "thick" and "thin" wedges. The thick wedge had a body thickness of 3/32-inch and was built with wedge angles of 4° and 8°. After a few runs, the 8° angle was cut down to 2°. The reasons for this will be discussed in Section 4.5. The thin wedge was 3/64-inch thick (i.e., half that of the thick wedge), and was built with wedge angles of 2° and 4°.

The trailing edge of the wedge was sufficiently far downstream of the leading edge that all interactions measured in the first two or three supersonic-stream wavelengths (i.e., the first 8 to 12 inches) were free of trailing-edge effects. This fact is well supported by both theoretical and experimental data, and will be discussed in detail later in this chapter. Thus, we had within the region of interest the fairly simple case of a constant-angle flow deflection at the wall, followed by a wall parallel to the original line but displaced outward by a small amount. Only leading edge interactions were studied.

The area blockages for the two wedges were 1.09 per cent and 2.18 per cent of the original flow area. The size of this blockage was chosen in an effort to remain within the range of linear behavior. Nevertheless, there were distinct nonlinear effects in the data, and in some of the experiments the tunnel appeared to be close to choking.

A major goal of the wedge experiments was to study the transmission and reflection off the shear layer of a disturbance wave generated in either the supersonic or subsonic stream. A point of special interest was in the way a disturbance wave generated in the supersonic stream might enter the subsonic stream, propagate up-

stream, and re-enter the supersonic stream, thus modifying the stream ahead of the disturbance source.

The wedges were usually installed with the leading edge 10 inches downstream of the nozzle exit plane. At this point, the shear layer has a maximum-slope velocity thickness of 0.62 inch and a perceptible thickness of about 1.00 inch, and extends almost equal distances to either side of the plane of the splitter plate, $y = 0$. It was also possible to mount the wedge plates at the station $x = 17$ inches, where the maximum-slope thickness is 0.94 inch, in order to note the effect of shear layer thickness.

The baseline case about which parametric studies were performed was that of the 4^{o} angle, 3/32-inch thick wedge attached at $x = 10$ inches. Data were obtained as wall and wedge surface pressures and by schlieren photography. It was not possible to obtain reliable data from probes introduced into the flow due to the inherent sensitivity of the perturbed transonic flow field in the interaction region.

In Section 4.2, a qualitative discussion of the response to a shock wave impinging on a zero-thickness shear layer is presented, followed by a consideration of the modifications when the shear layer has finite thickness. The governing equations, accurate to first order, for perturbations to a general shear layer are obtained.

Section 4.3 presents the development of the first-order mathematical solution to the shear layer of zero thickness for the wedge problems. In Section 4.3.1, the basic method to be employed is outlined. It is based on Fourier transforms, and draws heavily on work

by H. S. Tsien and M. Finston concerning a similar problem [18]. The general solution to the transformed governing equation is obtained. The solution for the supersonic wedge problem is found in Section 4.3.2, and that for the subsonic wedge problem in Section 4.3.3. In Section 4.3.4 the algorithm by which numerical results were obtained is briefly outlined. A more complete discussion is presented in Appendix C.

Section 4.4 compares the present calculation with the results of Tsien and Finston [18], which are a limiting case, and finds general agreement.

The supersonic wedge case is studied in Section 4.5. First, it is seen that theory and experiment show good agreement for a selected reference case. Next, perturbations of various parameters (wedge angle and thickness, and shear layer thickness) about the reference case are studied both theoretically and experimentally, and the limits of validity of the first order theory are established. Finally, theoretical parametric studies are presented of variation of properties which were fixed by the design of the wind tunnel (M_1, M_2, and h_1/h_2) and whose influence thus could not be established experimentally.

Similar theoretical studies are presented in Section 4.6 for the subsonic wedge. Due to problems with the repeatability of the tunnel, experimental verification of these results generally was not possible. The amplitude of the pressure perturbation is related to the choking margin (see Section 3.4) of the unperturbed flow for a given disturbance geometry.

A summary discussion of these studies is presented in Section 4.7.

4.2 Simplified Shock Reflection and Transmission

To get some sort of intuitive feel for the processes at work when a shock wave strikes a subsonic flow, consider the simplified model of Figure 4.1a, in which there are two distinct streams of uniform upstream Mach number with a zero-thickness shear layer between them.

There are two extreme cases, which are presented in parts b and c of Figure 4.1. Most practical problems in this experiment fall between the extremes and combine certain of the characteristics of each.

In the first case, Figure 4.1b, the subsonic stream is unbounded. The impinging shock wave, of deflection angle δ_o, strikes the interface. Because the subsonic layer cannot support a discontinuous increase in pressure, an expansion fan of deflection angle δ_1 must be generated at the interface so that the pressure downstream of the expansion is the same as that upstream of the shock. The net deflection of both streams at the impingement point (taken positive into the supersonic stream) is $-(\delta_o+\delta_1)$. The subsonic stream obeys the dictates of potential flow and is stagnant at this cusp in the interface. This means that locally upstream of the cusp the subsonic stream must also be at a somewhat elevated pressure. With the requirement of constant pressure on each side of the interface, this elevated pressure must be generating compression waves in the

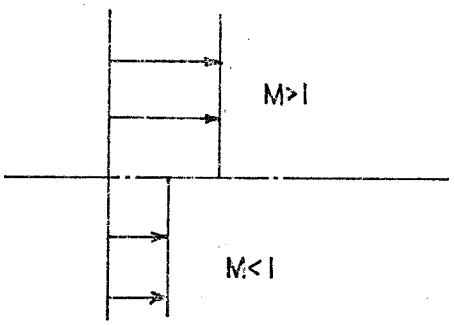

A) SIMPLIFIED FLOW MODEL

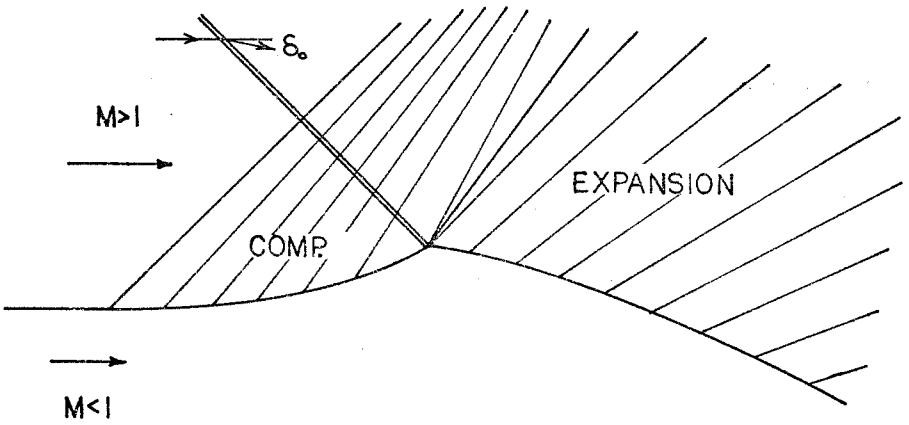

B) UNBOUNDED SUBSONIC MEDIUM

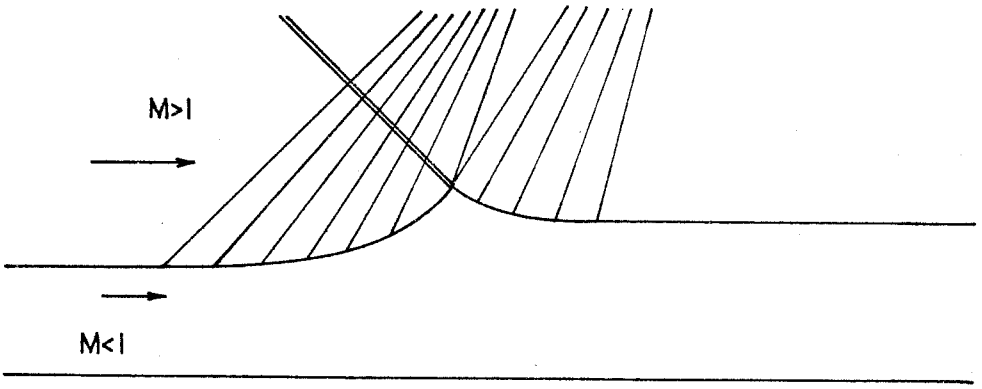

C) BOUNDED SUBSONIC MEDIUM

Figure 4.1: Simplified Shock Reflection and Transmission

supersonic stream upstream of the impingement point. Similarly, downstream of the impingement point (or the cusp), the pressure must fall and thus expansion waves must be passed into the supersonic stream. Knowing all the flow properties, we can readily determine the angular deflection immediately ahead of and behind the cusp, and far downstream, but the length scale of the interaction region must be found in some other manner.

In the other extreme case, a wall bounding the subsonic stream is sufficiently close to the interface that the subsonic flow must quickly return to its original direction, though its stream-tube area and pressure will be larger than before. The possibility of a pressure rise large enough to cause stagnation of the subsonic stream, or separation as in boundary layer theory, will not be considered here.

As before, the requirement of no discontinuous pressure increase in the subsonic layer means that a cusp will form in the interface, requiring a stagnation point in the subsonic stream. The analysis remains the same upstream of the cusp, but downstream of the cusp the expansion waves will be partially replaced by the compression waves necessary to turn the flow back to the horizontal. The net pressure will increase, and thus the subsonic stream must have larger area than upstream. This problem was treated analytically in some detail by Tsien and Finston [18].

It should be noted that this entire discussion is only valid if $P_{t2} \leq P_1^*$, where P_1^* is the pressure at which a fluid element in the supersonic stream has sonic speed under isentropic changes. This requirement can also be expressed as

$$M_2^2 \leq \frac{2}{\gamma+1}(M_1^2 - 1) \quad . \tag{4.1}$$

At $M_1 = 1.4$, the requirement is that M_2 be less than 0.894. The relation is satisfied for all M_2 less than one if M_1 is greater than 1.484.

The next step is to estimate the effect of finite shear layer thickness on the response just outlined. If a wave in an unbounded flow strikes an interface between two supersonic flows, each separately having a uniform Mach number, part of the wave will be transmitted through the interface and part will be reflected (see Figure 4.2). For a small difference in Mach number between the two layers, the strength of the reflected wave (in terms of deflection angle) is

$$r = \frac{2-M^2}{2(M^2-1)} \frac{\Delta M}{M} \quad , \tag{4.2}$$

and the strength of the transmitted wave is (1-r), where the incoming wave has a strength of one. It can be seen that the reflected wave is of the same sign as the incoming wave (compression or expansion) if $M < \sqrt{2}$ and is of opposite sign if $M > \sqrt{2}$, with zero reflection at $M = \sqrt{2}$. If we now consider a flow of three supersonic layers rather than two (see Figure 4.2b), we find repeated reflection of a wave in the middle layer trapped between the two interfaces. It should be noted that the reflection coefficient, r, is generally quite small and the strength of the trapped wave is substantially reduced at each reflection. Using this observation as a guide, we can now construct a plausible situation for a continuous velocity gradient (i.e., infinitely many shear layers) as is shown in Figure 4.2c. Within the shear

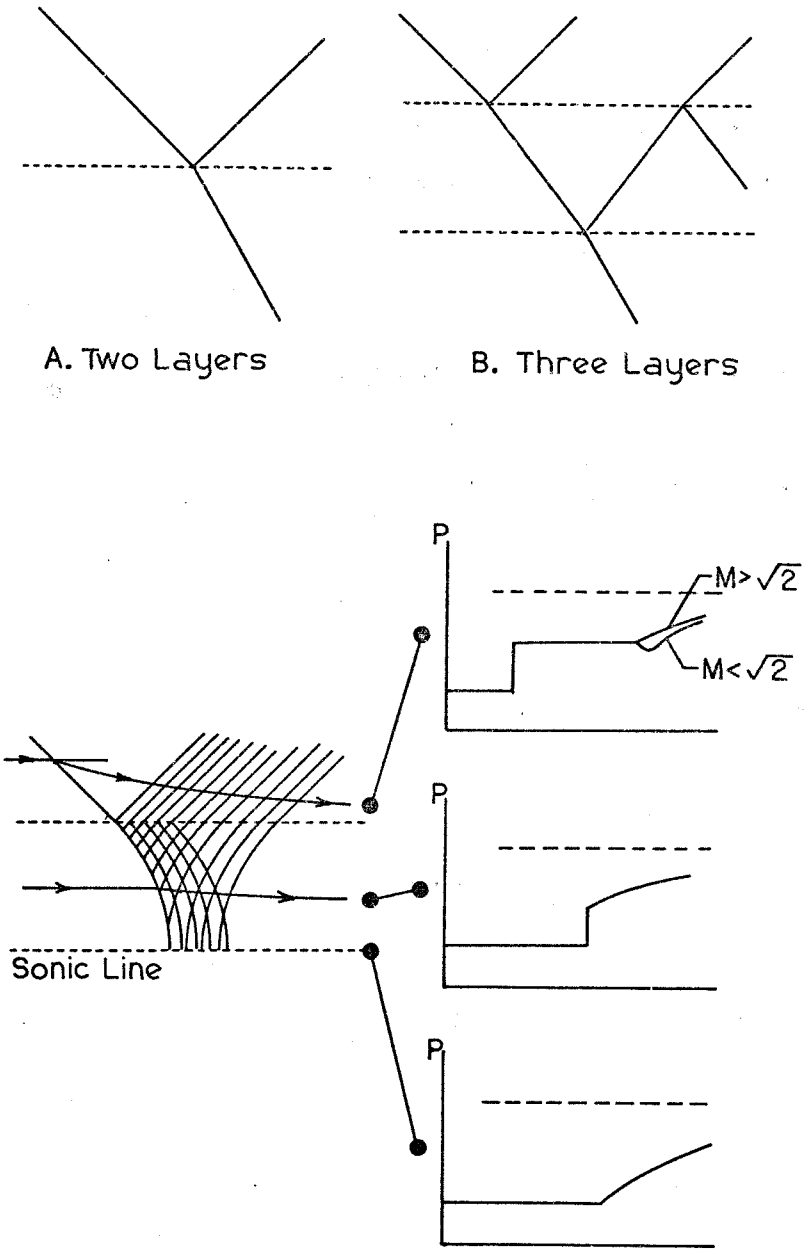

Figure 4.2: Supersonic Shear Layer

layer, there is a discontinous jump in pressure at the leading portion of the wave (the magnitude of the jump being reduced as the wave passes into the shear layer until it has vanishingly small strength at the sonic line) with a region of continuous compression (preceded by an expansion if the Mach number is greater than $\sqrt{2}$) behind the leading portion of the wave. The strength of these compressions decreases spatially to zero downstream from the leading wave. The thickness of the incoming wave can be considered to be zero, but the reflected wave has a thickness of the same order as that of the supersonic portion of the shear layer (see Figure 4.2c). The disturbance imposed on the subsonic portion of the flow at the sonic line is a continuously increasing pressure, compared with the result of a discontinuous change in flow inclination angle for the shear layer of zero thickness.

The next step is a mathematical investigation of disturbances to the uniform two-dimensional shear layer. A perturbation expansion scheme will be used. The parameter ε will be used as an indicator of the magnitude of the disturbance. A well known result is that changes of entropy in a compressible flow are of third order in the disturbance strength when the Mach number is close to one. Thus, consideration of effects of first and second order may properly assume that a fluid element behaves isentropically. In addition, transport properties such as viscosity and heat conduction will be neglected. Then, in two-dimensional flow, the mass continuity equation becomes

$$\frac{\partial \rho u}{\partial x} + \frac{\partial \rho v}{\partial y} = 0 \quad ,$$

and the momentum equations are

$$\rho u \frac{\partial u}{\partial x} + \rho v \frac{\partial u}{\partial y} + \frac{\partial P}{\partial x} = 0 \quad ,$$

$$\rho u \frac{\partial v}{\partial x} + \rho v \frac{\partial v}{\partial y} + \frac{\partial P}{\partial y} = 0 \quad .$$

By eliminating density and pressure from these equations (using the isentropic condition), we find that

$$(a^2 - u^2) \frac{\partial u}{\partial x} + (a^2 - v^2) \frac{\partial v}{\partial y} - uv \left(\frac{\partial u}{\partial y} + \frac{\partial v}{\partial x} \right) = 0 \qquad (4.3a)$$

$$\left(u \frac{\partial}{\partial x} + v \frac{\partial}{\partial y} \right) \left(\frac{\partial v}{\partial x} - \frac{\partial u}{\partial y} \right) = 0 \qquad (4.3b)$$

where a is the local speed of sound. By defining the local vorticity, ω, as

$$\omega = \frac{1}{2} \left(\frac{\partial v}{\partial x} - \frac{\partial u}{\partial y} \right) \quad , \qquad (4.4)$$

we see that eq. (4.3b) tells us that a fluid element retains constant vorticity.

Consider a flow in the x-direction whose unperturbed properties vary only in the y-direction. Superimposed on the flow are perturbations. Call the main flow velocity profile $U_o(y)$; the x- and y-components of the perturbation velocities are $u'(x, y)$ and $v'(x, y)$. Then the net velocity components are

$$u(x, y) = U_o(y) + u'(x, y) \quad , \qquad (4.5a)$$

$$v(x, y) = v'(x, y) \quad . \qquad (4.5b)$$

Substituting into eq. (4.4), we see that

$$\frac{\partial u'}{\partial x} = \frac{\partial v'}{\partial y} \quad . \qquad (4.6)$$

Expressing the perturbation velocity vector as the gradient of a scalar potential, Φ, we get

$$\Phi = \varepsilon\phi' + \varepsilon^2\phi'' + \ldots \quad , \tag{4.7a}$$

$$u' = \partial\Phi/\partial x \quad , \tag{4.7b}$$

$$v' = \partial\Phi/\partial y \quad . \tag{4.7c}$$

Equation (4.6) is now satisfied identically by this approach. Equation (4.7) can be substituted into eq. (4.3a) to give a series of terms in powers of ε. The first-order result (terms containing ε^1), which is valid only in the limit as the disturbances become vanishingly small, is

$$(1-M_o^2)\frac{\partial^2\phi'}{\partial x^2} + \frac{\partial^2\phi'}{\partial y^2} - \frac{M_o}{a_o}\frac{dU_o}{\partial y}\frac{\partial\phi'}{\partial y} = 0 \quad . \tag{4.8a}$$

Should a second-order correction to the first-order result be desired, then after obtaining $\phi'(x, y)$ it would be necessary to solve for $\phi''(x, y)$ the following equation:

$$(1-M_o^2)\frac{\partial^2\phi''}{\partial x^2} + \frac{\partial^2\phi''}{\partial y^2} - \frac{M_o}{a_o}\frac{dU_o}{\partial y}\frac{\partial\phi''}{\partial y} = \tag{4.8b}$$

$$\frac{M_o}{a_o}\frac{\partial\phi'}{\partial x}\left[(\gamma+1)\frac{\partial^2\phi'}{\partial x^2} + (\gamma-1)\frac{\partial^2\phi'}{\partial y^2}\right] + \frac{1}{a_o^2}\frac{\partial\phi'}{\partial y}\left(\frac{dU_o}{dy}\frac{\partial\phi'}{\partial x} + 2U_o\frac{\partial^2\phi'}{\partial x\partial y}\right).$$

Of course, in the general problem, M_o, a_o, and U_o are all known functions of y. Equation (4.8a) is relatively easily solved only when M_o, a_o, and U_o are constants; then the equation has only two terms and the coefficients are constant.

To treat the present problem, divide the flow region into n strips with boundaries on lines of constant y. Each has its own uniform values of M_o and a_o. Two boundary conditions must be im-

posed at each interface between the strips: continuity of pressure and flow inclination angle. One boundary condition, that of flow inclination angle, must be applied at each wall. For small perturbations the boundary conditions can be applied to the walls and interfaces at their undisturbed locations. In a region composed of n strips there are 2n boundary conditions.

The simplest non-trivial example relevant to the present problem is that of two strips, one supersonic and the other subsonic, with a shear layer of zero thickness separating them. This example is a good approximation to the present study because the shear layer in fact is fairly thin. In Section 4.3 the first-order solution to this problem is obtained.

4.3 Linearized Theory Development

4.3.1 General considerations and derivations. Consider the unperturbed flow model of Figure 4.3, and using linearized small-perturbation theory let us develop solutions which consider wave-like behavior in both stream tubes in a two-dimensional manner. This will permit, for example, the imposition of various wall profiles on the top and bottom walls. Specifically, a full linear theory to treat the experimental cases of wedges on each wall will be presented. The calculations are analytic rather than based on a finite-difference scheme, though the results are sufficiently complex to require their numerical evaluation on a digital computer. For this purpose, the IBM 370/158 of the Computing Center of the California Institute of Technology was used.

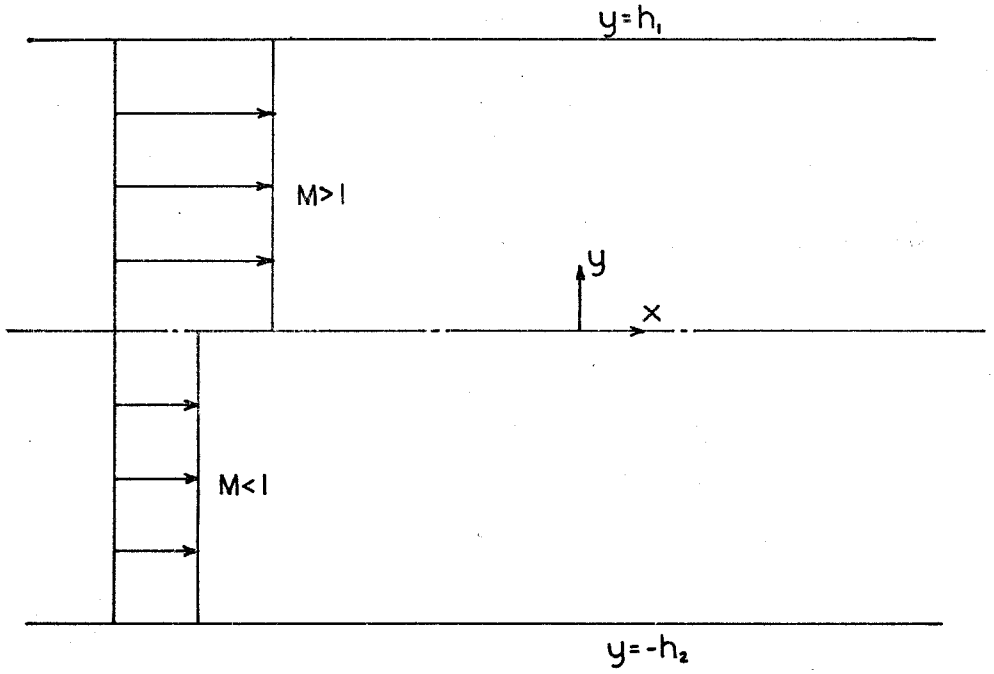

Figure 4.3: Simplified Flow Model

Consistent with linear theory, the first-order effects in the imposed disturbances will be treated and higher-order effects will be disregarded as insignificant. This approximation, strictly speaking, is valid only for infinitesimal perturbations. Both the subsonic and supersonic flows will be assumed inviscid, irrotational, non-heat-conducting, and two-dimensional. Velocities will be related to the gradient of a scalar potential, and will be calculated using the techniques of Fourier and complex analysis which will express solutions as infinite series whose convergence can be demonstrated.

Throughout this analysis the subscripts 1 and 2 will be used to identify respectively the supersonic and subsonic streams. Subscripts x and y preceeded by a comma, will indicate partial differentiation. Thus, $P_{1,x}$ is the partial derivative of the supersonic stream pressure with respect to x.

The unperturbed velocity in each stream is uniform, so eq. (4.8a) becomes

$$(M_1^2-1)\phi_{1,xx}-\phi_{1,yy} = 0 \qquad h_1 \geq y \geq 0 \qquad M_1 > 1 \qquad (4.9a)$$

$$(1-M_2^2)\phi_{2,xx}+\phi_{2,yy} = 0 \qquad -h_2 \leq y \leq 0 \qquad M_2 < 1 \qquad (4.9b)$$

where the interface is the plane $y = 0$ and the flow is supersonic or subsonic respectively where y is greater than or less than zero. All calculations will be accurate to first order only, and the "prime" superscript on the velocity potential will be deleted.

Within each stream, U is constant. Thus, it becomes permissible to modify slightly the definition of the relation between the perturbation velocity vector and the velocity potential:

$$\vec{u}' = U_o \operatorname{grad} \phi \quad . \tag{4.10}$$

This is not the standard usage, but it does greatly simplify the application of boundary conditions to the problem under study, since the local flow inclination angle is $(\partial\phi/\partial y)$ rather than $\left(\frac{1}{U_o}\frac{\partial\phi}{\partial y}\right)$.

Equation (4.9) shows the expected hyperbolic behavior of ϕ_1 and elliptic behavior of ϕ_2. Take the Fourier transform of these equations with respect to x:

$$(x, y) \rightarrow (k, y) \quad .$$

Denote the Fourier transform of $f(x, y)$ by $\tilde{f}(k, y)$ and, using the transform relations

$$\tilde{f}(k, y) = \frac{1}{\sqrt{2\pi}} \int_{-\infty}^{\infty} f(x, y)\, e^{ikx} dx \tag{4.11a}$$

$$f(x, y) = \frac{1}{\sqrt{2\pi}} \int_{-\infty}^{\infty} \tilde{f}(k, y)\, e^{-ikx} dk \quad , \tag{4.11b}$$

write the general equations as

$$\tilde{\phi}_{1,yy} + k^2(M_1^2 - 1)\tilde{\phi}_1 = 0 \tag{4.12a}$$

$$\tilde{\phi}_{2,yy} - k^2(1 - M_2^2)\tilde{\phi}_2 = 0 \quad . \tag{4.12b}$$

The general solution of these equations can be found by the method of separation of variables. Defining the quantity β simplifies the notation:

$$\beta = \sqrt{|M^2 - 1|} \quad . \tag{4.13}$$

The general solution of eq. (4.12) can be found:

$$\tilde{\phi}_1(k, y) = C_{11}(k)\cos k\beta_1(y - h_1) + C_{12}(k)\sin k\beta_1(y - h_1) \tag{4.14a}$$

$$\tilde{\phi}_2(k, y) = C_{21}(k)\cosh k\beta_2(y + h_2) + C_{22}(k)\sinh k\beta_2(y + h_2) \tag{4.14b}$$

where the walls are at $y = h_1$ and $-h_2$. Four boundary conditions will be applied to find the four coefficients $C_{ij}(k)$. They will be in the form of specified flow inclination angle at the walls (two walls, thus two conditions) and equal pressure and inclination angle at the interface in each stream. Two basic types of problem must be considered, in which the perturbation is specified on either the supersonic or the subsonic wall; two of the four boundary conditions are formed differently in each case. Since the problem is linear, composite solutions can be formed by superposition of solutions of each of these two types.

Three of the four boundary conditions to be applied are in the form of the flow inclination angle, $v'/U = \phi_{,y}$. This is why the non-standard relation of eq. (4.10) was introduced: confusing factors of U_1 and U_2 are not introduced. The expression of inclination angle for each stream is more concise.

4.3.2 Supersonic wedge problem. In this problem, a flow inclination angle $V_w(x)$ will be specified on the supersonic wall and the subsonic wall will be unperturbed. Each boundary condition will be expressed in working form in (k, y) coordinates, i.e., under a Fourier transformation, rather than in (x, y) space.

The first condition is the specified supersonic wall inclination angle:

$$\begin{aligned} \phi_{1,y} &= V_w(x) \qquad \text{at } y = h_1 \ , \\ \tilde{\phi}_{1,y} &= \tilde{V}_w(k) \qquad \text{at } y = h_1 \ . \end{aligned} \tag{4.15}$$

Continuity of flow inclination angle across the interface yields the

condition

$$\begin{aligned} \phi_{1,y} &= \phi_{2,y} \qquad \text{at } y = 0 \\ \tilde{\phi}_{1,y} &= \tilde{\phi}_{2,y} \qquad \text{at } y = 0 \ . \end{aligned} \tag{4.16}$$

Since each stream has a uniform total pressure, the pressure perturbation is given by

$$P' = -\rho u u' = -\gamma P M^2 \phi_{,x} \tag{4.17}$$

and the condition of pressure continuity across the interface can be written as

$$\begin{aligned} M_1^2 \phi_{1,x} &= M_2^2 \phi_{2,x} \qquad \text{at } y = 0 \\ M_1^2 \tilde{\phi}_1 &= M_2^2 \tilde{\phi}_2 \qquad \text{at } y = 0 \ , \end{aligned} \tag{4.18}$$

since the unperturbed pressure, P, is the same in both streams. The final condition, applied at the subsonic wall, is

$$\begin{aligned} \phi_{2,y} &= 0 \qquad \text{at } y = -h_2 \\ \tilde{\phi}_{2,y} &= 0 \qquad \text{at } y = -h_2 \ . \end{aligned} \tag{4.19}$$

Using these boundary conditions to solve for the coefficients $C_{ij}(k)$ in eq. (4.14) and inverting the Fourier transform gives the velocity potential for a general wall profile $V_w(x)$:

$$\phi_1(x, y) = \frac{1}{\sqrt{2\pi}} \int_{-\infty}^{\infty} \frac{\tilde{V}_w(k)}{k} \left\{ \frac{f(k)}{q(k)} \cos k\beta_1 (y - h_1) + \frac{1}{\beta_1} \sin k\beta_1 (y - h_1) \right\} e^{-ikx} dk \tag{4.20a}$$

$$\phi_2(x, y) = \frac{M_1^2}{\sqrt{2\pi}} \int_{-\infty}^{\infty} \frac{1}{kq(k)} \tilde{V}_w(k) \cosh k\beta_2 (y + h_2) e^{-ikx} dk \tag{4.20b}$$

where

$$f(k) = M_2^2 \cos k\beta_1 h_1 \cosh k\beta_2 h_2 + \frac{\beta_2 M_1^2}{\beta_1} \sin k\beta_1 h_1 \sinh k\beta_2 h_2 \ , \tag{4.21}$$

$$q(k) = \beta_2 M_1^2 \cos k\beta_1 h_1 \sinh k\beta_2 h_2 - \beta_1 M_2^2 \sin k\beta_1 h_1 \cosh k\beta_2 h_2 \ . \quad (4.22)$$

The boundary condition $V_w(x)$ is presented in Figure 4.4, and represents the supersonic wedge problem described previously. The function $V_w(x)$, which is the flow inclination angle at the wall, is:

$$\begin{aligned} V_w(x) &= 0 && x < -\beta_1 h_1 \\ V_w(x) &= -\varepsilon && -\beta_1 h_1 < x < -\beta_1 h_1 + t/\varepsilon \\ V_w(x) &= 0 && x > -\beta_1 h_1 + t/\varepsilon \end{aligned} \quad (4.23)$$

Applying the Fourier transform gives the result

$$\tilde{V}_w(k) = \frac{i\varepsilon}{k\sqrt{2\pi}} \left[e^{-ik(\beta_1 h_1 - t/\varepsilon)} - e^{-ik\beta_1 h_1} \right] \quad (4.24)$$

and the expressions for the velocity potentials are determined. The potentials themselves are not needed; what are required are the x- and y-derivatives of each potential. By expressing sines and cosines in terms of complex exponentials, the potentials can be expressed as

$$\phi_{1,x} = \varepsilon(I_{11} + I_{12} - I_{13} - I_{14}) \quad (4.25a)$$

$$\phi_{1,y} = \varepsilon\beta_1(I_{11} - I_{12} - I_{13} + I_{14}) - \varepsilon(I_{21} - I_{23}) \quad (4.25b)$$

$$\phi_{2,x} = \varepsilon M_1^2 (I_{31} - I_{32}) \quad (4.25c)$$

$$\phi_{2,y} = -\varepsilon\beta_2 M_1^2 (I_{41} - I_{42}) \quad (4.25d)$$

where

$$I_{1n} = \frac{1}{4\pi} \int_{-\infty}^{\infty} \frac{f}{kq} e^{-ikS_{1n}} dk \qquad n = 1, 2, 3, 4 \quad (4.26a)$$

$$I_{2n} = -\frac{i}{4\pi} \int_{-\infty}^{\infty} \frac{1}{k} e^{-ikS_{1n}} \left(1 + e^{-2ik\beta_1 h_1}\right) dk \qquad n = 1, 3 \quad (4.26b)$$

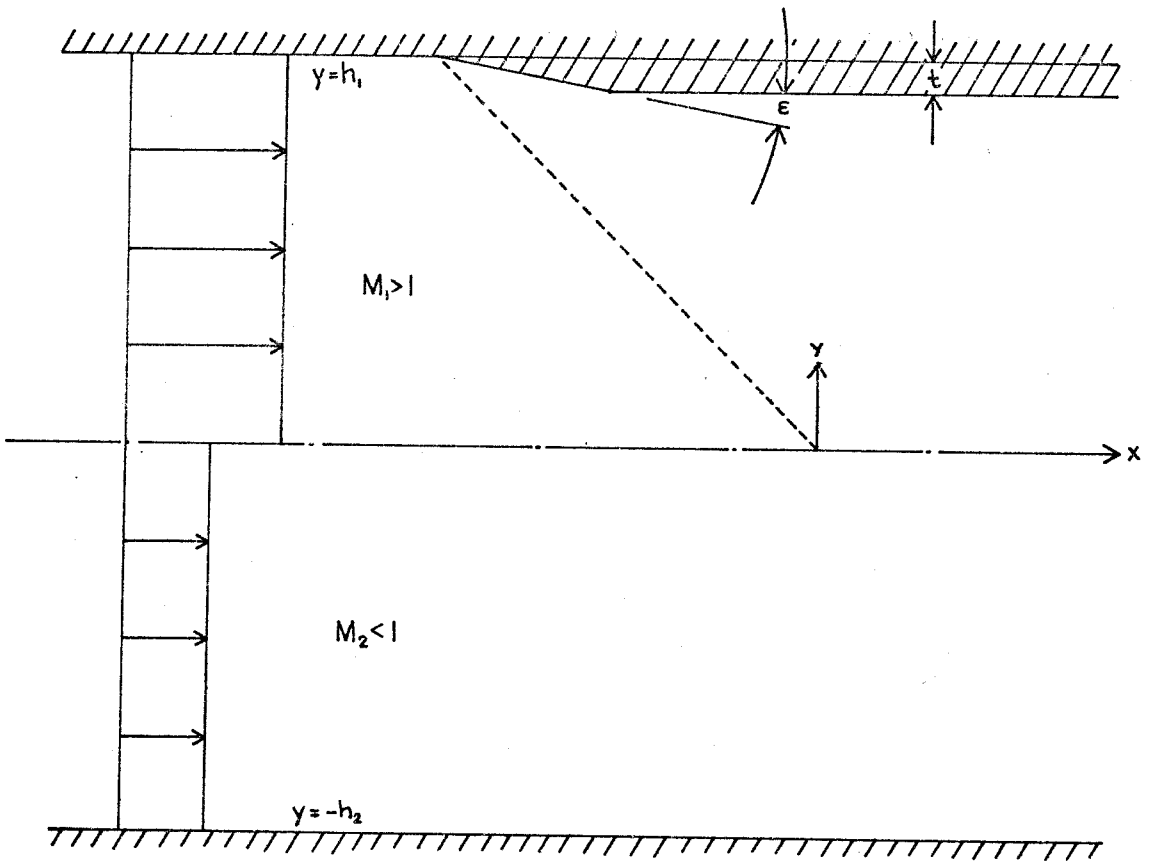

Figure 4.4: Supersonic Wedge Problem

$$I_{3n} = \frac{1}{2\pi}\int_{-\infty}^{\infty} \frac{f}{kq}\, e^{-ikS_{2n}} \cosh k\beta_2(y+h_2)\,dk \qquad n = 1, 2 \qquad (4.26c)$$

$$I_{4n} = -\frac{i}{2\pi}\int_{-\infty}^{\infty} \frac{1}{kq}\, e^{-ikS_{2n}} \sinh k\beta_2(y+h_2)\,dk \qquad n = 1, 2 \qquad (4.26d)$$

and

$$S_{11} = x - t/\epsilon + \beta_1 y \qquad (4.27a)$$

$$S_{12} = x + 2\beta_1 h_1 - t/\epsilon - \beta_1 y \qquad (4.27b)$$

$$S_{13} = x + \beta_1 y \qquad (4.27c)$$

$$S_{14} = x + 2\beta_1 h_1 - \beta_1 y \qquad (4.27d)$$

$$S_{21} = x + \beta_1 h_1 - t/\epsilon \qquad (4.27e)$$

$$S_{22} = x + \beta_1 h_1 \qquad (4.27f)$$

All the integrals of eq. (4.26) have poles on the path of integration in the complex k-plane, and all but eq. (4.26b) have poles in the plane away from the path of integration as well. Equation (4.26b) has a single pole at $k = 0$; the others have poles at all points where $kq(k) = 0$, i.e., at the origin $k = 0$ and at all points where $q(k) = 0$, $k \neq 0$.

The integrals will be evaluated through contour integration and the method of residues. To do this, it is first necessary to find all the poles. The equation $q(k) = 0$ reduces to

$$\tanh k\beta_2 h_2 = r \tan k\beta_1 h_1 \qquad (4.28)$$

where

$$r = \frac{\beta_1 M_2^2}{\beta_2 M_1^2} \quad . \qquad (4.29)$$

Resolve the complex k of this equation into real and imaginary parts:

$$k = k_r + ik_i \qquad (k_r \text{ and } k_i \text{ real}) \quad .$$

It can be seen that except for singular cases the poles are either pure real or pure imaginary, i.e., poles lie only on the axes of the complex k-plane, and are governed by the equations

$$k_i = 0 \qquad \tanh k_r \beta_2 h_2 = r \tan k_r \beta_1 h_1 \quad , \qquad (4.30a)$$

$$k_r = 0 \qquad \tan k_i \beta_2 h_2 = r \tanh k_i \beta_1 h_1 \quad . \qquad (4.30b)$$

Note that the solution for the poles depends only on M_1, M_2, h_1, and h_2, and not on x and y. Thus, for a given set of these parameters, the set of poles is the same for all (x, y). Due to the periodic nature of the tangent function, each part of eq. (4.30) defines an infinite set of poles $\{k_r^{(j)}\}$ and $\{k_i^{(j)}\}$ (see Figure 4.5). We can see that

$$j\pi < k_r^{(j)}\beta_1 h_1 < j\pi + \tan^{-1}(1/r)$$

$$j\pi < k_i^{(j)}\beta_2 h_2 < j\pi + \tan^{-1}(r) \quad ,$$

restricting the poles so that

$$j \geq 0 \quad , \quad k_r^{(j)} > 0 \quad , \quad k_i^{(j)} > 0 \quad .$$

Under this formulation there are five groups of poles: $k = 0$, $k = \pm k_r^{(j)}$, and $k = \pm ik_i^{(j)}$, as shown in Figure 4.5. For each positive j, there can be one and only one solution $k_r^{(j)}$ and $k_i^{(j)}$. However, for $j = 0$ there may be no positive (i.e., excluding zero) solution at all, as is illustrated in Figure 4.6.

In finding a numerical solution for these poles, it will be necessary to know the conditions for which a given pole with $j = 0$ vanishes, as poles at the origin must be treated differently from those not at $k = 0$. It can be seen that one and only one of the two poles with $j = 0$ will (in general) vanish. The division between these two

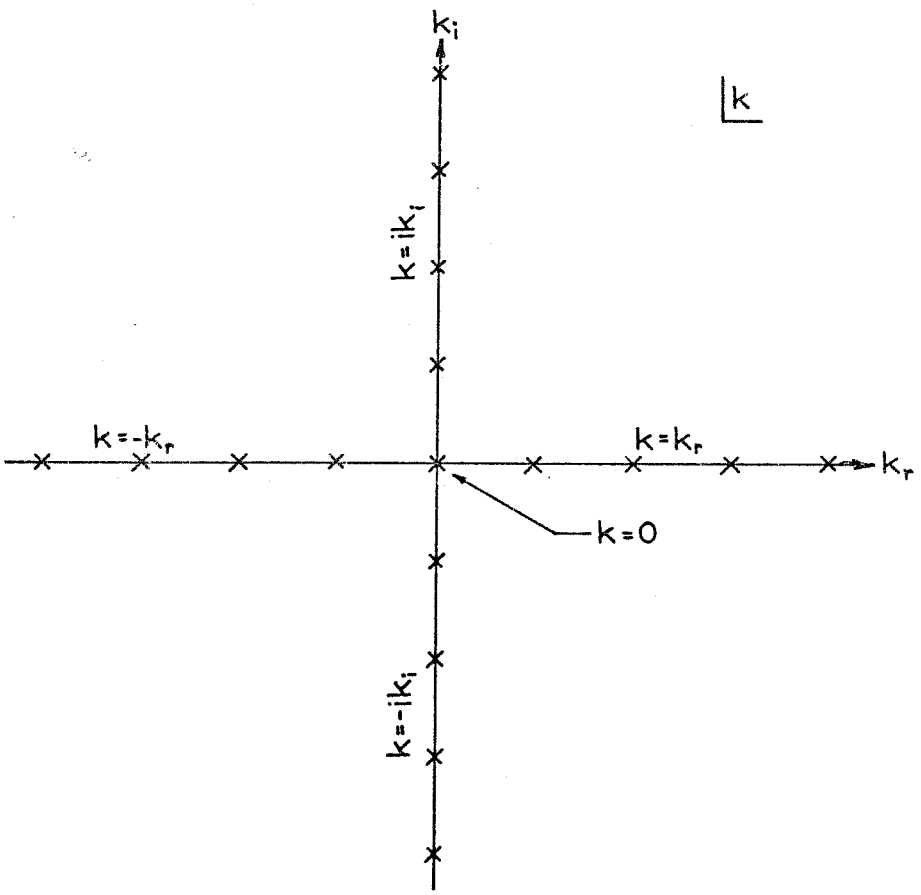

Figure 4.5: Integrand Poles

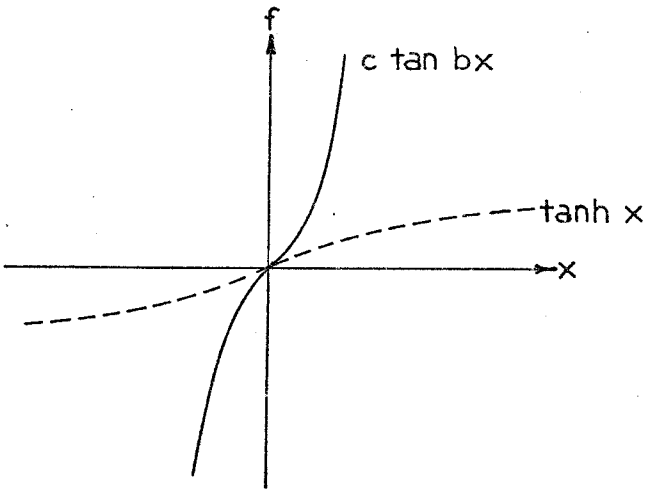

NO NONZERO SOLUTION

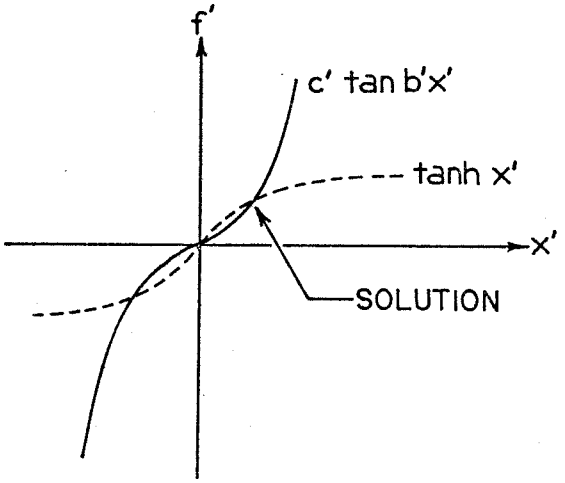

ONE POSITIVE SOLUTION

Figure 4.6: Qualitative Character of Solution of $k_i^{(0)}$ and $k_r^{(0)}$

regions is the line

$$F(M_1, M_2, h_1/h_2) \equiv \left(\frac{M_1^2 - 1}{M_1^2}\right)\left(\frac{h_1}{h_2}\right) - \frac{1 - M_2^2}{M_2^2} = 0 , \qquad (4.31)$$

which is the line on which the flow is choked at the unperturbed condition. If F is negative, the behavior of the flow for area changes is "subsonic-like" (i.e., area increases cause a rise in pressure) and the valid terms of the $k_r^{(j)}$ series start at j = 0 while the $k_i^{(j)}$ series starts at j = 1. Conversely, if F is positive, the behavior is "supersonic-like" (area increases cause a drop in pressure) and the $k_r^{(j)}$ series starts at j = 1 while the $k_i^{(j)}$ series starts at j = 0. When F = 0, the unperturbed flow is choked and the first-order linearized theory breaks down for even the smallest perturbations.

Integration from k = -∞ to k = ∞ can be represented as a limit:

$$\int_{-\infty}^{\infty} = \lim_{\substack{\delta \to 0 \\ \delta > 0}} \int_{-\infty + i\delta}^{\infty + i\delta}$$

in which the contour of integration is displaced an infinitesimal amount above the real k-axis so that the path of integration does not pass through the poles on the real axis. To see that the path must be displaced upward rather than downward, we must realize that the poles on the real axis represent spatially-oscillating solutions, while those on the imaginary axis are spatially-damped solutions. It will be shown later that for points (x, y) far upstream of the disturbance sources, only poles above the integration path will contribute to the solution.

Physical intuition tells us that disturbances must die out upstream, and thus the real axis must be excluded. Therefore, the path of integration must be displaced above the real axis, and the formulation presented here is the proper one. The contour will be closed in either the upper or lower half plane at a radius of infinity, whichever half plane causes the semicircular portion of the contour to make zero contribution to the result (see Figure 4.7). The rejected half-plane contour will generally cause the result to blow up. Then, from residue calculus:

$$\int_{-\infty}^{\infty} f(k)dk = \int_C f(k)dk = \pm 2\pi i \sum_n R_n ,$$

where the plus or minus sign depends respectively on whether the direction of the path of integration on the contour C is positive (counterclockwise) or negative (clockwise), which refers respectively to contours in the upper or lower half plane. The factor $\sum_n R_n$ is the sum of the residues of all the poles within C. If C is closed in the upper half plane, then this refers to the single set of poles $k = ik_i^{(j)}$. However, if C is closed in the lower half plane, then C encloses the poles $k = 0$, $k = \pm k_r^{(j)}$, and $k = -ik_i^{(j)}$ and the summation must be performed over all these poles. The condition for choosing the proper contour will be discovered later in this analysis.

All poles away from the origin (except possibly for isolated cases, depending on the initial data) are first order. If the integrands are expressed as $p(k)/q_o(k)$ where p and q_o are polynomials, then the residue of a first-order pole at $k = k_o$ is given by

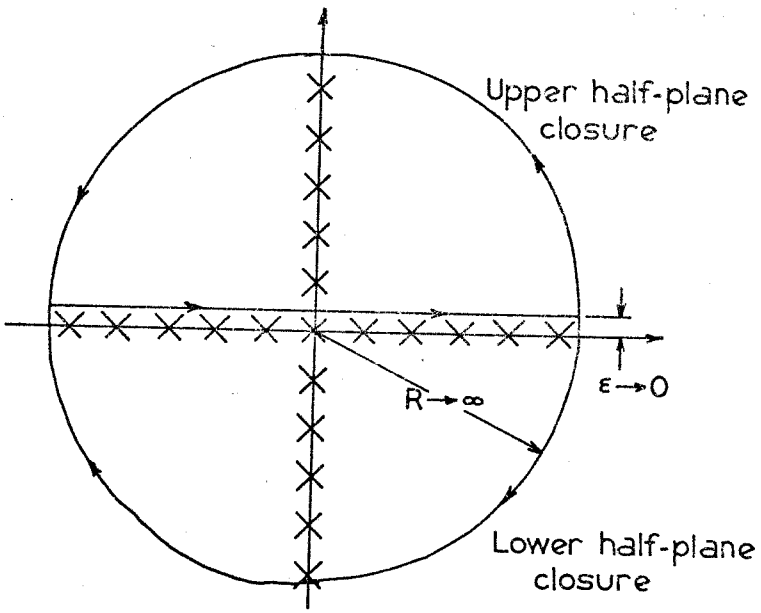

Figure 4.7: Contours of Integration

$$\mathrm{Res}\left[\frac{p(k)}{q_o(k)}\ ,\ k_o\right] = \frac{p(k_o)}{q_o'(k_o)} \quad .$$

Integral (4.26b) will be discussed later, since it is of a much simpler form than (4.26a, c, and d). These other integrals have at the origin either a second-order pole or a first-order pole and a removable singularity. In both of these cases, since the third derivative of the denominator vanishes at the origin, the residue is given by

$$\mathrm{Res}\left[\frac{p(k)}{q_o(k)}\ ,\ 0\right] = \frac{2p'(o)}{q_o''(o)} \quad .$$

Now consider the integral of eq. (4.26b):

$$I_{2n} = -\frac{i}{\pi}\int_{-\infty}^{\infty}\frac{1}{k}\,e^{-ikS_{1n}}(1+e^{-2ik\beta_1 h_1})dk \qquad n = 1, 3 \qquad (4.26b)$$

With a single pole at the origin (k = 0), this is the easiest of all the integrals to evaluate:

$$I_{2n} = -H(S_{1n}) \ , \qquad (4.32)$$

where H(x) is the unit step function. The singular lines $S_{11} = 0$ and $S_{13} = 0$ are the physically-expected lines for such a calculation: they are the Mach lines into the flow from the shoulder and leading edge, respectively, of the wedge.

The other integrals become the sum over all relevant poles of the residues of the integrand, i. e.,

$$I_{1n} = \pm\sum \mathrm{Res}\left(\frac{i}{2}\,\frac{f}{qk}\,e^{-ikS_{1n}}, k\right) = \pm\sum_n \mathrm{Res}(\vartheta_{1n}, k) \qquad (4.33a)$$

$$I_{3n} = \pm\sum \mathrm{Res}\left(\frac{i}{kq}\,e^{-ikS_{2n}\cosh k\beta_2(y+h_2)}, k\right) = \pm\sum_n \mathrm{Res}(\vartheta_{3n}, k) \qquad (4.33b)$$

$$I_{4n} = \pm\sum \mathrm{Res}\left(\frac{i}{kq} e^{-ikS_{2n}} \sinh k\beta_2(y+h_2), k\right) = \pm\sum \mathrm{Res}(\vartheta_{4n}, k) \tag{4.33c}$$

The factor of $(2\pi i)$ has been included in these expressions. From this point on, the superscript (j) on the notation of the poles will be dropped. It is to be understood that a reference to k_r or k_i refers to the entire set.

At the real poles $k = k_r$ (which does not include the pole $k = 0$), we have $q = 0$ and $q' = 0$ (the poles are first order) and the terms of the series can be evaluated as

$$\mathrm{Res}(\vartheta_{1n}, k_r) = \frac{i}{2} \frac{f \exp[-ik_r S_{in}]}{k_r q'(k_r)} \tag{4.34a}$$

$$\mathrm{Res}(\vartheta_{3n}, k_r) = \frac{i}{k_r q'(k_r)} \exp[-ik_r S_{2n}] \cosh k_r \beta_2(y+h_2) \tag{4.34b}$$

$$\mathrm{Res}(\vartheta_{4n}, k_r) = \frac{1}{k_r q'(k_r)} \exp[-ik_r S_{2n}] \sinh k_r \beta_2(y+h_2) \ . \tag{4.34c}$$

Note that the residues of the real poles occur only in pairs of k_r and $-k_r$. Taking advantage of this, put

$$R_{mn}(k_r) = \mathrm{Res}(\vartheta_{mn}, k_r) + \mathrm{Res}(\vartheta_{mn}, -k_r) \ ,$$

$$R_{1n}(k_r) = \frac{f(k_r) \sin k_r S_{1n}}{k_r q'(k_r)} \tag{4.35a}$$

$$R_{2n}(k_r) = \frac{2 \cosh k_r \beta_2(y+h_2) \sin k_r S_{2n}}{k_r q'(k_r)} \tag{4.35b}$$

$$R_{4n}(k_r) = \frac{2 \sinh k_r \beta_2(y+h_2) \cos k_r S_{2n}}{k_r q'(k_r)} \tag{4.35c}$$

Differentiate eq. (4.22) with respect to k and get:

$$q'(k) = (\beta_2^2 h_2 M_1^2 - \beta_1^2 h_1 M_2^2)\cos k\beta_1 h_1 \cosh k\beta_2 h_2 -$$

$$-\beta_1\beta_2(h_1 M_1^2 + h_2 M_2^2)\sin k\beta_1 h_1 \sinh k\beta_2 h_2 \quad . \qquad (4.36)$$

Adopt the notation that $f(ik_i) = f^*(k_i)$. Then

$$q^{*'}(k_i) = (\beta_2^2 h_2 M_1^2 - \beta_1^2 h_1 M_2^2)\cosh k_i\beta_1 h_1 \cos k_i\beta_2 h_2$$

$$+\beta_1\beta_2(h_1 M_1^2 + h_2 M_2^2)\sinh k_i\beta_1 h_1 \sin k_i\beta_2 h_2 \quad , \qquad (4.37)$$

$$f^*(k_i) = M_2^2 \cosh k_i\beta_1 h_1 \cos k_i\beta_2 h_2 - \frac{\beta_2 M_1^2}{\beta_1} \sinh k_i\beta_1 h_1 \sin k_i\beta_2 h_2 \quad , \qquad (4.38)$$

and

$$R_{1n}^*(k_i) = \frac{1}{2} \frac{f^*(k_i)\exp(k_i S_{1n})}{k_i q^{*'}(k_i)} \qquad (4.35d)$$

$$R_{3n}^*(k_i) = \frac{\exp(k_i S_{2n})\cos k_i\beta_2(y+h_2)}{k_i q^{*'}(k_i)} \qquad (4.35e)$$

$$R_{4n}^*(k_i) = \frac{\exp(k_i S_{2n})\sin k_i\beta_2(y+h_2)}{k_i q^{*'}(k_i)} \quad . \qquad (4.35f)$$

The next task is the calculation of the residues at $k = 0$. Recall that for polynomials $p(k)$ and $q(k)$,

$$\text{Res}\left(\frac{p}{q}, 0\right) = \frac{2p'(0)}{q''(0)}$$

when $q'''(0) = 0$ as it does for all these poles. The residues at $k = 0$ can be found to be

$$R_{1n}^{(o)} = \frac{M_2^2 S_{1n}}{2q'(0)} \qquad (4.35g)$$

$$R_{3n}^{(o)} = \frac{S_{2n}}{q'(0)} \qquad (4.35h)$$

$$R_{4n}^{(o)} = \frac{\beta_2(y+h_2)}{q'(0)} \quad . \tag{4.35i}$$

No analytic form has been found for the infinite series described by the R_{ij} of eq. (4.35 a-f). The character of the series is complicated considerably by the nonuniform spacing of the poles k_i and k_r. However, the repetition of the poles does become uniform in the limit as j becomes large and the hyperbolic tangent of eq. (4.30) becomes close to unity. This limit describes an asymptotic solution.

A different series, based on the asymptotic representation of k_i and k_r, can be shown to be a hypergeometric function, and the terms of the actual series will become vanishingly close to the terms of the asymptotic series as j approaches infinity. In fact, it can be seen that the error is less than one part in 10^5 when only 6 or 7 actual terms are included. Calling the cutoff value $j = J$, the method which will be adopted can be described as

$$\text{actual solution} = \text{asymptotic solution} + \sum_{j=0,1}^{J} [\text{actual } j^{th} \text{ term} - \text{asymptotic } j^{th} \text{ term}] ,$$

where "asymptotic solution" means the hypergeometric function covering the series from $j = 0$ or 1, whichever is proper according to the condition of eq. (4.31). The advantage of this rather than a "brute force" method of simply summing the actual terms as long as necessary lies in the simplifications available in treating cases where convergence, although uniform, is quite slow. Analytic approximations are available in treating a hypergeometric series under these conditions. The problem of slow convergence will be seen later to come up frequently, especially in some of the more interesting

evaluations.

To find the asymptotic poles, replace the hyperbolic tangent in eq. (4.30) by unity wherever it appears. This is equivalent to the following replacements:

$$\sinh k_r\beta_2 h_2,\ \cosh k_r\beta_2 h_2 \rightarrow \tfrac{1}{2}\exp(k_r\beta_2 h_2)$$

$$\sinh k_i\beta_1 h_1,\ \cosh k_i\beta_2 h_2 \rightarrow \tfrac{1}{2}\exp(k_i\beta_2 h_2)$$

and the poles are then given by

$$k_r\beta_1 h_1 = \theta_r + j\pi \tag{4.39a}$$

$$k_i\beta_2 h_2 = \theta_i + j\pi \tag{4.39b}$$

where

$$\theta_r = \tan^{-1}(r)\ , \tag{4.40a}$$

$$\theta_i = \tan^{-1}(1/r)\ . \tag{4.40b}$$

In order to simplify slightly the coming algebra, let

$$\xi = \sqrt{\beta_1^{\,2}M_2^{\,4} + \beta_2^{\,2}M_1^{\,4}}\ . \tag{4.41}$$

Then another way of expressing eq. (4.40) would be

$$\sin\theta_r = \cos\theta_i = \frac{\beta_2 M_1^2}{\xi} \tag{4.42a}$$

$$\cos\theta_r = \sin\theta_i = \frac{\beta_1 M_2^2}{\xi} \tag{4.42b}$$

As has been mentioned previously, the procedure will be to evaluate the integral I_{mn} by an infinite series of residues. These residues are of four types; denote each type by $I_{mn\nu}$:

$\nu = 1$ sum over all real non-zero poles,

$\nu = 2$ sum over positive imaginary poles,

$\nu = 3$ pole at origin,

$\nu = 4$ sum over negative imaginary terms.

Then, if the contour of integration is closed in the upper half plane,

$$I_{mn} = I_{mn2} \; ; \tag{4.43a}$$

and if the contour closes in the lower half plane,

$$I_{mn} = -I_{mn1} - I_{mn3} - I_{mn4} \; , \tag{4.43b}$$

the change of sign being due to the sense of the contour of integration being opposite that which defines a positive residue.

No asymptotic form is required for the residue $\nu = 3$. We have from eq. (4.35) the results

$$I_{1n3} = \frac{M_2^2 S_{1n}}{2q'(0)} \tag{4.44a}$$

$$I_{3n3} = \frac{S_{2n}}{q'(0)} \tag{4.44b}$$

$$I_{4n3} = \frac{\beta_2 (y+h_2)}{q'(0)} \tag{4.44c}$$

Using eq. (4.35), the remaining series (still in terms of actual rather than asymptotic poles) are

$$I_{1n1} = \sum_j \frac{f(k_r)}{k_r q'(k_r)} \sin k_r S_{1n} \tag{4.45a}$$

$$I_{1n2} = \frac{1}{2} \sum_j \frac{f^*(k_i)}{k_i q^{*\prime}(k_i)} \exp(k_i S_{1n}) \tag{4.45b}$$

$$I_{1n4} = -\frac{1}{2} \sum_j \frac{f^*(k_i)}{k_i q^{*\prime}(k_i)} \exp(-k_i S_{1n}) \tag{4.45c}$$

$$I_{3n1} = 2\sum_j \frac{1}{k_r q'(k_r)} \cosh k_r\beta_2(y+h_2)\sin k_r S_{2n} \qquad (4.45d)$$

$$I_{3n2} = \sum_j \frac{1}{k_i q^{*\prime}(k_i)} \cos k_i\beta_2(y+h_2)\exp(k_i S_{2n}) \qquad (4.45e)$$

$$I_{3n4} = -\sum_j \frac{1}{k_i q^{*\prime}(k_i)} \cos k_i\beta_2(y+h_2)\exp(-k_i S_{2n}) \qquad (4.45f)$$

$$I_{4n1} = 2\sum_j \frac{1}{k_r q'(k_r)} \sinh k_r\beta_2(y+h_2)\cos k_r S_{2n} \qquad (4.45g)$$

$$I_{4n2} = \sum_j \frac{1}{k_i q^{*\prime}(k_i)} \sin k_i\beta_2(y+h_2)\exp(k_i S_{2n}) \qquad (4.45h)$$

$$I_{4n4} = \sum_j \frac{1}{k_i q^{*\prime}(k_i)} \sin k_i\beta_2(y+h_2)\exp(-k_i S_{2n}) \qquad (4.45i)$$

The notation will be adopted that the superscript ($\hat{}$) denotes a function or series whose poles are found by the asymptotic substitutions of eq. (4.39). Each of these asymptotic series will be evaluated by placing it in the form of a hypergeometric function:

$$F(\alpha, 1; \alpha+1; z) = \sum_{n=0}^{\infty} \frac{1}{n+\alpha} z^n \ ,$$

where z may be complex. The limits of convergence for this series are that $|z| \leq 1$ and $z \neq 1$. Adopting the conventional usage that Re(z) and Im(z) respectively refer to the real and imaginary parts of z, the result is

$$\hat{I}_{1n1} = -\frac{1}{\pi\beta_1} \mathrm{Im}\left[e^{\theta_r A_1} \sum_n \frac{1}{n+\theta_r/\pi} (e^{\pi A_1})^n \right] \qquad (4.46a)$$

$$\hat{I}_{1n2} = \frac{2\beta_2 M_1^2 M_2^2}{\pi\xi^2} e^{\theta_i A_2} \sum_n \frac{1}{n+\theta_i/\pi} (e^{\pi A_2})^n \qquad (4.46b)$$

$$\hat{f}_{1n4} = -\frac{2\beta_2 M_1^2 M_2^2}{\pi\xi^2} e^{\theta_i A_2} \sum_n \frac{1}{n+\theta_i/\pi} (e^{\pi A_2})^n \tag{4.46c}$$

$$\hat{I}_{3n1} = -\frac{2}{\pi\xi} \mathrm{Im}\left[e^{\theta_r A_4} \sum_n \frac{1}{n+\theta_r/\pi} (-e^{\pi A_4})^n + e^{\theta_r A_5} \sum_n \frac{1}{n+\theta_r/\pi} (e^{-\pi A_5})^n \right] \tag{4.46d}$$

$$\hat{I}_{3n2} = \frac{2}{\pi\xi} \mathrm{Re}\left[e^{\theta_i A_6} \sum_n \frac{1}{n+\theta_i/\pi} (-e^{\pi A_6})^n \right] \tag{4.46e}$$

$$\hat{f}_{3n4} = -\frac{2}{\pi\xi} \mathrm{Re}\left[e^{\theta_i A_7} \sum_n \frac{1}{n+\theta_i/\pi} (-e^{\pi A_7})^n \right] \tag{4.46f}$$

$$\hat{I}_{4n1} = -\frac{2}{\pi\xi} \mathrm{Re}\left[e^{\theta_r A_4} \sum_n \frac{1}{n+\theta_r/\pi} (-e^{\pi A_4})^n - e^{\theta_r A_5} \sum_n \frac{1}{n+\theta_r/\pi} (-e^{\pi A_5})^n \right] \tag{4.46g}$$

$$\hat{I}_{4n2} = \frac{2}{\pi\xi} \mathrm{Im}\left[e^{\theta_i A_6} \sum_n \frac{1}{n+\theta_i/\pi} (-e^{\pi A_6})^n \right] \tag{4.46h}$$

$$\hat{i}_{4n4} = \frac{2}{\pi\xi} \mathrm{Im}\left[e^{\theta_i A_7} \sum_n \frac{1}{n+\theta_i/\pi} (-e^{\pi A_7})^n \right] \tag{4.46i}$$

where

$$A_1 = i \frac{S_{1n}}{\beta_1 h_1} \tag{4.47a}$$

$$A_2 = \frac{S_{1n} - 2\beta_1 h_1}{\beta_2 h_2} \tag{4.47b}$$

$$A_3 = -\frac{S_{1n} + \pi\beta_1 h_1}{\beta_2 h_2} \tag{4.47c}$$

$$A_4 = \frac{1}{\beta_1 h_1} (\beta_2 y + i S_{2n}) \tag{4.47d}$$

$$A_5 = \frac{1}{\beta_1 h_1} [-(2 + y/h_2)\beta_2 h_2 + i S_{2n}] \tag{4.47e}$$

$$A_6 = \frac{S_{2n} - \beta_1 h_1}{\beta_2 h_2} + i(1 + y/h_2) \tag{4.47f}$$

$$A_7 = -\frac{S_{2n}+\beta_1 h_1}{\beta_2 h_2} + i(1+y/h_2) \qquad (4.47g)$$

We can see that the conditions for convergence are those presented in Table 4-1. In Table 4-2 are presented the admissible range for integration contours to be closed in the upper or lower half plane for each integral. A glance at this table will reveal that the convergence conditions have some ambiguity as to the proper value of S_{ij} at which the integration contour should switch from the upper half plane to the lower half plane.

This ambiguity can only be resolved by considering the physical situation in terms of where it seems reasonable for the physical flow to undergo a (possibly) sudden change. This physical layout is presented in Figure 4.8.

The natural lines of discontinuity on the supersonic stream are $S_{11} = 0$ and $S_{13} = 0$. Either through similar reasoning or preferably through mathematical consideration of the condition of continuity of pressure and inclination angle across the interface, it can be shown that the corresponding switching points in the subsonic stream are the lines $S_{21} = \beta_1 h_1$ and $S_{22} = \beta_1 h_1$. The final choice of integration contour is presented in Table 4-3. In a condition where the integration is in the upper half plane,

$$I_{mn} = I_{mn2} \; ; \qquad (4.43a)$$

and in the lower half plane,

$$I_{mn} = -I_{mn1} - I_{mn3} - I_{mn4} \; . \qquad (4.43b)$$

4.3.3 Subsonic wedge problem. This problem considers the same type of boundary condition discussed previously, that of a thin

TABLE 4-1. Integral Convergence Conditions

Integral	$\|z\| < 1$	or $z \neq 1$
I_{1n1}	(not relevant)	$S_{1n} = j\beta_1 h_1$, $j = 0, 1, 2, 3, \ldots$
I_{1n2}	$S_{1n} < 2\beta_1 h_1$	--
I_{1n4}	$S_{1n} > -2\beta_1 h_1$	--
I_{3n1}, I_{4n1}	$y < 0$	$y = 0$, $S_{2n} \neq \beta_1 h_1 (2j+1)$ $j = 0, 1, 2, \ldots$
I_{3n2}, I_{4n2}	$S_{2n} < \beta_1 h_1$	$S_{2n} = \beta_1 h_1$, $y \neq 0$
I_{3n4}, I_{4n4}	$S_{2n} > -\beta_1 h_1$	$S_{2n} = -\beta_1 h_1$, $y \neq 0$
I_{5n1}	converges everywhere	
$I_{6n1}, I_{7n1}, I_{8n1}, I_{9n1}$	$y > -h_2$	$y = h_2$, $S_{6n} \neq 2j\beta_1 h_1$ $j = 0, 1, 2, \ldots$
I_{5n2}	$S_{5n} < \beta_1 h_1$	$S_{5n} \neq \beta_1 h_1$
$I_{6n2}, I_{7n2}, I_{8n2}, I_{9n2}$	$S_{6n} < 0$	$S_{6n} = 0$, $y \neq -h_2$
I_{5n4}	$S_{5n} > -\beta_1 h_1$	$S_{5n} \neq \beta_1 h_1$
$I_{6n4}, I_{7n4}, I_{8n4}, I_{9n4}$	$S_{6n} > 0$	$S_{6n} = 0$, $y \neq -h_2$

TABLE 4-2. Integration Contours for Convergence

Integral	Upper Half Plane	Lower Half Plane
I_{1n}	$S_{1n} < 2\beta_1 h_1$	$S_{1n} > -2\beta_1 h_1$
I_{3n}, I_{4n}	$S_{2n} < \beta_1 h_1$	$S_{2n} > -\beta_1 h_1$
I_{5n}	$S_{5n} < \beta_1 h_1$	$S_{5n} > -\beta_1 h_1$
$I_{6n}, I_{7n}, I_{8n}, I_{9n}$	$S_{6n} < 0$	$S_{6n} > 0$

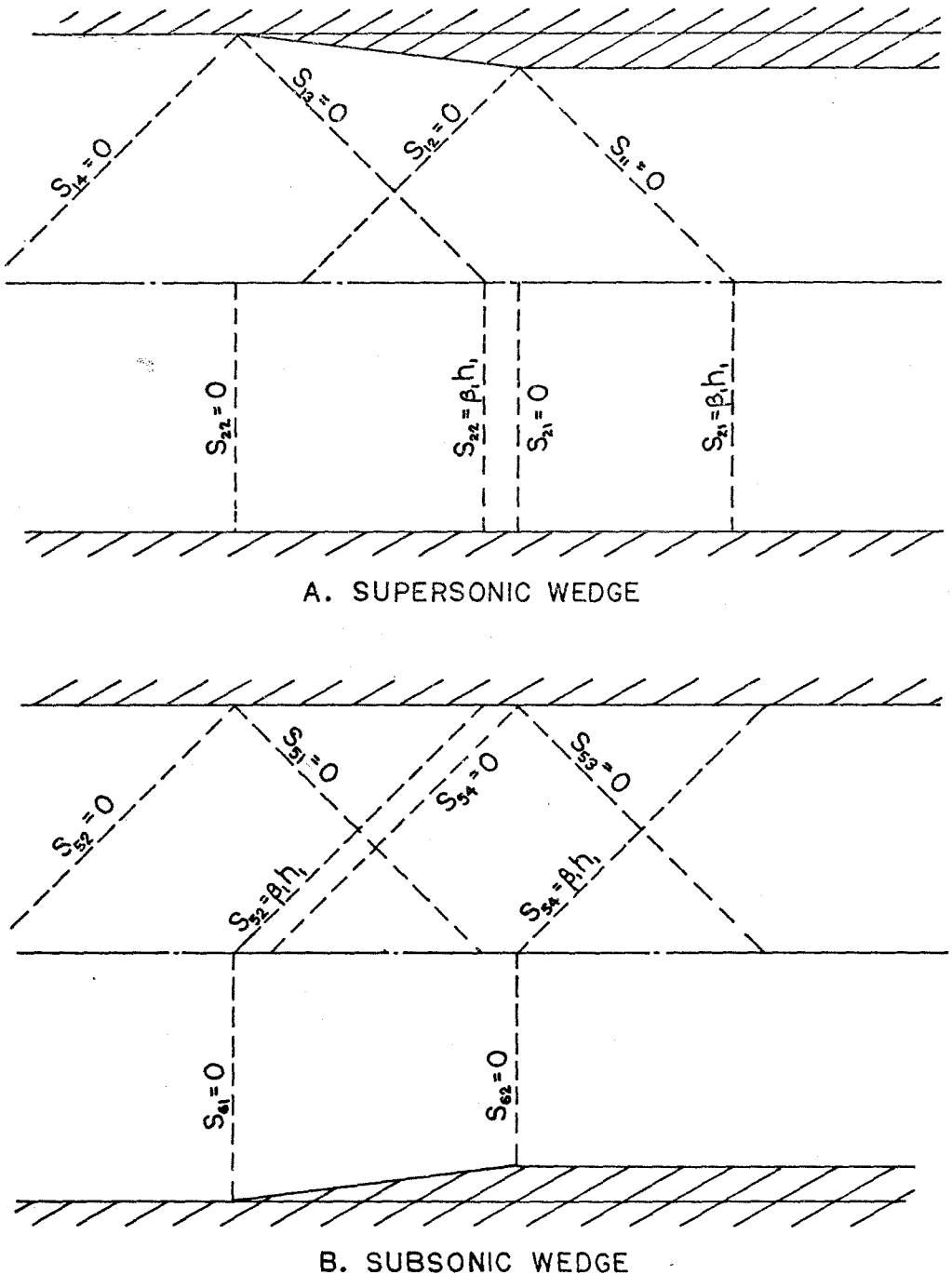

Figure 4.8: Physical Layout of the Wedge Problems

TABLE 4-3. Final Choice of Integration Contours

Integral	Upper Half Plane	Lower Half Plane
I_{11}, I_{12}	$S_{11} < 0$	$S_{11} > 0$
I_{13}, I_{14}	$S_{13} < 0$	$S_{13} > 0$
I_{31}, I_{41}	$S_{21} < \beta_1 h_1$	$S_{21} > \beta_1 h_1$
I_{32}, I_{42}	$S_{22} < \beta_1 h_1$	$S_{22} > \beta_1 h_1$
I_{51}, I_{52}	$S_{52} < \beta_1 h_1$	$S_{52} > \beta_1 h_1$
I_{53}, I_{54}	$S_{54} < \beta_1 h_1$	$S_{54} > \beta_1 h_1$
$I_{61}, I_{71}, I_{81}, I_{91}$	$S_{61} < 0$	$S_{61} > 0$
$I_{62}, I_{72}, I_{82}, I_{92}$	$S_{62} < 0$	$S_{62} > 0$

wedge of finite extent turning the flow inward, although in this case the wedge is fitted on the subsonic wall rather than on the supersonic wall.

The governing equation (4.9) and the general solution (4.14) are still valid. The first boundary condition is that there be no vertical velocity component at the supersonic wall:

$$\begin{aligned} \phi_{1,y} &= 0 \quad \text{at} \quad y = h_1 \ , \\ \tilde{\phi}_{1,y} &= 0 \quad \text{at} \quad y = h_1 \ . \end{aligned} \tag{4.48}$$

The conditions of continuity of pressure and inclination angle at the interface (eqs. (4.16) and (4.18)) are still valid. The final boundary condition is that the flow inclination angle at the subsonic wall must meet the prescribed distribution $V_w(x)$:

$$\begin{aligned} \phi_{2,y} &= V_w(x) \quad \text{at} \quad y = -h_2 \ , \\ \tilde{\phi}_{2,y} &= \tilde{V}_w(k) \quad \text{at} \quad y = -h_2 \ . \end{aligned} \tag{4.49}$$

Applying these boundary conditions to the general solution yields the expressions:

$$\phi_1(x,y) = -\frac{M_2^2}{\sqrt{2\pi}} \int_{-\infty}^{\infty} \frac{1}{kq(k)} \tilde{V}_w(k) \cos k\beta_1 (y-h_1) e^{-ikx} dk \tag{4.50a}$$

$$\phi_2(x,y) = \frac{1}{\sqrt{2\pi}} \int_{-\infty}^{\infty} \frac{\tilde{V}_w(k)}{k} \left\{ \frac{g(k)}{q(k)} \cosh k\beta_2 (y+h_2) + \frac{1}{\beta_2} \sinh k\beta_2 (y+h_2) \right\} e^{-ikx} dk \tag{4.50b}$$

where $q(k)$ is the same function defined in eq. (4.22), and

$$g(k) = \frac{\beta_1 M_2^2}{\beta_2} \sin k\beta_1 h_1 \sinh k\beta_2 h_2 - M_1^2 \cos k\beta_1 h_1 \cosh k\beta_2 h_2 \ . \tag{4.51}$$

The geometry of the problem is illustrated in Figure 4.9. In

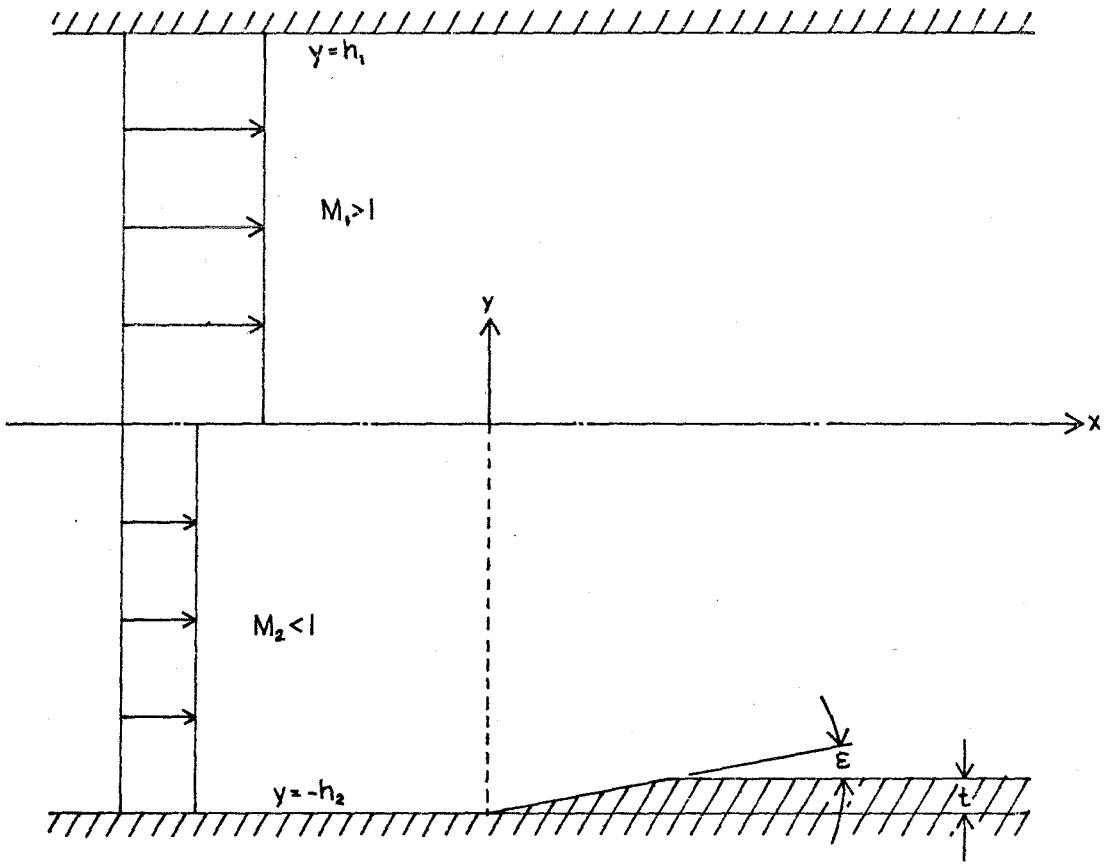

Figure 4.9: Subsonic Wedge Problem

this case, the function $V_w(x)$ is

$$V_w(x) = 0 \qquad x < 0$$

$$V_w(x) = \varepsilon \qquad 0 < x < t/\varepsilon \tag{4.52}$$

$$V_w(x) = 0 \qquad x > t/\varepsilon$$

and under the Fourier transformation,

$$\tilde{V}_w(k) = \frac{i\varepsilon}{k\sqrt{2\pi}} \left(1 - e^{ikt/\varepsilon}\right) . \tag{4.53}$$

Putting eq. (4.53) into eq. (4.50) and taking the partial derivatives with respect to x and y as before, we get that

$$\phi_{1,x} = \varepsilon M_2^2 (I_{51}+I_{52}-I_{53}-I_{54}) \tag{4.54a}$$

$$\phi_{1,y} = \varepsilon\beta_1 M_2^2 (I_{51}-I_{52}-I_{53}+I_{54}) \tag{4.54b}$$

$$\phi_{2,x} = \frac{\varepsilon}{\beta_2} (I_{61}-I_{62}+I_{71}-I_{72}) \tag{4.54c}$$

$$\phi_{2,y} = \varepsilon (I_{81}-I_{82}+I_{91}-I_{92}) \tag{4.54d}$$

where

$$I_{5n} = -\frac{1}{4\pi} \int_{-\infty}^{\infty} \frac{1}{kq} e^{-ikS_{5n}} dk \qquad n = 1, 2, 3, 4 \tag{4.55a}$$

$$I_{6n} = -\frac{\beta_1 M_2^2}{2\pi} \int_{-\infty}^{\infty} \frac{1}{kq} e^{-ikS_{6n}} \sin k\beta_1 h_1 \sinh k\beta_2 y \, dy \qquad n = 1, 2 \tag{4.55b}$$

$$I_{7n} = -\frac{\beta_2 M_1^2}{2\pi} \int_{-\infty}^{\infty} \frac{1}{kq} e^{-ikS_{6n}} \cos k\beta_1 h_1 \cosh k\beta_2 y \, dy \qquad n = 1, 2 \tag{4.55c}$$

$$I_{8n} = -\frac{i\beta_1 M_2^2}{2\pi} \int_{-\infty}^{\infty} \frac{1}{kq} e^{-ikS_{6n}} \sin k\beta_1 h_1 \cosh k\beta_2 y \, dy \qquad n = 1, 2 \tag{4.55d}$$

$$I_{9n} = -\frac{i\beta_2 M_1^2}{2\pi} \int_{-\infty}^{\infty} \frac{1}{kq} e^{-ikS_{6n}} \cos k\beta_1 h_1 \sinh k\beta_2 y \, dy \qquad n = 1, 2 \tag{4.55e}$$

and

$$S_{51} = x+\beta_1(y-h_1) \tag{4.56a}$$

$$S_{52} = x-\beta_1(y-h_1) \tag{4.56b}$$

$$S_{53} = x - \frac{t}{\epsilon} + \beta_1(y-h_1) \tag{4.56c}$$

$$S_{54} = x - \frac{t}{\epsilon} - \beta_1(y-h_1) \tag{4.56d}$$

$$S_{61} = x \tag{4.56e}$$

$$S_{62} = x - t/\epsilon \tag{4.56f}$$

All these integrands have poles at the entire set of singular points considered in the supersonic wedge case; specifically, there are poles at $k = \pm k_r^{(j)}$, $k = \pm ik_i^{(j)}$, and $k = 0$. These integrals will be evaluated as before, using the same three-index notation to identify the various series.

At the origin, the integrals I_{5n} and I_{7n} have a second-order pole; I_{8n} and I_{9n} have a first-order pole and a removable singularity; and I_{6n} has a double removable singularity. The results for the pole at the origin are:

$$I_{5n3} = -\frac{S_{5n}}{2q'(o)} \tag{4.57a}$$

$$I_{6n3} = 0 \tag{4.57b}$$

$$I_{7n3} = -\frac{\beta_2 M_1^2 S_{6n}}{q'(o)} \tag{4.57c}$$

$$I_{8n3} = \frac{\beta_1 M_2^2 S_{6n}}{q'(o)} \tag{4.57d}$$

$$I_{9n3} = \frac{\beta_2 M_1^2 y}{q'(o)} \quad . \tag{4.57e}$$

All the poles where k is non-zero are first order. The result for the entire set of real poles is:

$$I_{5n1} = -\sum_j \frac{1}{k_r q'} \sin k_r S_{5n} \tag{4.58a}$$

$$I_{6n1} = -2\beta_1 M_2^2 \sum_j \frac{1}{k_r q'} \sin k_r S_{6n} \sin k_r \beta_1 h_1 \sinh k_r \beta_2 y \tag{4.58b}$$

$$I_{7n1} = -2\beta_2 M_1^2 \sum_j \frac{1}{k_r q'} \sin k_r S_{6n} \cos k_r \beta_1 h \cosh k_r \beta_2 y \tag{4.58c}$$

$$I_{8n1} = 2\beta_1 M_2^2 \sum_j \frac{1}{k_r q'} \cos k_r S_{6n} \sin k_r \beta_1 h_1 \cosh k_r \beta_2 y \tag{4.58d}$$

$$I_{9n1} = 2\beta_2 M_1^2 \sum_j \frac{1}{k_r q'} \cos k_r S_{6n} \cos k_r \beta_1 h_1 \sinh k_r \beta_2 y \quad . \tag{4.58e}$$

The series for the k_i poles are:

$$I_{5n2} = -\tfrac{1}{2} \sum_j \frac{1}{k_i q^{*'}} e^{k_i S_{5n}} \tag{4.59a}$$

$$I_{6n2} = \beta_1 M_2^2 \sum_j \frac{1}{k_i q^{*'}} e^{k_i S_{6n}} \sinh k_i \beta_1 h_1 \sin k_i \beta_2 y \tag{4.59b}$$

$$I_{7n2} = -\beta_2 M_1^2 \sum_j \frac{1}{k_i q^{*'}} e^{k_i S_{6n}} \cosh k_i \beta_1 h_1 \cos k_i \beta_2 y \tag{4.59c}$$

$$I_{8n2} = \beta_1 M_2^2 \sum_j \frac{1}{k_i q^{*'}} e^{k_i S_{6n}} \sinh k_i \beta_1 h_1 \cos k_i \beta_2 y \tag{4.59d}$$

$$I_{9n2} = \beta_2 M_1^2 \sum_j \frac{1}{k_i q^{*'}} e^{k_i S_{6n}} \cosh k_i \beta_1 h_1 \sin k_i \beta_2 y \tag{4.59e}$$

$$I_{5n4} = \tfrac{1}{2} \sum_j \frac{1}{k_i q^{*'}} e^{-k_i S_{5n}} \tag{4.60a}$$

$$I_{6n4} = -\beta_1 M_2^2 \sum_j \frac{1}{k_i q^{*'}} e^{-k_i S_{6n}} \sinh k_i \beta_1 h_1 \sin k_i \beta_2 y \tag{4.60b}$$

$$I_{7n4} = \beta_2 M_1^2 \sum_j \frac{1}{k_i q^{*'}} e^{-k_i S_{6n}} \cosh k_i \beta_1 h_1 \cos k_i \beta_2 y \tag{4.60c}$$

$$I_{8n4} = \beta_1 M_2^2 \sum_j \frac{1}{k_i q^{*'}} e^{-k_i S_{6n}} \sinh k_i \beta_1 h_1 \cos k_i \beta_2 y \qquad (4.60d)$$

$$I_{9n4} = \beta_2 M_1^2 \sum_j \frac{1}{k_i q^{*'}} e^{-k_i S_{6n}} \cosh k_i \beta_1 h_1 \sin k_i \beta_2 y \qquad (4.60e)$$

Now make the substitutions for the asymptotic forms of the series as before. Note that I_{6n} and I_{7n} appear only as $(I_{6n}+I_{7n})$, and that I_{8n} and I_{9n} appear only as $(I_{8n}+I_{9n})$. It will not affect the result if that portion of these series that vanishes under the additions is deleted here.

$$\hat{I}_{5n1} = \frac{2}{\pi\xi} \operatorname{Im}\left[e^{\theta_r B_1} \sum_n \frac{1}{n+\theta_r/\pi} \left(-e^{\pi B_1}\right)^n \right] \qquad (4.61a)$$

$$\hat{I}_{6n1} = \hat{I}_{7n1} = \frac{2\beta_1\beta_2 M_1^2 M_2^2}{\pi\xi^2} \operatorname{Im}\left[e^{\theta_r B_2} \sum_n \frac{1}{n+\theta_r/\pi} \left(e^{\pi B_2}\right)^n \right] \qquad (4.61b)$$

$$\hat{I}_{8n1} = \hat{I}_{9n1} = -\frac{2\beta_1\beta_2 M_1^2 M_2^2}{\pi\xi^2} \operatorname{Re}\left[e^{\theta_r B_2} \sum_n \frac{1}{n+\theta_r/\pi} \left(e^{\pi B_2}\right)^n \right] \qquad (4.61c)$$

$$\hat{I}_{5n2} = -\frac{1}{\pi\xi} e^{\theta_i B_4} \sum_n \frac{1}{n+\theta_i/\pi} \left(-e^{\pi B_4}\right)^n \qquad (4.62a)$$

$$\hat{I}_{6n2} = \frac{\beta_1 M_2^2}{\pi\xi} \operatorname{Im}\left[e^{\theta_i B_5} \sum_n \frac{1}{n+\theta_i/\pi} \left(-e^{\pi B_5}\right)^n \right] \qquad (4.62b)$$

$$\hat{I}_{7n2} = -\frac{\beta_2 M_1^2}{\pi\xi} \operatorname{Re}\left[e^{\theta_i B_5} \sum_n \frac{1}{n+\theta_i/\pi} \left(-e^{\pi B_5}\right)^n \right] \qquad (4.62c)$$

$$\hat{I}_{8n2} = \frac{\beta_1 M_2^2}{\pi\xi} \operatorname{Re}\left[e^{\theta_i B_5} \sum_n \frac{1}{n+\theta_i/\pi} \left(e^{\theta_i B_5}\right)^n \right] \qquad (4.62d)$$

$$\hat{I}_{9n2} = \frac{\beta_2 M_1^2}{\pi\xi} \operatorname{Im}\left[e^{\theta_i B_5} \sum_n \frac{1}{n+\theta_i/\pi} \left(e^{\theta_i B_5}\right)^n \right] \qquad (4.62e)$$

$$\hat{I}_{5n4} = \frac{1}{\pi\xi} e^{\theta_i B_6} \sum_n \frac{1}{n+\theta_i/\pi} \left(-e^{\pi B_6}\right)^n \tag{4.63a}$$

$$\hat{I}_{6n4} = -\frac{\beta_1 M_2^2}{\pi\xi} \mathrm{Im}\left[e^{\theta_i B_7} \sum_n \frac{1}{n+\theta_i/\pi} \left(-e^{\pi B_7}\right)^n \right] \tag{4.63b}$$

$$\hat{I}_{7n4} = \frac{\beta_2 M_1^2}{\pi\xi} \mathrm{Re}\left[e^{\theta_i B_7} \sum_n \frac{1}{n+\theta_i/\pi} \left(-e^{\pi B_7}\right)^n \right] \tag{4.63c}$$

$$\hat{I}_{8n4} = \frac{\beta_1 M_2^2}{\pi\xi} \mathrm{Re}\left[e^{\theta_i B_7} \sum_n \frac{1}{n+\theta_i/\pi} \left(-e^{\pi B_7}\right)^n \right] \tag{4.63d}$$

$$\hat{I}_{9n4} = \frac{\beta_2 M_1^2}{\pi\xi} \mathrm{Im}\left[e^{\theta_i B_7} \sum_n \frac{1}{n+\theta_i/\pi} \left(-e^{\pi B_7}\right)^n \right] \tag{4.63e}$$

where

$$B_1 = \frac{1}{\beta_1 h_1} \left(-\beta_2 h_2 + iS_{5n}\right) \tag{4.64a}$$

$$B_2 = \frac{1}{\beta_1 h_1} \left(-\beta_2 h_2 + \beta_2 y + iS_{6n}\right) \tag{4.64b}$$

$$B_3 = \frac{1}{\beta_1 h_1} \left(-\beta_2 h_2 - \beta_2 y + iS_{6n}\right) \tag{4.64c}$$

$$B_4 = \frac{1}{\beta_2 h_2} \left(S_{5n} - \beta_1 h_1\right) \tag{4.64d}$$

$$B_5 = \frac{S_{6n}}{\beta_2 h_2} + i\frac{y}{h_2} \tag{4.64e}$$

$$B_6 = -\frac{1}{\beta_2 h_2} \left(S_{5n} + \beta_1 h_1\right) \tag{4.64f}$$

$$B_7 = -\frac{S_{6n}}{\beta_2 h_2} + i\frac{y}{h_2} \tag{4.64g}$$

The conditions for convergence of these series are presented in Table 4-1. Table 4-2 presents the admissible range for closure of the lower half plane. As before, the mathematical requirements of convergence alone are not sufficient to permit an unambiguous definition of the proper closure for one of the integrals, in this case, I_{5n}. Consideration of the physical situation (Figure 4.8) or the mathe-

matics of the requirement of continuity of pressure and inclination angle at the interface resolves this conflict and shows that the preferred lines of discontinuity are $S_{52} = \beta_1 h_1$ and $S_{54} = \beta_1 h_1$. These are compatible with the convergence conditions. Table 4-3 presents the final choice of integration contour.

4.3.4 Computer Calculation Description. The calculations described in the previous section were executed in a FORTRAN IV program run on the IBM 370/158 computer of the Computing Center of the California Institute of Technology. The program is described in Appendix C.

In brief outline, the program is provided with such basic information as M_1, M_2, h_1, and h_2, together with the wedge angle ϵ and the wedge thickness t. Next, a modified form of Newton's method is used to solve for the first 50 poles of the series $k_r^{(j)}$ and $k_i^{(j)}$ [eq. (4.30)]. Since the entire derivation assumes the validity of linear superposition, a composite solution can be built up as desired from several of these simple solutions. This can be accomplished easily within the main program by repeated calling of the subroutine XPHI, which generates one simple solution for either the supersonic or subsonic wedge. This subroutine acts as a controller and causes the calculation of poles, real terms, and asymptotic series, as necessary.

The heart of the program is the evaluation of the series

$$S = \sum_{n=0}^{\infty} \frac{1}{n+\alpha} z^n , \qquad (4.65)$$

which, in cases where $|z|$ is approximately unity, may converge quite slowly. By manipulating eq. (4.65), the series expansions for

$(1-z)^m \log \frac{1}{1-z}$ where m is an integer can be obtained and S may be converted to a series that converges more rapidly. In this way, for instance, one can obtain

$$S = \frac{1}{\alpha} - \alpha + \left[1 - \alpha \frac{1-z}{z} - \frac{\alpha(1-\alpha)}{2}\left(\frac{1-z}{z}\right)^2\right] \log \frac{1}{1-z}$$

$$+ \frac{\alpha(1-\alpha)}{2}\left(\frac{1}{z} - \frac{3}{2}\right) - \alpha(1-\alpha)(2-\alpha) \sum_{n=1}^{\infty} b_n \quad , \tag{4.66a}$$

where

$$b_n = \frac{1}{n(n+1)(n+2)(n+\alpha)} z^n \tag{4.66b}$$

is an equivalent form with much more rapid decrease of the early terms of the series. Of course, the expression still does not converge for $z = 1$.

4.4 Linearized Theory Results

The computational algorithms of the computer calculation involve summing exponentials of arguments of order (nh_1/h_2) and (nx). Several cutoff switches were placed in the program to stop the summation of the series as the magnitude of the argument becomes unmanageably large (about 175 for the IBM 370), which means that the results are accurate within the first couple of wave cycles of the initial disturbance $(n|x| \leq 175)$ and are accurate when h_1 and h_2 are of the same order, and lose accuracy due to truncation of the series occurring at lower n as these limits are passed. For $h_1 = h_2 =$ 2.15 inches, satisfactory results are obtained for $|x|$ less than about 14 inches. Note that the x referred to here is not the same tunnel-based x employed elsewhere. In the computer calculation only, x is fixed to the disturbance (as in Figures 4.4 and 4.9).

A study was made of the cases $\left(\frac{\beta_1 h_1}{h_2}\right) = 10.5$ and 42 for the supersonic wedge and 21.1 for the subsonic wedge, which corresponds to the supersonic wall being moved away from the interface so that effects of subsequent return of a wave reflected away from the interface in the supersonic stream are removed from the initial interaction (by 10.5, 42, etc., thicknesses of the subsonic layer). This is approaching the limit represented by the study of Tsien and Finston[18] in which this parameter is infinite, as is the parameter $(t/\varepsilon h_2)$. This second parameter is the number of subsonic layer thicknesses separating the leading edge and the shoulder of the wedge. As the parameter becomes large, the interaction effects due to each are separated so that the subsonic stream response to the leading edge interaction is complete before the start of the shoulder-wave interaction. Thus, as both parameters become very large, the first subsonic stream interaction is a response only to the leading-edge compression wave. In the study, values of $(t/\varepsilon h_2)$ of 26.8 and 107.3 were used for the supersonic wedge and 53.7 for the subsonic wedge. This was considered ample, since Tsien and Finston's results predicted that the subsonic-layer pressure disturbance due to a discrete incoming wave is confined to two or three subsonic layer thicknesses upstream and downstream of the point where the supersonic wave strikes the interface. Comparisons were also made for the case of a wedge attached to the subsonic wall.

The results of this comparison study are presented in Figure 4.10. The Mach numbers selected were $M_1 = 1.4$ and $M_2 = 0.744$.

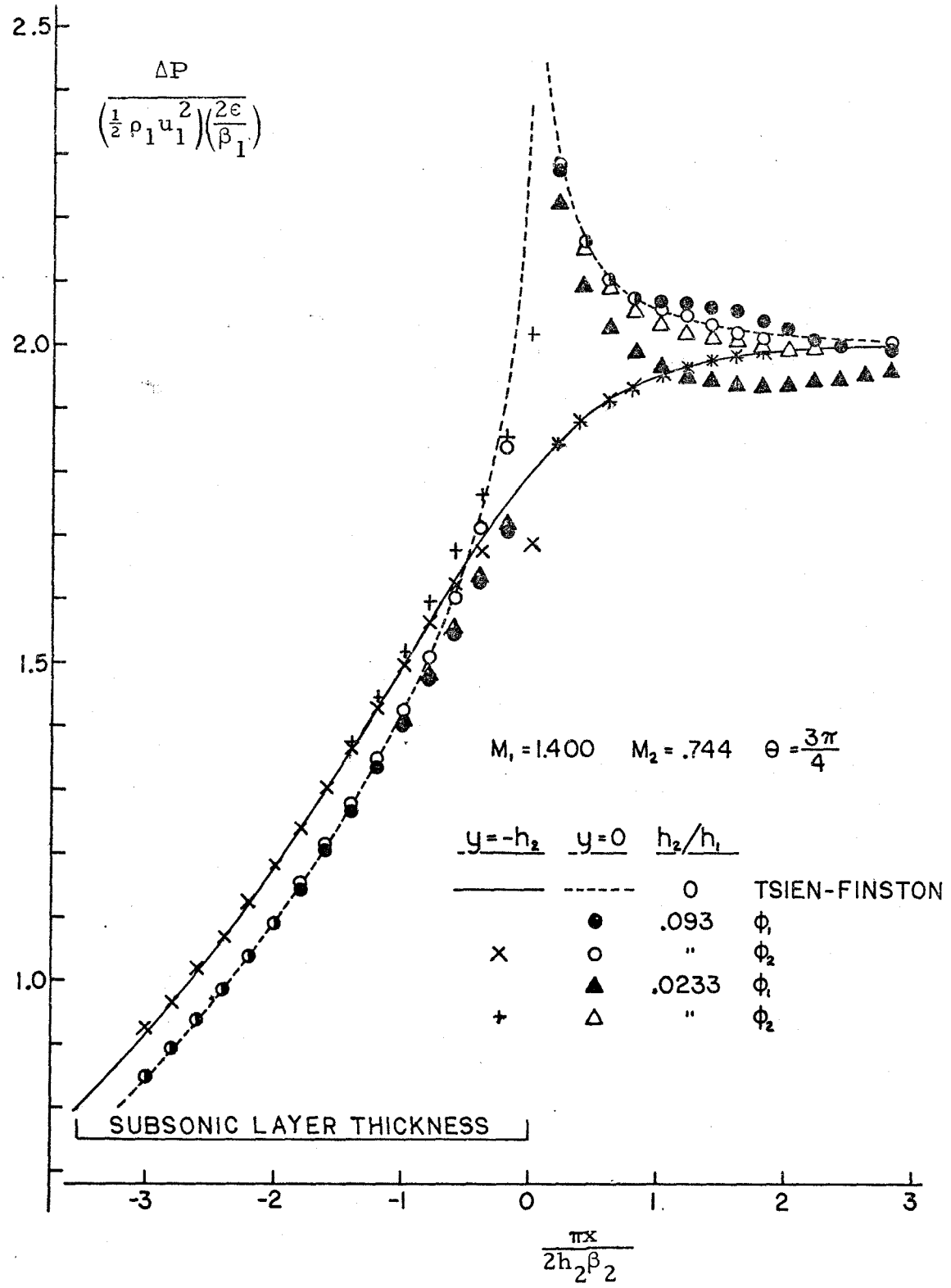

Figure 4.10a: Comparison of Theories, Supersonic Wedge

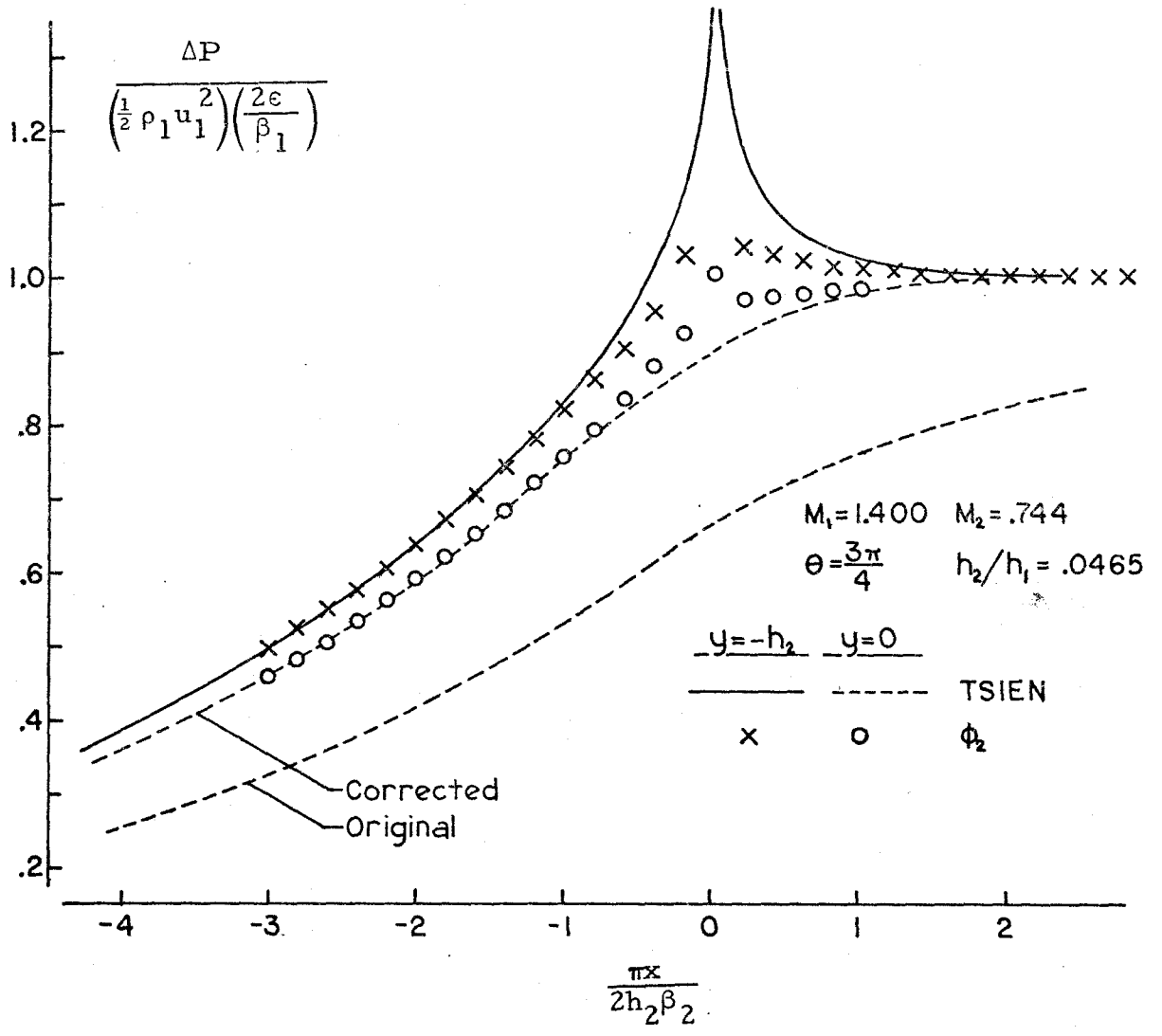

Figure 4.10b: Comparison of Theories, Subsonic Wedge

Tsien and Finston present their data for specific values of a parameter θ, defined by:

$$\cos\frac{\theta}{2} = \left(\frac{M_2^2}{M_1^2}\right) \Bigg/ \sqrt{\left(\frac{M_2^2}{M_1^2}\right)^2 + \frac{1-M_2^2}{M_1^2-1}}\,, \qquad 0 \le \theta \le \pi\,.$$

The Mach numbers chosen yield $\theta = .75\pi$, which is one of their tabulated cases.

As can be seen in Figure 4.10a, agreement between the present calculation and that of Tsien and Finston for the supersonic wedge is quite good except in the immediate region of the primary wave impingement (i.e., within about 0.2 subsonic-layer thicknesses upstream and downstream of $x = 0$). This is ascribed to numerically unstable behavior in the present calculation as the logarithmic singularity of the supersonic wave is approached; the curve would presumably converge to the actual solution if a larger computing capability or a better algorithm were available which permitted evaluation of more terms in the series. As it is, the solution with $\left(\frac{\beta_1 h_1}{h_2}\right) = 10.5$ actually agrees more closely with the Tsien-Finston result than does the solution with $\left(\frac{\beta_1 h_1}{h_2}\right) = 42$. This is because both values are sufficiently high that the leading-edge wave interaction is independent of all others, but the lower value permits including more terms in the series without exceeding the capability of the computer. It should be noted that changing the computational mode from single precision to double precision does not alleviate this problem; the difficulty is in evaluating terms like e^z where z is too large in absolute magnitude for the capability of the computer. A better computational algorithm,

one intended from the start for cases where h_1 and h_2 are not of the same order, could be expected to yield better results in the limit as $\left(\frac{\beta_1 h_1}{h_2}\right)$ approaches infinity.

Tsien and Finston developed their subsonic wedge calculation to model the case of a wedge placed on a wall in a supersonic boundary layer so that flow angle changes and pressure differences caused by the wedge must first be transmitted through the subsonic layer to reach the supersonic stream. A comparison between the present calculation and the Tsien-Finston work can be made as before in the dual limit of $\left(\frac{\beta_1 h_1}{h_2}\right)$ and $(t/\epsilon h_2)$ approaching infinity. This comparison is presented in Figure 4. 10b.

The agreement between the two theories is fairly good on the subsonic wall, especially more than 0.4 h_2 upstream of the leading edge (at $x = 0$). However, agreement concerning the interfacial pressure was disappointing, to say the least. Upon checking both derivations carefully, an error was found in equation 53 of the paper by Tsien and Finston[18], which accounts for the discrepancy. The corrected solution, also shown on Figure 4. 10b, is in good agreement with the results of the present work (see Appendix F).

The good agreement between the present computation and that of Tsien and Finston provides a check on the accuracy of the solution. We can now proceed to apply this theory to the evaluation of the problems of interest.

4.5 Results -- Supersonic Wedge

The primary case of interest in the wedge studies was that of

the 4°, 3/32-inch thick wedge attached to the supersonic wall with its leading edge at the station x = 10 inches. This is referred to as the "baseline supersonic" case, and is illustrated in Figure 4.11.

Several perturbations about this baseline case were possible. The leading angle could be increased to 8° or decreased to 2° while maintaining the same thickness; the thickness could be halved (to 3/64 inch) at either the 2° or 4° angle; and the leading edge could be placed at x = 17 inches so that the shear layer in the region of the shock impingement point would be about 50 per cent thicker.

All data used for comparison purposes have been corrected; i.e., they are expressed not in absolute terms but in terms of a deviation from the pressure measured at the same point in undisturbed (e.g. empty-tunnel) flow. As usual, pressures have been normalized by the nozzle exit pressure. This permits elimination of effects due to boundary layer growth on the sidewalls and the static pressure gradient through the test section. To a considerable extent, the effects in the subsonic stream of the splitter plate shock system can be removed. Unfortunately, in the supersonic stream, this shock system is not very repeatable; this lack of repeatability prevents the formulation of a systematic method for eliminating its effects in the data. The wall pressure rise due to the shock is about 10 per cent of its ambient value in its first cycle, and the strength diminishes about one-third on each subsequent cycle as the wave is reflected off the shear layer and wall. However, the strength of the initial wave in fact varies in a seemingly random manner between 6 per cent and 14 per cent (in terms of pressure rise) on separate runs. Several

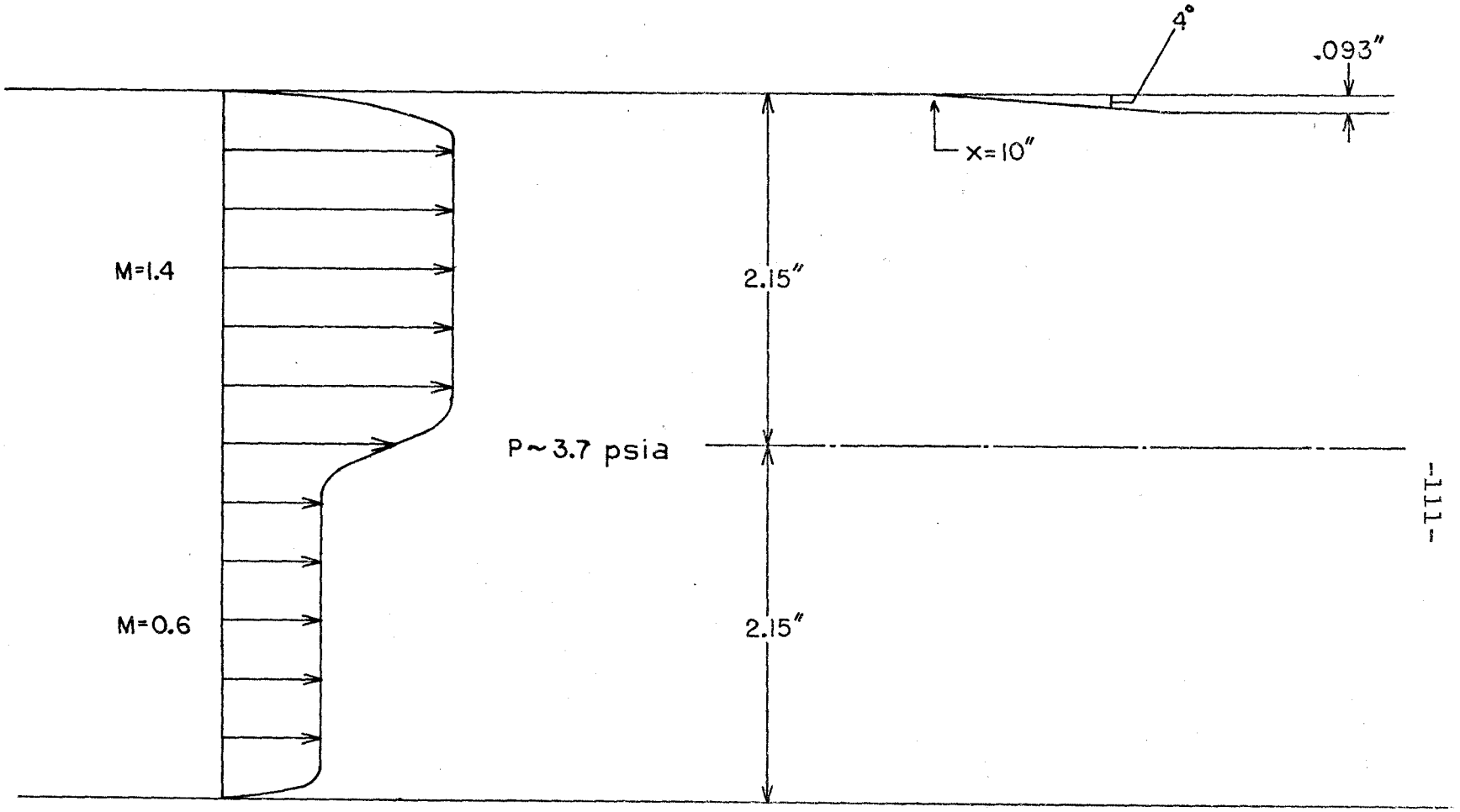

Figure 4.11: Baseline Supersonic Wedge Case

methods were tried to make this shock more uniform (at any strength) on different runs; unfortunately, nothing seemed to help. Quantitative comparisons of pressure data from the supersonic wall are subject to a fairly large uncertainty; therefore, they are not generally presented in the following sections. In the subsonic stream, however, repeatability was excellent; pressure measurements often agreed within 0.2 per cent on separate days for the same model.

Figure 4.12 illustrates the correction procedure. Part "a" of the figure presents the raw subsonic wall pressure data for Run 52, which was run at the baseline supersonic wedge configuration. The raw data were examined over the first 7 or 8 inches to determine which empty-tunnel run provided the best agreement in the initial region where the flow was unaffected by the presence of a model. Once the desired reference run (Run 53, in this case) was selected, the pressure was recast as a perturbation from the reference condition (Figure 4.12b).

4.5.1 Baseline Case. With a relatively straightforward data reduction procedure in hand for the subsonic wall data, the first task was to examine the baseline supersonic case (4°, 3/32-inch thick wedge on the supersonic wall with its leading edge at x = 10", trailing edge at x = 25"). Attention was at first directed toward upstream propagation of disturbances in the inviscid flow, which meant that the subsonic stream rather than the supersonic stream was to receive attention (since no perturbation to the supersonic stream could propagate upstream without first entering the subsonic flow). The type of data generally studied were subsonic wall pressures. This form of comparison

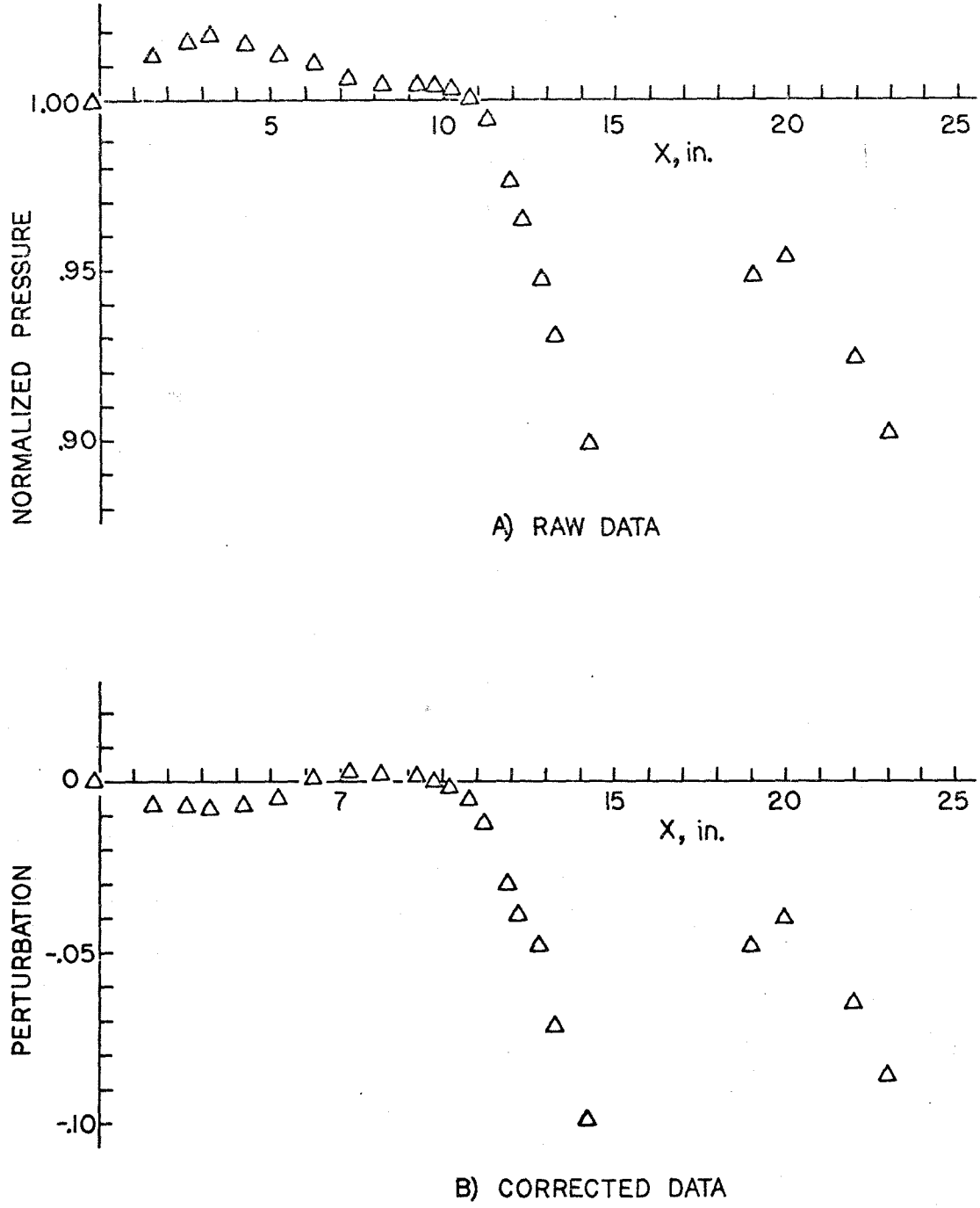

Figure 4.12: Correction of Subsonic Wall Pressure Data (Run 52: 4°, 3/32 inch thick supersonic wedge at x = 10 inches)

was also attractive because of its good repeatability from run to run.

Figure 4.13 presents subsonic wall pressure for the baseline supersonic case. Both the corrected experimental data and the results of the calculation from linearized theory are shown. It is felt that the ~.008 perturbation for x less than 4" is not a real effect, but is rather due perhaps to an unintentional change in wall installation which modified the flow (compared to the reference run). Note that both theory and experiment indicate no substantial pressure changes propagate upstream more than an inch or two from the shock impingement point, even though the 4°-deflection-angle shock carries a pressure ratio of over 1.20*. In fact, the pressure drops in the subsonic stream. This is due to a net displacement downward of the dividing streamline (DSL) and all the streamlines in the subsonic flow, causing an area contraction. The DSL actually displaces downward about twice as far as the displacement of the wedge on the supersonic wall (this displacement ratio depends on M_1 and especially on M_2). This downward displacement is due to the fact that, to first order, the 4° incoming compression wave reflects as a 4° (approximately) expansion wave at the shear layer in order not to impose a discontinuous change of pressure on the subsonic stream. This means that the shear layer is turned downward about 8°. The process repeats with opposite sign for the expansion fan from the shoulder of the wedge, and for waves which return to the shear layer after reflecting from the supersonic wall (though these additional reflections are not the current point of discussion).

*The fact that the theoretical subsonic stream perturbation begins at x = 10 inches, the leading edge position in the supersonic stream, is coincidental.

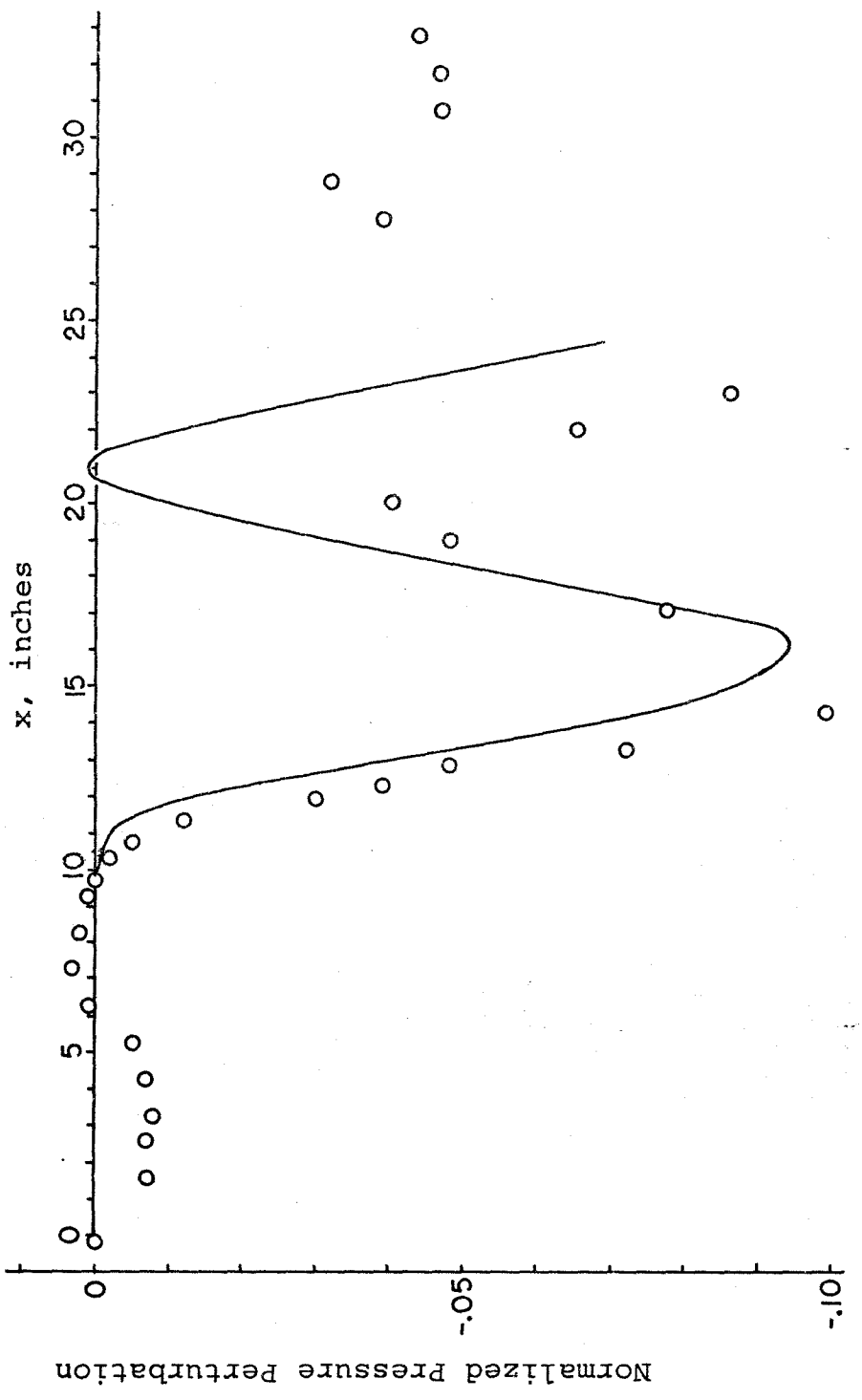

Figure 4.13: Results of Baseline Supersonic Wedge Case (Subsonic Wall Pressure)

In another sense, the pressure drops rather than rises because the entire flow is qualitatively subsonic. The unperturbed static pressure is greater than that for choking, and in a one-dimensional sense a small area reduction of the entire duct causes the pressure to drop. Thus, the response of the subsonic stream pressure is dominated by the large-scale area changes rather than by the details of the shock wave reflection.

Note in referring to Figure 4.13 that the initial downward curve of experimental data seems to be displaced forward of the theoretical data by a nearly constant distance of about 0.7 inch. The linear theory, with its necessary assumption of isentropic flow, makes all disturbances in the supersonic stream, including the leading edge shock, move along lines inclined at the Mach angle to the unperturbed flow direction. In reality, however, the leading shock has a finite magnitude and assumes an angle of 51° with respect to the flow rather than the value of 45.6° required by the first-order theory. This angular difference, with its consequent effect on the shock/interface impingement point, accounts for 0.4 inch of the 0.7 inch translation in the region of x from 10 to 14 inches. The remainder of the difference is attributed to the fact that the wall boundary layer is thickened ahead of the wedge, and thus moves the effective origin of the shock system upstream. These advanced compression waves can be seen in the flow with the aid of the schlieren system.

A glance at Figure 4.13 shows that while the first-order theory predicts the subsonic wall pressure will recover to its unperturbed value at about x = 21 inches, the experimental data fall short

by about 4 per cent. To understand this, we must realize that two separate response mechanisms are in action: a change in the equilibrium pressure due to the thickness of the wedge, and streamwise variations about that mean pressure due to the presence of a train of compression and expansion waves in the supersonic stream.

The linear theory pressure distribution has a mean perturbation of about -0.047. This is in complete agreement with the linearized prediction of one-dimensional equilibrium pressure for the same Mach number profile assumed by the theory. The experimental oscillations are about a somewhat lower mean value, approximately -0.06. Based on the measured Mach number distribution at the region of interest, the equilibrium pressure perturbation can be estimated through the usual one-dimensional computation to be -0.030. The effect of the loss of total pressure through the leading edge shock wave is to lower the equilibrium normalized pressure an additional 0.005. The remaining perturbation, about -0.025, presumably is due to the thickening of the boundary layers over the wedge and sidewalls of the tunnel as they flow through the adverse pressure gradients caused by the shock wave. An increase of the mean displacement thickness of about 0.010 inch would fully account for the discrepancy.

The oscillating portion of the theoretical solution continues indefinitely because no processes are present to damp it out. When the wave system (in the theory) first strikes the interface, the interface is deflected downward into the subsonic flow and the waves reflect into the supersonic stream with reversed sign (i.e., compressions become expansions and vice versa). In reflecting from the wall, the

waves retain the same sign, so at the next encounter with the interface, the perturbations from the previous wave/interface interaction are exactly reversed. The first reflection drives the normalized pressure down about 0.10, the second reflection returns it to the unperturbed value, etc.

The experimental data show that this streamwise variation of pressure is soon attenuated. This weakening of the oscillation is due to a number of causes. Even if the supersonic region were unbounded, the interference between the compression wave from the leading edge and the expansion wave from the shoulder would gradually weaken the system. The shear layer, by dispersing the waves still more at each reflection, promotes this weakening. To a lesser extent, the same thing happens wherever the waves encounter a boundary layer. As the wave pattern spreads out, the successive cycles of reflection between the supersonic wall and the shear layer (which have offsetting effect) begin to overlap and thus lower the magnitude of the perturbation still more.

Figure 4.14 presents experimental data from the tunnel sidewall, showing lines of constant pressure (isobars). The compression waves from the supersonic stream ahead of the leading edge are revealed quite clearly. Unfortunately, the boundary layers on the sidewall wash out most of the detail of the interaction between the shock wave and the shear layer. Away from this interaction region, the vertical pressure gradients in the subsonic stream are relatively minor. Near the impingement point, the subsonic stream responds mainly as an unconfined stream, i.e., the static pressure remains

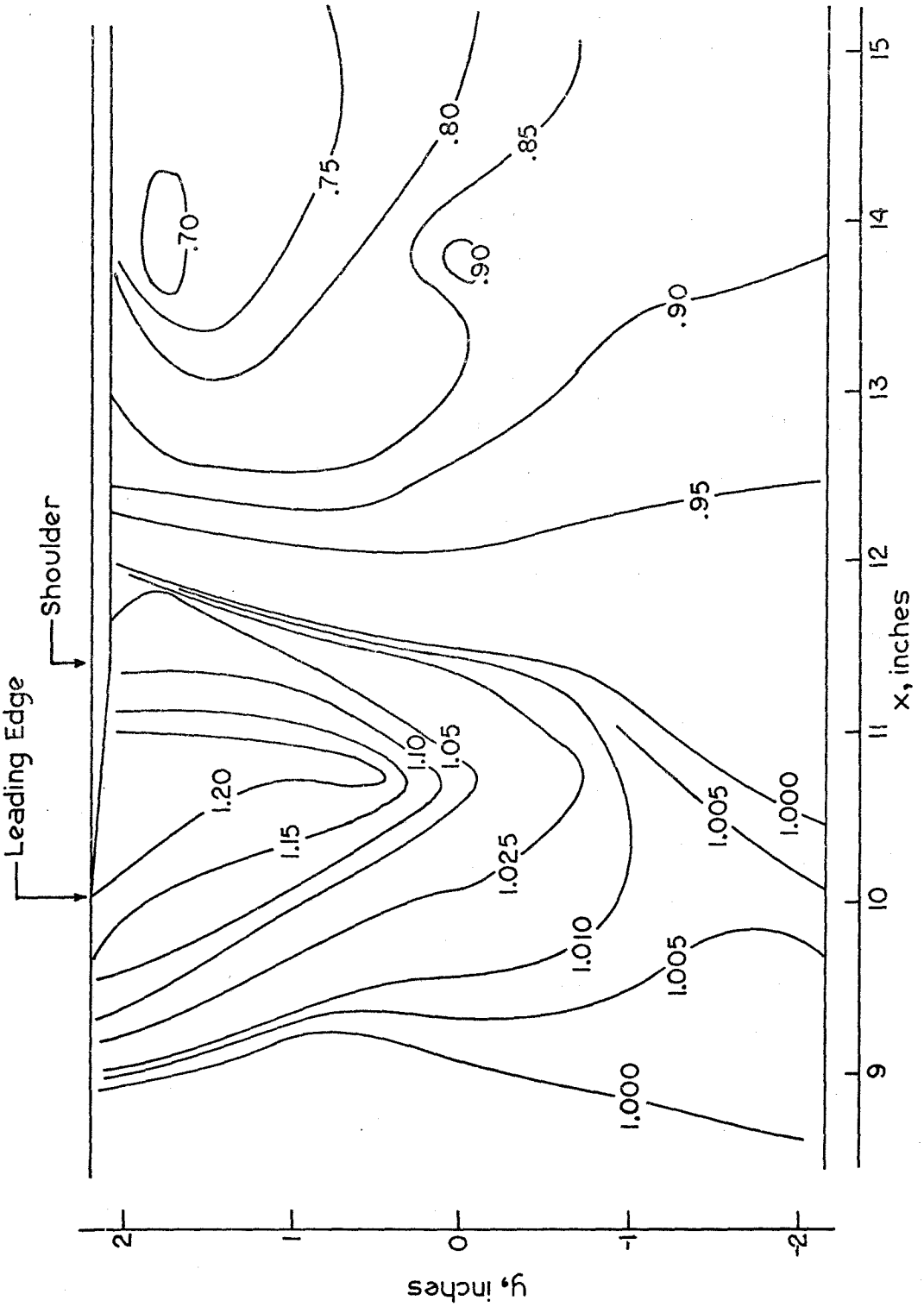

Figure 4.14: Baseline Supersonic Wedge Case (Sidewall Pressure)

nearly at its unperturbed value. Changes in pressure in the subsonic stream occur somewhat further downstream, in response to variations in the net flow area.

Another comparison to be noted in Figure 4.13 is that the overall wavelength of the pressure perturbation is smaller in experiment than in theory. This is attributed to the assumption made in deriving the theory that the shear layer has zero thickness. Since in reality the shear layer causes some stream tubes near the interface (the $y = 0$ plane) to have a Mach number closer to unity than the free-stream value, the path of a disturbance in the supersonic stream in this region will be steeper, and the wave will complete a cycle of motion from the supersonic wall to the sonic surface and back to the supersonic wall in less distance in the x-direction compared to the first-order theory. Another action causing this is the difference in wave angle mentioned previously. The linear theory assumes the waves move through the flow at the Mach angle, while actually the finite amplitude waves make a steeper angle. However, after the first cycle, the wave has been diffused and the individual wavelets do in fact cut the flow at the Mach angle. Thus, the angular difference probably has little effect, compared to the shear layer thickness, in contracting the wavelength of the disturbance after the primary wave.

4.5.2 Effect of Wedge Thickness. The next study to be performed was an examination of the effect of wedge thickness on the flow field. Both theoretical and experimental studies were performed, concentrating on determining the effect on the subsonic stream of the 4^{o} wedge mounted on the supersonic wall with its lead-

ing edge at x = 10". The two wedges compared had thicknesses of 3/64" and 3/32". In the experiment, the trailing edge of the wedge plate was at x = 25", ending with a 2^{o} angle. The theoretical calculations were stopped at x = 24". This was upstream of the trailing edge, and it was assumed that in this region the trailing edge had no influence. This assumption was supported by the severely limited upstream influence of the leading edge. Farther downstream, the flow is affected by boundary layer separation at the aft shoulder of the wedge.

The theoretical and experimental data are presented in Figure 4.15. It is felt that the experimental perturbations seen upstream of the leading edge are so small as not to be significant but rather are due to imperfect removal of empty-tunnel phenomena in the data reduction. In any event, this is not a genuine upstream-propagating wave, since such a wave upstream of the leading edge should not be oscillatory but rather should be monotonically decaying to zero.

The experimental perturbation amplitudes seem to compare well with those predicted by the theory, indicating that the linear equations are still valid and that choking is not modifying the behavior. The thick wedge has a geometrical blockage ratio of 2.18 per cent. It will be recalled that the one-dimensional prediction of the choking margin without boundary layers is 2.86 per cent and with boundary layers, etc., it is about 7.5 per cent (see Figure 3.11). Of course, the effective blockage ratio of the wedge is modified somewhat by changes in boundary layer growth. The geometric blockage ratio is about one-third of the actual choking margin.

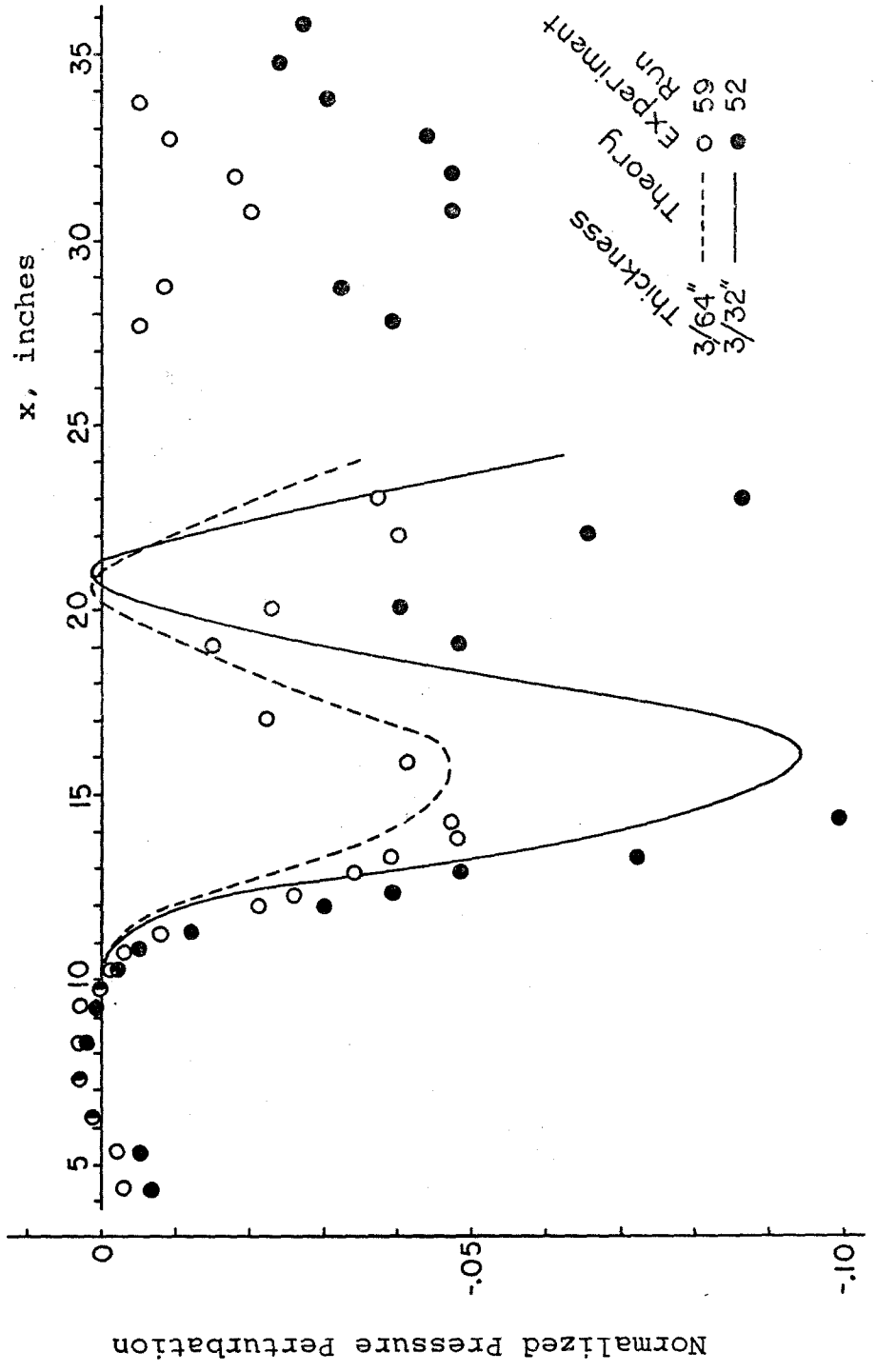

Figure 4.15: Effect of Wedge Thickness on Subsonic Wall Pressure (Supersonic 4^{0} Wedge at x = 10 inches)

As before, the initial dip in the experimental pressure data is displaced upstream from the linear prediction, and the experimental perturbation wavelength seems shorter. These differences are all felt to be due to the phenomena previously discussed which are omitted from a linear theory: boundary layer compression in advance of the leading edge of the wedge, the difference in angle between infinitesimal and finite-amplitude waves, and the finite thickness of the shear layer. The first and second of these will tend to shift upstream the initial part of the pattern, and the second and third will tend to decrease the perturbation wavelength.

The notable difference between the wedges in the experimental data is seen in the static pressure far downstream, x = 30" to 35". The pressure from the thin wedge seems to recover to a net loss of acout 1 per cent, while the thick wedge shows a net loss on the order of 4 per cent. Because the test section ends at about x = 40", it is not clear whether the pressure would, if permitted, recover more fully (with oscillations) to its unperturbed value.

The boundary layer is known (through oil flow studies) to separate at the trailing shoulder of the wedge. As the displacement thickness of the free shear layer and subsequently re-attached boundary layer returns to its unperturbed level, the flow will respond to a gradually increasing net flow area with a mean pressure recovering to its unperturbed value. A complete recovery seems unlikely, as the equilibrium static pressure has been lowered slightly (about 0.5 per cent) by the 0.4 per cent loss of total pressure in the supersonic stream due to the leading-edge shock wave. In addition, it is not

clear whether the boundary layer would ever return to its unperturbed state.

Sidewall pressure data are not presented here or in the following sections. In the subsonic stream, vertical pressure gradients generally vanish (see Figure 4. 14) and thus the subsonic wall pressure distribution depicts quite well the response of that stream. Data from the supersonic stream are flawed by the inhomogeneous wave structure present, which introduces large-scale inaccuracies, and details of the shock/shear layer interaction are obscured by the sidewall boundary layers.

Figure 4. 16 presents the same data as Figure 4. 15 except that the pressure is scaled with the thickness of the wedge. The experimental data seem to show the same variation with thickness as the theoretical data. The initial drop in static pressure is shifted upstream about 0. 3 to 0. 4 inch for the thin wedge (compared to the thick wedge). This is due to the geometry of the problem: the wedge angle was held constant at 4^{o} while the thickness was varied by a factor of two. Thus, the distance from the leading edge to the shoulder was 1. 34 inch for the thick wedge and 0. 68 inch for the thin wedge. This represents a shift upstream for the thin wedge of 0. 34 inch in the location of the center of the disturbance, agreeing well with the experimentally and theoretically observed shifts. The amplitude of the measured pressure perturbations scales very well with the wedge thickness. This good agreement indicates that for cases where the geometric blockage ratio is less than one-third of the choking margin, nonlinear effects have negligible influence on the pressure data. Note

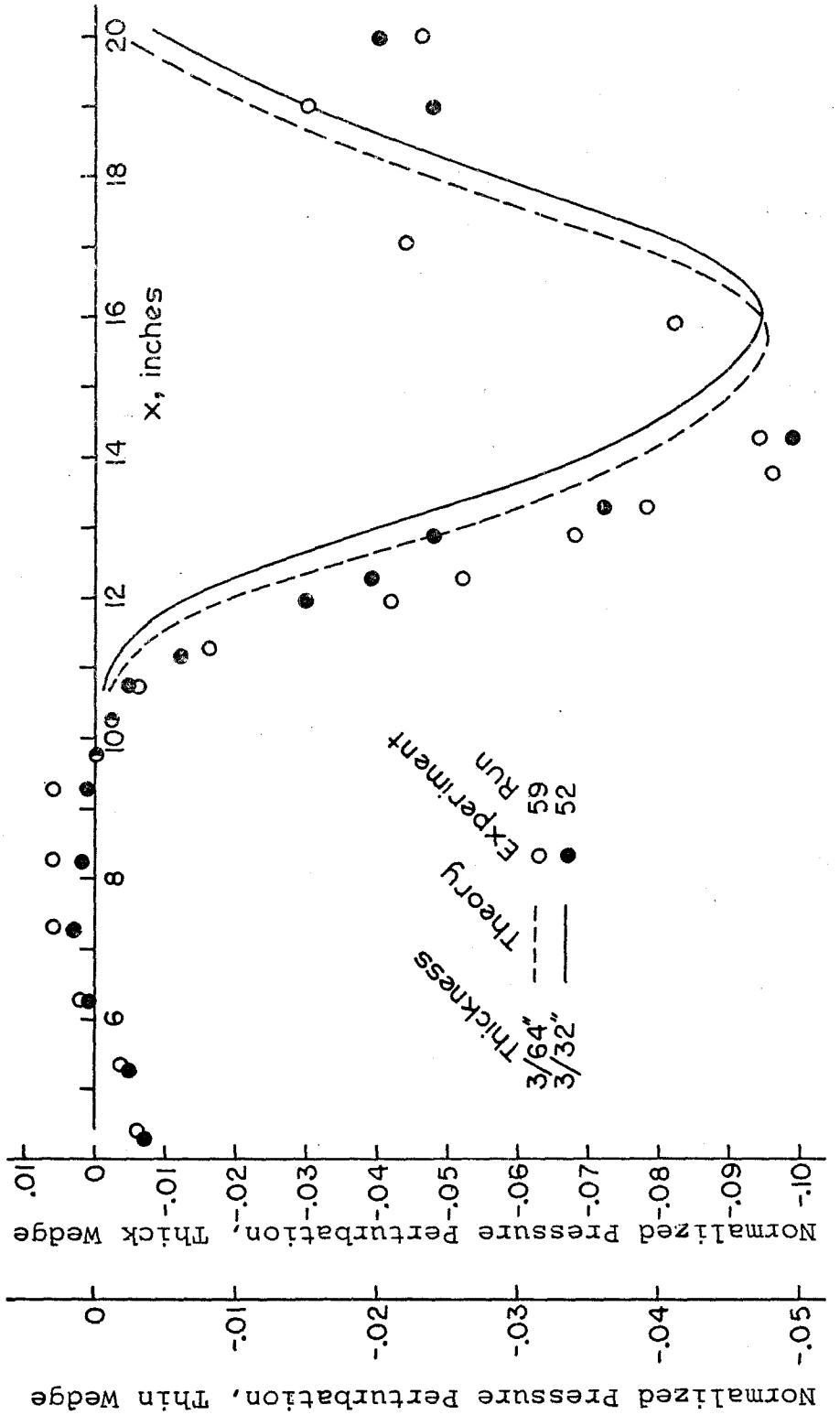

Figure 4.16: Effect of Wedge Thickness on Subsonic Wall Pressure (Supersonic Wedge)

that the first pressure rise around x = 19" also scales well.

4.5.3 Effect of Wedge Angle. The next comparison performed was a study of the effect of leading edge angle for the supersonic wedge of 3/32-inch thickness with its leading edge at the station x = 10". As before, both theoretical and experimental results were obtained. The experimental data were for wedge angles of 2°, 4°, and 8°; the linearized calculations were for angles of 1°, 2°, 4°, 6°, and 8°. The results of each are presented in Figure 4.17.

The linearized theory shows that for angles larger than about 4°, the wedge angle has little effect on either the location (x = 15.5") or magnitude (9.5 per cent drop) of the pressure minimum. However, for lesser angles the minimum pressure becomes higher (i.e., less perturbation) and moves downstream somewhat. This is because the angle at the leading edge was studied in wedges of constant thickness: increasing the angle moved the shoulder of the wedge closer to the leading edge. For wedge angles above 4°, the expansion fan from the shoulder weakens the leading-edge shock before it strikes the interface. In addition, the close proximity of the shock and expansion on the interface means that within the subsonic stream there will be a partial cancellation of effects.

The length of the inclined face in the flow direction is t/ϵ (where t is the wedge thickness and ϵ is the flow deflection angle). These data suggest that the subsonic stream pressure is sensitive to ϵ only when

$$\frac{t}{\epsilon h_2} > 0.6 \ , \qquad (4.67)$$

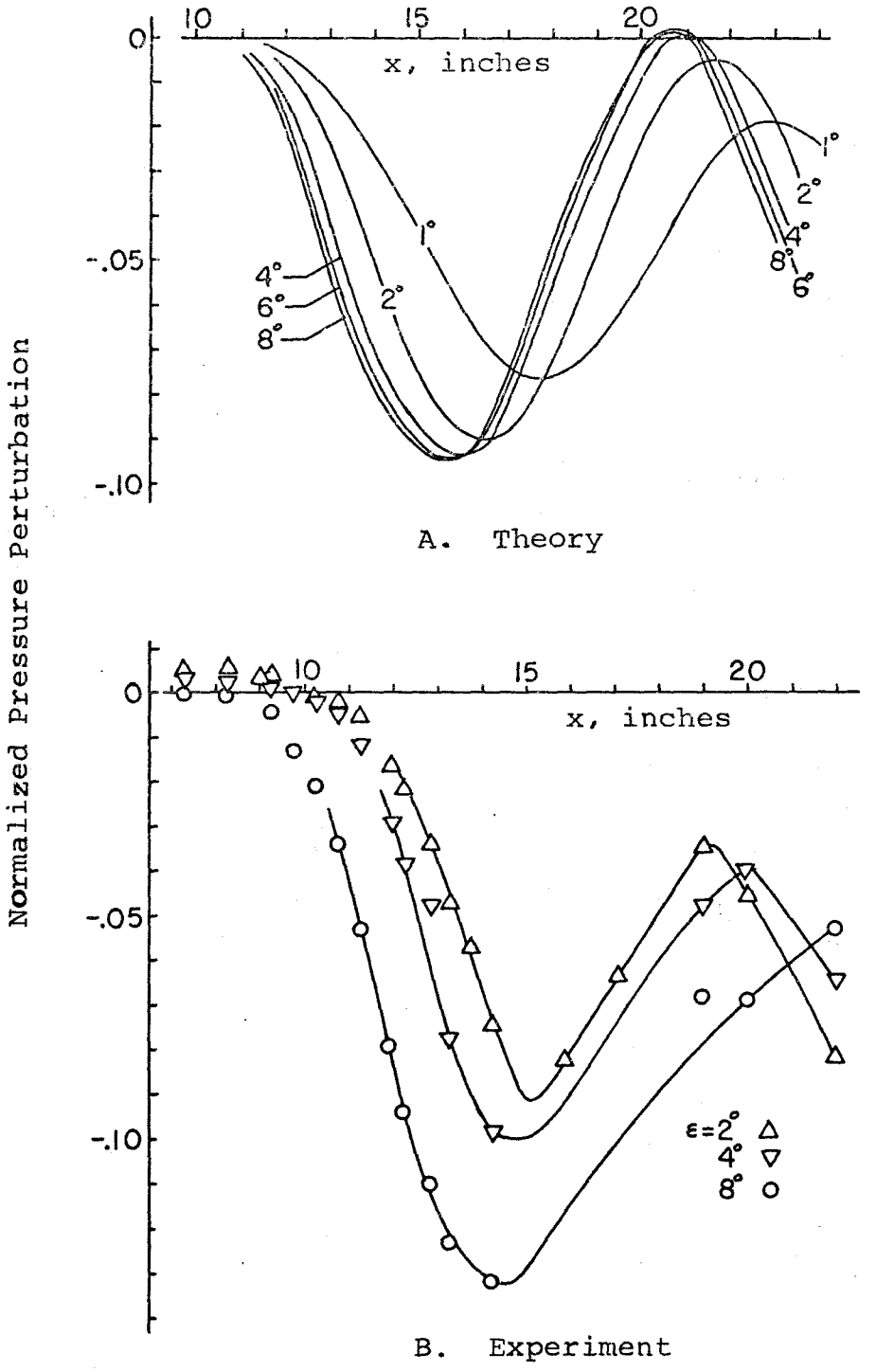

Figure 4.17: Effect of Supersonic Wedge Angle on Subsonic Wall Pressure (x = 10 inches, 3/32 inch thick)

which in turn implies that in some sense a disturbance to the subsonic stream has a region of influence of about $0.6\,h_2$ upstream from its source (this is 1.29 inches for our case). For the 4° baseline wedge, the shock impinges on the shear layer at about x = 11.74". Thus, the suggestion is made that the limit of upstream influence is about x = 10.45". This seems to agree with the experimental data of Figure 4.15 for the 2° and 4° wedges.

Similarly, the adjacent cycles of reflection of the upstream perturbation overlap and interfere with each other when the inclined face length (t/ε) becomes of the same order as the supersonic stream wavelength $(2\beta_1 h_1)$. When this interference occurs, the amplitude of the perturbation is materially reduced. The computer data suggest this occurs for ε less than 2°, or

$$\frac{t}{2\varepsilon\beta_1 h_1} > 0.6 \quad . \tag{4.68}$$

With some sort of qualitative understanding of the linearized results, we will now proceed to consider the experimental data. As before, it is felt that the small perturbations upstream of x = 8" to 9" are not "real" effects, but rather are due to imperfect correction procedures.

The minimum pressure points of the 2° and 4° experiments seem to compare well with the linear calculation. The experimental amplitudes are greater than calculated by 2 per cent of the predicted amplitude (2° wedge) and 7 per cent (4° wedge), though the discrepancy increases to 40 per cent for the 8° wedge. The amplitude error in the 2° case falls within the measurement error. For larger angles, the

onset of nonlinearity (especially in the 8° wedge case) is visible as the flow deflection angle becomes sufficiently large that the higher order terms assume importance. Thus, a linearized theory seems inappropriate for a wedge angle larger than about 4 or 5°.

Table 4.4 presents certain parameters of interest in making these comparisons. It was felt that study of the value of x at which $\Delta P/P = -0.050$ would be the best basis for examination of the effects by which the pressure perturbation in the subsonic stream is translated upstream from the linearized isentropic solution. Line 6 of the table presents the difference in x at which this pressure is reached, and Line 7 identifies that portion of the difference that is due to the finite-amplitude versus infinitesimal wave angle. The remainder (Line 8) is attributed to the boundary layer compression ahead of the leading edge of the wedge, and in fact agrees well with the precompression lengths measured from schlieren photographs in the case of the 4° and 8° wedges (Line 9). Schlieren photography failed to reveal the shock wave in the case of the 2° wedge; therefore, for the wave to be invisible, boundary layer compression must have occurred in this case as well and "washed out" the wave.

As long as the leading edge angle of the wedge is less than about 5°, the agreement between theory and experiment is good. Those differences which are present can be understood in terms of the dependence of wave angle on Mach number and the upstream transmission of pressure disturbances through a supersonic boundary layer. For wedge angles greater than 5° (approximately), the nonlinear effect in the pressure distribution assumes greater importance

TABLE 4-4. Effect of Wedge Angle

Experiment (Theory)

1.	Wedge Angle	2^{o}	4^{o}	8^{o}
2.	Minimum Pressure	-0.092(-0.090)	-0.101(-0.094)	-0.133(-0.095)
3.	Discrepancy	-0.002	-0.007	-0.038
4.	x at Minimum Pressure (in.)	15.2(16.5)	14.7(16.0)	14.6(15.8)
5.	x at $\Delta P/P$ = -0.050 (in.)	13.5(14.0)	12.6(13.3)	11.2(12.9)
6.	Discrepancy (in.)	0.5	0.7	1.7
7.	Discrepancy Due to Wave Angle (in.)	0.18	0.37	0.83
8.	Remainder (in.)	0.32	0.33	0.87
9.	Boundary Layer Separation Distance from Schlieren (in.)	-	0.4	1.0

and the first-order theory fails to adequately model the problem. It is seen that the upstream transmission of pressure disturbances through the subsonic stream is limited to distances of about $0.6\,h_2$.

4.5.4 Effect of Shear Layer Thickness. The final set of experimental comparisons for the supersonic wedge study concerned the effect of shear layer thickness. The 3/32-inch thick, 4^{o} angle wedge was mounted on the supersonic wall with its leading edge at x = 10" (normal position) and x = 17" (displaced position) where the maximum slope thicknesses of the shear layer were respectively

0.63 and 0.94 inch (in each case, this thickness is about 60 per cent of the perceptible thickness of the shear layer).

The experimental data are presented in Figure 4.18 . Since the linearized theory makes the assumption of zero shear layer thickness, no theoretical comparisons were possible. However, the baseline theoretical calculation is also presented in the figure for reference.

As before, we see that the initial perturbation is translated upstream somewhat, due to wave angle differences and supersonic boundary-layer precompression. The initial minimum pressure is approximately that predicted by linear theory in the thin shear layer case, while in the thicker case the minimum is considerably lower. This suggests the increasing dominance of nonlinear effects as the shear layer thickens and the choking margin of the combined flow is reduced. (Figure 3.11 shows the calculated choking margin of the tunnel based on measured Mach number profiles at various stations.)

This margin is affected by several things (cf. Section 3.4). First, the empty-tunnel uncorrected pressure data showed static pressure continually decreasing in the downstream direction as the shear layer thickened. The one-dimensional studies showed that as the choking limit is approached the static pressure decreases. Thus, the farther downstream in the tunnel the closer the flow is to being choked. The increasing shear layer thickness of itself will also reduce the choking margin.

In addition, we know that the area decreases and pressure perturbations of the wedge experiments are a substantial fraction of those

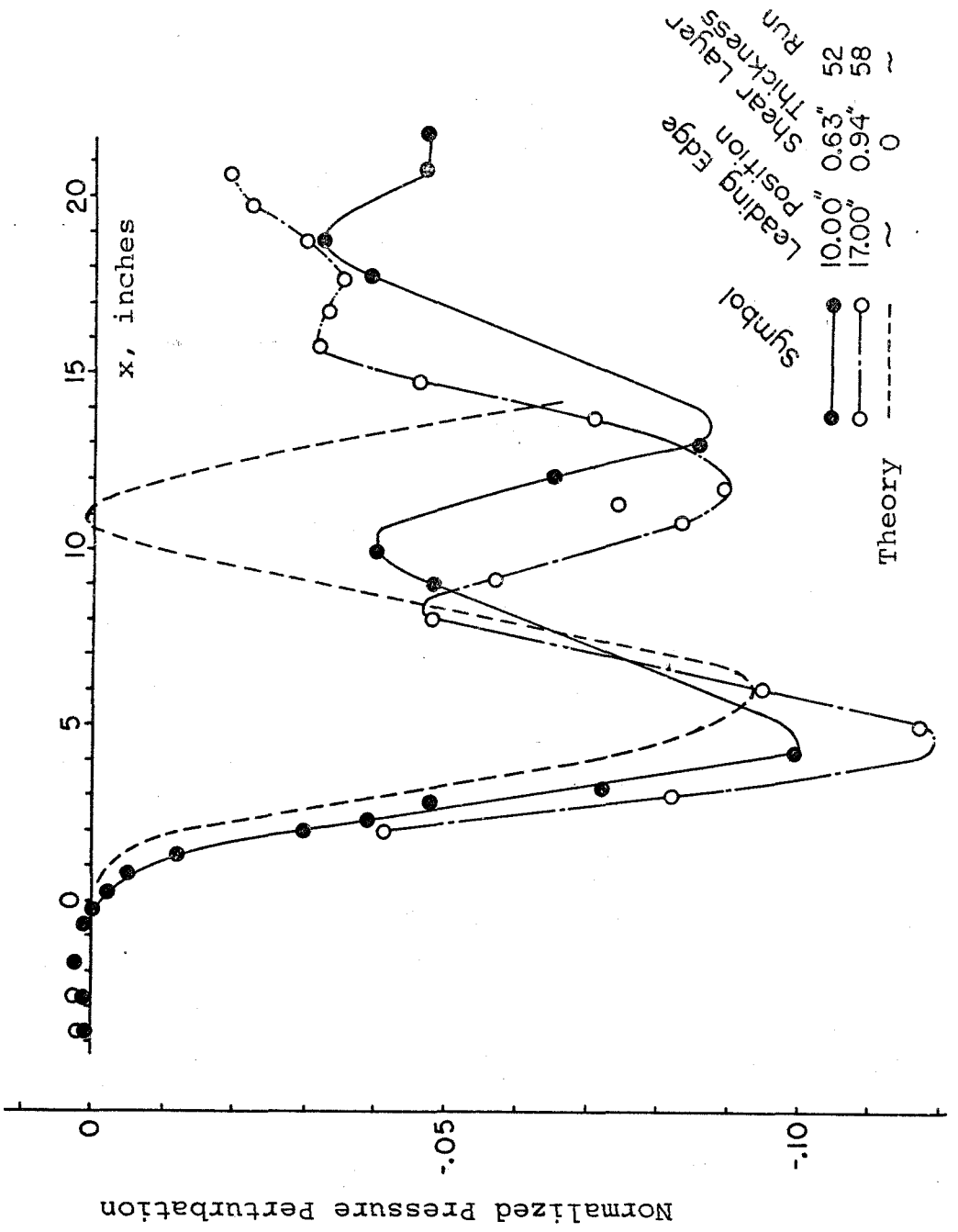

Figure 4.18: Effect of Shear Layer Thickness on Subsonic Wall Pressure (4^0 angle, 3/32 inch thick wedge)

necessary for one-dimensional choking. The wedge has a geometric blockage ratio of 2.18 per cent. At the normal wedge position (x = 10 inches) the choking margin is seen in Figure 3.11 to be about 7.5 per cent, while at the displaced wedge position (x = 17 inches) the margin is about 4 per cent. In the latter case, the ratio of geometric blockage to choking margin is above 0.5. This is a strong suggestion that non-linear effects related to choking become increasingly important at the displaced location.

Finally, we must note that choking, being essentially a non-linear phenomenon, is not embraced in the linearized theory. Thus, as the wedge experiment is translated downstream, one reasonably expects increasing departures from the linearized theory, largely due to the reduction of choking margin, but also aggravated by the increasing thickness of the shear layer failing to fit the zero-thickness model.

Next, we see that the pressure fails to make a full recovery to its unperturbed state in the vicinity of 9 inches downstream of the leading edge of the wedge. This is due to the attenuation of the supersonic wave pattern, as described in Section 4.5.1.

Once the trailing edge (15 inches downstream of the leading edge) is passed, the pressure should begin a recovery to nearly its unperturbed value as the boundary layer re-attaches and its displacement thickness returns to the reference condition (see the discussion of Section 4.5.2, 'Effect of Wedge Thickness').

The decreasing wavelength of the perturbation as the shear layer thickness increases is due to the decreasing Mach number in portions of the supersonic stream, which causes a local steepening of

waves in the supersonic stream and the completion in less streamwise distance of a cycle of reflections off the shear layer and the supersonic wall.

A substantial cause of the departure of the experimental data from the theoretical calculation is the effect on the kinematics of the wave reflection system in the spreading shear layer in a manner not considered in the model. The dispersion of the waves incident on the shear layer becomes increasingly dominant, causing the oscillations to die out more rapidly as the shear layer thickness is increased.

An increase of the ratio of geometric blockage to choking margin above about 0.4 seems to mark the point beyond which the first-order calculation does not predict well the amplitude of the disturbance pressure. This amplitude, as would be expected, exceeds the linearized result. In addition, the increasing shear layer and boundary layer thicknesses, which are not included in the computational model, introduce deviations from the linearized result. At the normal leading edge station, the perceptible shear-layer thickness is about 25 per cent of the flow area; it is closer to 40 per cent at the displaced leading-edge station. The latter value seems to exceed the range of validity of the theory in comparison with actual measurements.

4.5.5 Additional Studies. This section describes the theoretical results of those parametric studies which could not be verified experimentally; examinations of the effect of M_1, M_2, and h_2. A discussion of the effect of h_1 is not included because the dependence of the system on h_1 is mainly in terms of the distance required for a

wave leaving the interface to return to the interface after an intervening reflection off the supersonic wall.

Figure 4.19 shows the dependence of the subsonic wall pressure on M_1. The shift upstream and decreasing amplitude of the pattern with decreasing M_1 are expected results for a constant-deflection wedge. The minimum pressure, and the value of x at which it occurs, scale linearly with β_1:

$$x_{min} = 9.38'' + 6.81\beta_1 \text{ in.} \tag{4.69}$$

$$P_{min} = 0.964 - 0.059\beta_1 \tag{4.70}$$

The effect of M_2 is shown in Figure 4.20. The increasing magnitude of the pressure drop with increasing M_2 is due to the system approaching unperturbed choked flow at $M_2 = 0.8195$. It is not proper to say that choking is included within the linearized theory, because any area reduction can be evaluated without a breakdown of the equations. However, as the area is reduced, the linearized results lose validity and eventually become nonsensical (e.g., negative pressures). It is not believed, for instance, that an experiment duplicating the curve at $M_2 = 0.7$ would agree at all with the data. The curve presented simply represents the first of a series of functions in the exact solution: the higher-order functions, which were not included in the calculation, play an increasingly important role near the choking limit.

The effect of subsonic layer thickness, h_2, on the wall pressure distribution is presented in Figure 4.21. The comments of the preceding paragraphs apply to this figure as well. Since the choking

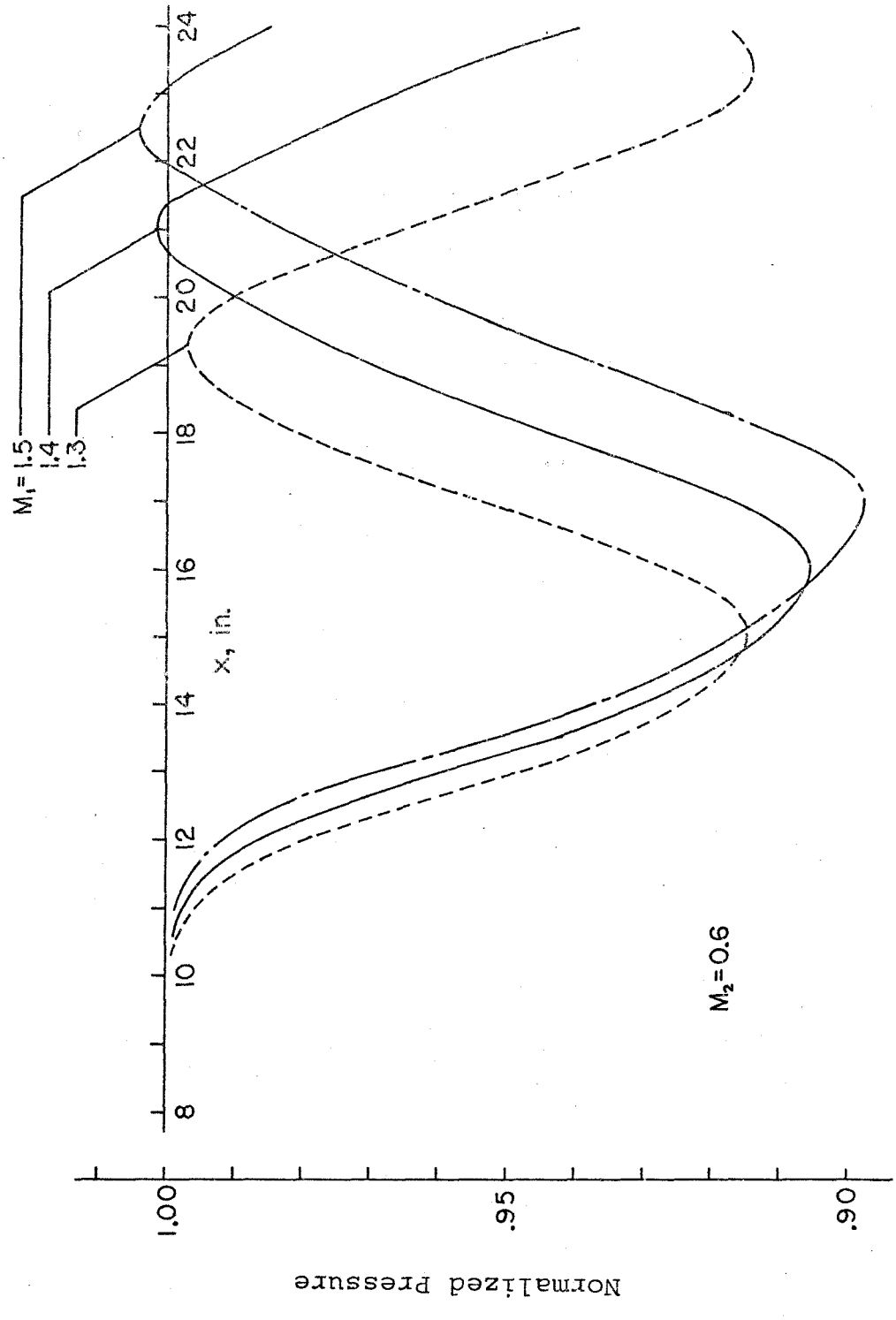

Figure 4.19: Effect of M_1 on Subsonic Wall Pressure (Supersonic Wedge)

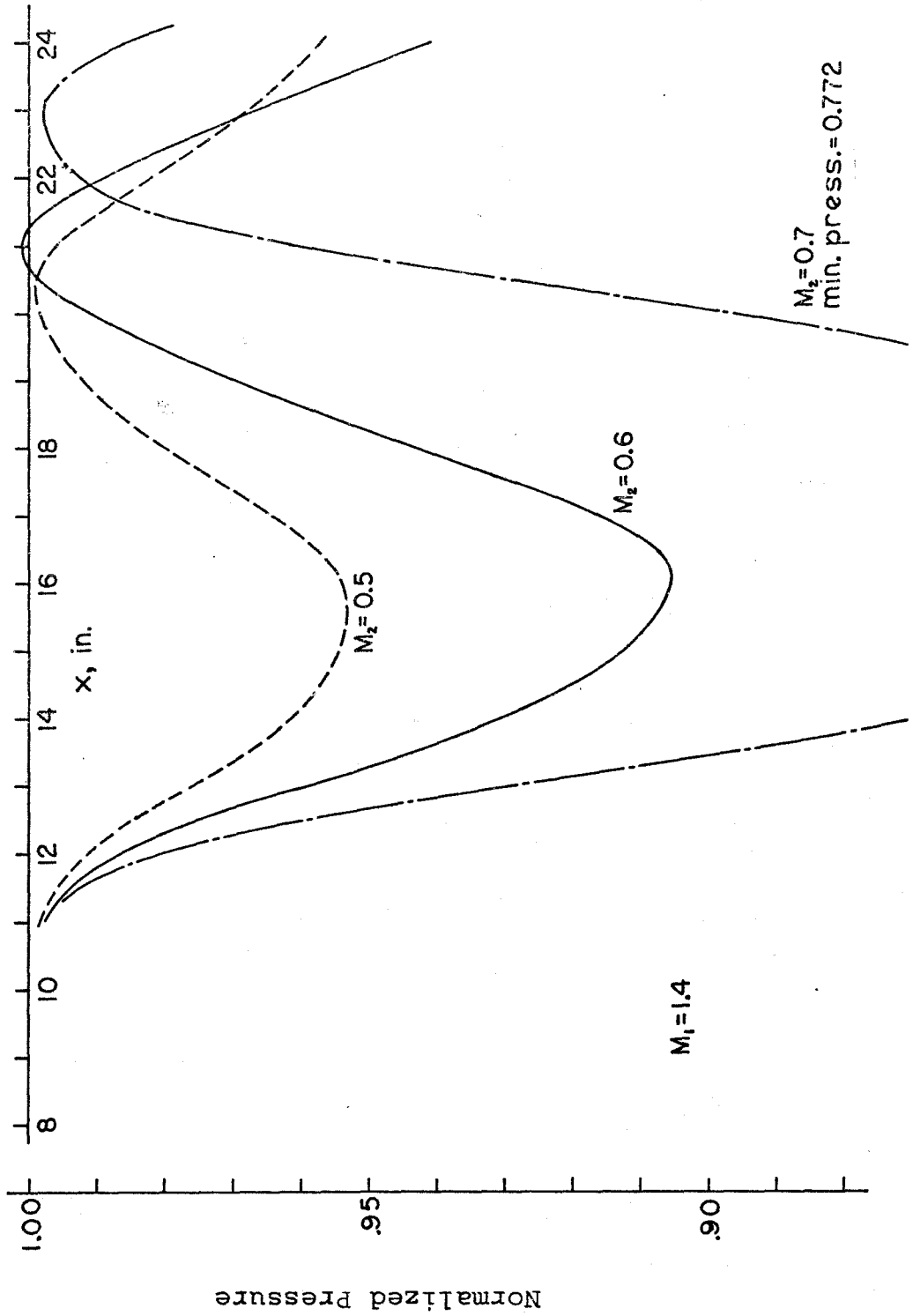

Figure 4.20: Effect of M_2 on Subsonic Wall Pressure (Supersonic Wedge)

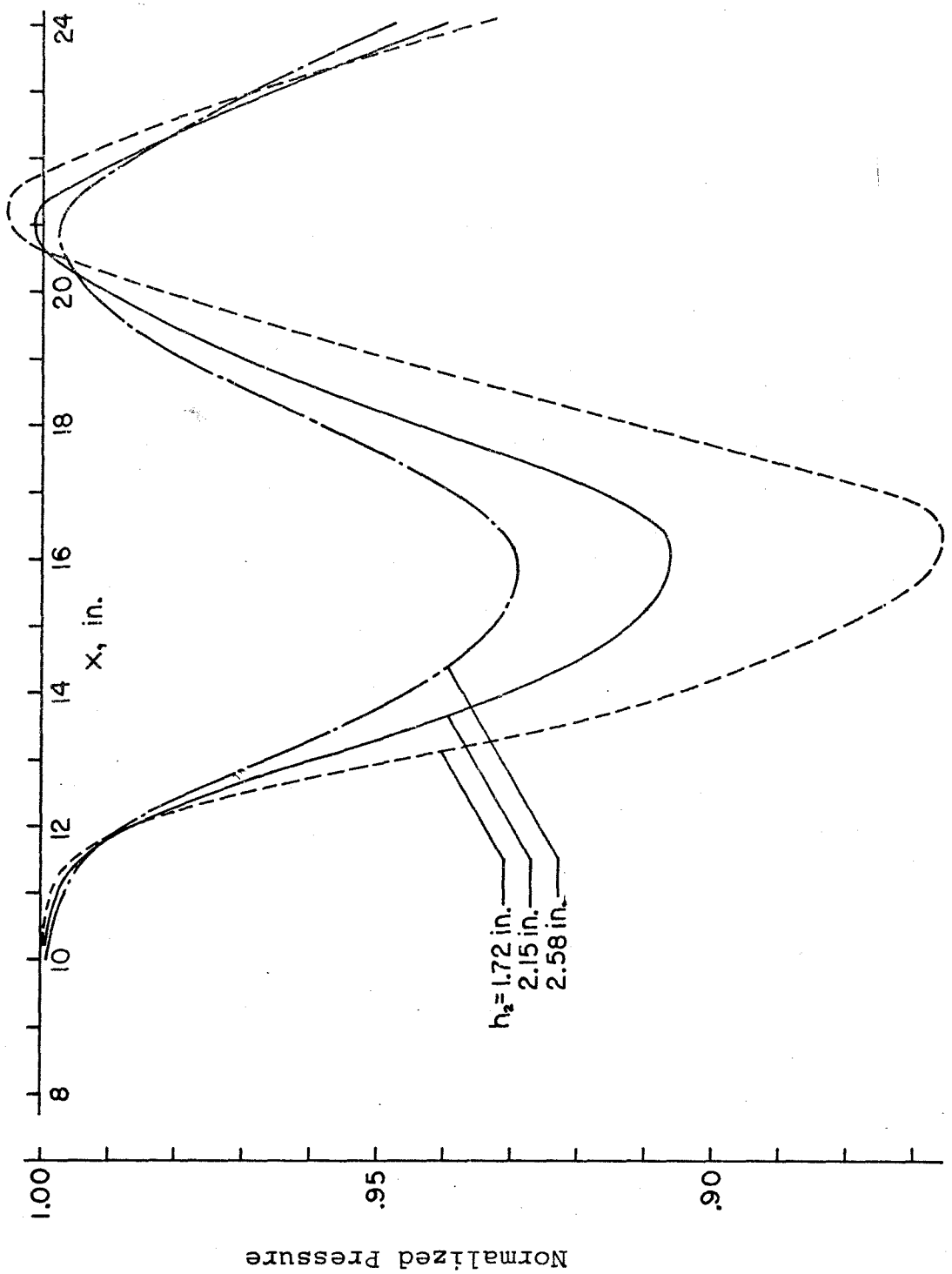

Figure 4.21: Effect of h_2 on Subsonic Wall Pressure (Supersonic Wedge)

margin depends also on (h_1/h_2), the choking limit is being approached in this study, too. This occurs because the choking margin is based on the combined properties of the entire flow. The unperturbed flow is qualitatively subsonic. Therefore, a reduction of h_2 causes a lessening of the relative influence of the subsonic stream compared to the supersonic stream. The qualitative behavior of the supersonic stream becomes more important, and the combined flow tends toward supersonic behavior, which implies a tendency also toward choked flow.

In another sense, the supersonic wave system imposes the same disturbance pattern on the interface in all the cases, but as the subsonic layer becomes thinner the area changes within the layer become proportionally larger and the amplitude of the response is increased.

For completeness, the first-order solution for the pressure on the supersonic wall in the case of the baseline supersonic wedge is presented (Figure 4.22). However, the inherent deficiencies in the calculation (zero-thickness shear layer, first-order accuracy) are particularly acute in this case, and this figure is scarcely realistic. It was felt that parametric studies of the supersonic wall pressure would be an academic exercise only and would have no physical meaning, since the supersonic wall boundary layer and the dispersion of shock waves at the shear layer (see Section 4.2) strongly influence the supersonic wall pressure distribution. Both of these phenomena, of course, were omitted from the theoretical model. Therefore, parametric studies of the supersonic wall pressure will

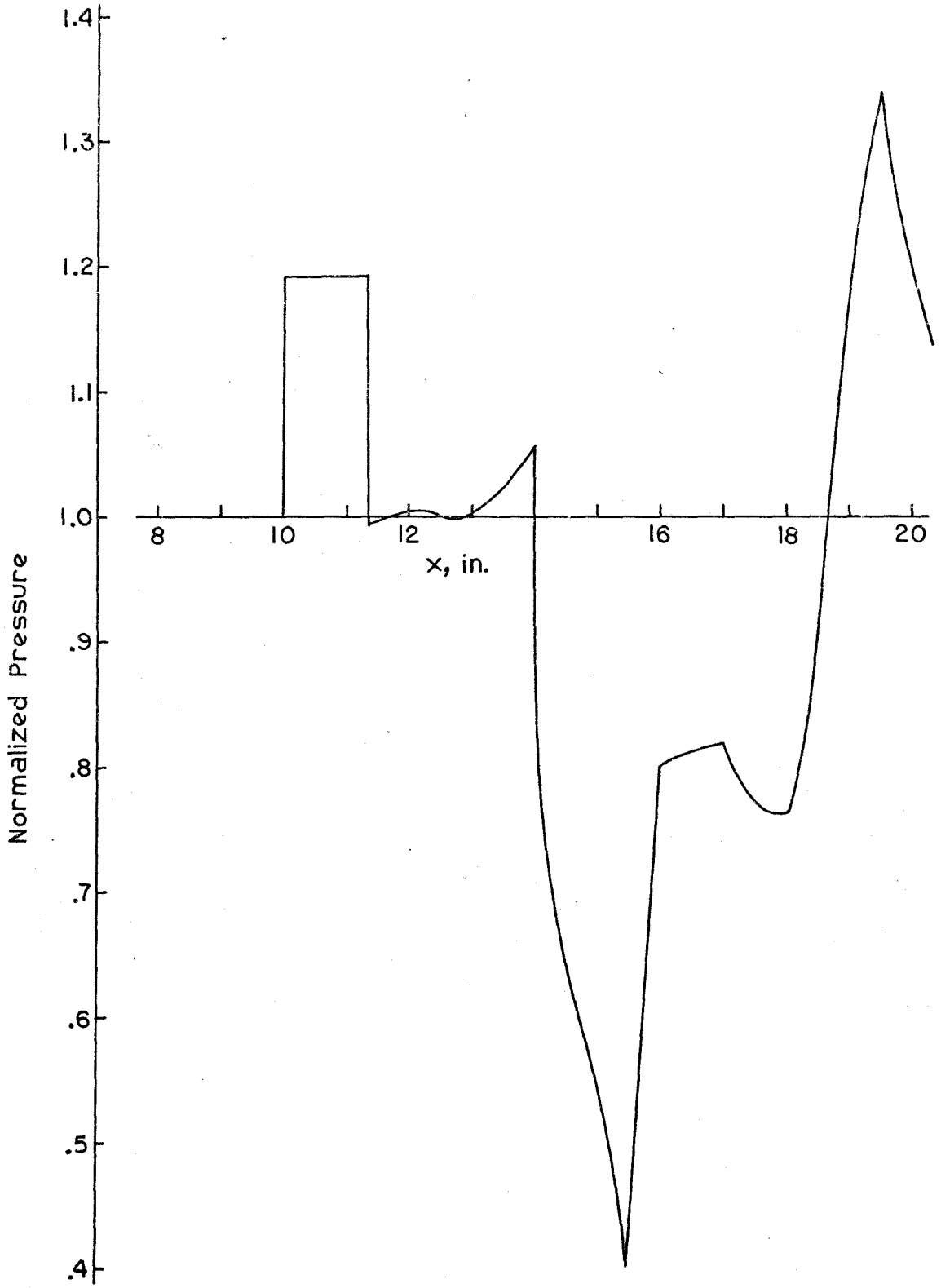

Figure 4.22: Supersonic Wall Pressure for the Baseline Supersonic Wedge

not be included.

4.6 Results -- Subsonic Wedges

A program of experimental and theoretical work was undertaken for the wedge attached to the subsonic wall, similar to that described in Section 4.5 for the wedge fixed to the supersonic wall. Data taken on the supersonic wall were subject to a fairly large amount of scatter due to the non-repeatable wave structure in the supersonic stream. In addition, data from the subsonic wall in the region covered by the wedge plate were tainted because of the difficulty in obtaining an airtight seal in the subsonic wall seam at x = 15 inches. There was a tendency for air to leak in through the seam into the space between the wedge plate and the wall, affecting data in the region of x from 13 to 17 inches. Because of these difficulties, which reduced the quality of data for the subsonic wedge problems, only a limited program was undertaken.

The work already described in this chapter gave us a reasonable level of confidence in the first-order calculation. Indeed, because the disturbance pressure gradients are considerably lessened when the wedge is transferred from the supersonic wall to the subsonic wall, it seems that the accuracy of the calculation will be improved.

One of the more interesting results of the linear theory is the "wall equality paradox." This is the prediction that, to first order, a specified geometric disturbance (t and ε) in a flow of constant parameters (M_1, M_2, h_1, and h_2) will produce the same pressure dis-

tribution on the unperturbed wall of the wind tunnel whether the disturbance wedge is attached to the supersonic wall or the subsonic wall.

The apparent paradox perhaps can best be understood by considering identical disturbances on each wall. In a linear approximation, the supersonic disturbance will be transmitted with unchanged form along a Mach line to the interface; it will be diffused to some extent in the subsonic stream, and a more dispersed pressure distribution will be seen on the subsonic wall. Conversely, the disturbance originating on the subsonic wall will be diffused to exactly the same degree between the subsonic wall and the interface. From the interface to the supersonic wall, this pattern moves up into the supersonic stream with unchanged form along the Mach lines. Because the entire system is linear (in the first-order calculation), the disturbance fields due to subsequent reflections off the supersonic wall simply add up.

Figure 4.23 presents the experimental data that were obtained in support of this prediction. The basic trends seem to support the theory. However, due to the difficulties already discussed, there is a superimposed structure on the data from the supersonic wall. This is particularly noticeable at $x = 13$ to 14 inches and around $x = 17$ inches, which correspond roughly to pressure extremes previously noted in the empty-tunnel flow (see Figure 3.8a, page 37).

The other experimental comparison made was a study of the effect of wedge angle on the subsonic wall pressure, the results of which are presented in Figure 4.24. Agreement between theory and

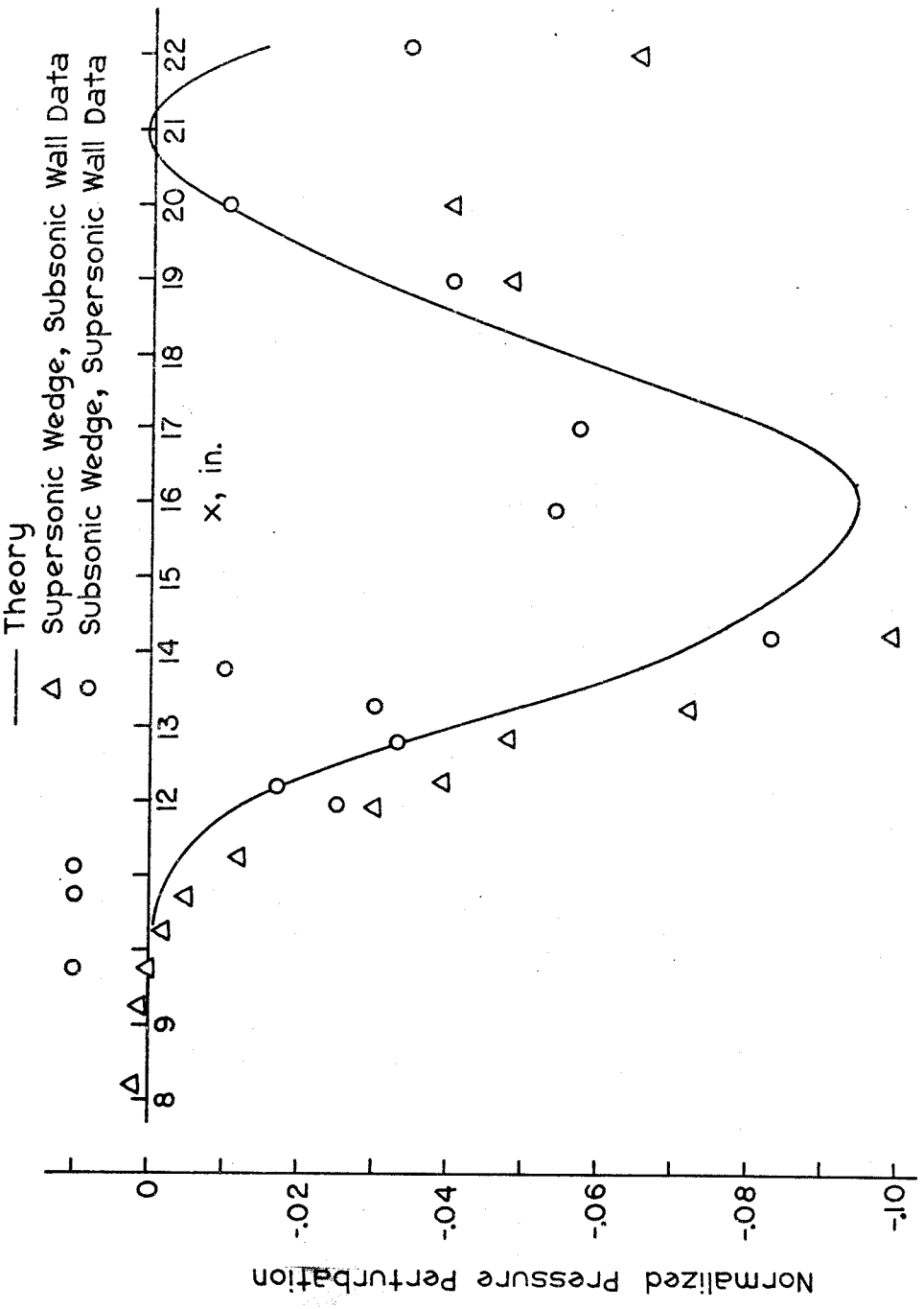

Figure 4.23: Experimental Verification of "Wall Equality Paradox"

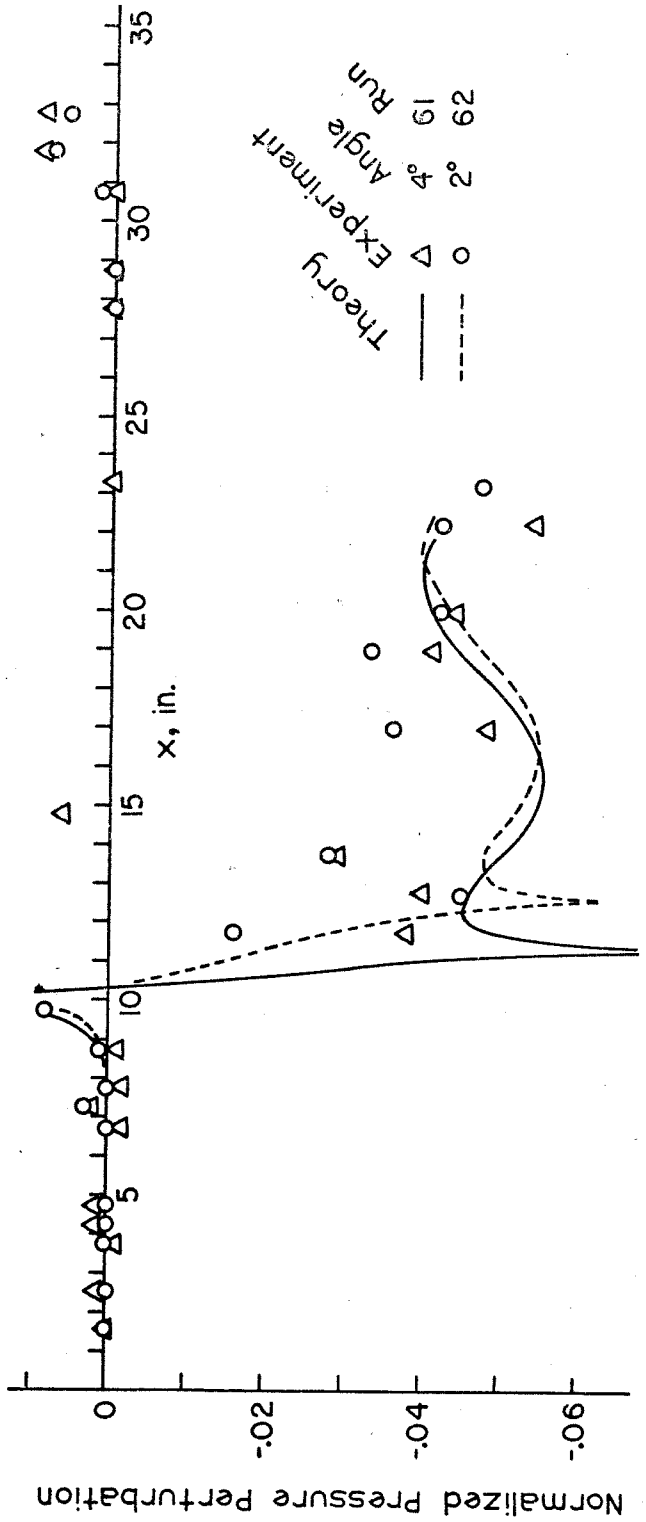

Figure 4.24: Effect of Wedge Angle on Subsonic Wall Pressure (Subsonic Wedge)

experiment is only qualitative at best. The theory predicts that the wedge angle has little effect on the subsonic wall pressure. If anything, the experimental data present the unpredicted result that the 4^{o} angle causes an additional 0.01 drop of normalized pressure beyond that caused by the 2^{o} angle. Perhaps the cause of this is a nonlinear response of the subsonic wall boundary-layer displacement thickness with increasing wedge angle, which may cause the wedge to appear thicker than it actually is. It seems at least as likely, though, that this is not a real effect but rather is due to some experimental or correction error (though it seems too large to be a subsonic stream correction error).

As with the supersonic wedge experiments, additional computations were made to ascertain the effect of wedge thickness t, M_1, M_2, and h_2 on the subsonic wall pressure. Recall that in all cases in this first-order theory, the supersonic wall pressure for the subsonic wedge is the same as the subsonic wall pressure for the supersonic wedge, already presented.

The effect of wedge thickness on the subsonic wall pressure is shown in Figure 4.25. A negative singularity is seen as expected in the region of $x = 10.8''$ to $12.0''$ at the shoulder of the wedge, similar to the singularity at $x = 10.0''$ at the leading edge of the wedge. Downstream of the shoulder, the pressure oscillates with a wavelength of about $8.5''$ in response to the reflection of waves off the supersonic wall and the interface. The pressure amplitude shows linear dependence on t at all points beyond about $x = 13''$.

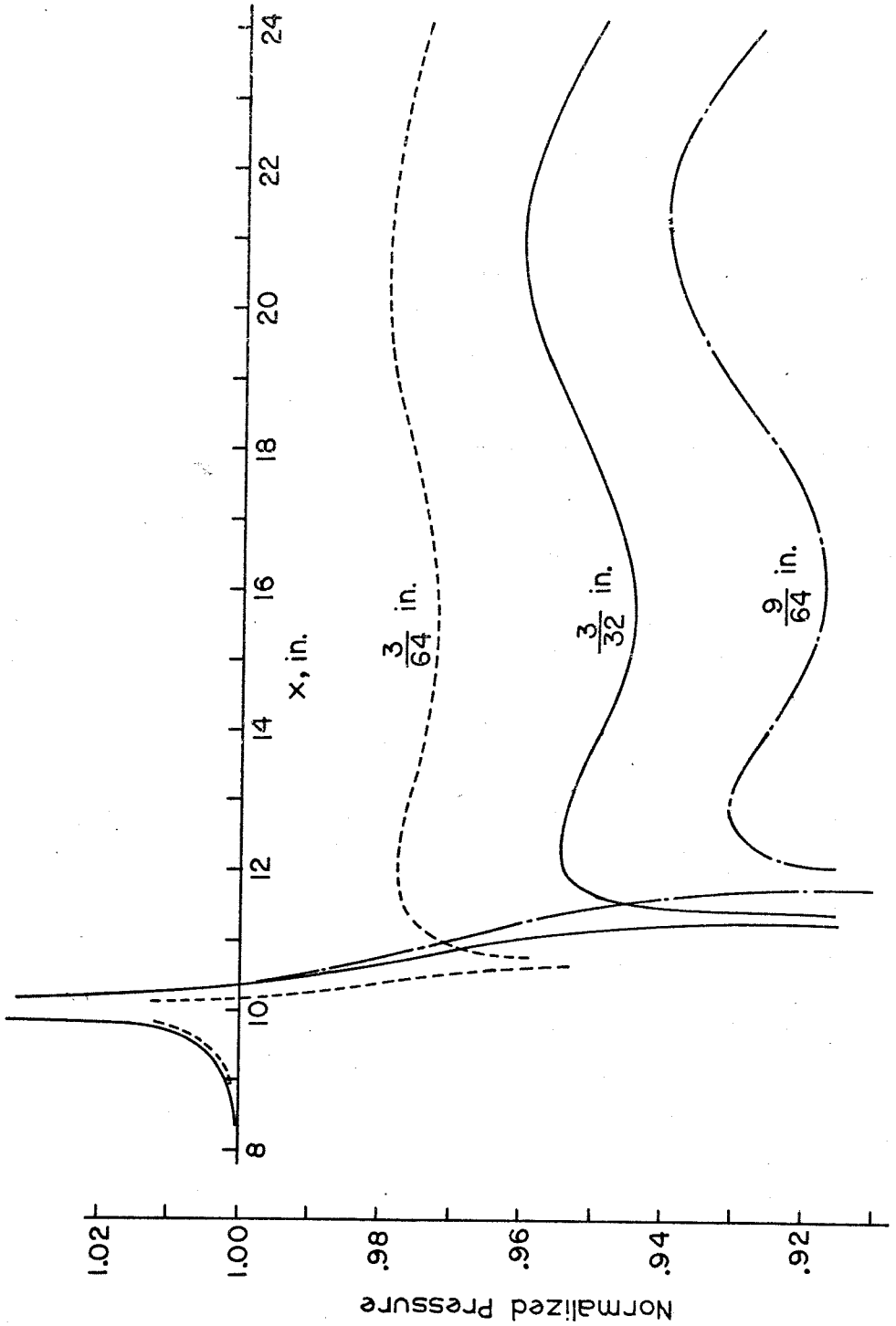

Figure 4.25: Effect of Wedge Thickness on Subsonic Wall Pressure (Subsonic Wedge)

Figure 4.26 describes the effect of M_1 on the subsonic wall pressure. No effect can be seen until x = 12" to 13" when the first waves from the initial perturbation return to the interface after rebounding off the supersonic wall. The increasing wavelength of the disturbance with increasing M_1 reflects the change of β_1 in the quantity $(2\beta_1 h_1)$, the supersonic stream disturbance cycle length. The amplitude of the disturbance after about x = 12" reflects the decreased choking margin of the unperturbed flow as M_1 increases.

The effects of varying M_2 (Figure 4.27) and h_2 (Figure 4.28) show a similar dependence on the unperturbed choking margin. It should be repeated for emphasis that choking as such is not embraced in the first-order theory; the amplitude of the disturbances, however, can be related to the unperturbed choking margin.

Figure 4.29 correlates for Figures 4.27 and 4.28 the minimum pressure in the vicinity of x = 16" and the maximum pressure in the vicinity of x = 21" with the choking margin. In all cases the flow is "qualitatively subsonic," i.e., the static pressure at choking is less than the unperturbed static pressure, and decreases in the flow area therefore cause the equilibrium static pressure to fall. As is seen in Figure 4.29, the correlation is quite good.

In an attempt to verify experimentally some of the results of the theory of Tsien and Finston[18], a study similar to the present subsonic wedge experiment was performed by Holder, Chinneck, and Gadd[19] with an apparatus in which $M_1 = 1.6$, $h_1 = 5.9$"; M_2 could be varied from 0.50 to 0.98, and h_2 from 0.1" to 0.4". Wedges of deflection angles $2\frac{1}{2}^\circ$ and 5° were attached to the subsonic wall at

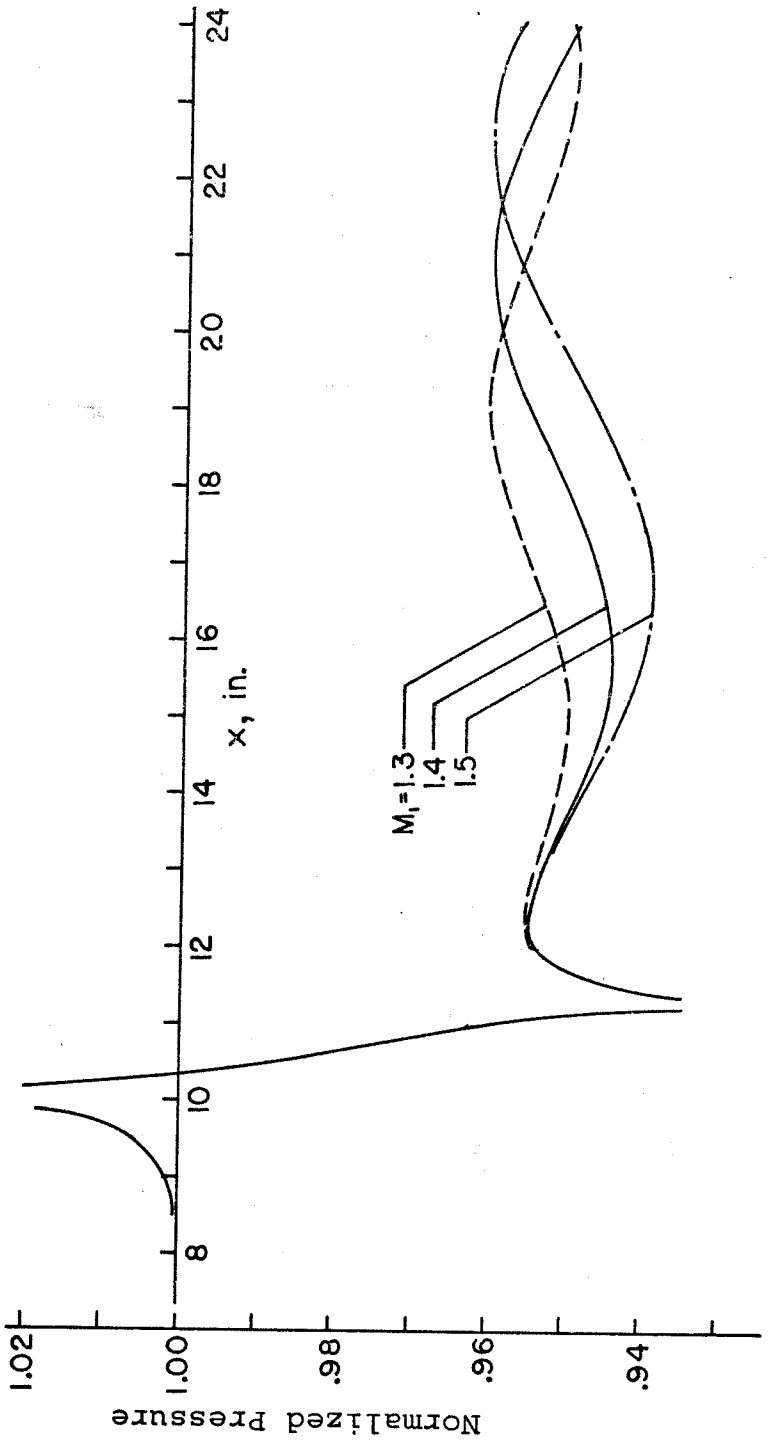

Figure 4.26: Effect of M_1 on Subsonic Wall Pressure (Subsonic Wedge)

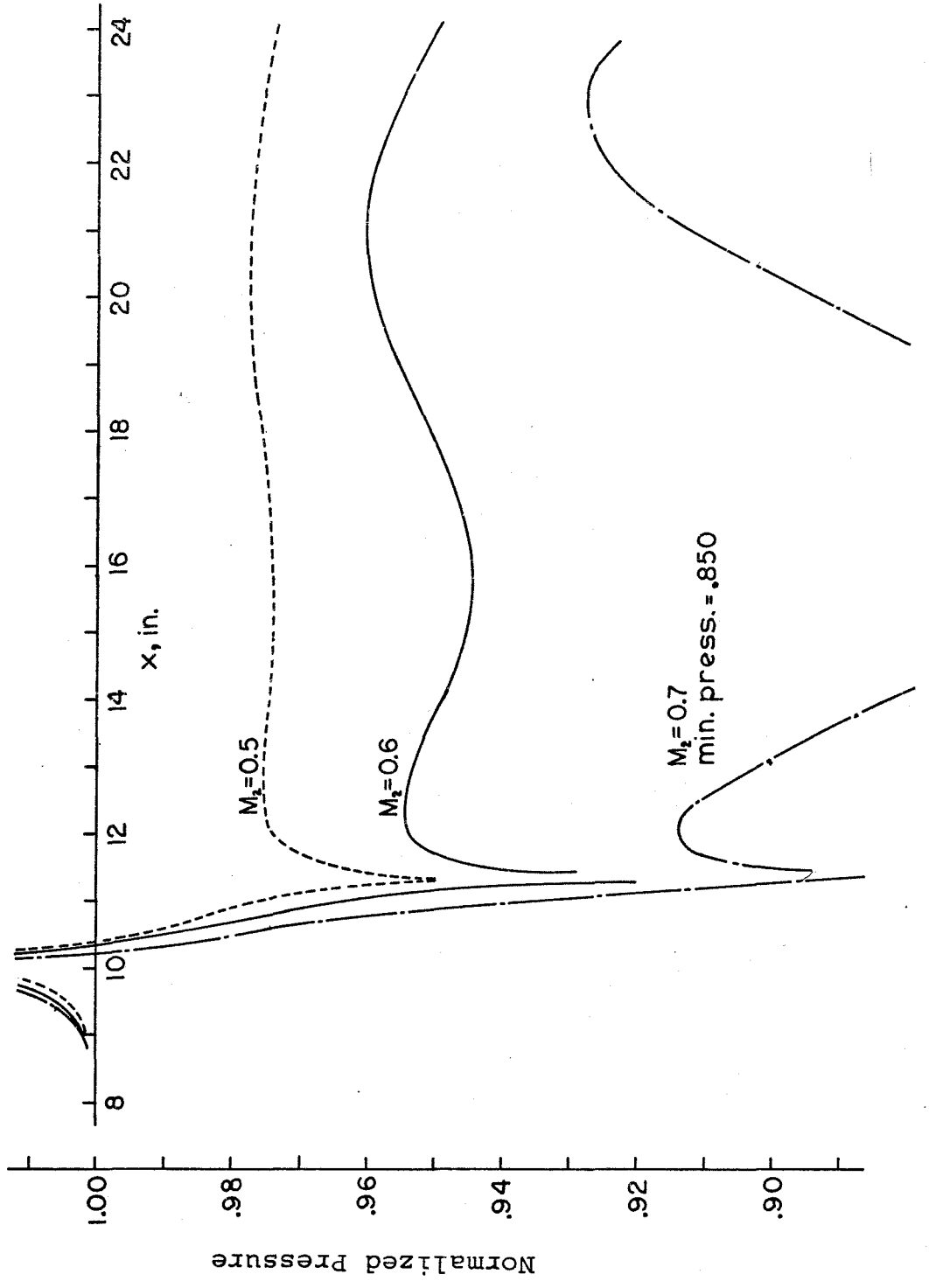

Figure 4.27: Effect of M_2 on Subsonic Wall Pressure (Subsonic Wedge)

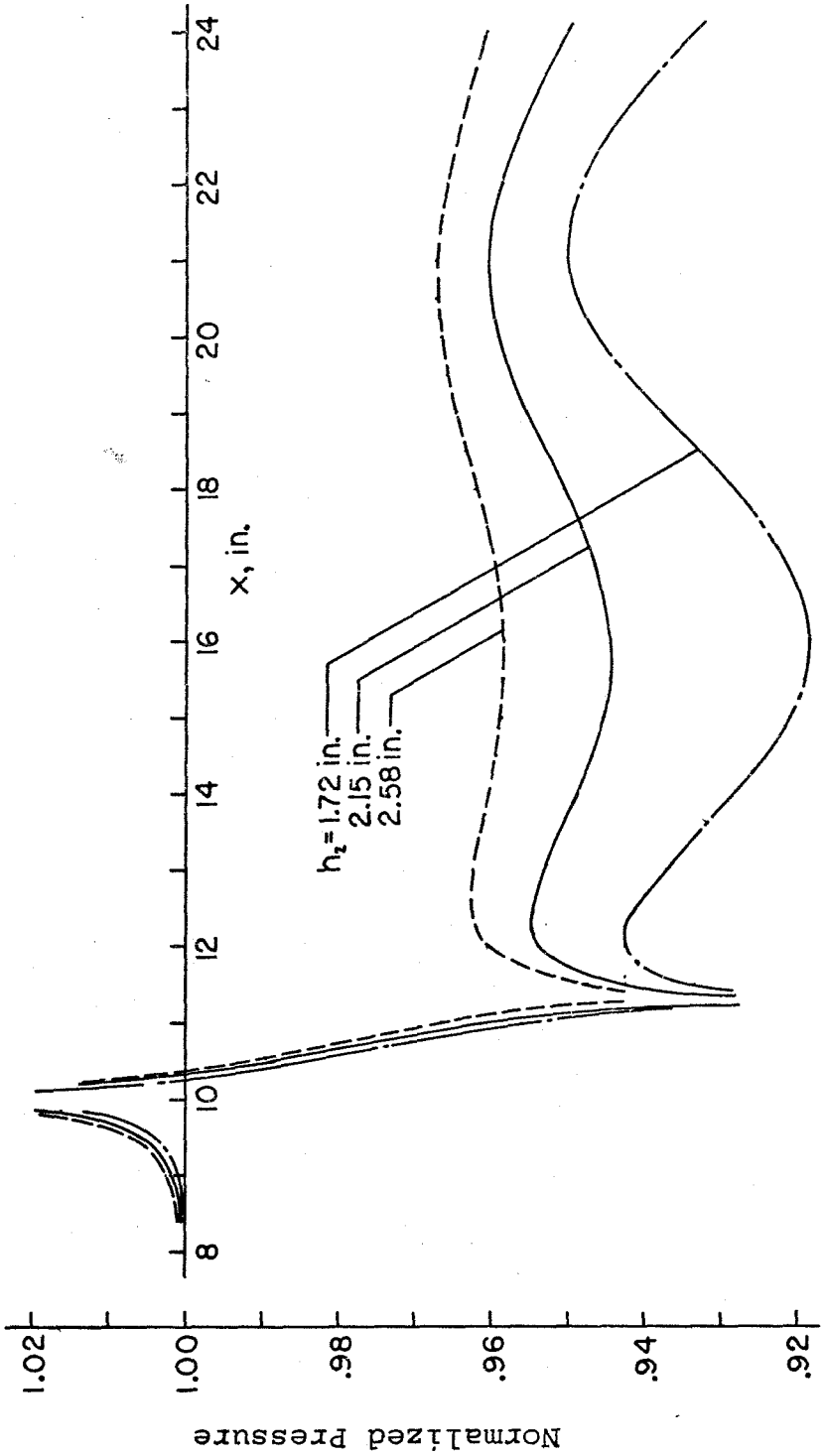

Figure 4.28: Effect of h_2 on Subsonic Wall Pressure (Subsonic Wedge)

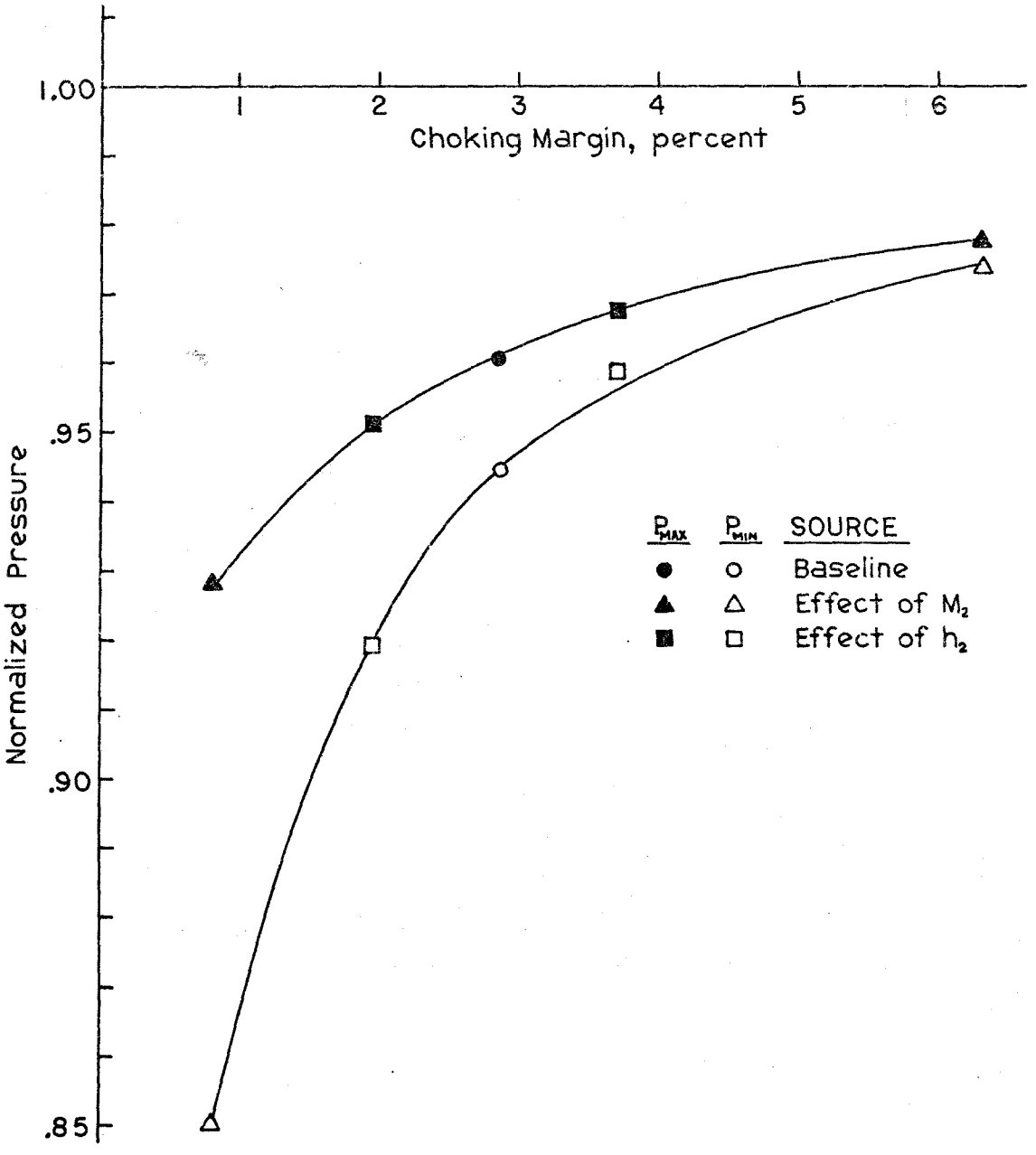

Figure 4.29: Dependence of Disturbance Pressure on Unperturbed Choking Margin (Subsonic Wedge)

$x = 3.1''$ or $6.1''$.

By $x = 3.1''$, there was no uniform region in the subsonic stream. With vorticity throughout the low-speed flow, their experiment more closely resembled a boundary layer (as it was intended to) than does the current study, and the results were more typical of boundary layer results. Significant pressure disturbances were found as much as $10\,h_2$ upstream of the leading edge of the wedge, compared with the present results of $0.6\,h_2$.

Furthermore, their results did not scale with h_2 as that parameter was varied: a reduced h_2 was accompanied by enhanced upstream propagation in terms of x/h_2. As h_2 is decreased, the mean distance of a subsonic stream tube from the vorticity source (the dividing streamline in the shear layer) is lessened. Thus, the mean subsonic flow receives more vorticity through momentum diffusion. The velocity profile is smoothed out and resembles much more closely a supersonic boundary layer. A slight suggestion of this dependence of upstream compression on the vorticity content of the subsonic stream is seen in Figure 4.18, though it is not a strong effect.

The present study and those of Tsien and Finston[18]; Holder, Chinneck, and Gadd[19]; and Liepmann, Roshko, and Dhawan[20]; illuminate substantial differences between the combined shear layer/subsonic stream/subsonic boundary layer in the current study and a supersonic laminar boundary layer. In the present study, there are substantial regions of uniform (irrotational) subsonic flow, for which potential theory is a good representation. Potential theory, of course,

breaks down where vorticity is present, and in the limiting case of a supersonic boundary layer there is a smooth distribution of velocity from the freestream value to zero velocity at the wall.

The upstream propagation of disturbances through the subsonic layer (scaled with the thickness of the subsonic layer) is strongly related to the smoothness of the velocity distribution. Where a significant plateau of uniform flow is present, as in the current work, upstream propagation of disturbances is very slight (confined to a distance of about $0.6\,h_2$). As the velocity distribution becomes smoother (the cases of reduced h_2 in ref. 19, for example), the disturbances propagate upstream several subsonic layer thicknesses. This should not be compared with a supersonic laminar boundary layer, in which upstream propagation distances are governed by boundary layer separations.

4.7 Discussion of Results

The work described in this chapter was undertaken as a preliminary to the study of a blade in a flow of spanwise-varying Mach number, discussed in Chapter V. In these experiments, the objectives were to gain experience with the new Transonic Shear Flow Wind Tunnel, and to gain understanding of the interactions between the supersonic and subsonic streams, especially in terms of wave propagation upstream of a source and in large-scale response to area changes. In addition, it was hoped that agreement between the first-order theory and the experiments could be demonstrated within some range of validity.

The comparisons between theory and experiment have been noted. Agreement is reasonably good where the blockage/choking margin ratio is less than about 0.4, and where inclination angles to the unperturbed flow are less than 5^{o}. The computational model assumes a zero-thickness shear layer. The actual thickness seems to affect the agreement between theory and experiment when the perceptible shear-layer thickness is about one-third of the tunnel height. The general shape of the pressure distribution is well predicted within the subsonic stream.

In the subsonic stream, the upstream propagation of perturbations is limited to a length of about $0.6\,h_2$ from the source (the shock impingement point in the case of the supersonic wedge). Based on a comparison of the present study with work by Holder, et al.[19], it appears that as the transonic shear layer spreads into the subsonic stream, i.e., as the velocity profile in the subsonic stream is smoothed out, the upstream propagation of disturbances is enhanced. The combined flow behaves more nearly as a supersonic boundary layer, in which precompression distances on the order of tens of subsonic layer thicknesses have long been measured[20, 21].

Precompression of pressure disturbances was also noted in the supersonic boundary layer ahead of the leading edge of the wedge. This perturbation agreed with numerous studies of a supersonic boundary layer over a wedge.

The experimental data supported the prediction of the first-order theory that for specified flow conditions (M_1, M_2, h_1/h_2) a given disturbance geometry may be attached to either the supersonic

or subsonic wall and the pressure distribution on the unperturbed wall in both cases will be the same.

A parametric study, using the linear theory, was made to determine the effect of M_1, M_2, and h_2 for the subsonic wedge. This showed a strong inverse dependence between the disturbance amplitude on the subsonic wall and the unperturbed choking margin.

V. AIRFOILS

5.1 General Discussion

The ultimate portion of the experiment was the qualitative simulation of the compressibility effects on a transonic compressor rotor blade by placing in the wind tunnel an airfoil passing spanwise through the transonic shear layer (see Figure 5.1). The goal was to gain an understanding of the inviscid flow field ahead of the blade and within the blade passage.

The experiment proceeded in three stages. The first stage was the examination from another point of view of the data taken in the empty-tunnel runs with the pitot strut installed at various stations in the tunnel. This strut has very nearly a diamond cross section, with a chord of 5/16-inch and a maximum thickness of 1/16-inch. It was hoped that an examination of already available data in the form of wall pressures and schlieren photographs would yield some insight to the flow processes involved.

The next step in the experiment was the attachment of a half-profile of diamond cross section to one of the side walls. This, of course, could only represent a zero-lift blade, and to some extent the desired features were "washed out" by the sidewall boundary layers flowing over the profile. Since using one of the steel side walls for mounting the half-airfoil precludes the use of the schlieren system, observations were limited to wall pressure measurements and surface oil flow visualization.

These studies were considered preliminary and will not be discussed in detail. The final and most important step, which will be

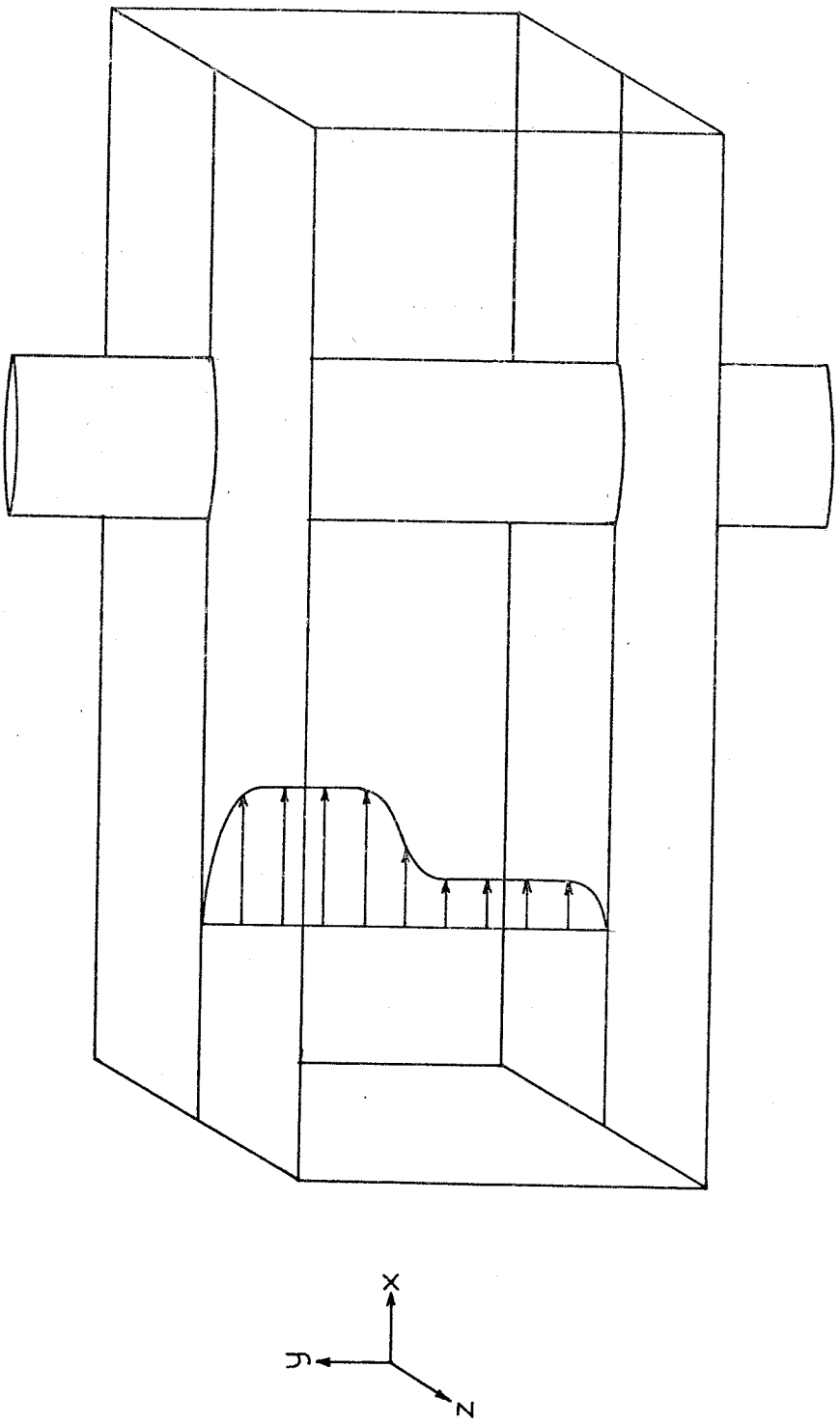

Figure 5.1: Sketch of the Free Airfoil Experiment

considered more carefully, was the mounting of an airfoil to pass spanwise through the shear layer in the middle of the tunnel. In addition to the zero-lift case, this permitted studies with the airfoil at small angles of attack. Schlieren and spark shadowgraph photography were also possible except where the shadow of the airfoil eclipsed the view. Wall pressure measurements and surface flow visualization studies were obtained. A biconvex (circular-arc) airfoil section was chosen with a thickness ratio (t/c) of 6 per cent. No roughness bands or other devices were applied to any of the models to trip the boundary layer.

An attempt was made to extend the two-dimensional theory of Chapter IV to the three-dimensional airfoil problem. This extension is described in Appendix D. Fundamental problems were encountered in the mathematics, which represents the solution as double-infinite series, and this line was not pursued.

5.2 Strut

It has already been mentioned that due to the similarity of the pitot strut to a diamond-section airfoil a study of the strut flow field is educational in terms of understanding the larger airfoil flow field. The principal difference between the strut and the sidewall airfoil is that the leading-edge deflection angle is 14° for the strut, and 4° for the sidewall airfoil (also a diamond section). This difference is especially significant because at Mach 1.4, a shock cannot remain attached to the leading edge of a wedge if the deflection angle is greater than about 9.5°. Geometrically, the strut has a thickness ratio (t/c) of 20 per cent, while for both types of airfoils (sidewall-mounted and

free) the thickness is about 6 per cent.

Therefore, while there are significant differences, the basic form of the perturbation to the flow is nevertheless similar. In addition, data from the installation of the pitot strut were available quite early in the project.

The principal factor in the flow field is that a detached shock, as expected, stands ahead of the strut in the supersonic stream at all times, due to the large leading-edge wedge angle. In the sidewall and free airfoil experiments, the shock would be expected to remain attached (except as affected by the sidewall boundary layer or by leading edge bluntness). As revealed by schlieren photography, the shock as viewed from upstream of the strut is convex, standing about an inch ahead of the strut near the supersonic wall and about 1/2 inch ahead near the sonic surface in the shear layer. Presumably, the shock bends around the strut to either side until it strikes the sidewalls. The shock wave has only a weak effect on the sidewall pressure, due to the closeness of the expansion from the shoulder of the strut to the leading-edge shock, causing a closely-following cancellation of the pressure rise.

The detachment of the leading shock complicates the flow field to the point that non-empirical analyses fail completely. Nevertheless, a rough parallel with both experimental and theoretical data of the wedge experiments is noted. Experimental pressure measurements show that in neither the supersonic nor the subsonic stream does the presence of the strut affect the flow field more than about 1/2 inch (i.e., 1/4 of the duct width) upstream of the shock or, in the sub-

sonic stream, upstream of the shock/shear layer intersection (see Figure 5.2).

This knowledge lends credibility to the pitot-tube data of Chapter III, in which the measuring plane of the pitot tube stood 1.75 inches to 2 inches upstream of the strut (i.e., completely away from the measured disturbance).

Figure 5.3 shows the general features of the pitot strut flow field as revealed by the schlieren system. The origin of the waves described as "secondary" will be discussed in the following section. It should be noted that the strut thickness of 1/16-inch represents a tunnel blockage of 3.18 per cent, exceeding the one-dimensional choking limit of 2.86 per cent. The limited upstream influence of the strut together with the presence of supersonic flow indicates that choking has not occurred. This is ascribed to the increased choking margin related to short-span disturbances, previously discussed in Section 3.4. The differences between the supersonic boundary layer and the shear layer in their effect on the leading detached shock will be outlined in Section 5.4.1.2.

5.3 Sidewall Airfoil

The "sidewall airfoil" is a symmetric diamond airfoil of 6 per cent thickness ratio and a 3-inch chord, cut on the plane passing through the leading and trailing edges. A certain number of static pressure taps were drilled through the airfoil in a pattern to match the taps drilled in one of the steel sidewalls, in the manner described previously for the supersonic and subsonic wedges. The airfoil is

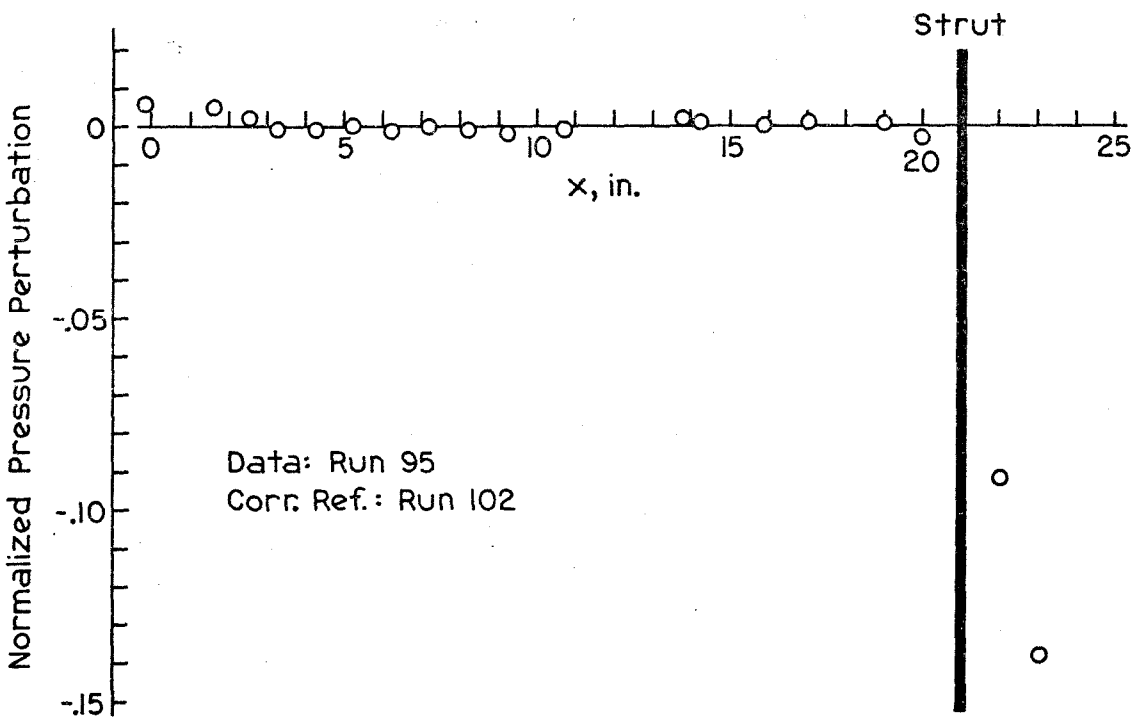

Figure 5.2: Subsonic Wall Centerline Pressure Data Showing Limited Upstream Influence of Pitot Strut

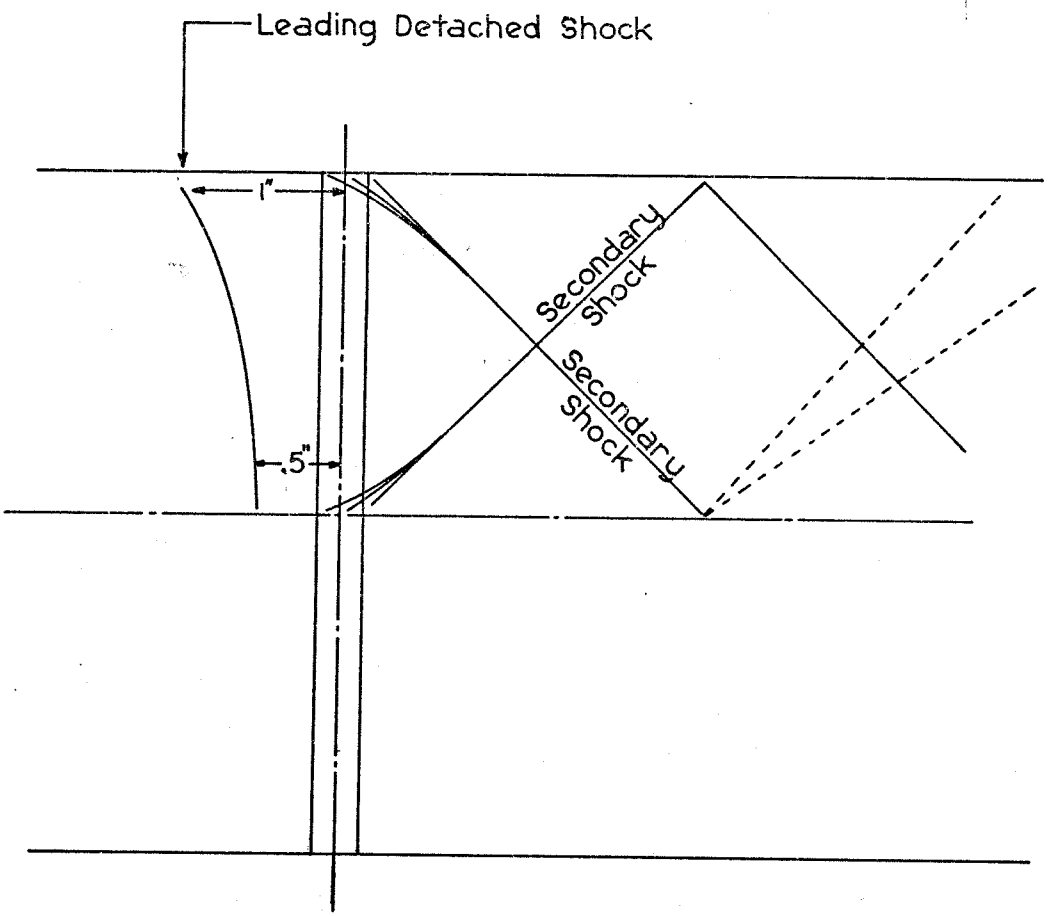

Figure 5.3: Pitot Strut Flow Field Structure
(Strut centerline at x = 12.25 inches)

secured to the sidewall by 4 socket-head cap screws of size 1-64. The leading-edge deflection angle is 4°, and the maximum half-thickness is .093-inch. Both these values correspond well to the baseline case of the wedge experiments.

The airfoil could be mounted on either the instrumented sidewall (leading edge at x = 9.75") or the plain sidewall (x = 10.00"), so that the free stream Mach number varied in the spanwise direction. Pressure data could be taken on both the supersonic and subsonic walls of the wind tunnel and on the instrumented sidewall, whether the airfoil was attached to it or to the solid sidewall at the opposite side of the tunnel.

This was intended only as a preliminary to the full set of experiments on the free airfoil, and hence it was not intended that a great deal of quantitative data should be obtained. Rather, the goal of these experiments was a first-cut qualitative understanding of the processes at work.

5.3.1 Discussion of Flow Field. As the sidewall airfoil of necessity is mounted on one of the steel walls, it was not possible during this series of experiments to mount both glass windows, and thus schlieren photography was not possible. Consequently, the data used to analyze the flow field were static pressures on the walls, supplemented by oil flow observations.

To a reasonable degree, the flow field exhibited run-to-run repeatability. This is illustrated in Figures 5.4 and 5.5, which present measured static pressures on the centerlines of the supersonic and subsonic walls for all runs performed with the sidewall airfoil.

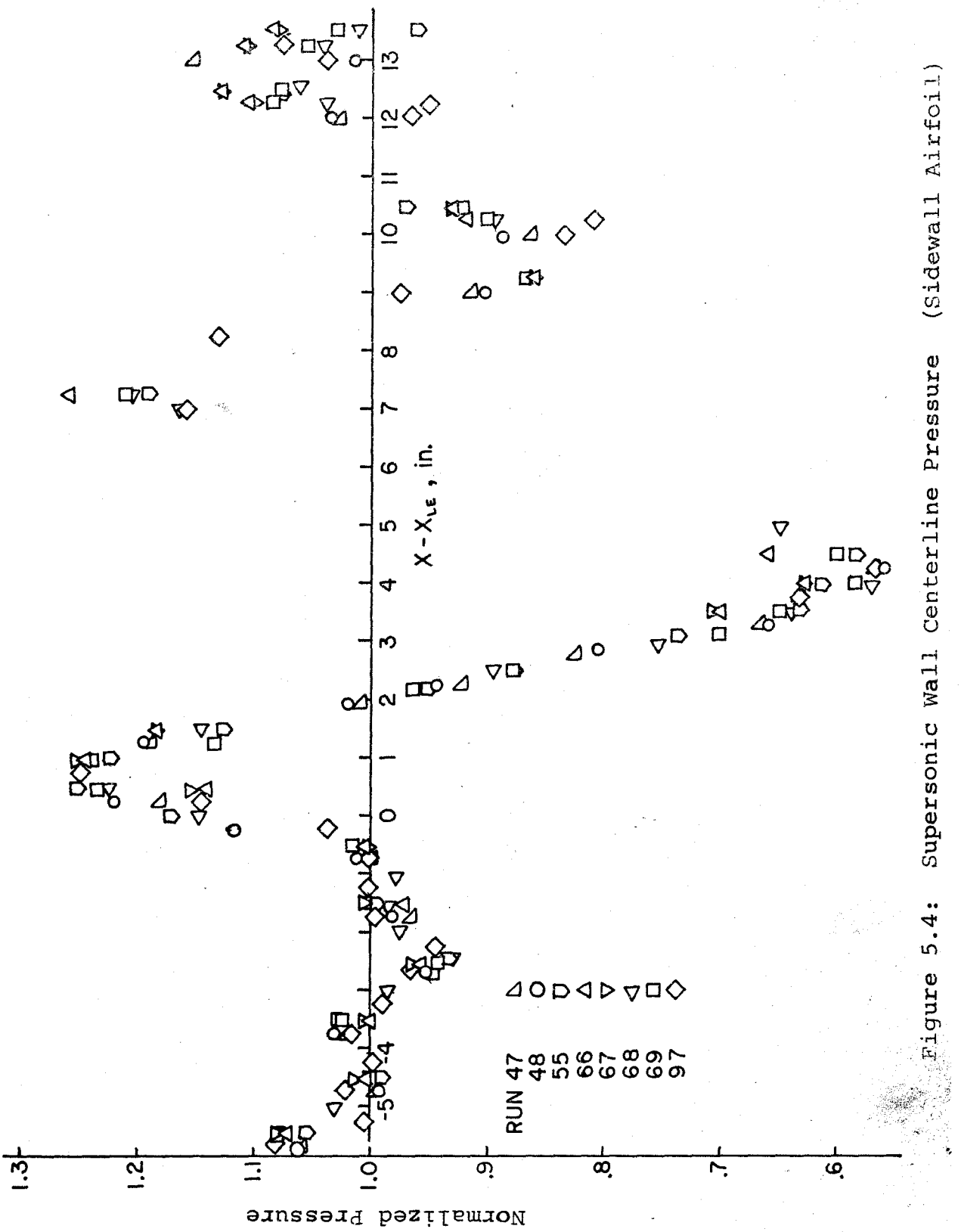

Figure 5.4: Supersonic Wall Centerline Pressure (Sidewall Airfoil)

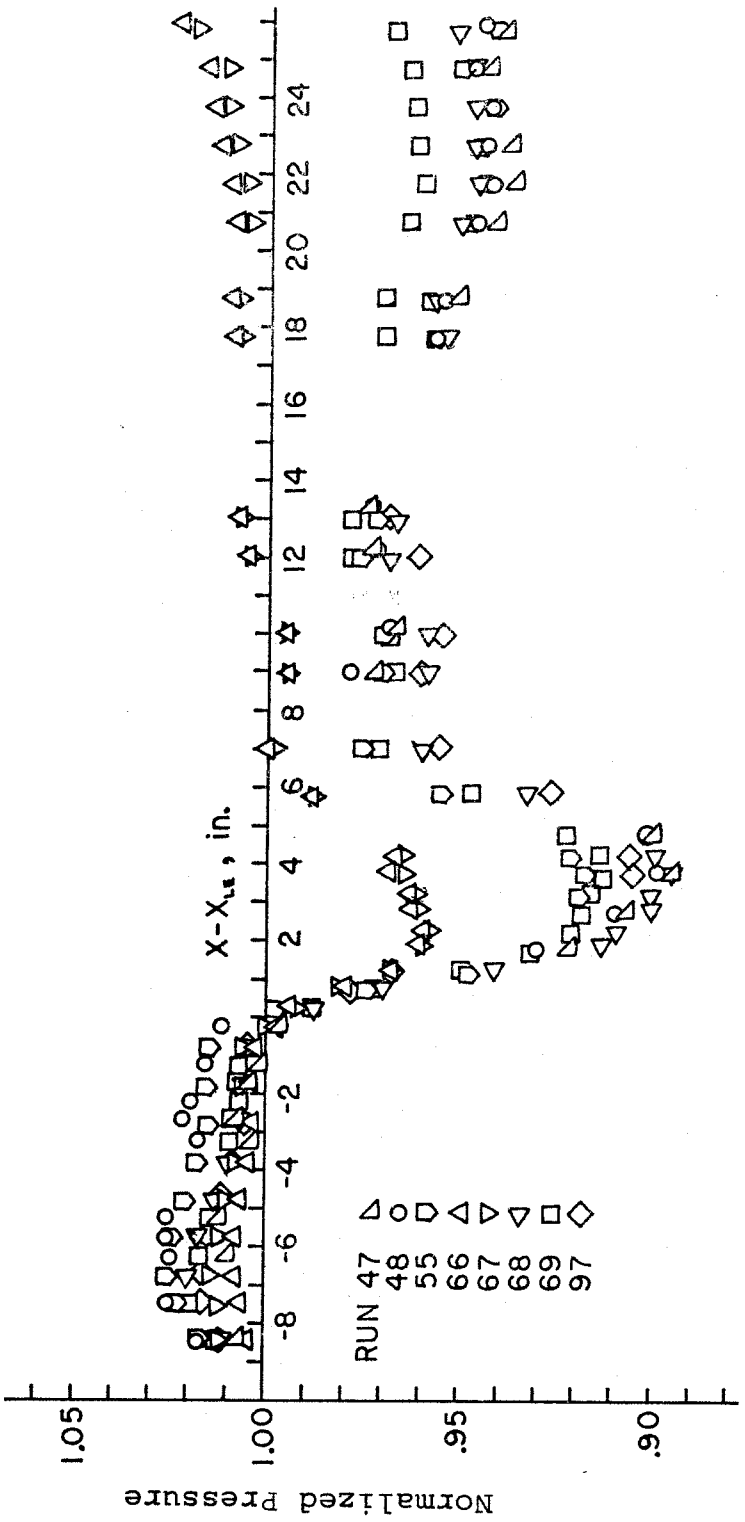

Figure 5.5: Subsonic Wall Centerline Pressure (Sidewall Airfoil)

One quickly notices, especially in Figure 5.5 (subsonic wall pressure) that while the data from all other runs form a reasonably compact band, data from Runs 66 and 67 show basic differences and yet are consistent among themselves. A glance at Table 5-1, which shows nozzle exit Mach numbers for all the runs, reveals the cause of this: in Runs 66 and 67, M_2 was considerably lower than in all the other runs. Thus, the response of the subsonic stream was much "softer" in that the influence of the wall was considerably less. The subsonic layer, therefore, experienced a reduced perturbation pressure amplitude.

TABLE 5-1. Flow Properties for Sidewall Airfoil Runs

Run	x_{LE} (in.)	Day	M_1	M_2	Wall Attached
47	10.00	26 June 74	1.40	0.61	solid
48	10.00	2 July 74	1.39	0.63	"
55	9.75	1 Aug 74	1.40	0.63	instrumented
66	9.75	12 Dec 74	1.44	0.52	"
67	9.75	8 Jan 75	1.43	0.53	"
68	9.75	13 Jan 75	1.40	0.61	"
69	9.75	15 Jan 75	1.40	0.60	"
97	10.00	27 May 75	1.42	0.60	solid

A primary factor affecting the sidewall data certainly was the boundary layer from the wall that flowed over the airfoil. It is assumed that the boundary layer affected the initial compression wave of the airfoil in the same way (approximately) that it did the super-

sonic wedge. Both models were mounted at the same leading edge station (within 1/4 inch) and had the same leading-edge deflection angle, the difference of course being that the airfoil was fixed to the sidewall while the wedge was fixed to the top wall.

The boundary layer caused the pressure rise to be dispersed over a small region near the leading edge. The distributed compressions (in the case of the wedge) coalesced within the first inch from the source into a sharp wave which was displaced upstream about 1/4 inch from the expected inviscid wave location. This is in qualitative agreement with photographs at Mach 1.4 to 1.5 of a shock wave in a corner from Liepmann, Roshko, and Dhawan[20], which show apparent shifts upstream in the concentrated wave on the order of the boundary layer thickness.

At Mach 1.4, both isentropic and real 4^{o} shocks have a theoretical pressure ratio of 1.219. However, the data already presented in Figure 5.4 and the pressure map for the supersonic wall presented in Figure 5.6 show an overcompression to about 1.24 or 1.25 in normalized pressure. This is a fairly common feature of shock/boundary layer interactions, and is shown in data presented by McCabe[22] in considering the three-dimensional interaction of an oblique shock propagating across a boundary layer so that one edge of the shock is continually grazing the boundary layer. These results show that at least $10\delta^{*}$ and often a considerably longer distance from the point of contact is required for the overcompression to be relieved. It should be noted that the pressure distribution of Figure 5.6 is based on data taken on the tunnel centerline and 1/2 inch to either side of the center-

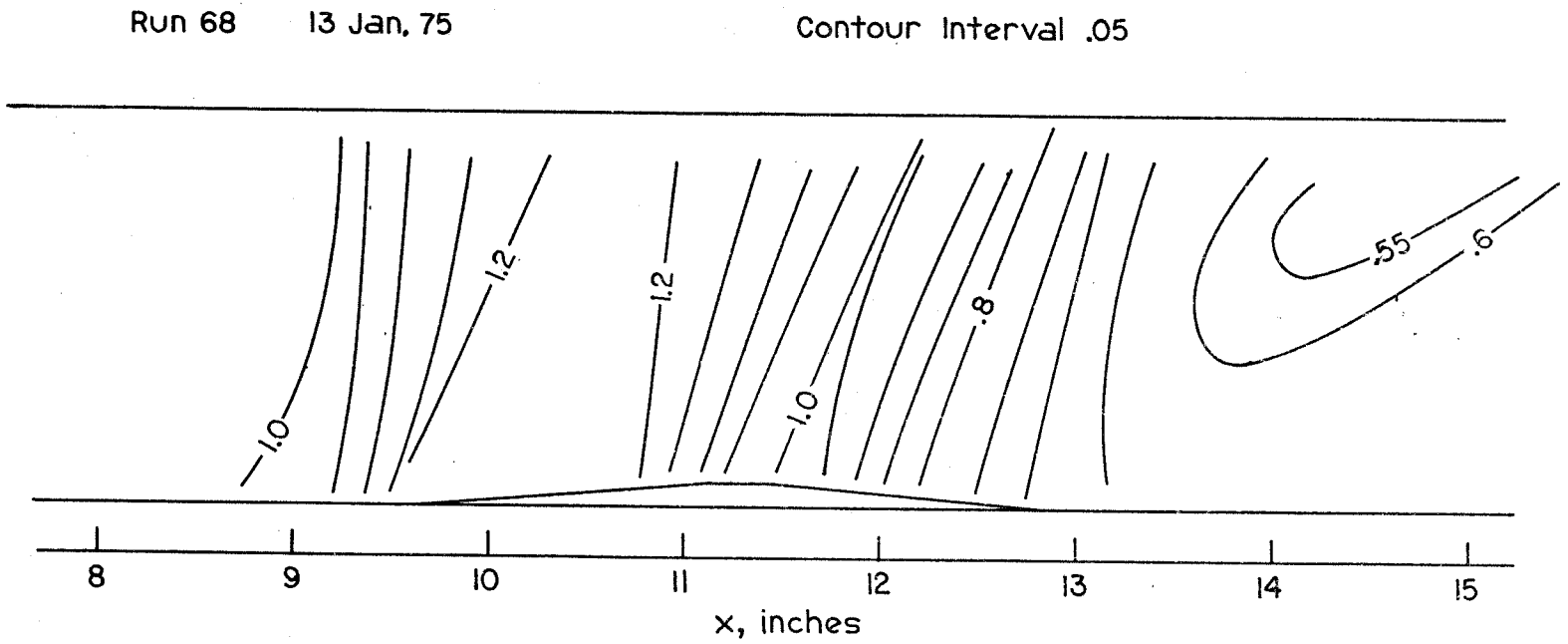

Figure 5.6: Supersonic Wall Pressure Contours (Sidewall Airfoil)

line at 1/2-inch intervals in the streamwise direction.

With the primary shock being attenuated at one end by the grazing interaction with the boundary layer and at the other end by a similar interaction with the shear layer, one would expect the shock to have a maximum strength in the center of the supersonic stream, and to be considerably reduced in strength toward either the interface (about $y = 0$) or the supersonic (top) wall. This expectation is borne out by the static pressure contours on the opposite sidewall, presented in Figure 5.7. The maximum pressure measured on the wall in the vicinity of $(x,y) = (11.0, 1.0)$ was 1.33. Since the theoretical wall pressure for inviscid reflection of a 4^{o} shock at Mach 1.4 is 1.57, there is a reasonably strong interaction with the boundary layer that reduces the pressure. By this stage, the two-dimensionality of the flow has been destroyed, and cross flows of significant proportion are present.

Observed oil-flow patterns from the supersonic wall and the sidewall on which the airfoil is mounted are sketched in Figure 5.8. Unfortunately, attempts to photograph the oil patterns were frustrated by bad camera angles and inability to color the oil sufficiently to obtain adequate contrast. Part "a" of Figure 5.8 contains no surprises: the oil deflects in the direction expected, and the pattern repeats with alternating direction for several cycles as the lateral (i.e., two-dimensional) wave reflects between the sidewalls. Part "b" provides more interesting information. Note that a small compression wave is created in the shear layer near the leading edge and propagates obliquely into the supersonic stream. Its effect can be noted on even

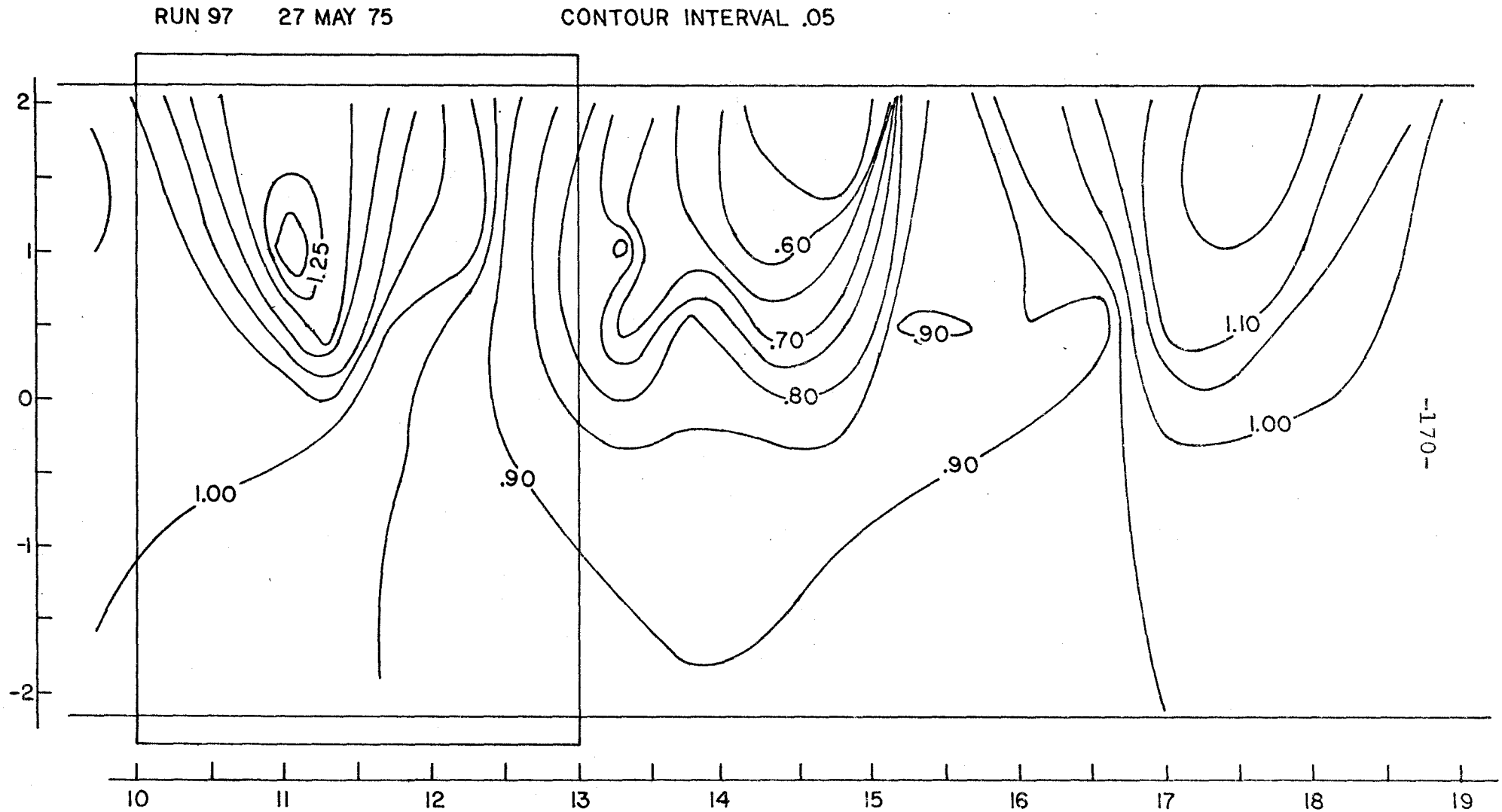

Figure 5.7: Pressure Distribution on Unperturbed Sidewall (Showing Superimposed Airfoil Position on the Opposite Wall)

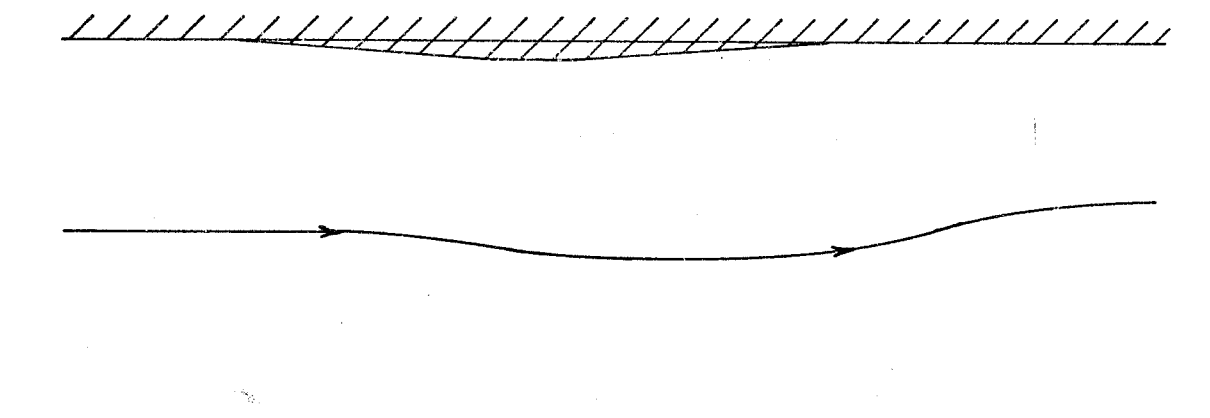

A. Supersonic Wall

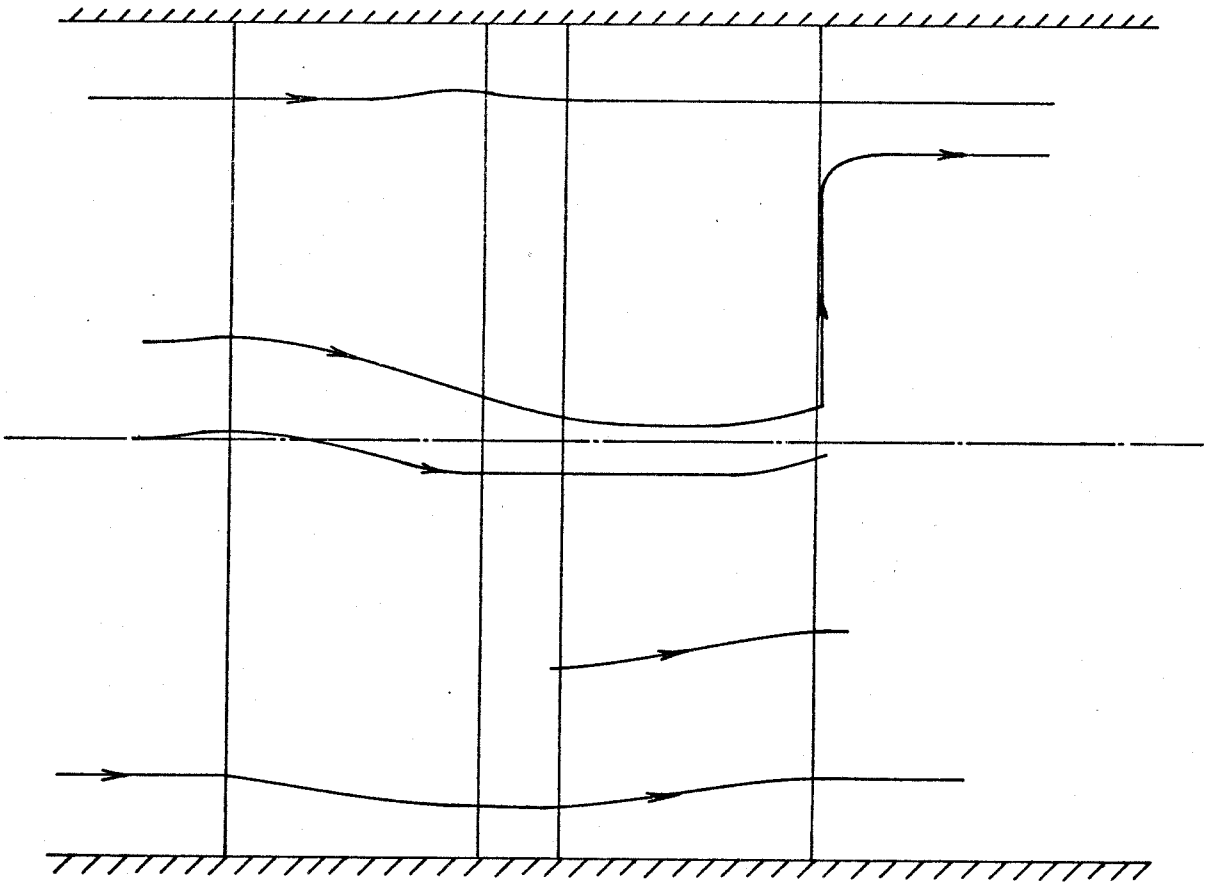

B. Sidewall and Airfoil

Figure 5.8: Sketch of Observed Oil Flow Patterns (Sidewall Airfoil, Run 67, Drawing Not to Scale)

the uppermost streamline.

This is caused by the presence of an elevated pressure in the subsonic stream in all directions near the leading edge of the airfoil, while in the supersonic stream the pressure is unperturbed at all points ahead of the bow shock wave. Thus, for some region near the leading edge, the subsonic stream is at elevated pressure compared to the supersonic stream, and a compression wave is passed up into the high-speed flow.

After this precompression wave, the interface at the centerline of the runnel deflects downward, passing expansion waves into the supersonic stream and relieving considerably the pressure that would otherwise be imposed locally on the shear layer. As the influence of the lower wall is felt, the subsonic streamlines return to the horizontal. The process is repeated with opposite sign as the convex corners near the centerline of the airfoil are passed. The trailing edge of the airfoil is blunted about .010 inch; thus, the pressure in this region responds as some sort of base pressure. This would be expected to be lower in the supersonic flow than in the subsonic flow, and the slow secondary flow of oil into the supersonic stream at the trailing edge is a consequence of this. Beyond the trailing edge, no substantial oil deflections were observed.

The sidewall pressure contours of Figure 5.7 show generally that oblique vertical waves quickly lose dominance downstream of the trailing edge. This is due primarily to the high level of attenuation and dispersion that occurs at each reflection off the shear layer. The lateral (two-dimensional) waves are considerably more persist-

ent, losing only a small fraction (about 10 per cent) of their pressure amplitude at each reflection.

Subsonic wall pressures are presented in Figure 5.9 on the following page (the locations of the pressure taps used in generating this figure are shown in Appendix A). These generally show that lateral pressure gradients exist only in the immediate vicinity of the airfoil. The mean subsonic stream pressure (on the wall at a given x-station) is lowered nearly 10 per cent in the vicinity of the trailing edge in response to the induced variations in the location of the sonic surface. The sonic surface, being generally deflected downward into the subsonic stream and thus reducing the flow area, causes the drop in static pressure on the subsonic wall. Figure 5.9 serves mainly to show the absence of lateral pressure gradients away from the airfoil. Deflections of the sonic surface are better inferred from Figure 5.5. It should be noted that the perturbations upstream of the leading edge agree well with the empty-tunnel variations previously discussed.

Figure 5.10 presents a comparison of experimentally-measured pressures on the airfoil and the opposite wall deep in the subsonic stream ($y = -1.75$ inch) versus calculations from first-order linearized theory for the same airfoil in uniform flow at Mach 0.6. The measurement error in the experimental data is estimated at .003. This suggests that at stations upstream of the leading edge of the airfoil, uniform-flow linearized theory is an accurate model. This then implies that upstream interactions between the supersonic and subsonic streams are negligible.

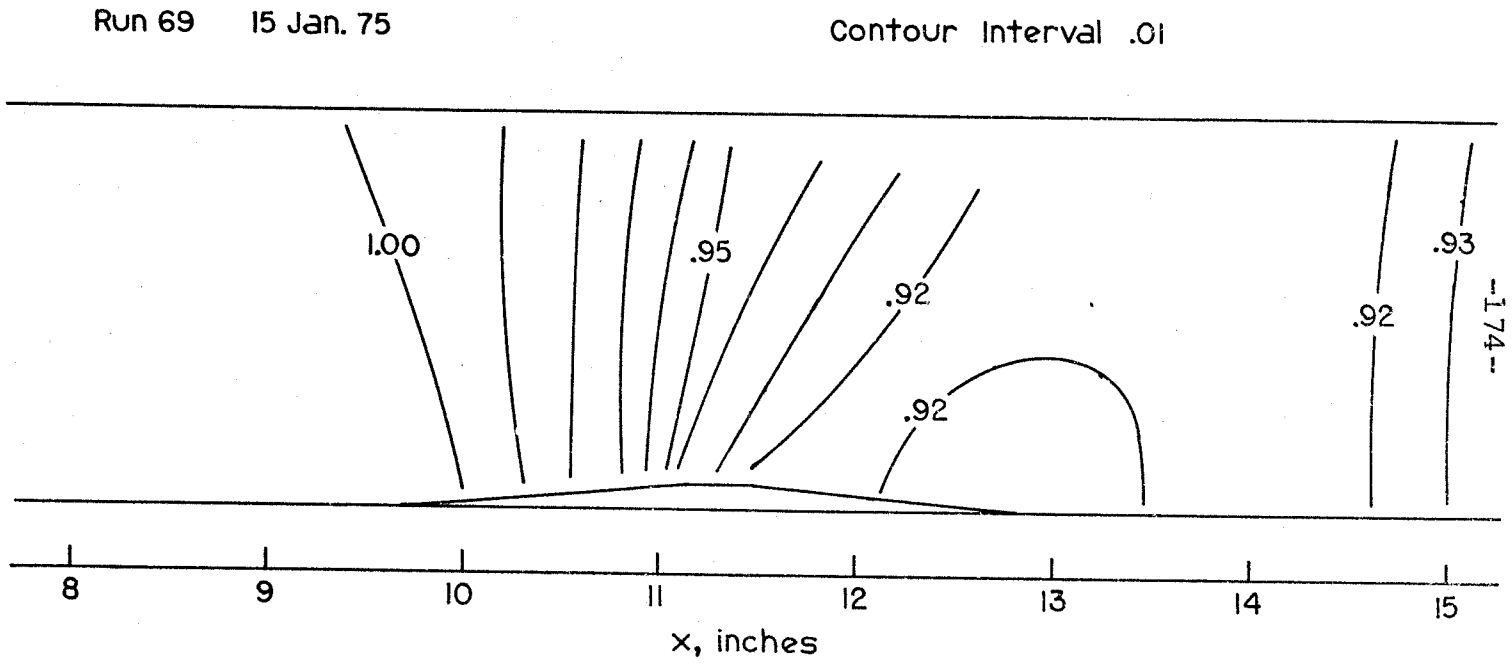

Figure 5.9: Subsonic Wall Pressure Contours (Sidewall Airfoil)

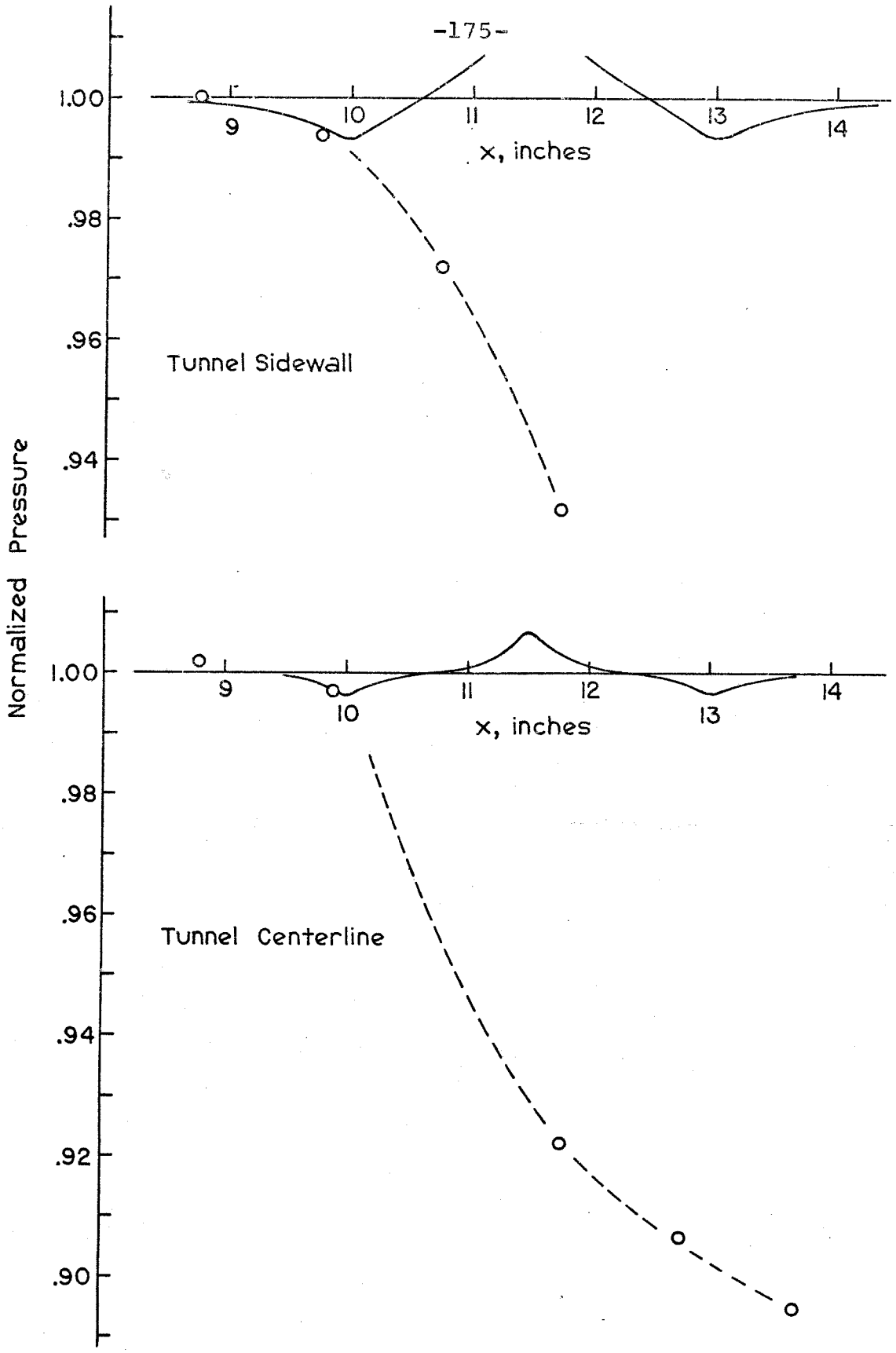

Figure 5.10: Comparison of Experiment to Uniform-Flow Linearized Theory in the Subsonic Stream

5.4 Free Airfoil

The ultimate objective of the experiment was to place a free airfoil in the wind tunnel passing spanwise through the transonic shear layer (see Figure 5.1). Since such an airfoil would be supported only at the supersonic and subsonic walls and not at the sidewalls, the use of glass windows permitting schlieren and shadowgraph photography was possible. Of course, the steel sidewalls could also be used as desired for pressure measurements.

The goal was to place static pressure taps in the airfoil at several chordwise stations and, by traversing the airfoil spanwise while the tunnel was in operation, to obtain continuous pressure distributions for each tap. The need to keep the tunnel blockage ratio limited to 5 per cent meant that the maximum thickness of the airfoil could not exceed about .098 inch. This ruled out traditional methods of constructing metal wind-tunnel airfoils with pressure taps, and our attention was drawn to the method of Collins[23] in which an airfoil is cast of epoxy with pressure lines down the middle of the casting. After the epoxy hardens, holes are drilled through one side of the airfoil into the lines at the desired locations.

It was decided first to cast a pilot model, referred to as the "solid" airfoil, and to cast the "tapped" airfoil later after experience had been gained in the first job. A section view of both airfoils is presented in Figure 5.11. The casting of the airfoils and the problems encountered are described in Appendix E.

5.4.1 Zero Angle of Attack. The flow field around the airfoil at zero angle of attack is dominated by strong three-dimensional

DRAWING IS NOT TO SCALE

A. SOLID AIRFOIL

13 tubes .049" O.D.
6 tubes .033" O.D.
static taps .020" dia.

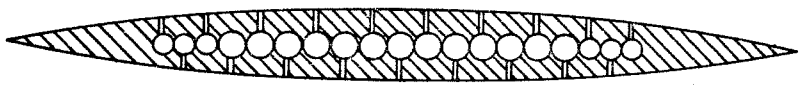

B. TAPPED AIRFOIL

Figure 5.11: Section View of the Cast Epoxy Airfoils

effects, both within the airfoil/wall passage and downstream of the trailing edge. The origin of these disturbances, aside from the more obvious boundary layer effects, is in the velocity gradient of the shear layer. These interactions have two basic causes. The first is the basic qualitative difference between subsonic and supersonic flow in the pressure profile over a given airfoil: the region near the shear layer must make a transition in the pressure distribution due to Mach number effects. This, in turn, will introduce departures from two-dimensionality. The second cause is the large difference in total pressure (a factor of 2.5) across the shear layer, which means that pressure perturbations on the supersonic portion of the airfoil will be much larger than those on the subsonic portion. The difference in dynamic pressure is even larger ($q_1/q_2 = 5.5$).

The three-dimensional effects are not confined to viscous-dominated regions such as boundary layers and separated-flow areas, though the presence of these phenomena aids the disruption of local two-dimensionality. Inviscid three-dimensional interactions, causing large displacements of the sonic line of the shear layer from its unperturbed position, generate waves with strong spanwise components in the vicinity of the airfoil in both the supersonic and subsonic streams. The lateral waves in the supersonic stream, reflecting from one sidewall to the other, experience very little attenuation. Vertical waves in the supersonic stream, reflecting between the shear layer and the top wall of the tunnel, are dispersed considerably on each reflection from the shear layer, and thus decay more rapidly. Pressure waves in the subsonic stream vanish within one chord

length downstream of the trailing edge, except as excited by waves in the supersonic stream.

The leading-edge shock wave in the supersonic stream undergoes a strong Mach-reflection interaction with the wall because its strength is too great for regular reflection regardless of shock wave - boundary layer interaction. This situation is further confused by the boundary layers on the wall. As a result, the shock configuration somewhat resembles choked flow at the entrance to a duct. However, the word "choked" is highly misleading in this case. The situation will be discussed in detail in the next section.

Due to the bluntness of the leading edge of the airfoil, a detached shock, made visible by the schlieren system, stands ahead of the airfoil.

There is the expected upstream propagation of pressure perturbations in the supersonic wall boundary layer from the leading-edge shock wave impingement point. As expected, the extent of this was seen to be approximately $2\,\delta_{.99}$. However, upstream transmission of pressures within the inviscid subsonic flow is virtually nonexistent. Without inviscid modification of the upstream subsonic flow, no similar modification of the upstream supersonic flow (except for the shock/boundary layer interaction already mentioned) was expected, and none was observed.

Discussion of the flow field will proceed in three stages. First, the leading-edge shock wave system and its interaction with the sidewall will be discussed. Consideration will focus on regions in the supersonic stream far enough from the shear layer so that

three-dimensional effects, while still present to some degree, are much less important than the two-dimensional interaction of the wave with the wall and boundary layer. Second, the detached shock ahead of the airfoil leading edge will be considered. Third, the full flow field will be described.

An additional section will discuss modifications to the previously-outlined analysis in the case of the shear layer being about twice as thick. Experiments conducted at x_{LE} = 11.50 in. (δ_s = 0.72 in.) will be contrasted with the data used for the preceding commentary (x_{LE} = 5.00 in., δ_s = 0.31 in.).

5.4.1.1 The bow shock system. In this discussion, it will be assumed that the region of influence of the leading edge bluntness is confined to the immediate neighborhood of the airfoil, and that the fact that the leading edge is blunted up to .010 inch is immaterial in the flow channel. This assumption will be supported in Section 5.4.1.2.

The basic sources of experimental data available which permit the inference of the form of the blow shock system are static pressures on the surface of the airfoil and the sidewall, and pitot pressure surveys several inches downstream of the trailing edge. Unfortunately, the schlieren system cannot be aligned along the span of the airfoil to reveal waves within the airfoil/wall passage. The region of the bow shock system, which was wholly within the passage, was thus in the shadow of the airfoil and was inaccessible to optical measurements. Pressures on the top and bottom walls of the tunnel were only of slight interest in determining the wave shape because the

presence of the mounting attachments on the walls at either end of the airfoil did not permit the placement of pressure taps within the airfoil passage.

The data taken from one surface of the airfoil are illustrated in Figure 5.12. As usual, the pressures have been normalized by the nozzle exit pressure. To obtain these points, the airfoil was moved a small distance in the spanwise direction and the static pressure in each tube was read by means of a Scanivalve and transducer with a digital voltmeter (DVM). Earlier, the pressures were read continuously by an X-Y plotter, but the use of a DVM permitted greater accuracy in an observation with less time and less wear and tear on the airfoil (since it was not necessary to traverse the airfoil once for each individual tap) at the expense of missing any fine detail in the surface pressures.

From a collection of the individual surface pressure data points (such as that shown in Figure 5.12), a computer-driven data reduction program plotted contours of constant pressure for each surface of the airfoil (Figure 5.13) and interpolated between the readings of each airfoil tap to calculate chordwise pressure distributions at a number of spanwise stations (Figure 5.14).

The pressure contour plots of Figure 5.13 are quite striking in their demonstration of the departure from quasi-two-dimensional (QTD) flow, especially in the supersonic region adjacent to the shear layer (y = 0 to 0.7 inch). For QTD flow, the contours should be approximately elliptical and without relative maxima and minima in the shear layer. Outside the shear layer, the contours should be verti-

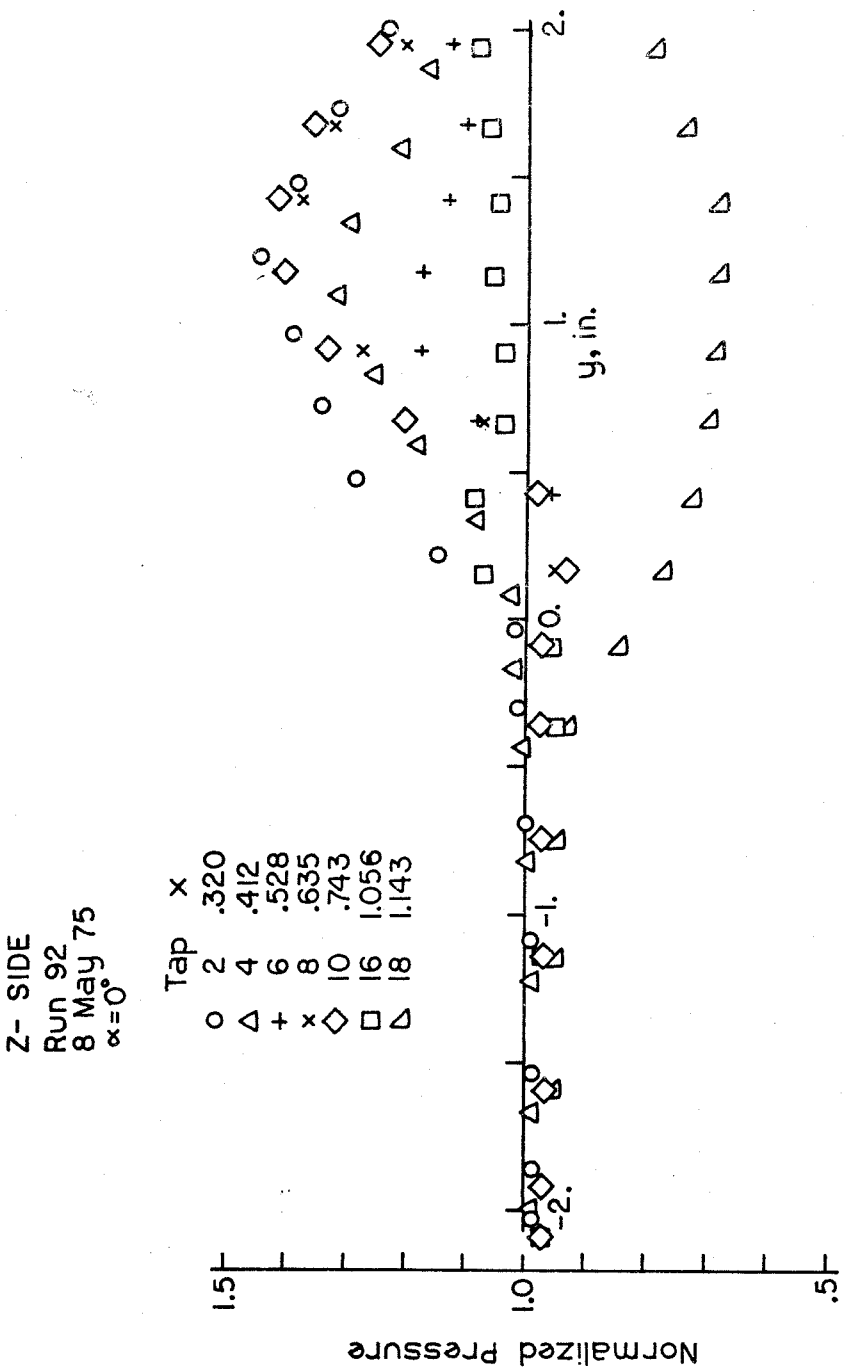

Figure 5.12: Airfoil Surface Pressure Data (Run 92, Zero Angle of Attack, Leading Edge at 5.00 inches; "x" in the figure refers to the distance in inches from the leading edge of the airfoil)

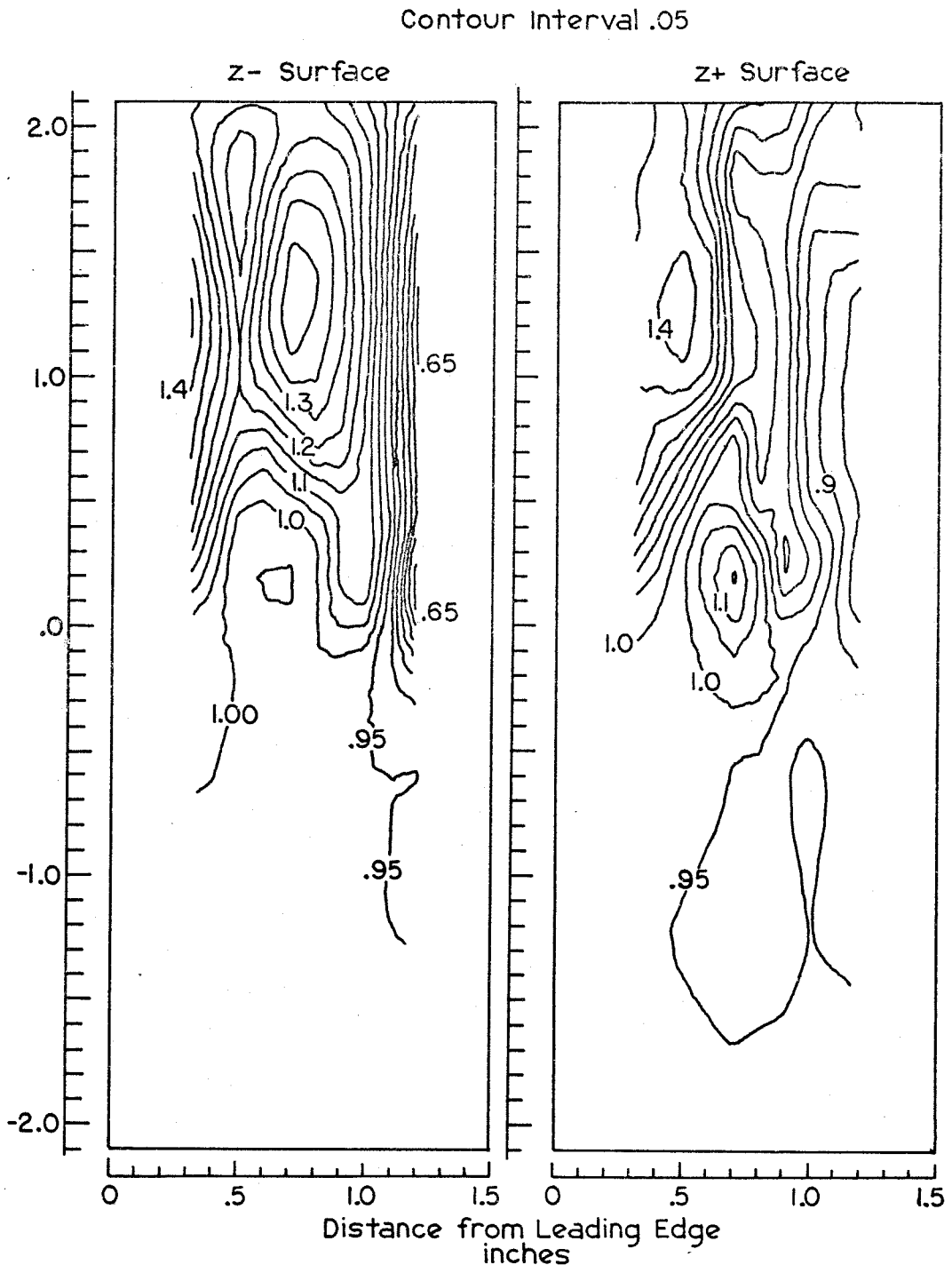

Figure 5.13: Airfoil Surface Pressure Contours (Run 92, Zero Angle of Attack, x_{LE} = 5.00 inches, Based on 133 points on each surface)

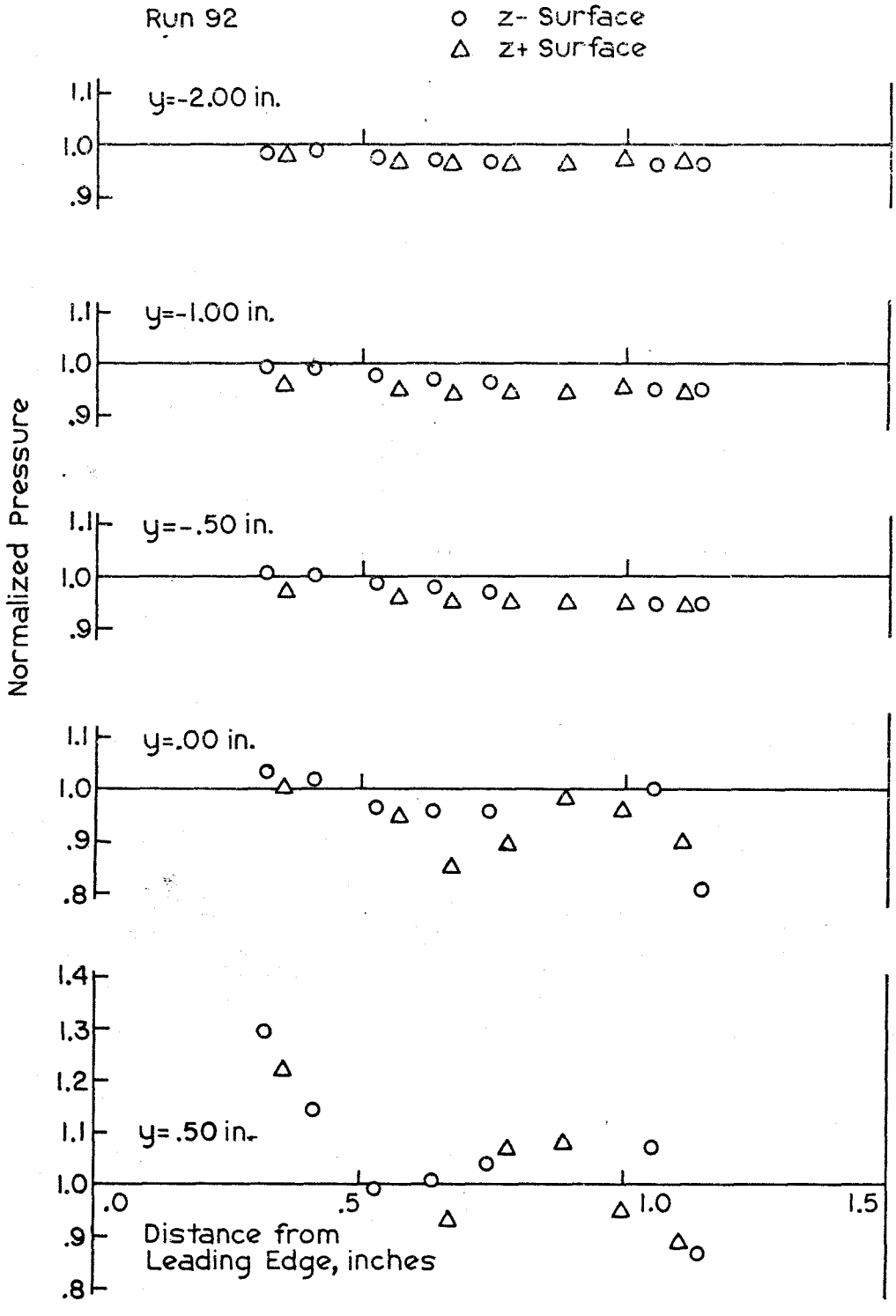

Figure 5.14: Chordwise Surface Pressure Distributions (Run 92, Zero Angle of Attack, x_{LE} = 5.00 inches)

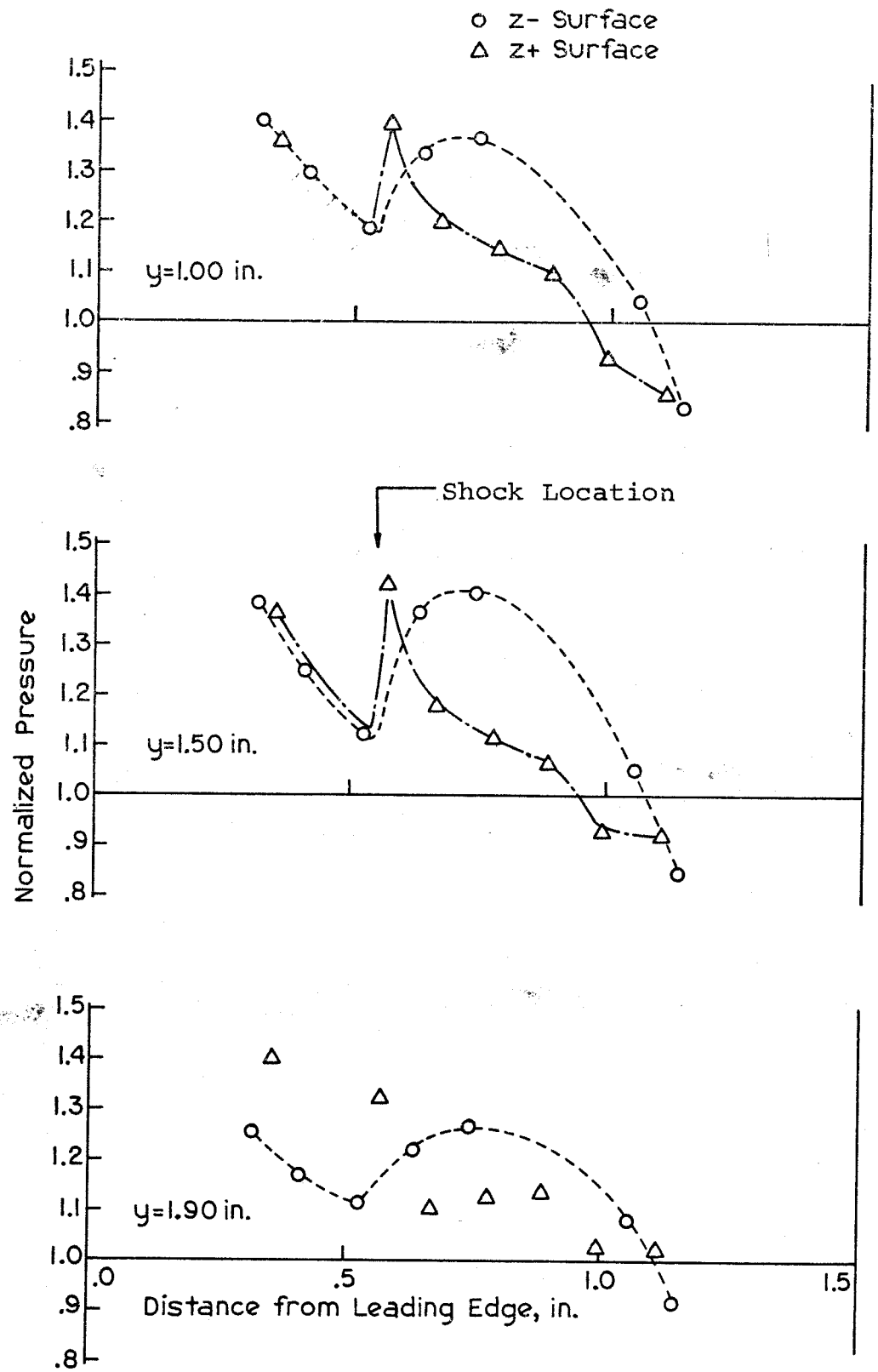

Figure 5.14, cont'd.; Chordwise Surface Pressure Distributions (Run 92, Zero Angle of Attack, x_{LE} = 5.00 inches)

cal. In addition, it is readily noted that substantial pressure fluctuations are confined to the supersonic stream. This is because the dynamic pressure of the supersonic stream is nearly 5.5 times that of the subsonic stream. Unfortunately, this figure also reveals some asymmetry in the airfoil. Because the data of this run were taken at a nominal geometric angle of attack of 0^{o} ($\pm 0.2^{o}$), the isobar plots should be identical for both surfaces. At least they show the same trends.

The chord Reynolds number in the supersonic stream is about 375,000. According to some published data[20], transition to a turbulent boundary layer is not expected at values less than 1,000,000 for a 6 per cent thick biconvex airfoil. Therefore, with a laminar boundary layer, the pressure rise due to a shock incident on the airfoil surface will be dispersed over several boundary-layer thicknesses. The presence of such a dispersed reflection, with a static pressure rise of about 20 per cent, can be seen in the isobar contours (about .55 inch aft of the leading edge within the range of y from 0.5" to 1.5") and more readily in the chordwise pressure distributions of Figure 5.14.

Figure 5.15 presents a construction of the supersonic flow at y = 1.00 inch (center of the supersonic stream) based on pressure data. The flow field behind the leading wave (before it is modified by the shock branch that rebounds to the airfoil) is known. Data from Kim[24] suggest that the sonic line in the region of the detached shock wave reaches the airfoil surface very close to the edge of the blunt section (see Section 5.4.1.2); after that, a Prandtl-Meyer expansion

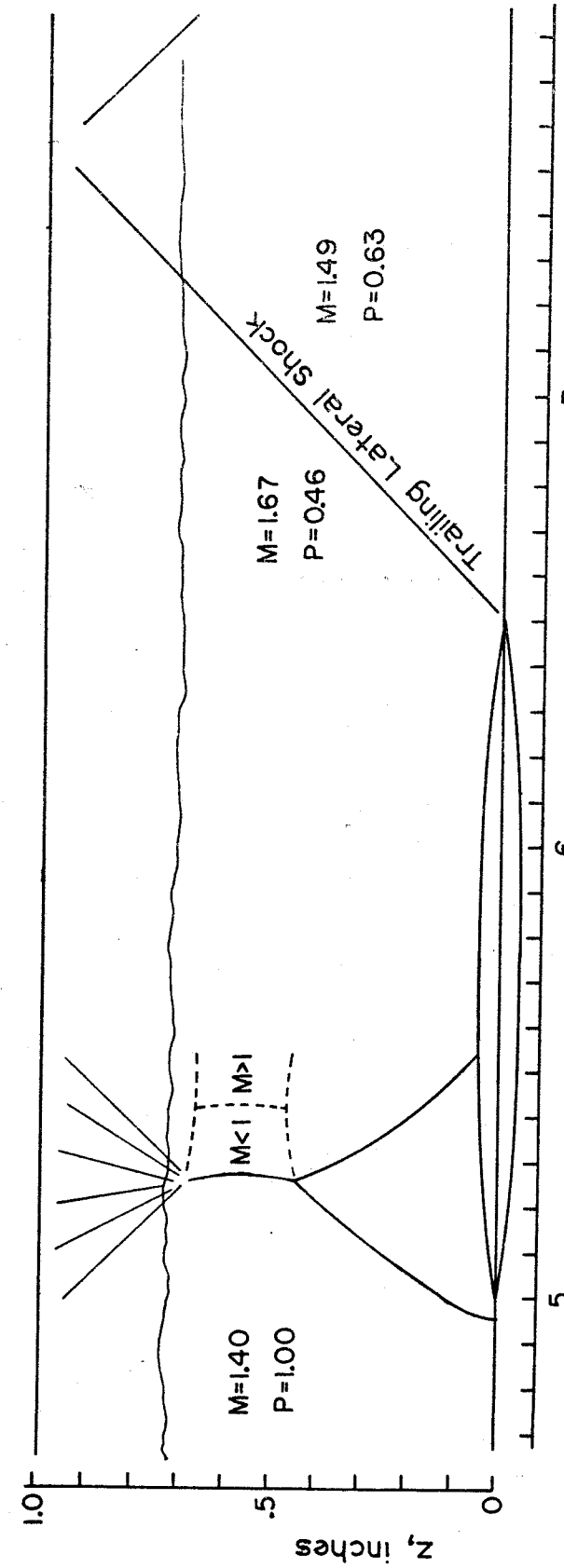

Figure 5.15: Constructed Supersonic Wave Locations, y = 1.00 inch
(Run 92, Zero Angle of Attack)

starting at the sonic point (modified by the reflection of expansion waves off the rear of the initial shock) yields the flow behind the shock. This enables us to trace the airfoil-incident wave back to its intersection with the bow wave.

Knowing that these two waves intersect and that a third wave must continue across the channel from the bifurcation point, the shock polars for Mach 1.4 (the free stream Mach number) and various rebounding waves are plotted together (Figure 5.16) in terms of pressure versus flow deflection angle. An intersection of the polars would indicate a triple point satisfying continuity of angle and pressure across the contact surface behind the shocks. The only such intersections found did not fit the physical reality of the system since they described the case of a stronger shock overtaking and merging with a weaker shock, rather than the case of a bifurcated shock.

A realistic steady solution is therefore possible only if the flow is subsonic somewhere behind the shock, i.e., if the main shock across the passage is nearly normal (as drawn in Figure 5.15). The existence of this normal shock is confirmed by the total pressure measurements of Figure 5.17. This figure compares experimentally-measured total pressures at x = 17.85" in the empty tunnel with those for the airfoil installed with its leading edge at x = 11.50". While the airfoil is at a different position from that in the preceding discussion (where the leading edge was at x = 5.00"), the features of the flow are the same. The probe was offset 0.3 inch from the centerline of the tunnel so that it would be away from the wake of the airfoil. Comparison of the data shows a loss of total pressure in the supersonic

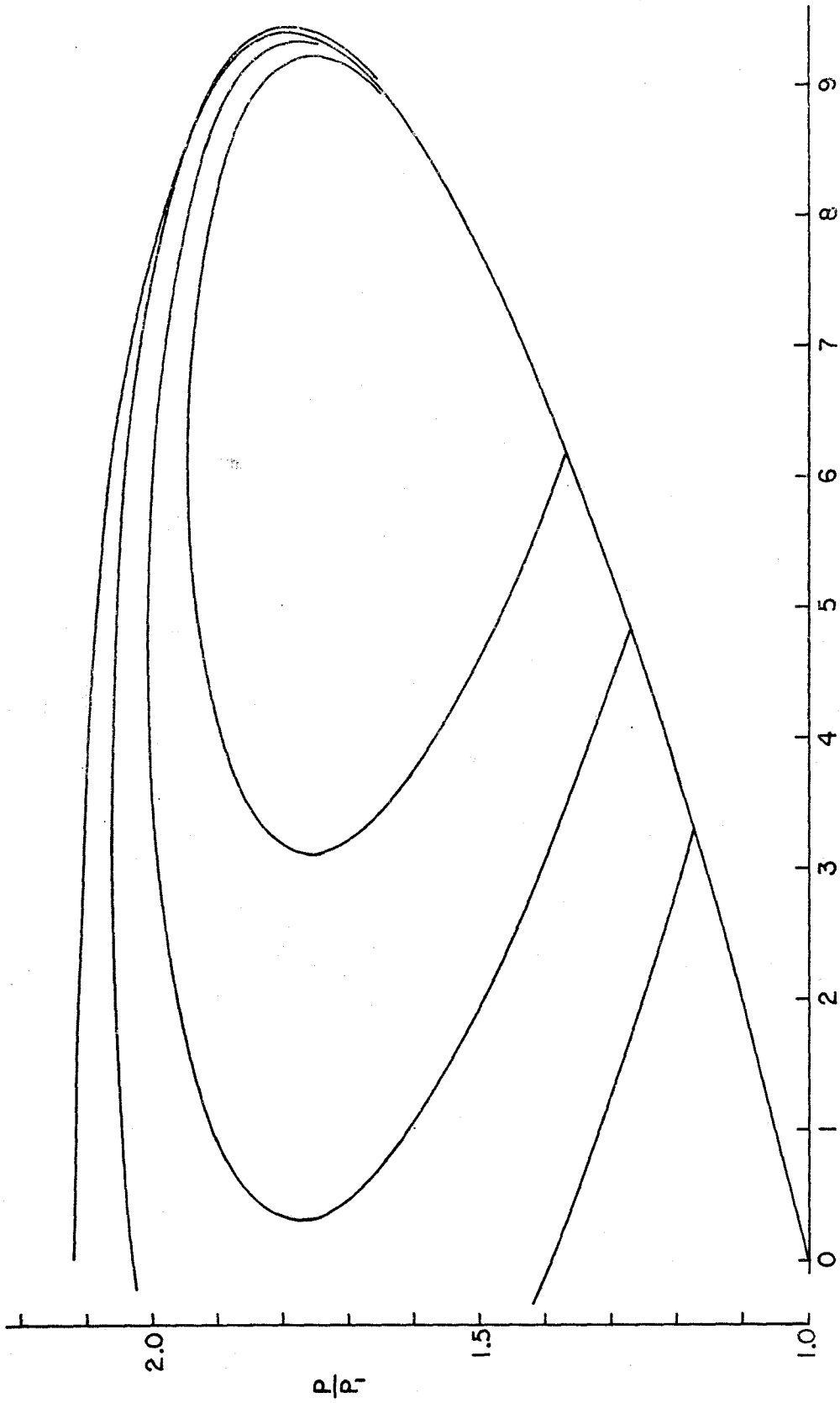

Figure 5.16: Shock Polar Families at Mach 1.40

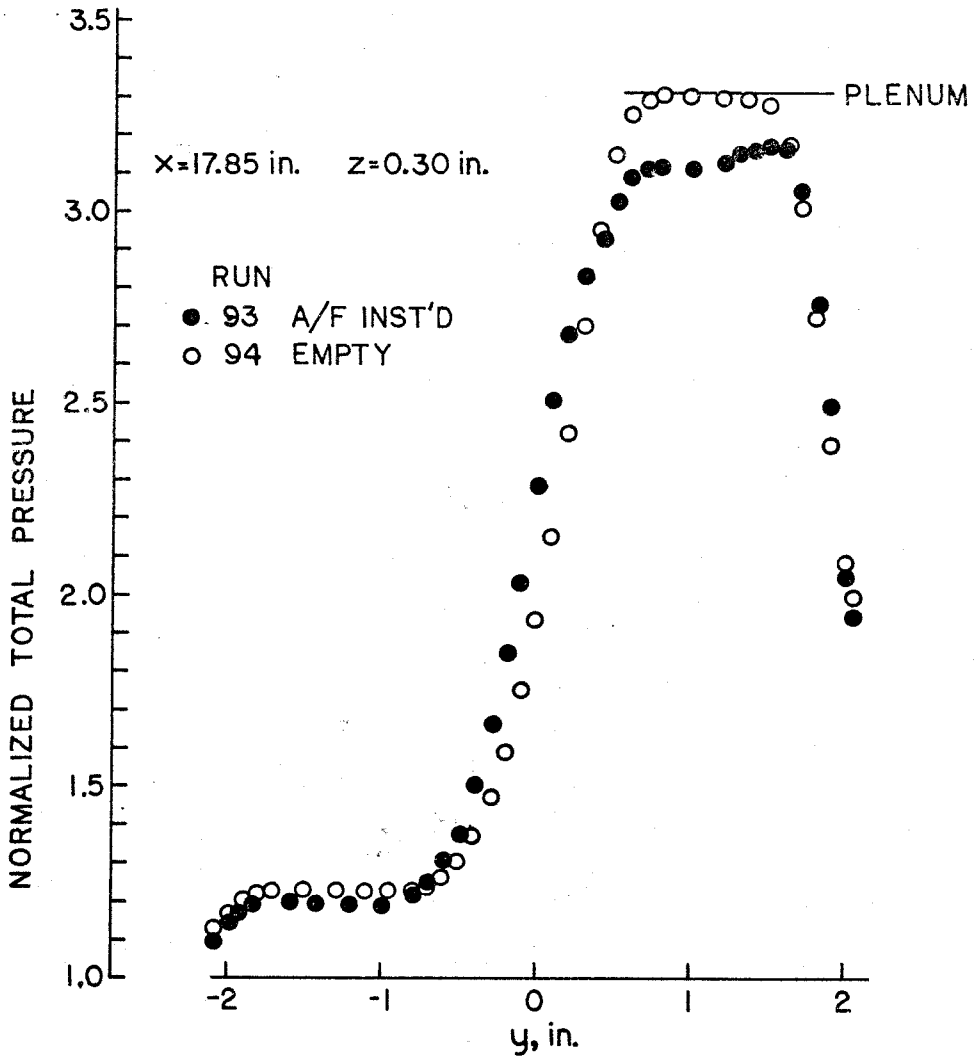

Figure 5.17: Effect of Airfoil on Downstream Total Pressure Distribution (Zero Angle of Attack, x_{LE} = 11.50 inches)

stream of 5 to 6 per cent. Computed data for one-dimensional flow[25] predict a loss of 4.2 per cent for a normal shock. The remainder of the loss presumably is due to several oblique shocks farther downstream (to be discussed in Section 5.4.1.3). Furthermore, note that the loss is confined to the region y = 0.5" to 1.6", which must define in the vertical direction the extent of the normal shock.

If the oblique shock at the leading edge continued without bifurcation or other modification to the plane of the wall, expansion waves from the airfoil surface would reduce its strength to about 5°. This is still above the limit for regular reflection at Mach 1.4 (which is about 4.5°). Thus, the normal shock is a Mach reflection phenomenon, and does not depend on boundary layers for its existence; it is inherent in the inviscid flow. Figure 5.18 illustrates the complexity of an inviscid Mach reflection. It is not believed, either, that this phenomenon is due to the thickness of the airfoil in view of the large amount of flow relief to the supersonic stream provided by the deflection of the sonic surface in the region of maximum thickness (also to be discussed in Section 5.4.1.3). The boundary layers and airfoil thickness govern the extent of the normal leg.

It should be noted that even the idealized Mach reflection model of Figure 5.18 is not completely accurate. In the vicinity of the triple point, the figure depicts the assumption of Guderley and Von Neumann that the shocks may be considered locally planar, i.e., that the shock curvatures are fairly modest, and the shocks therefore fit the Rankine-Hugoniot model of pseudo-one-dimensional flow. However, near this point there are in fact strong gradients of pressure and

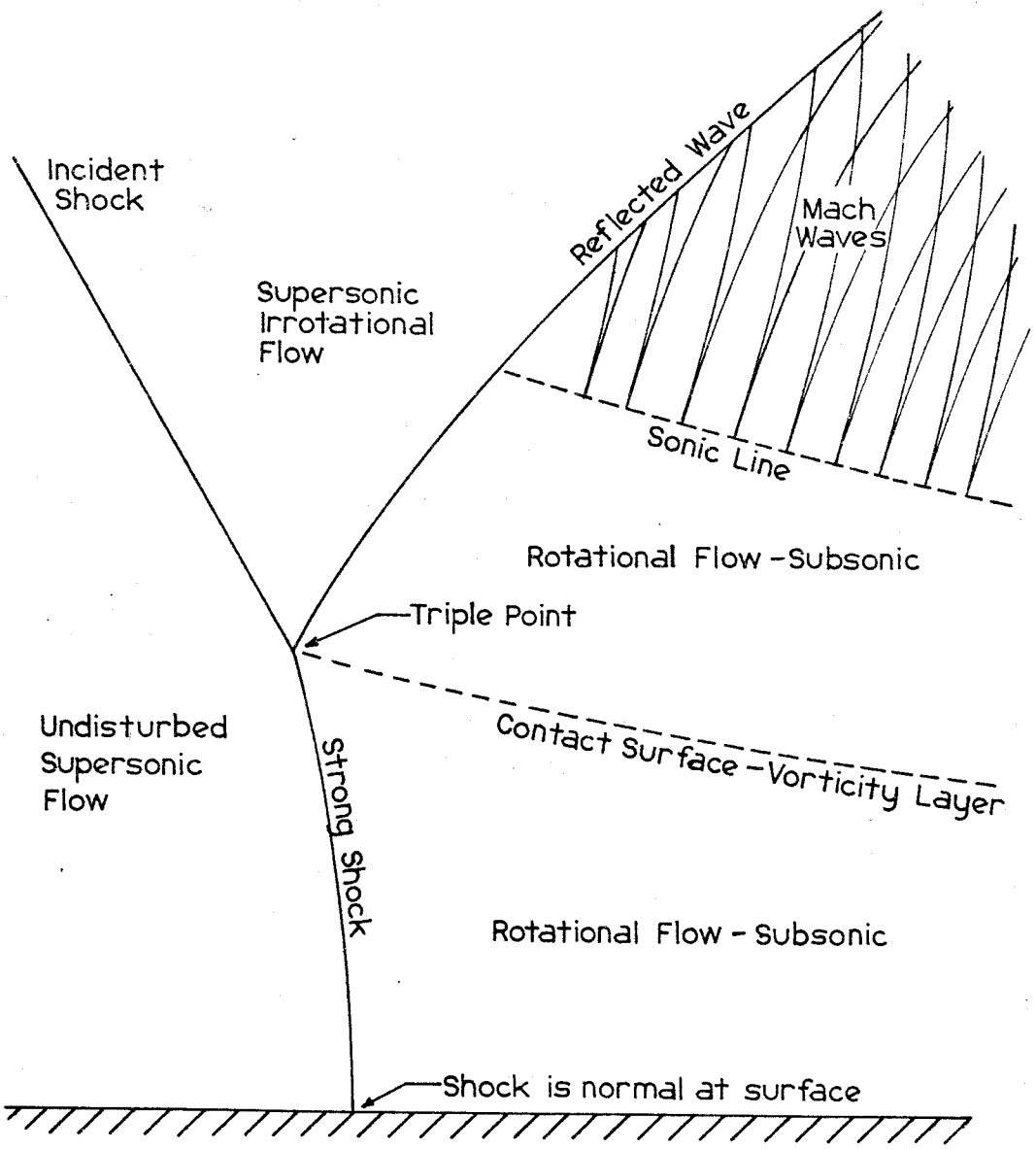

Figure 5.18: Inviscid Mach Reflection

temperature parallel to the shock front as well as normal to it. The triple point actually is a finite zone of continuous transition between the incident and reflected shocks on one side and the strong shock (sometimes referred to as the Mach stem) on the other[26]. This results in a significant modification of the actual flow near the triple point.

Because boundary layers are present, the foot of the shock (near the sidewall) is diffused upstream and downstream of the inviscid impingement point. This is shown in Figure 5.19, which presents isobar contours on the sidewall. A complex interaction between the normal shock and the boundary layer is created,[27] and it is not surprising that the pressure rise due to a normal shock (P = 2.120) is not measured on the wall[28, 29]. The point at which the pressure rise begins ahead of the shock enables us to fit the upstream compression waves shown in Figure 5.15.

As was mentioned previously, from data on the loss of total pressure the vertical extent of the normal shock is inferred to be y = 0.5" to 1.6". For y greater than 1.6", the shock is dispersed by a grazing interaction with the top wall boundary layer and thus the loss of total pressure through the shock is much reduced. At values of y less than 0.5", a similar grazing interaction occurs with the shear layer. These interactions were discussed in connection with the sidewall airfoil (Section 5.3.1).

The flow must quickly re-accelerate to supersonic speeds because the extent of the subsonic region behind the shock cannot be large compared to the thickness of the buffer layer between the wall

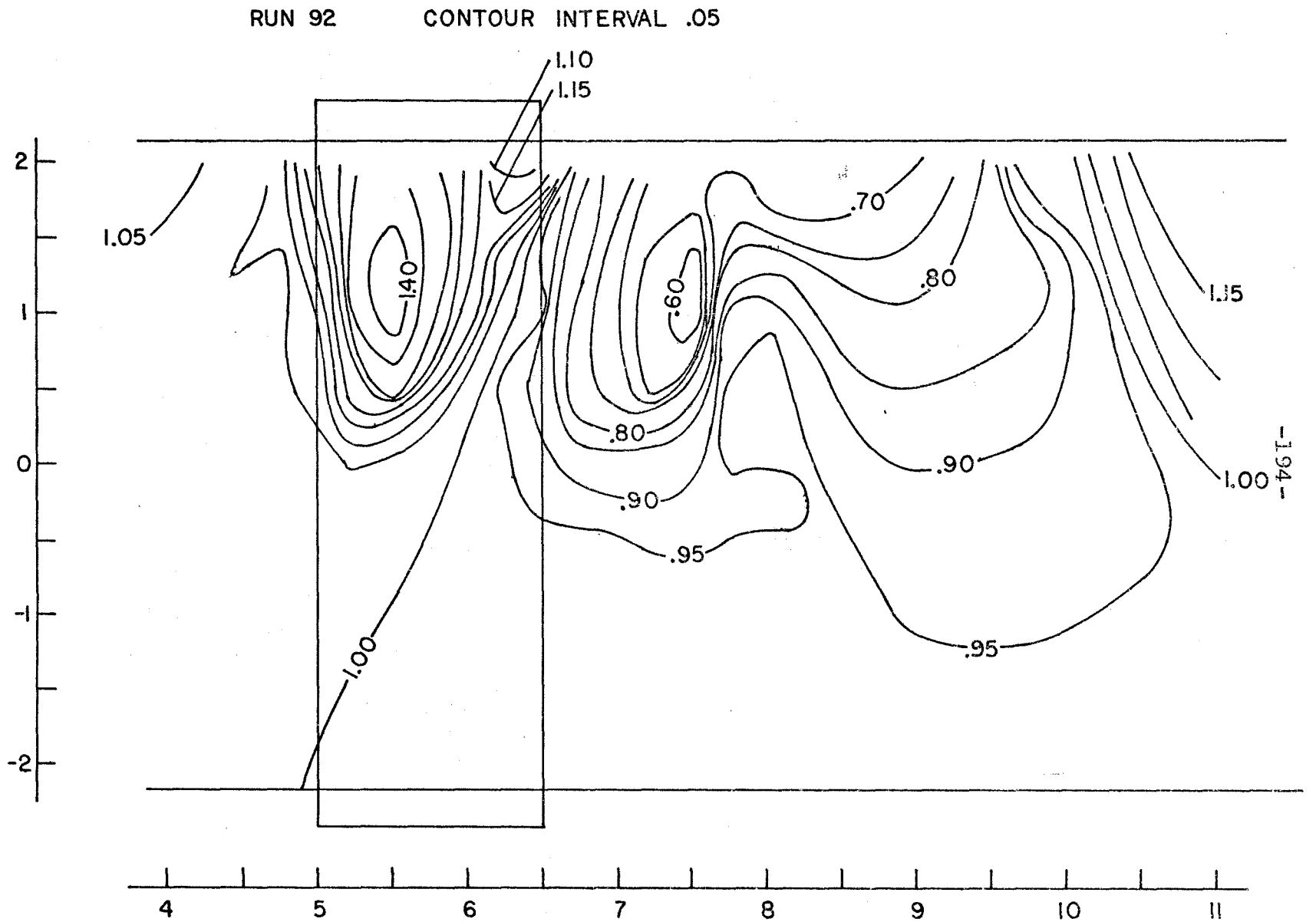

Figure 5.19: Sidewall Pressure Contours (Airfoil position is superimposed)
Run 92, x_{LE} = 5.00 inches

and the edge of the normal shock (see Figure 5.15). Otherwise, the high pressure associated with the subsonic flow would inevitably be transmitted to the wall. Since, for subsonic flow, the pressure must be at least 1.61, Figure 5.19 provides convincing evidence of the rapid re-acceleration. Presumably, the normal shock is slightly concave, so that behind the wave the streamlines are convergent and thus accelerating. It should also be noted that oil flow studies indicated that there are no boundary layer separations on the sidewall related to this shock system. This means the maximum pressure anywhere could not have gone above 1.80 (the normal shock pressure ratio is 2.120) and indicates that there was no high-pressure region near the wall so situated that it was not detected by the static pressure taps.[20,27]

5.4.1.2 The detached shock wave. Discussion of the detached shock wave standing ahead of the airfoil leading edge will proceed in two stages: first, verification of the assumption of a limited region of influence on leading-edge bluntness; and second, consideration of three-dimensionality as it affects the shock standoff distance.

To establish the lateral limit of bluntness influence in the main supersonic stream, a mathematical calculation was made for a blunted wedge of the same semivertex angle as the experimental airfoil (Figure 5.20). The parameters of the problem are δ_o (wedge semivertex angle), h (height of the blunted region), D (shock standoff distance), R (shock radius of curvature along the axis of the wedge), and M (freestream Mach number). The object was to find the lateral distance y' at which the pressure immediately behind the

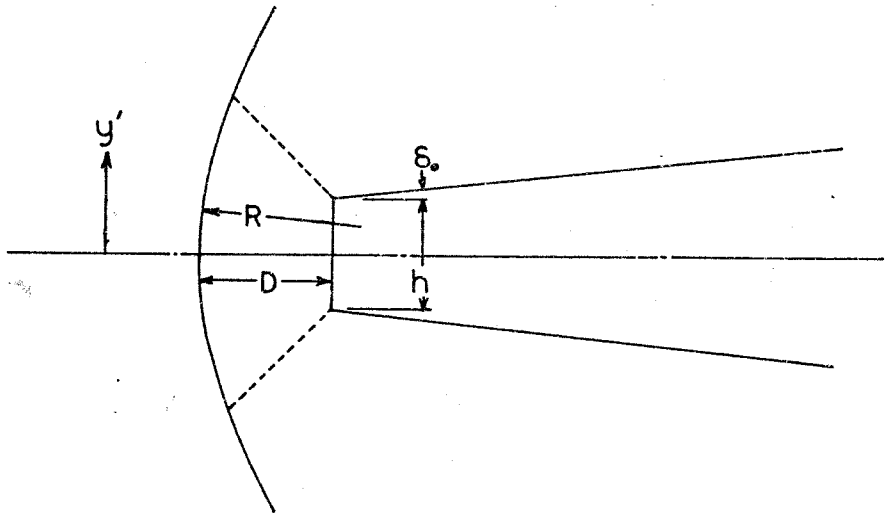

A. Assumed Bluntness Geometry

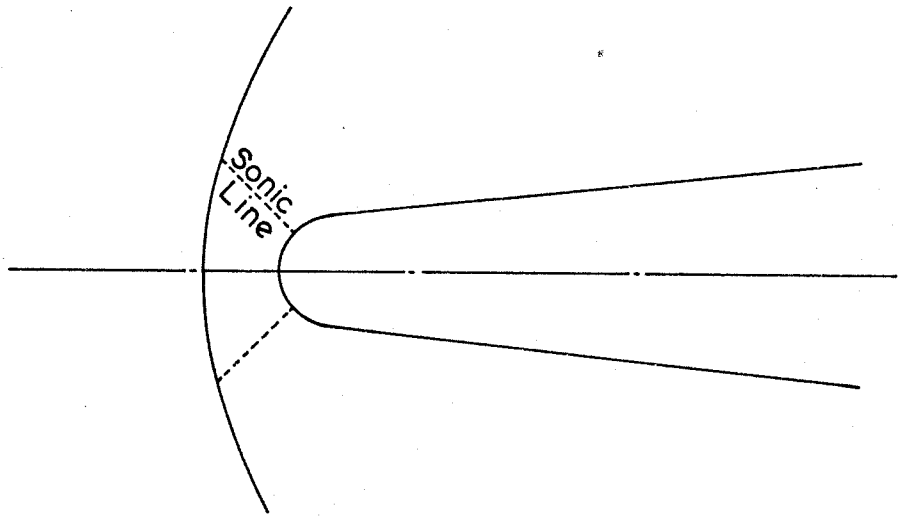

B. Computational Model

Figure 5.20: Leading-Edge Bluntness Models

detached wave is within a specified tolerance of the pressure behind the equivalent attached (i. e., sharp leading edge) wave.

The shock was assumed to be a hyperbola whose asymptotic angle to the freestream is θ_o, the wave angle relative to the stream for an attached shock at Mach number M with deflection angle δ_o. This hyperbola was fitted to the experimental data of Kim[24], matching D and R. The experiments of Kim are for a circular cylinder rather than a wedge. The presence of an afterbody behind the cylinder in the computational model does not affect the shock in the region just ahead of the nose of the model. Influence from the afterbody is only felt downstream of the Mach line starting at the transition point from cylinder to wedge. The flow at this point is known to be at supersonic speed (neglecting the presence of a very thin boundary layer). Experimental results show the angle around the surface of the cylinder from the leading stagnation point to the sonic point is 48.0^o at Mach 4[24] and 48.2^o at Mach 2[30]; while the transition from cylinder to wedge is at $(90^o - \delta_o)$, which for $\delta_o = 6.9^o$ works out to 83.1^o.

At Mach 1.4, Kim shows for a circular cylinder a standoff distance of 3.0h to 5.0h (where h is the cylinder diameter), while Moeckel[31] shows for a blunt rectangular plate D = 3.2h. This indicates that the computational model's assumption of a cylinder will not lead to gross errors compared to the actual situation in which a flat face is presented to the flow.

Using Kim's data, this exercise generated the curve of Figure 5.21 relating the perturbation in normalized pressure behind the

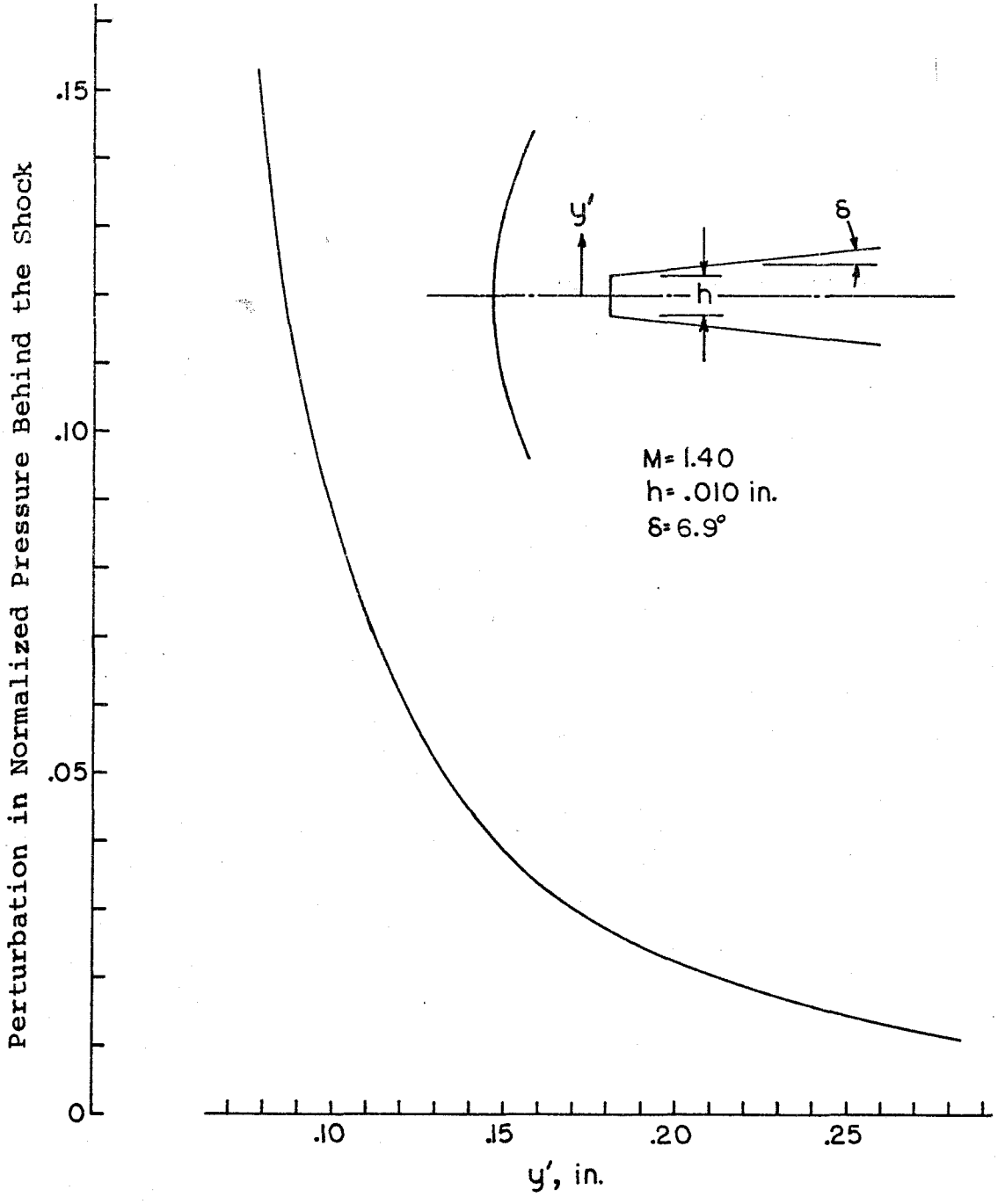

Figure 5.21: Region of Influence of Leading-Edge Bluntness

the shock (detached-shock pressure minus attached-shock pressure divided by pressure upstream) versus lateral distance from the wedge centerline. This shows that for perturbations on the order of a few per cent, the region of influence is confined relatively close to the leading edge. In examining the figure, it should be recalled that the sidewall is at $y' = 0.988$ inch.

Defining a small parameter ϵ such that

$$\epsilon = \frac{\Delta(\tan\theta)}{\tan\theta_o} \quad , \tag{5.1}$$

where $\Delta(\tan\theta)$ is the difference in wave slope between the detached and attached cases, the calculation yields

$$y' = \frac{R\cot\theta_o}{\sqrt{2\epsilon}} \quad . \tag{5.2}$$

Recourse to the standard oblique shock relations, with $(\ )'$ and $(\ )''$ respectively indicating quantities upstream and downstream of the wave at a given y, gives

$$\frac{\Delta p''}{p''} = \frac{4\gamma M^2 \sin\theta_o \cos\theta_o}{2\gamma M^2 \sin\theta_o - (\gamma - 1)}\ \Delta\theta \tag{5.3}$$

accurate to first order. Since

$$\Delta\theta = \epsilon \cos^2\theta_o \tag{5.4}$$

and the attached-shock pressure ratio (p''/p') is a known function of M and δ_o, the normalized pressure perturbation $(\Delta p''/p')$ is a known function of y, presented in Figure 5.21. In making this calculation, a value of $R = 8.0\,h\ (\pm 1.0\,h)$ has been estimated from Kim's figure 10.

The translation upstream of the asymptotic detached shock from the attached shock location can also be found:

$$\Delta = D + R\cot^2\theta_o - \frac{h}{2\tan\delta_o} \qquad (5.5)$$

which, for the case under consideration, is 0.034 inch, assuming h = 0.010 inch.

An illustration of the observed detached shock ahead of the airfoil is provided in Figure 5.22. This figure is based on a spark shadowgraph study during Run 99 and can be regarded as an instantaneous measure of shock location. The basic form of the shock remains the same in all observations, but pictures taken during the same run occasionally show variations in standoff distance, indicating that the shock is oscillating. A similar conclusion is reached by noting that schlieren photographs, taken with an exposure time of 1.25 second, sometimes show the detached shock as perfectly sharp and sometimes as blurred. The source of this apparently random transition between steady and oscillating behavior is not understood.

The variations in standoff distance are not due to small variations in installed airfoil angle of attack between runs. While all runs presently under discussion were performed at a nominal angle of attack of 0^o, schlieren photography of a run at a 2^o nominal angle of attack revealed a steady shock at a location agreeing well with the 0^o data (the installation error is estimated at 0.2^o).

The shock is approximately two-dimensional from y = 0.30" to y = 1.27" with a standoff distance of .035" to .040". This agrees well with the prediction of Kim using the formula

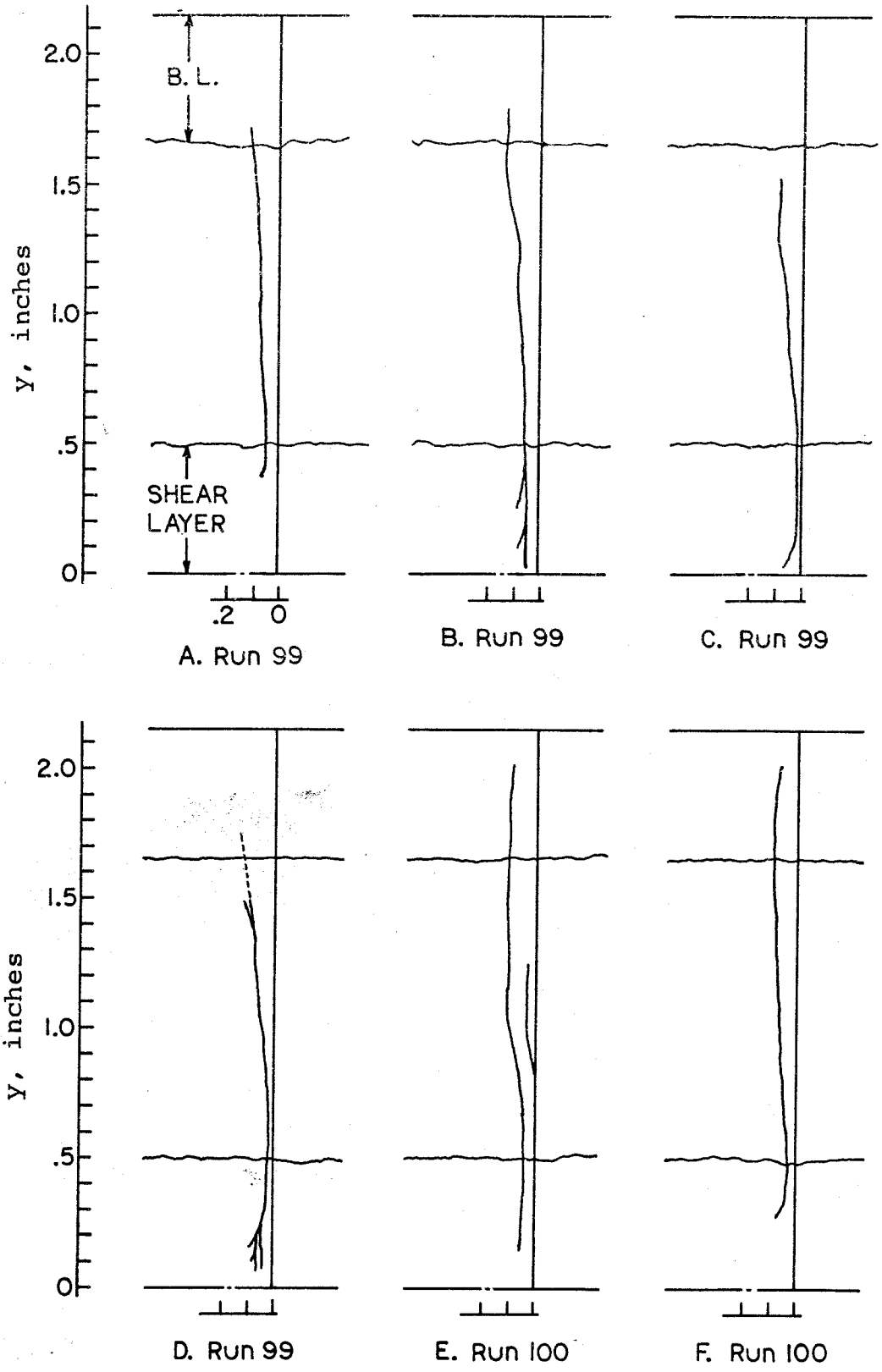

Figure 5.22: Illustration of Detached Shock Location (sketches D and F are most typical)

$$D = \frac{h}{M_\infty - 1}(2.729 - .5M_\infty) \qquad 1 < M_\infty < 2 \qquad (5.6)$$

modified from fig. 6 of his paper with a bluntness height of .010 inch. At values of y less than .30 inch, the shock shows apparent warpage and unsteadiness. This cutoff value of y is about 5 - 10 per cent of the shear layer thickness inside the layer from the supersonic edge. In this region, the mean standoff distance is somewhat larger as well -- .07 to .08 inch. No shock wave is visible for y less than .07 inch.

For y from 1.27 to 1.81 inch, the standoff distance D steadily increases to about .12 inch in a near-linear manner. In the region of y from 1.81 to 2.05 inches, the wave becomes dispersed in an interaction with the wall boundary layer, and no wave is visible from 2.05 inches to the wall (y = 2.15 inch).

Alperin[32] determined that at Mach numbers from 1.3 to 2.0 the detached wave ahead of a model is two-dimensional if the station of interest is at least 30h removed from contaminating influences such as tunnel boundary layers, the end of the model, etc. Since h = .010", this suggests a spanwise equilibrium distance of about .30 inch. The boundary layer on the supersonic wall is about .40 inch in this region, implying that the detached wave should not be two-dimensional for y greater than 1.45 inch, approximately. This agrees roughly with the present work. The shock is dispersed by developing a lambda foot near the boundary area, as would be expected. Interestingly, only a very slight flow separation occurred on the wall at the base of the shock. This separation was only .040

inch (estimated from oil flow patterns) in extent, indicating that the wave had undergone considerable attenuation and dispersion.

The modification of the shock within the shear layer is more interesting. No variation of the shock geometry is noticed until the edge of the shear layer; certainly, no relaxation on the order of 30 h. This is assumed to be because the spanwise variations of flow properties are an order of magnitude less in the shear layer than they were in the boundary layer.

In a quasi-two-dimensional (QTD) calculation, the shock standoff distance would be infinite at the sonic line, decreasing to .035 to .040 inch at the supersonic edge of the shear layer and remaining constant at that distance across the main supersonic stream. Of course, in fairing together these QTD surfaces in the spanwise direction, a composite detached shock is formed with large inclination angles in the spanwise direction on the extended centerline of the airfoil.

Where this three-dimensional curvature introduces inclinations greater than the local Mach angle, no steady shock can exist. A rough calculation indicates that this occurs for y less than 0.2 inch, where the freestream Mach number is about 1.16. The unsteadiness noted for y less than 0.3 inch therefore is not surprising; it is due to this and to excitation from the turbulent shear layer. Above this cutoff level, the observed shock standoff distance compares well to QTD predictions, though the shock consistently remains about .010 inch closer to the body within the shear layer region than expected. This seems due to the three-dimensional relief afforded by the shear region through the subsonic flow behind the

shock. The high pressures between the shock and the blunted leading edge are relieved by spanwise flow down into the lower-pressure portions of the layer, and into the subsonic stream.

Even though the basic outline of the shock agrees with QTD predictions in the upper reaches of the shear layer, the three-dimensional curvature considerably reduces the strength of the shock (nowhere in the shear layer is the shock normal), creating lower peak pressures and losses than expected through QTD theory.

5.4.1.3 The three-dimensional flow field. It often develops in transonic flow problems, even those that are nominally two-dimensional, that significant three-dimensional variations are present with time-unsteadiness[33, 34]. In addition, such flows are known to be highly sensitive to the freestream conditions and the state of the boundary layer on all surfaces, particularly where a shock wave is incident[20, 35-37]. The viscous interactions are not localized, but rather have a significant effect on major portions of the flow field, especially where flow separations are present. Presumably, therefore, the extent of viscous three-dimensional effects in the present study can be correlated with the magnitude of viscous-dominated regions such as boundary layers and wakes, and with the presence or absence of regions of separated flow.

Even neglecting viscosity, strong three-dimensional flow modifications are known to occur when an airfoil is attacked by a flow whose velocity varies in the spanwise direction across the transonic regime. The original impetus for studying this problem is in the analysis of transonic axial-flow compressors. These machines are

generally designed by a quasi-two-dimensional (QTD) theory which locally neglects spanwise effects in calculating the flow at a specific radial blade station. The occurrence of substantial spanwise effects, especially in the distortion of stream surfaces, has been known ever since the development of transonic compressors began. Analytic work in this field has been performed by McCune and his associates for a rotating blade system[4-7], and by Namba for a blade spanning two infinite walls with transonic shear in between[38, 39], a rotating system[40], and for a subsonic cascade[41]. Earlier calculations for a thin wing in shear flow were performed by Honda[42, 43]. The weakness of all these analytic calculations is that they are based on a linearization of the governing equations. Consequently, displacements of the stream surfaces are not represented. As will be shown, these displacements in the spanwise direction are substantial and strongly influence the overall flow field.

An analytical and experimental study of an airfoil in incompressible shear flow was performed by Kotansky[44], who also found strong inviscid three-dimensional effects. Useful summaries of knowledge in secondary flows[45] and shear flows[46, 47] are presented by W. R. Hawthorne. Reference to these works will be made throughout the following discussion. In addition, finite-difference calculations are currently being performed at the Massachusetts Institute of Technology which are not subject to the objections raised toward the linearized analytical results. Some results of these studies have been published[48].

The following discussion concerns inviscid main-stream flow

modifications. These effects on the flow would be essentially the same if boundary layers were not present: their existence is not a viscous phenomenon. Only a brief mention will be made of the effects of viscosity, for two reasons: study of inviscid flow modification was the primary goal of this study; and inviscid processes caused much larger perturbations to the flow than did viscous-induced effects.

The flow field within the airfoil passage (the region between the airfoil and the tunnel sidewall) is completely dominated by a strong interaction within the shear layer between the supersonic and subsonic streams. In the introduction to Section 5.4.1 it was pointed out that these interactions have two basic sources: the qualitative difference in the two-dimensional flow pressure distribution on the surface of identical airfoils in supersonic and subsonic flow, and the large differences in total pressure and dynamic pressure which affect the magnitude of the surface pressure distribution (the dynamic pressure effect in essence was that which Kotansky studied). Both of these effects, by introducing large gradients in the inviscid pressure distribution, set up significant three-dimensional flows near the shear layer. These flows are not confined to the boundary layer, though naturally they are quite noticeable there. The large pressure gradients in the inviscid flow induce appreciable streamline curvature in the spanwise direction.

Because the flow at speeds slightly greater than sonic will transmit disturbances laterally with minimal variations in amplitude, the three-dimensional perturbations are expected to be most severe at the slightly supersonic stations. This expectation is borne out by the

analytical work[5, 38-40]. Perturbations in the pressure are smoothed out away from the sonic surface in either direction along the span of the airfoil, though this is much more pronounced on the subsonic side. Distinct compression and expansion waves move up the blade on the supersonic sections[38-40].

Perhaps the most important single parameter is the local displacement of the sonic surface from its unperturbed location. It is this displacement that shows the breakdown of QTD theory (by revealing spanwise displacement of stream surfaces in general) and dominates the creation of spanwise effects.

Four methods are available in deducing the location of the sonic surface and/or its local inclination. The most reliable is from spark shadowgraph photographs of the shear layer. A fine grainy structure is visible within the shear layer. Presumably this is from turbulent eddies created by the mixing process. There is generally a distinct line, assumed to be the edge of the shear layer in the subsonic stream, below which these eddies lose their definition and the flow appears homogeneous. Thus, perturbations of this line represent perturbations of the shear layer as a whole and particularly the sonic line.

Another useful method, available only a considerable distance downstream of the airfoil, is to survey the shear layer with a pitot probe.

A third method, which is considered less precise than the first two but is useful within the airfoil passage, is based on wall static pressure measurements. These data can be used to infer changes in sonic line as follows. By reading at a given x the static pressure on

the wall and the airfoil (if the x in question lies in the airfoil passage) a mean value of the static pressure as a function of y, averaged over z (the lateral direction) can be estimated for the subsonic stream. (Use of the subsonic stream is to be preferred because pressure gradients are considerably reduced and of more regular behavior. Thus, estimation of a mean pressure is far more reasonable than it would be in the supersonic stream.)

Within the subsonic stream, the main portion of the flow is isentropic and perturbations in static pressure can be related to perturbations in flow area. By separating the subsonic stream into a number of lamina to be treated separately, a composite area change can be calculated and can be simply related to the deflection of the sonic line. The results of this estimation procedure are presented in Figure 5.23, along with those of the shadowgraph method, which seem in general agreement. This procedure only yields a mean value of the sonic surface displacement; deflections are greater near the airfoil and less near the sidewalls. The entire pattern of sonic surface displacements when viewed from above resembles the Kelvin ship wave pattern for deflections of a surface of water over which a ship is passing. The displacements generally travel at an oblique angle behind the source with diminishing amplitude as distance from the source increases.

The fourth method available is that of using oil flow patterns on the various surfaces to suggest surface streamlines. Unfortunately, these oil flow lines respond not only to the shear stress vector (parallel to the velocity vector) as desired, but also to the pressure-

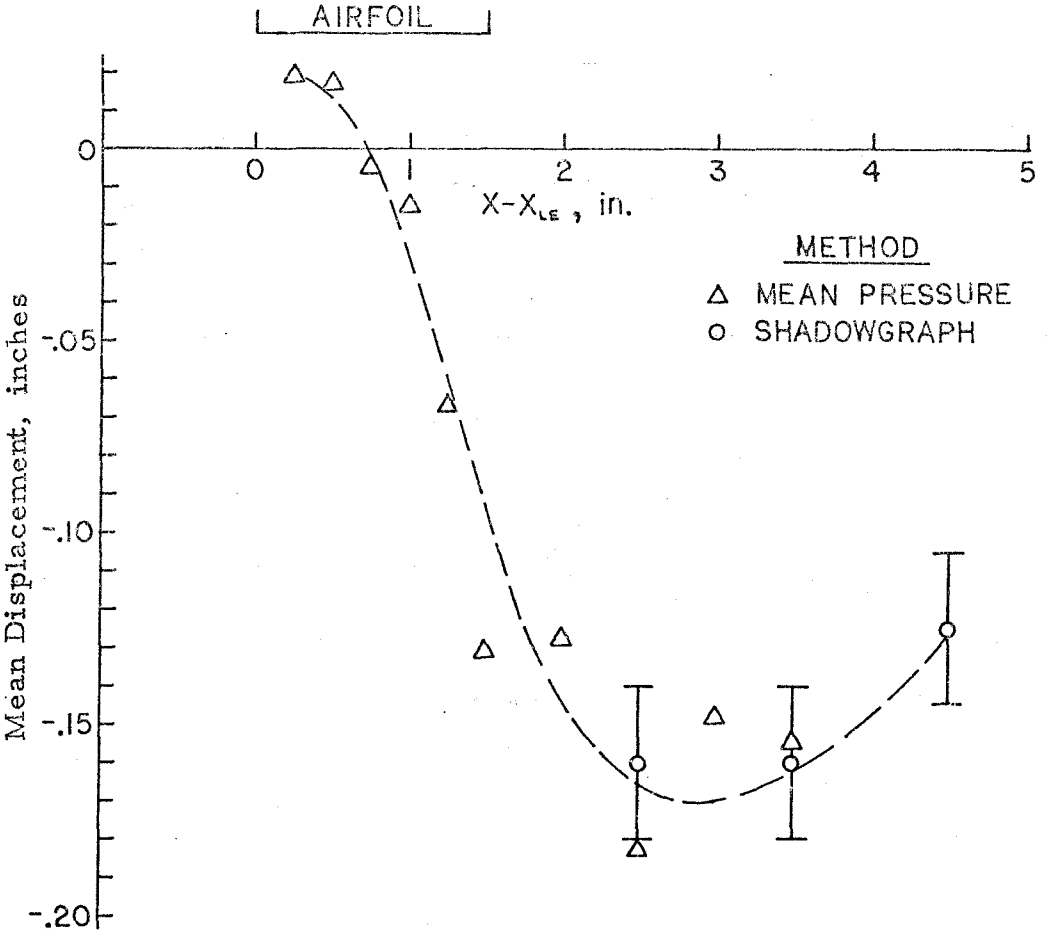

Figure 5.23: Calculated Sonic Line Displacement

gradient vector (i.e., the velocity-acceleration vector) and to a lesser extent the gravity vector. The oil flow lines show extensive curvature, as is seen in the sketch of Figure 5.24. The large curvatures show the presence of large pressure gradients normal to the velocity vector, which means that the oil cannot be assumed to follow closely the streamlines. The actual streamlines probably follow trajectories with somewhat less curvature than illustrated in the figure, where deflections on the order of 1/2 inch were noted.

All in all, Figure 5.23, based on shadowgraph and mean static pressure, seems reasonable for establishing in general terms the response of the sonic surface. No attempt should be made, however, to draw quantitative conclusions from this figure.

The leading-edge shock system is essentially two-dimensional away from the shear and boundary layers. This system has already been discussed. Deep within the supersonic stream and ahead of the Mach conoid centered at the leading edge/sonic surface intersection, the flow must also be two-dimensional, except as modified by shock/boundary layer interactions whose mechanism is independent of the presence of the inviscid subsonic layer. Behind the normal shock there is a thin subsonic region (see Figure 5.15) where the presence of the shear layer can be felt. This region is of the order of 1/4-inch thick, so the presence of the shear layer provides pressure relief about 1/2 inch (i.e., two thicknesses of the subsonic region) from itself. This condition is partly responsible for the disappearance of the normal shock near the shear layer, as has been noted. The required pressure ratio for the existence of a normal shock is

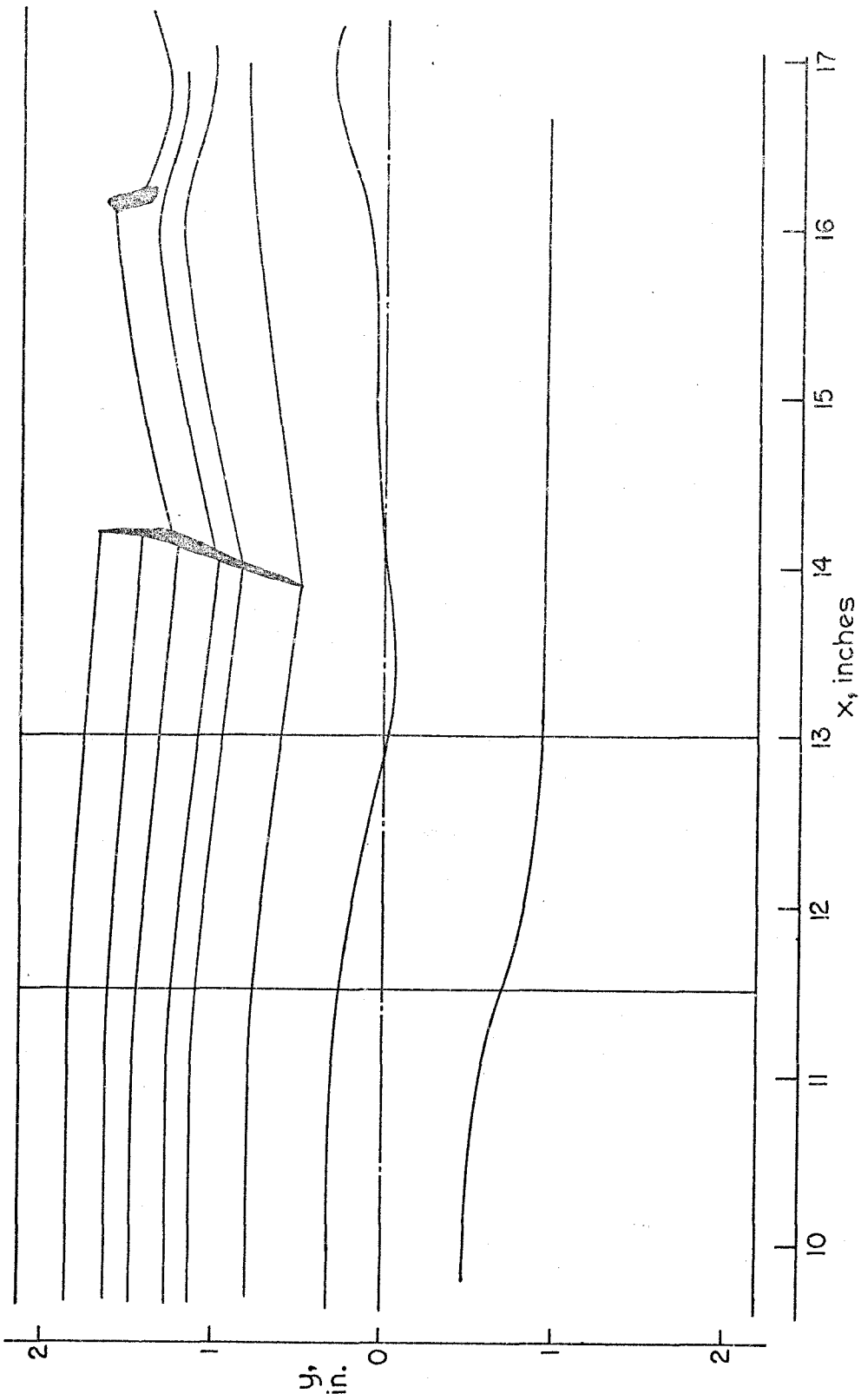

Figure 5.24: Sidewall Oil Flow Streamlines (Free Airfoil)

relieved and the shock cannot exist. This induces a strong downward flow in the mainstream near the interface about 0.7 inch downstream of the leading edge.

Ahead of this initial downward deflection, we see in Figure 5.23 that there is a slight upward deflection of the mean sonic surface. The subsonic stream is at elevated pressure throughout the region near the leading edge, while the supersonic stream is at increased pressure only at points behind the leading oblique wave. There exist regions near the leading edge, upstream of the initial shock, where the pressure is higher in the subsonic stream than in the supersonic stream, and hence the sonic surface is deflected upward. The deflection is quite small, as both the spatial extent (less than 1/2 inch) and the maximum possible pressure difference (about 0.20 in normalized pressure) in this upward-forcing pressure gradient are considerably smaller than those disturbances immediately following which favor a deflection of the sonic surface into the subsonic stream. The downward deflection, in response to the pressure gradient through the shear layer, begins immediately behind the leading shock wave.

The extent of the region in which the subsonic stream is at higher pressure than the supersonic stream determines the inviscid modification of the supersonic flow ahead of the leading edge. It was shown in Section 5.3.1 that ahead of the leading edge the subsonic stream pressure conforms reasonably well to that predicted by uniform-flow potential theory. It is known that no substantial upstream interaction is occurring for the case under study; if such an interaction were present, then potential theory represents an upper

bound to the subsonic stream pressure (since the interaction acts to relieve the subsonic stream overpressure).

Figure 5.25 presents first-order calculations of potential flow about the 6 per cent-thick biconvex airfoil at various values of M_2, showing that the upstream propagation of disturbances is enhanced by increasing M_2. It should be noted that the thickness distribution of this uncambered airfoil is symmetric about the mid-chord line. In subsonic potential flow, therefore, the pressure distribution must also be symmetric about this point. The figure presents data in terms of $|x-x_{\mathfrak{C}}|$, the distance upstream or downstream of the centerline (i. e., the mid-chord point) of the airfoil. The leading and trailing edges are 0.75 inch from this point.

Decreasing M_1 would also magnify upstream supersonic effects since perturbations to the supersonic flow originating in the subsonic stream ahead of the leading edge would move across the flow at a more nearly normal angle, thus staying ahead of the airfoil much deeper into the supersonic flow.

These changes to both M_1 and M_2 affect the choking margin of the flow. The processes just described do not depend on choking but rather on the nature of waves in subsonic and supersonic flow. However, choking effects will play an increasing role as M_1 and M_2 approach unity, or in general as the unperturbed choking margin is decreased.

Also, of course, the choking condition is approached as the thickness of the airfoil, t, or the stream blockage ratio, t/b, is increased. There will be some value of t/b slightly larger than the

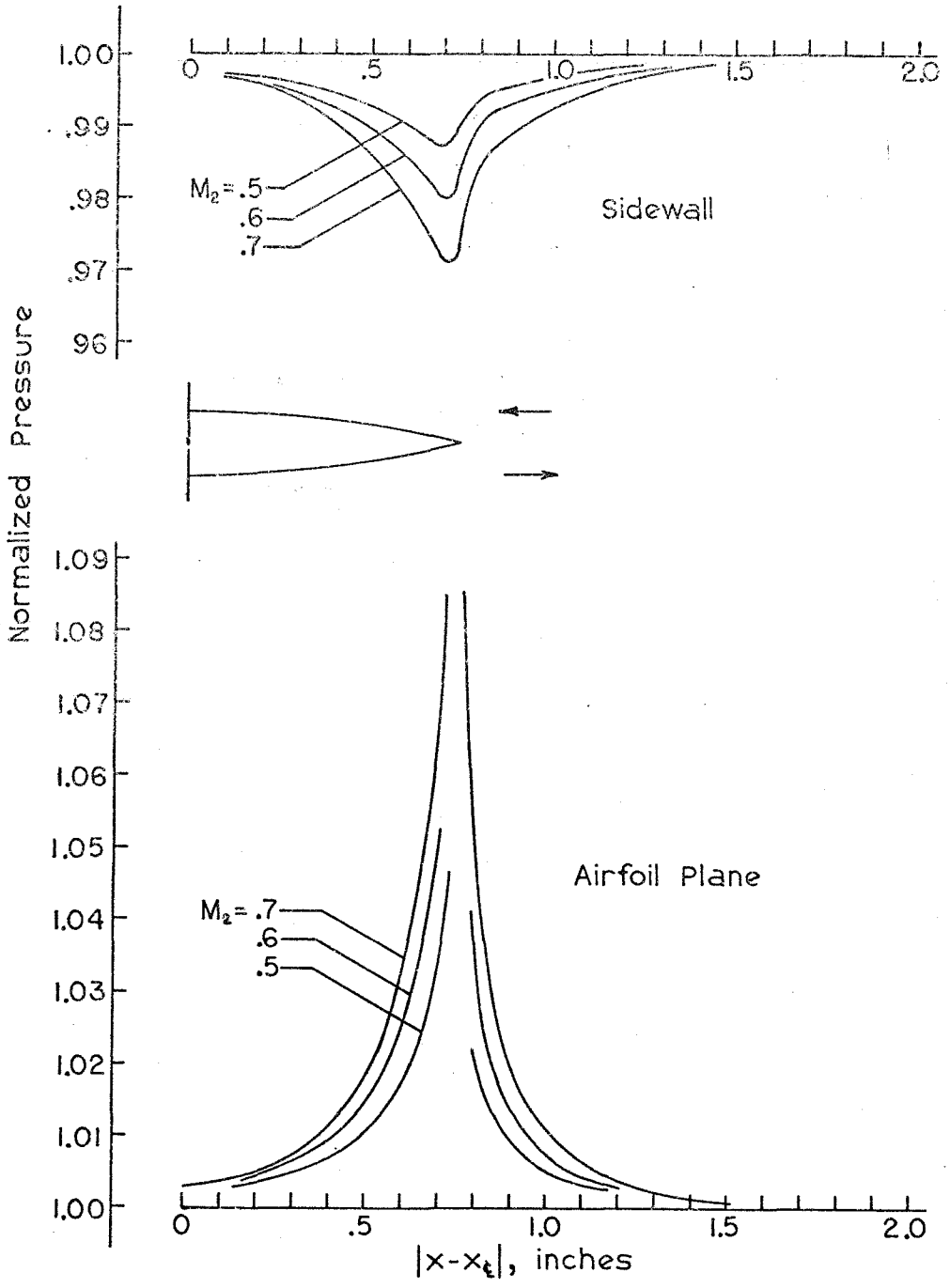

Figure 5.25: Effect of Subsonic Mach Number--6 per cent Thick Biconvex Airfoil (Linearized Computation)

unperturbed choking margin at which the minimum flow area will be inadequate. Then the region of upstream influence will naturally be unbounded except for the upstream confinement of the wind tunnel nozzles and the flow will be choked.

It has been seen that the initial downward deflection of the interface is due to the presence of regions of high pressure behind the normal shock. Relief of this pressure is caused by the deflection of the sonic line into the subsonic stream near the foot of the normal shock. This causes a series of expansion waves to be passed into the supersonic stream from the shear layer, as is illustrated in Figure 5.26.

From Figure 5.23, we see that the sonic surface takes a sharp deflection downward of about .13 inch or $.06\,h_2$ over the final third of the airfoil chord. There is no sudden drop of static pressure in the subsonic stream at the 0.7c to 0.8c location, which would reflect a sudden decrease of the net flow area (see Figure 5.14, y = -2" and -1"). Instead, the subsonic flow area changes at a relatively constant rate throughout the airfoil passage. The deflection of the sonic surface over the final one-third chord is caused by the rapid decrease in the thickness of the airfoil from 4.5 per cent local blockage to zero local blockage. To maintain the same net subsonic flow area, the sonic surface therefore would have to deflect into the subsonic stream about $0.045\,h_2$ (0.097 inch). The remainder of the deflection is due to the constant rate of reduction of the net flow area. Once the trailing edge is passed, the sonic surface remains at approximately the same position, displaced downward about

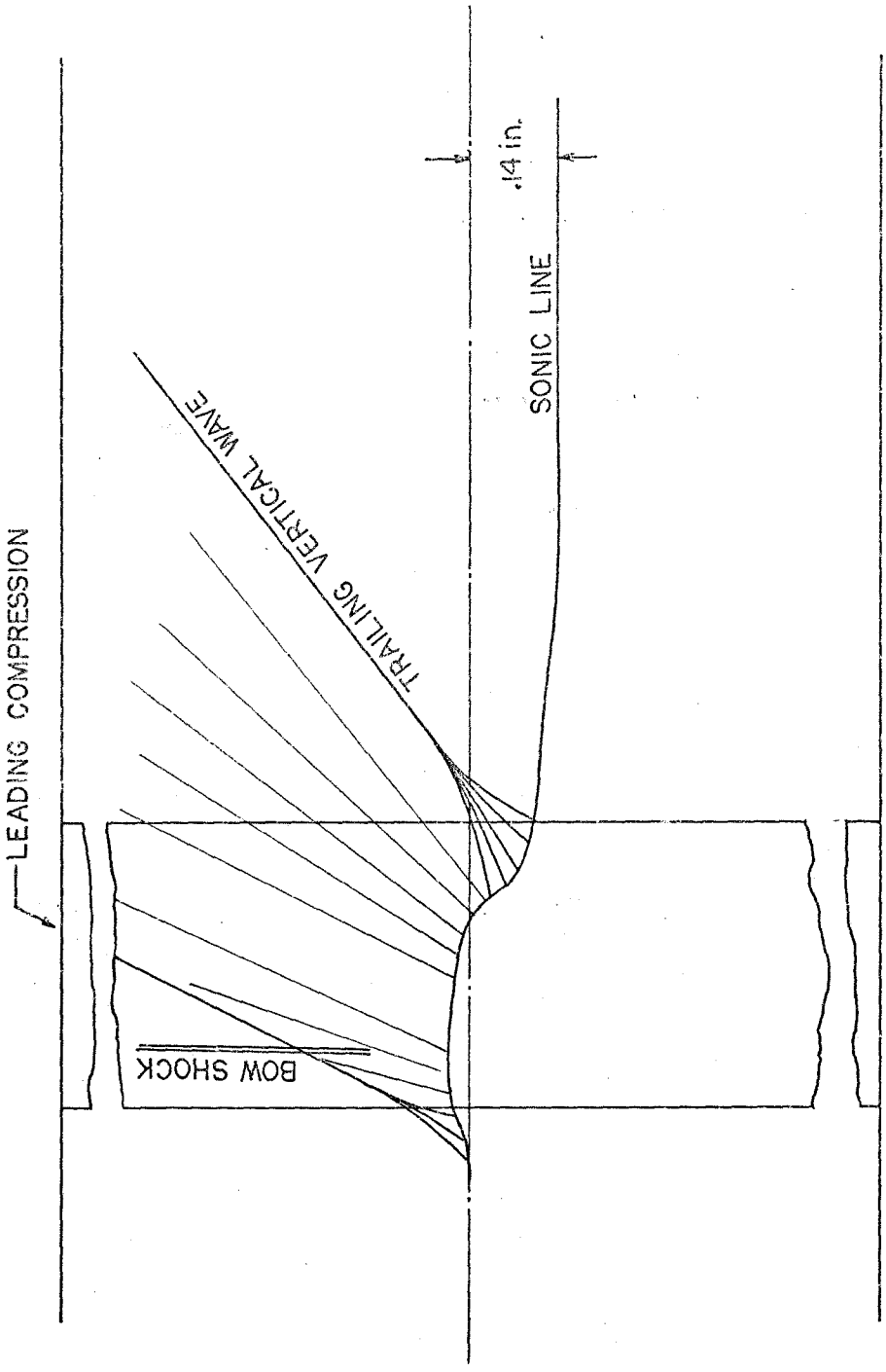

Figure 5.26: Plan View of Free Airfoil Showing Waves Generated Within the Shear Layer (not to scale)

0.14 inch, with minor fluctuations as waves in the supersonic stream impinge on the shear layer. The total pressure profiles of Figure 5.17, taken at a point about 4.85 inches downstream of the trailing edge (i.e., slightly more than three chord lengths) show a displacement downward of about 0.14 ± .01 inch in the shear layer, showing that this displacement is fairly steady.

With the basic geometry of the sonic surface now understood, let us return to consideration of the supersonic flow field. The subsonic region behind the normal shock quickly re-accelerates to supersonic flow, probably aided by a convexity in the shock surface (cf. Figure 5.15). Two families of Prandtl-Mayer expansions act on this flow: one family of lateral expansion due to the curvature of the airfoil surface; and a more complicated three-dimensional expansion due to the warpage of the sonic surface. The net expansion around the airfoil is 13.78°; the expansion due to the sonic surface is a function of position and is not amenable to computation. However, the relatively large increase in supersonic flow area suggests that the Mach number will be considerably larger than its unperturbed value (1.4) by the point where the trailing shock is reached.

The Mach number just ahead of the lateral trailing shock can be estimated by the inclination angle of the oblique compression wave ascending into the supersonic stream from the trailing edge/shear layer interface. The angle measured from schlieren photographs is 35.5° (taking the flow to be exactly horizontal), and assuming an uncertainty of 2.0° in the flow inclination angle we get M_1 = 1.72 ± .08. In this region, the flow angle is probably downward in

response to the expansion waves from the shear layer, which means the Mach number would be somewhat less than 1.72.

Another estimate of this Mach number can be obtained by noting the point at which the lateral trailing shock strikes the sidewall (1.05 ± .05 inch downstream of the trailing edge) and its pressure ratio including reflection at the sidewall (1.85 ± .05) in the line y = 1.00" (near the middle of the supersonic stream). Sidewall pressures in the streamwise (x) direction for various values of y are presented in Figure 5.27. This is a slightly different presentation of data similar to Figure 5.19, which makes it easier to infer shock pressure ratios.

In Figure 5.27 we also note the transition in the pressure distribution on the sidewall from a characteristic supersonic form dominated by distinct compression and expansion waves (5.27 a, b, c, and d) through a transition region in the shear layer (5.27 e and f) to a smooth subsonic wall pressure profile (5.27 g and h).

From these data one can calculate that just upstream of the lateral trailing shock the Mach number is 1.67 ± .06 and the shock deflection angle is $6.0^{\circ} \pm 0.7^{\circ}$. This angle is certainly in the right range considering the trailing-edge semivertex angle is 6.84° and that by the point where the shock reaches the wall the expansions from the airfoil surface should reduce its strength somewhat (a calculation of the reduced strength is not possible without better information on the sonic surface deflection). Then, as is illustrated in Figure 5.15, downstream of the reflected wave the Mach number is about 1.27.

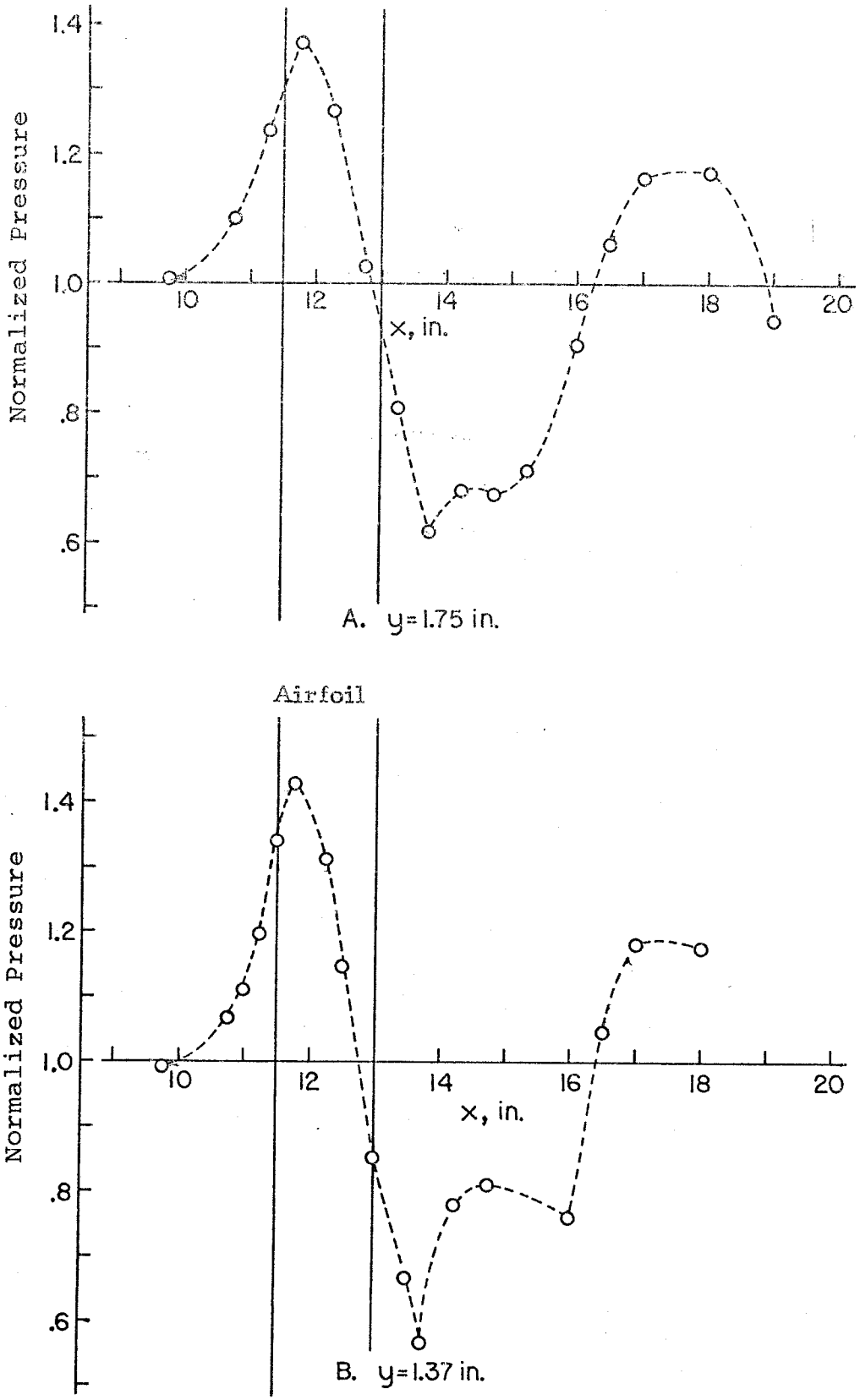

Figure 5.27: Streamwise Sidewall Pressure Profiles

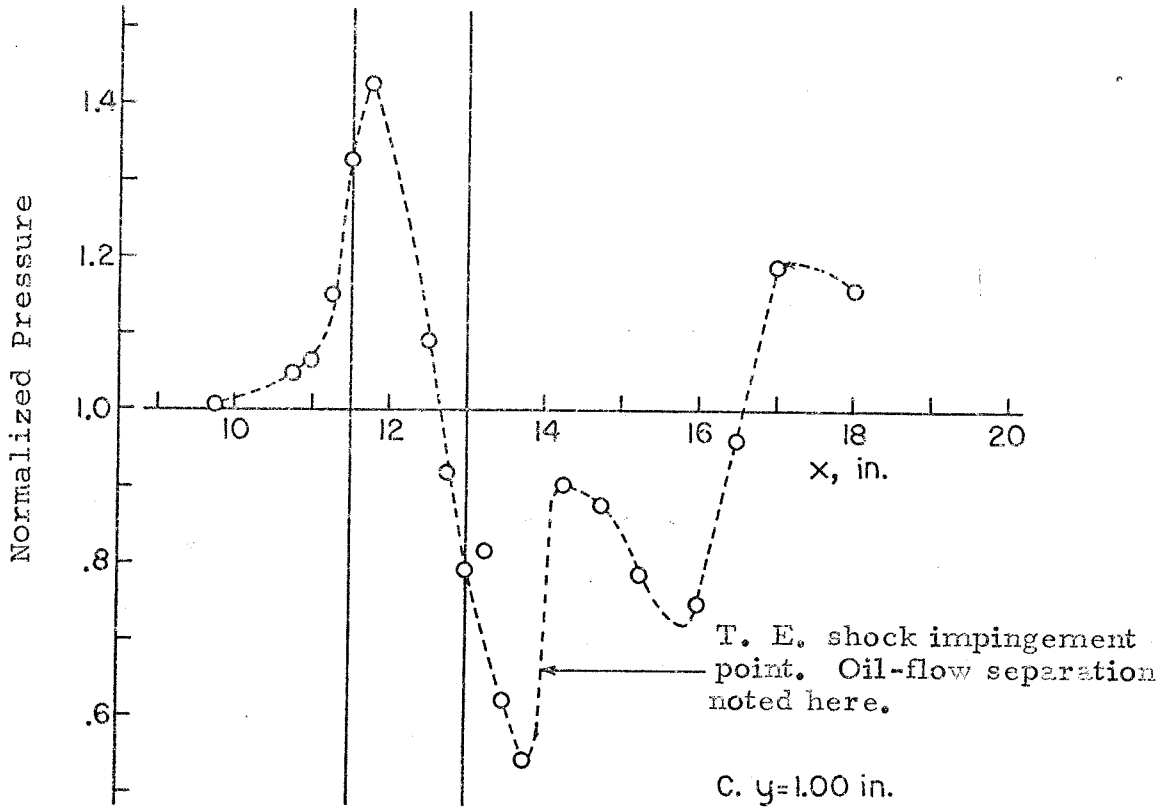

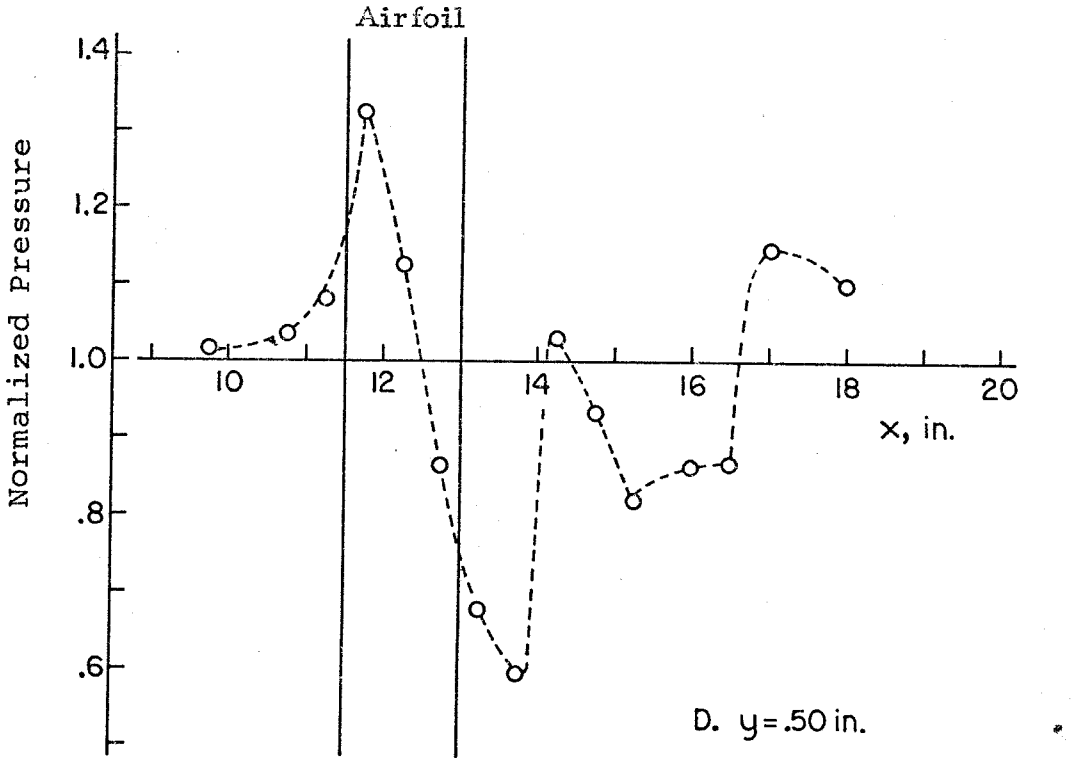

Figure 5.27, cont'd.: Streamwise Sidewall Pressure Profiles

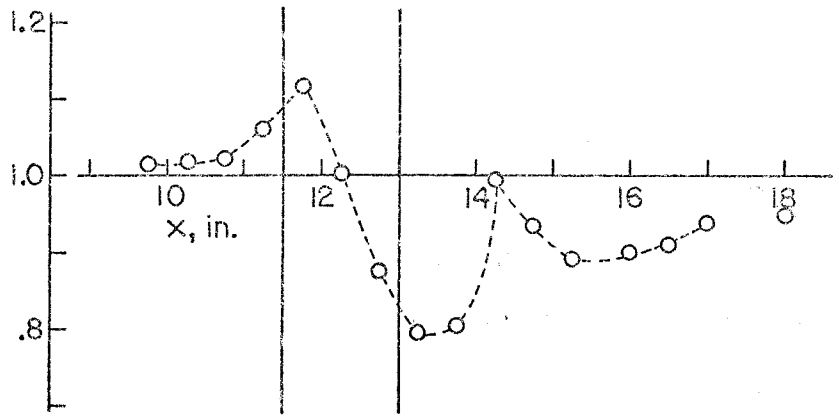

E. y=0

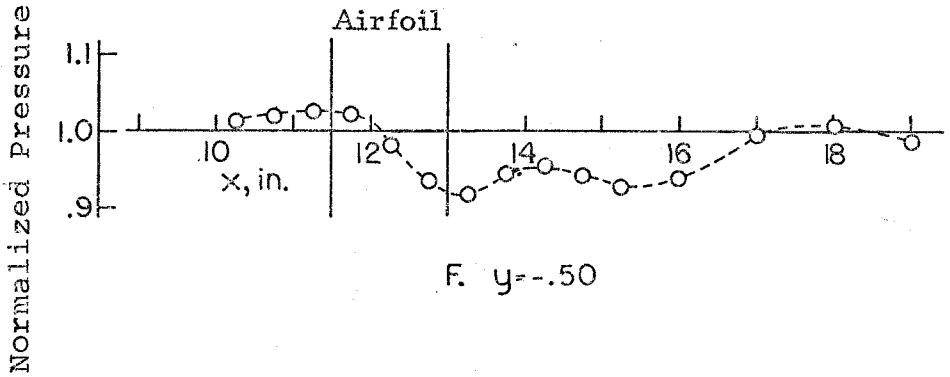

F. y=-.50

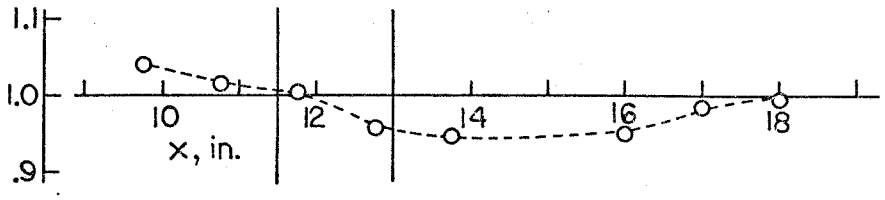

G. y=-1.00 in.

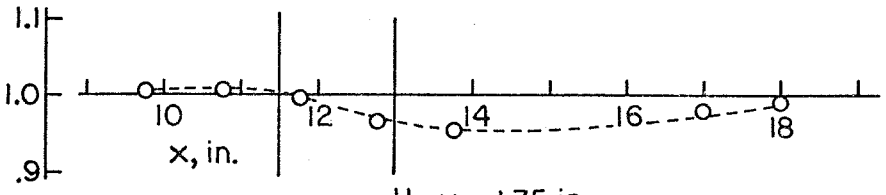

H. y=-1.75 in.

Figure 5.27, cont'd.: Streamwise Sidewall Pressure Profiles

At the point where this shock system strikes the sidewall (x = 14.1 inches), the boundary layer is observed to separate briefly. This separation extends vertically from about y = 0.6" to 1.6", which compares well with the previous estimate of the vertical extent of the supersonic core flow region. This separation is always in the same location (± 0.05 inch). Data from Fage and Sargent[27] suggest that for the flow to separate at the Mach numbers in question due to a shock incident on the boundary layer, a pressure ratio (with reflection) of at least 1.8 is required, agreeing with the measurements which show a pressure ratio of 1.85.

Figure 5.28 presents Mach number profiles, generated by pitot and static probe surveys, in a vertical cut at a station 4.85 inches downstream of the trailing edge and offset 0.3 inches in the z+ direction (so that the probe is not in the airfoil wake). For comparison purposes, Mach numbers at the same location with the airfoil removed are also presented. This figure shows the downward shift of the entire shear layer of about 0.14 inches. It also shows that 3 chord lengths downstream of the trailing edge the supersonic Mach number is 1.28 ± .03, about the same as it was after the reflection of the lateral trailing-edge shock from the wall about one chord length downstream of the trailing edge.

Note that M_1 is reduced throughout the supersonic stream from 1.41 to 1.28, while M_2 remains nearly constant at 0.53. Kotansky[44] observed a similar effect with a thin airfoil in an incompressible shear layer. In that case, the change in velocity ratio was due to a change in the areas of the two streams (increase of the high-

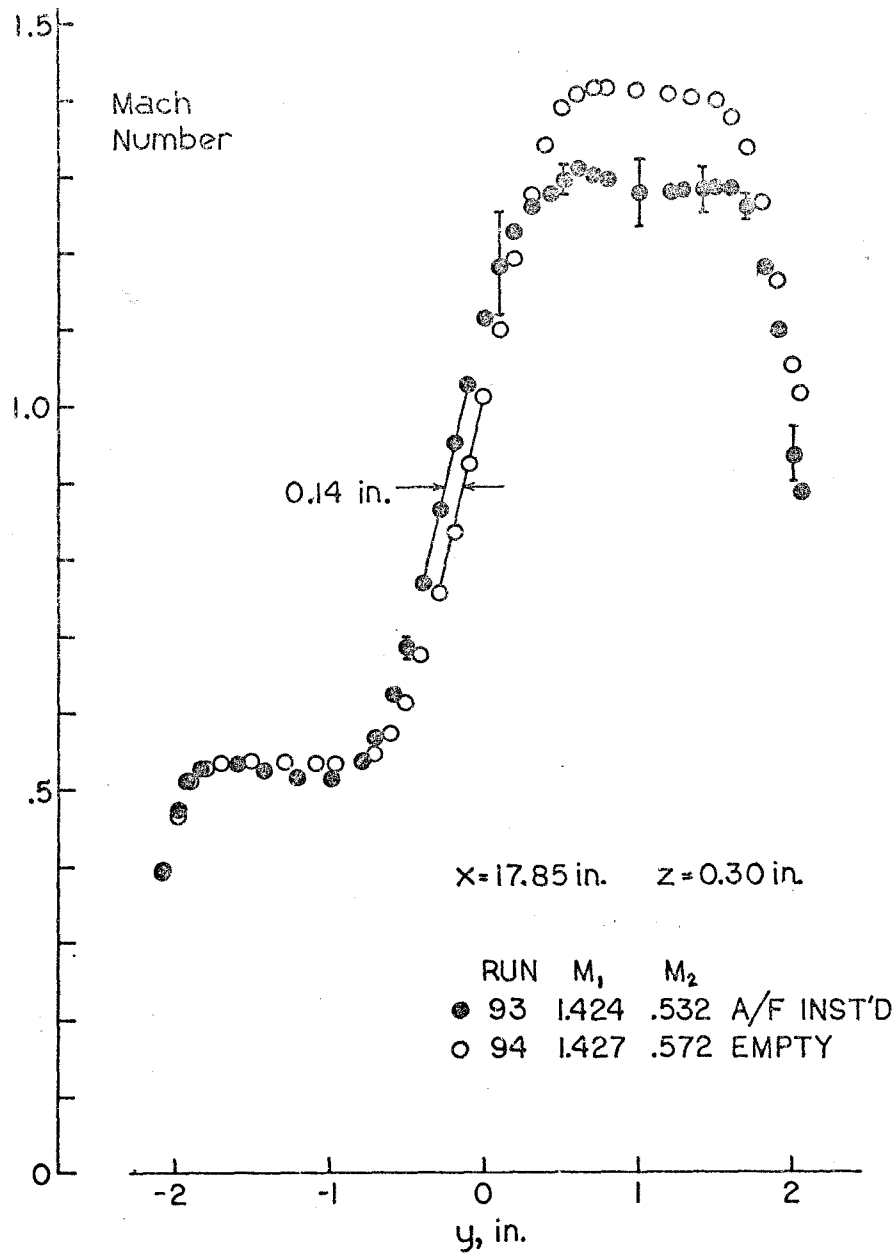

Figure 5.28: Mach Number Profile 4.85 Inches Downstream of Trailing Edge; Comparison with Empty Tunnel

speed flow area as the interface deflected into the low-speed stream caused a reduction in high-speed velocity and an increase in low-speed velocity). In the present study, the relationship between area and velocity ratio is somewhat ambiguous, since a deflection of the sonic surface into the subsonic stream will tend to accelerate both streams. The loss of total pressure in the supersonic stream appears more important, since to pass the same mass flow with a loss a larger area is required downstream of the airfoil.

Figure 5.19 (the sidewall pressure contours) shows readily that reflections of the lateral wave on the sidewall after the initial reflection are considerably weakened. This is because the lateral waves from the airfoil are continually being attenuated by their self-interactions: the set of expansions from the airfoil surface continually weakens the shocks from the leading and trailing edges. In addition, the wave grazes along the shear layer during its entire journey, resulting in a cumulative weakening as described by McCabe[22] and previously discussed in Section 5.3.1. A similar, though less severe, weakening occurs as the wave grazes the top (supersonic) wall boundary layer. Progressive weakening is to be expected, too, at each reflection from the sidewall boundary layer.

Figure 5.29 presents measured pressures on the supersonic wall centerline (i.e., in the plane of the airfoil) compared with data from a representative empty-tunnel run. The excursions of pressure more than an inch upstream of the leading edge are the various empty-tunnel phenomena that were discussed in Chapter III and do not represent an interaction due to the airfoil. Downstream of the

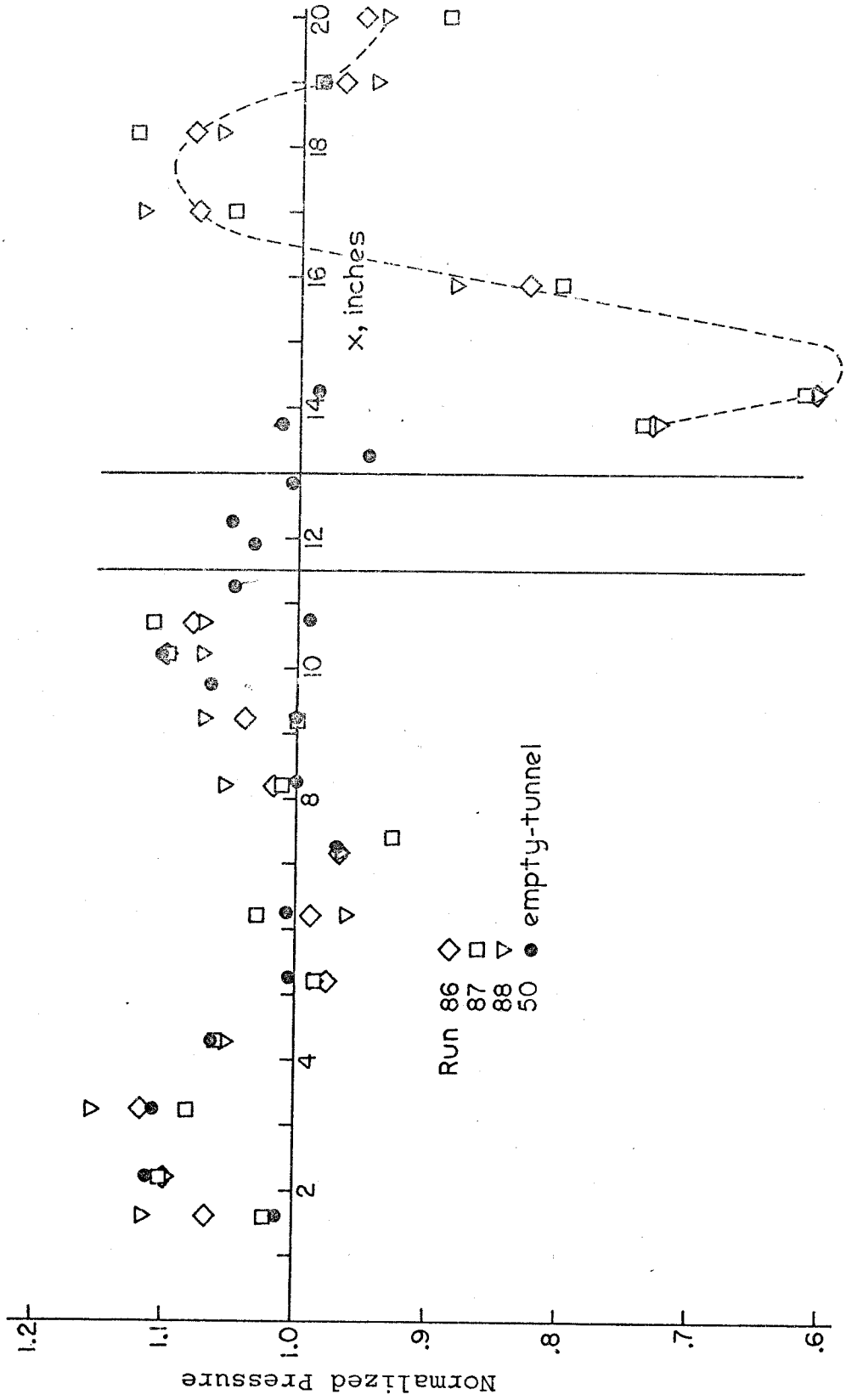

Figure 5.29: Supersonic Wall Centerline Pressure (Free Airfoil, $\alpha = 0^{\circ}$, $x_{LE} = 11.50$ Inches)

airfoil, the lateral trailing shock is dispersed somewhat by a grazing interaction, and the pressure rise due to it on the top wall is distributed over more than an inch, starting about 1 to 2 inches downstream of the trailing edge. About 3 inches downstream, the trailing vertical shock wave from the shear layer strikes the wall (see Figure 5.26). This impingement point is verified by schlieren photographs. Schlieren photographs reveal that in this location (x = 17") the lateral and vertical shocks unite and the wall pressure is elevated to about 1.16, followed by oscillations with a wavelength of 5 to 6 inches as the combined wave continues to reflect between the top wall, the sidewalls, and the shear layer. The amplitude of this wave is reduced about 50 per cent in each cycle through its interaction with the shear layer.

Subsonic wall centerline pressure data are presented in Figure 5.30. These data are shown in normalized form without any attempt to remove empty-tunnel effects. Consequently, the expected upstream variation due to the splitter plate shock system is present. The perturbation ahead of the leading edge is not due to the presence of the airfoil. This figure shows that the subsonic layer loses all significant oscillations by the point where the trailing vertical wave has returned to the shear layer after reflecting off the supersonic wall at about x = 17 inches, 5.5 inches downstream of the leading edge. Beyond about 7 inches from the leading edge, the only variation is the tunnel static-pressure gradient due to the inadequate adjustment limit of the top and bottom walls. This effect was discussed in Chapter III and is inherent in the current design of the

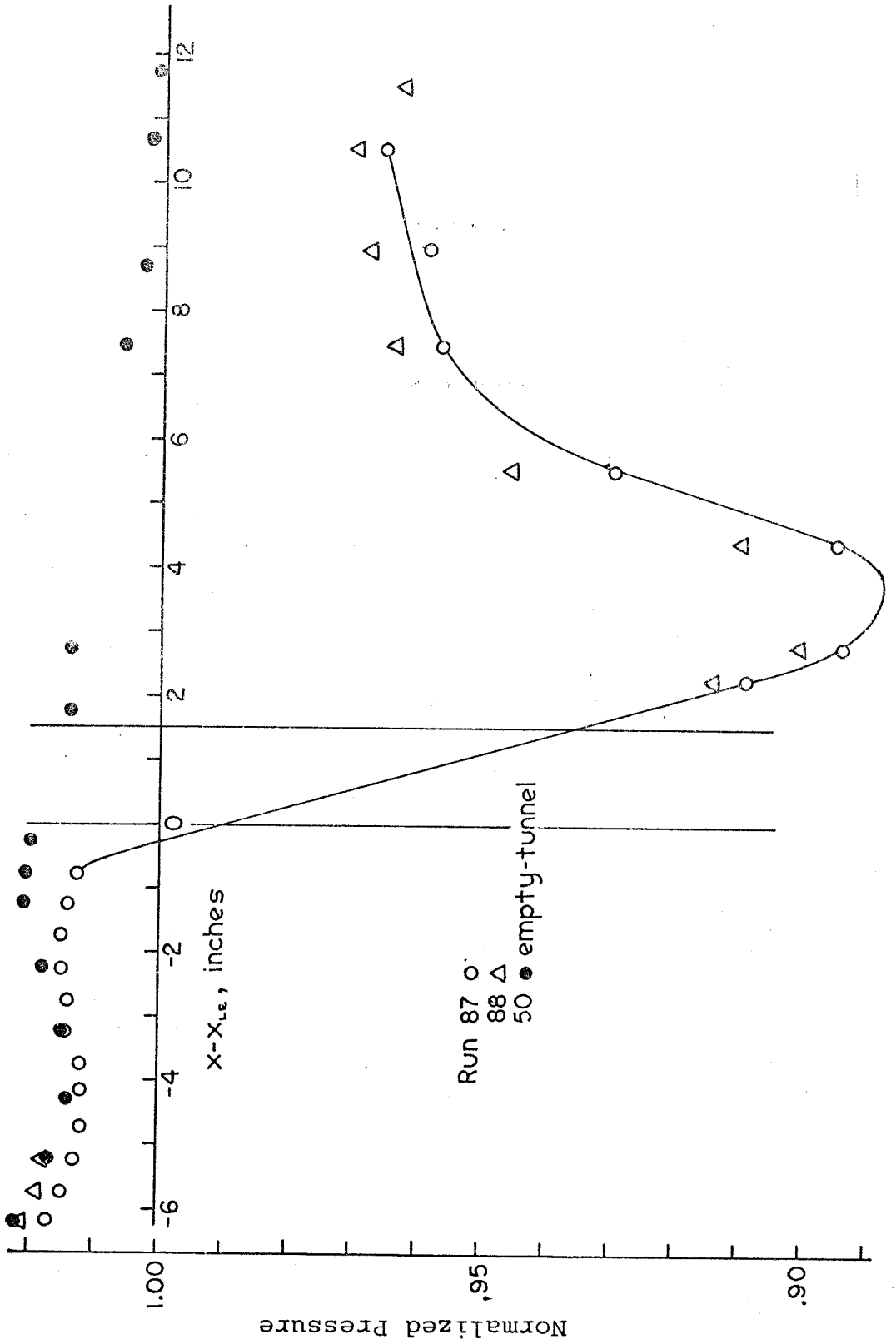

Figure 5.30: Subsonic Wall Centerline Pressure (Free Airfoil, $\alpha = 0^{\circ}$, $x_{LE} = 11.50$ Inches)

wind tunnel.

Figure 5.31 shows the rapid attenuation of all lateral pressure gradients in the subsonic layer downstream of the trailing edge of the airfoil. The data presented are for the subsonic wall centerline, and the sidewall and airfoil surface at y = -1.75". Discrepancies between the sidewall value and the other two at a given location are a measure of the lateral gradients. After about 0.7 inch downstream from the trailing edge, lateral gradients in the inviscid subsonic flow (i.e., outside of the shear and boundary layers) are insignificant, less than 0.004 in normalized magnitude. Not only has the subsonic stream lost its own lateral gradients, but it does not respond to the supersonic lateral waves (specifically, the lateral trailing edge shock) in a lateral mode but only in a vertical mode as caused by vertical displacements of the sonic surface.

Several conclusions have been drawn from the data of this section. Within the airfoil passage, the presence of the shear layer weakens considerably the shock waves expected in a quasi-two-dimensional consideration of the flow field.

Modification of the supersonic stream ahead of the leading edge due to disturbances passed upstream through the subsonic layer is very slight in the present study. More generally, an upper limit is set for this upstream modification of the subsonic stream by considering the potential flow pressure field at a uniform Mach number M_2 ahead of the same airfoil.

The initial deflection of the sonic surface into the subsonic stream occurs immediately behind the leading shock wave. How-

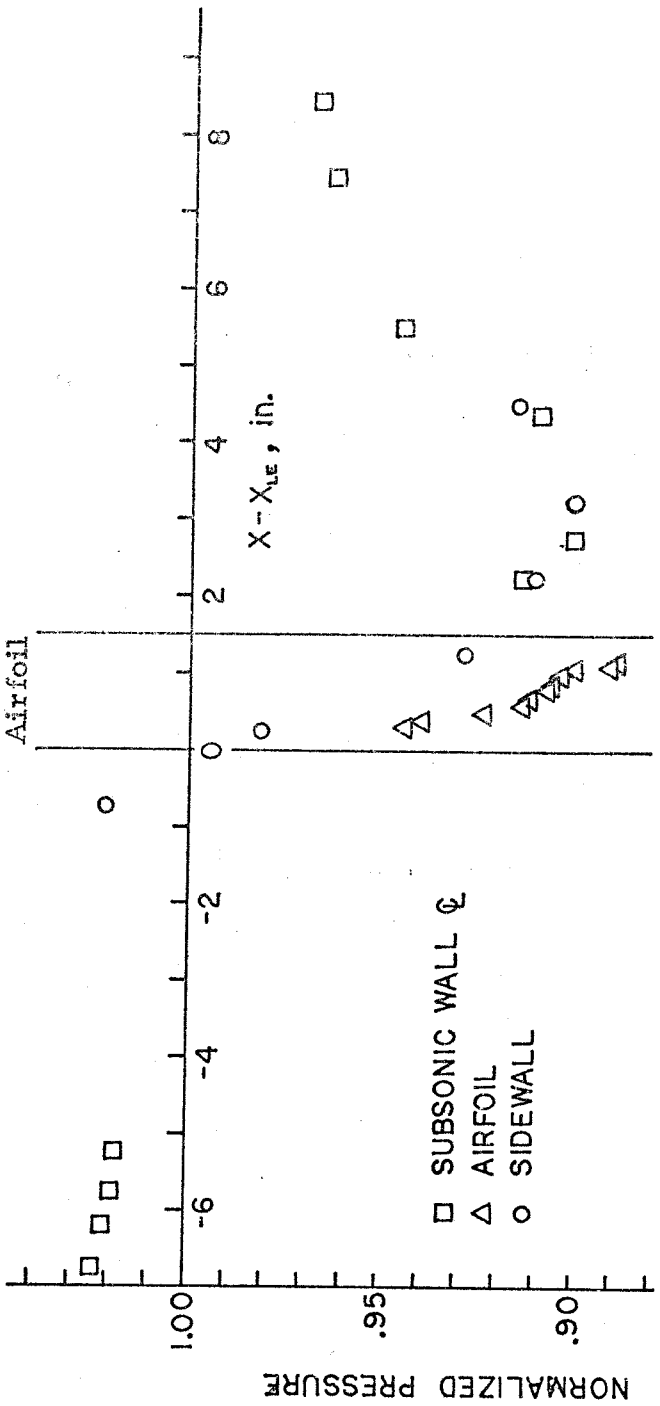

Figure 5.31: Comparison Between Subsonic Wall Centerline Pressure and Airfoil and Sidewall Surface Pressure (Free Airfoil, Run 88, x_{LE} = 11.50 Inches)

ever, the larger portion of the displacement of this surface occurs near the aft portions of the airfoil, where the thickness of the airfoil is decreasing most rapidly. In this region, the reduction of subsonic layer flow area due to the sonic surface displacement almost exactly offsets the increasing flow area as the thickness of the airfoil is reduced.

Most of the adjustment of the combined flow in reaching a new equilibrium is completed within 1 to 2 chord lengths downstream of the trailing edge. The most highly damped oscillations are lateral waves in the inviscid portion of the subsonic stream, which vanish within half a chord length. Vertical waves disappear as quickly, except where excited by waves in the supersonic stream. Vertical waves in the supersonic stream generally cease to affect the system after their first reflection off the shear layer. This is due to the dispersion of the wave, which has been discussed in Section 4.2. Only lateral waves in the supersonic stream, reflecting between the sidewalls, are more persistent. Their effect on the sidewall pressure distribution can be noted several chord lengths downstream of the airfoil. The effect of these waves on the subsonic layer is relatively minor.

5.4.1.4 Effect of shear layer thickness. To estimate the effect of shear layer thickness, comparisons were made between airfoil runs at a leading edge position x = 11.50" (δ_s = 0.70", the "thick" shear layer), with the position x = 5.00" (δ_s = 0.31", the "thin" shear layer). Kotansky[44] suggests the use of the dimensionless parameter

$$s = \frac{c}{U}\left.\frac{dU}{dy}\right|_{max} \doteq \frac{c}{\delta_s} \qquad (5.7)$$

to characterize shear flows; the larger the parameter becomes, the more dominant the three-dimensional effects are. Hawthorne[45] also adopts this measure of shear layer importance and concludes that as s becomes vanishingly small the flow approaches cascade flow (potential flow). The experiments performed here were at values of s of 4.92 (sidewall airfoil), 4.85 (free airfoil at 5.00") and 2.14 (free airfoil at 11.50"). The studies of Kotansky were performed at values of 0.30, 0.75, and 1.50.

The effect of thickening the shear layer was to weaken somewhat the three-dimensional effects, as expected both from Kotansky's work and from the realization that the strength of the three-dimensional waves depends on the magnitude of their source, the shear layer velocity gradient. A weakening of this source by thickening the shear layer must be expected to weaken the spanwise waves.

Figure 5.32 presents subsonic wall centerline pressure distributions for the two shear layer thicknesses. Data from a representative empty-tunnel run are also shown. While it appears that the thick shear layer might have a larger pressure amplitude (presumably due to the decreased choking margin) the effect is certainly minor. Furthermore, the equality of the pressure downstream of the airfoil suggests that the displacement of the sonic surface is not sensitive to the thickness of the shear layer for the 45% change in thickness affected here.

The basic character of the pressure distribution on the

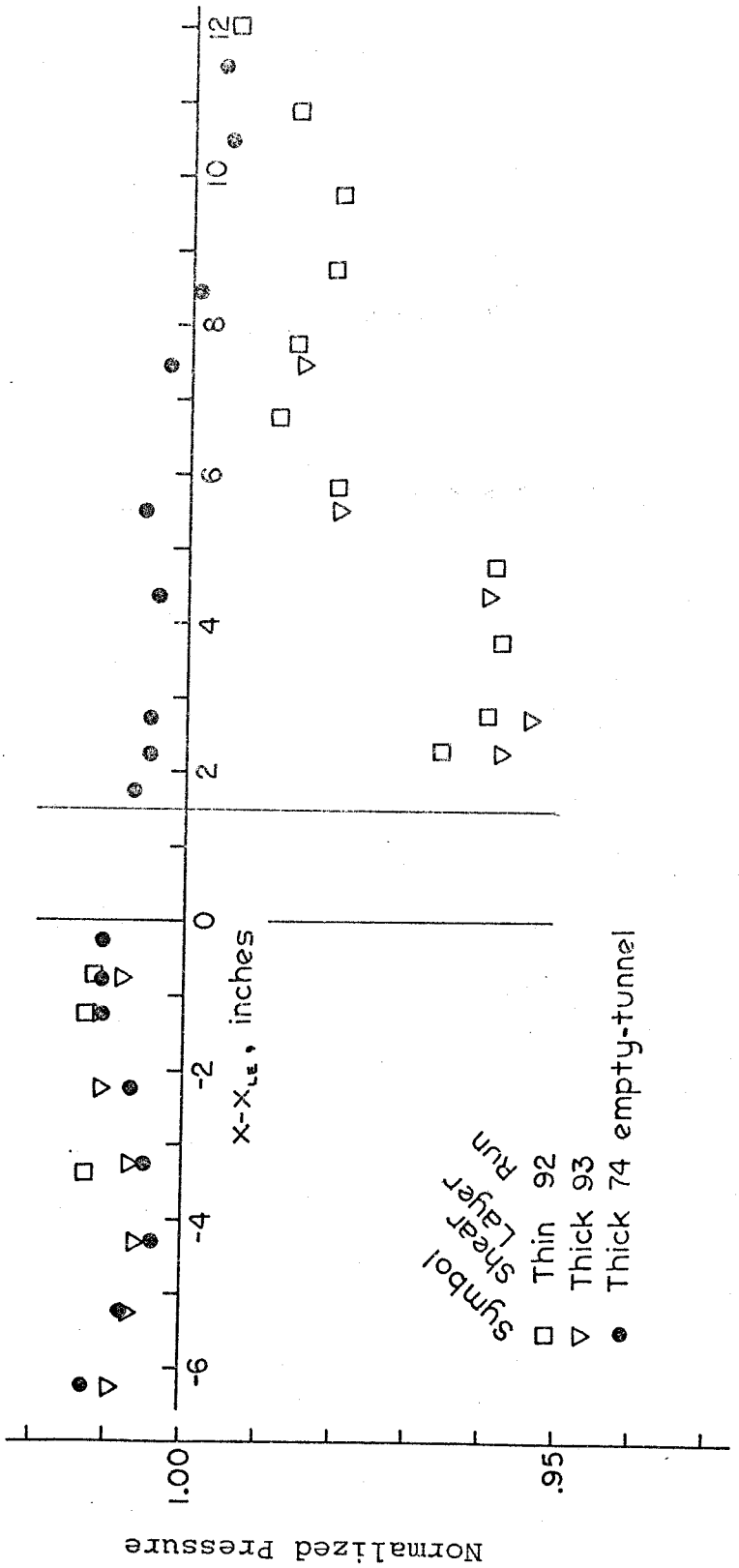

Figure 5.32: Effect of Shear Layer Thickness on Subsonic Wall Centerline Pressure (Free Airfoil, $\alpha = 0$)

sidewall seems unaffected by the thickened shear layer (see Figure 5.33 compared with Figure 5.19). On the surface of the airfoil, however, the differences are quite noticeable. The surface pressure contours (Figure 5.34 compared with Figure 5.13) show a marked smoothing of the pressure distribution over the entire airfoil. The comparison is most striking in the vicinity of the sonic line, where a complex set of maxima and minima have been diffused into a more nearly monotonic distribution (Figure 5.35 compared with Figure 5.14). The mid-chord shocks become considerably weaker and the supersonic pressure distribution in general conforms much better to the monotonic situation expected in two-dimensional flow.

Basic structural qualities of the flow, such as the shock and expansion waves and the interface displacement, all remain about the same. This is seen in the consistency of the subsonic wall pressure for each case (Fig. 5.32). Except for a greater dispersion of waves in the supersonic stream, no substantive changes were noted.

5.4.2 Effect of Angle of Attack. The tapped airfoil warped during the first run at an angle of attack and took on a permanent set. Attempts to bend the airfoil back to its original state were unsuccessful; the single-wave warpage was only changed to a multiple-wave deformation. Consequently, no further attempt was made to obtain quantitative data using the tapped airfoil. The dummy (i.e., solid) airfoil, however, was run at geometric angles of attack of 0°, $\pm 1^{\circ}$, and $\pm 2^{\circ}$ and wall pressure data and schlieren photographs were obtained.

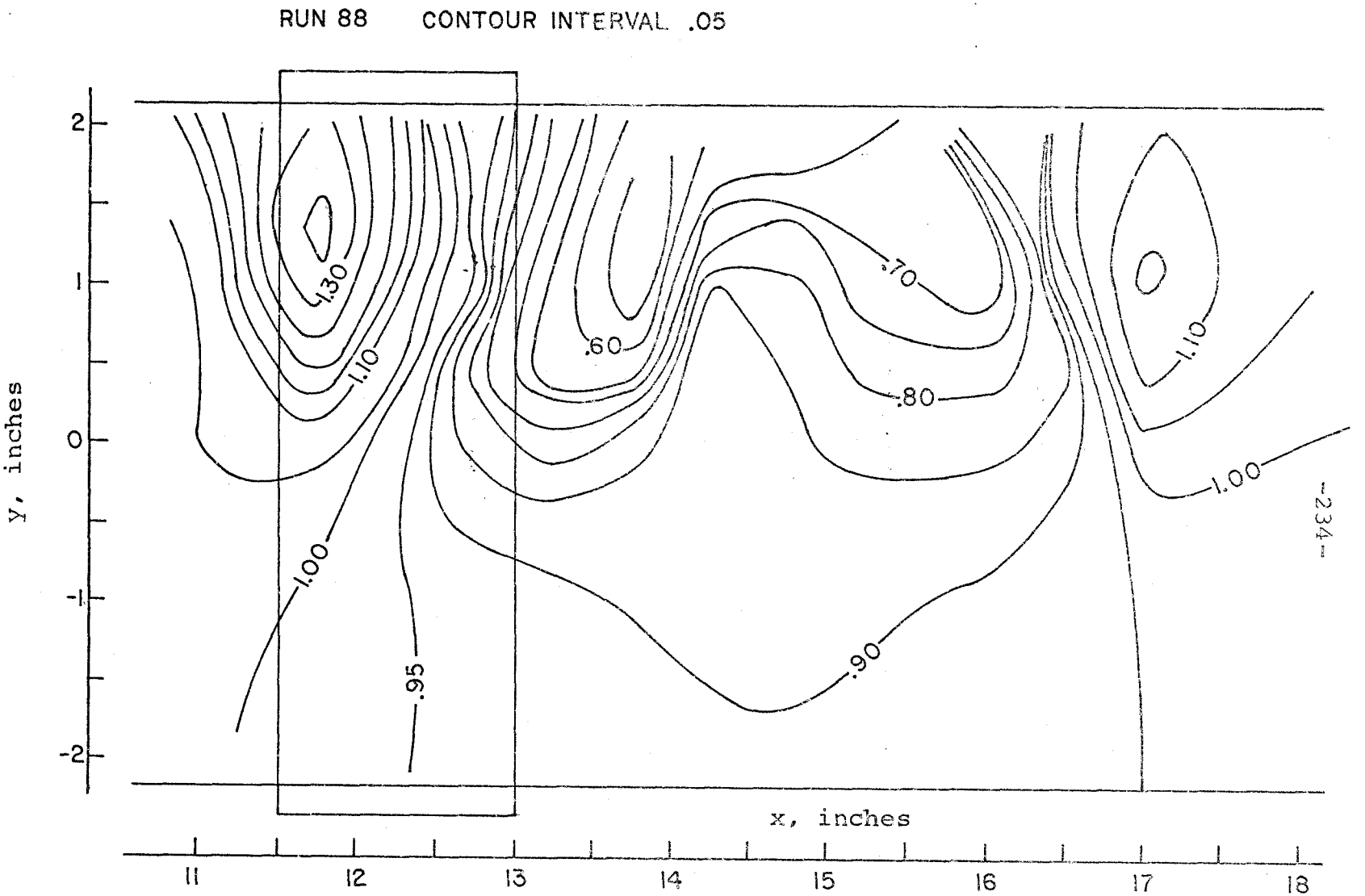

Figure 5.33: Sidewall Pressure Distribution, Thick Shear Layer (Run 88, x_{LE} = 11.50 Inches, α = 0)

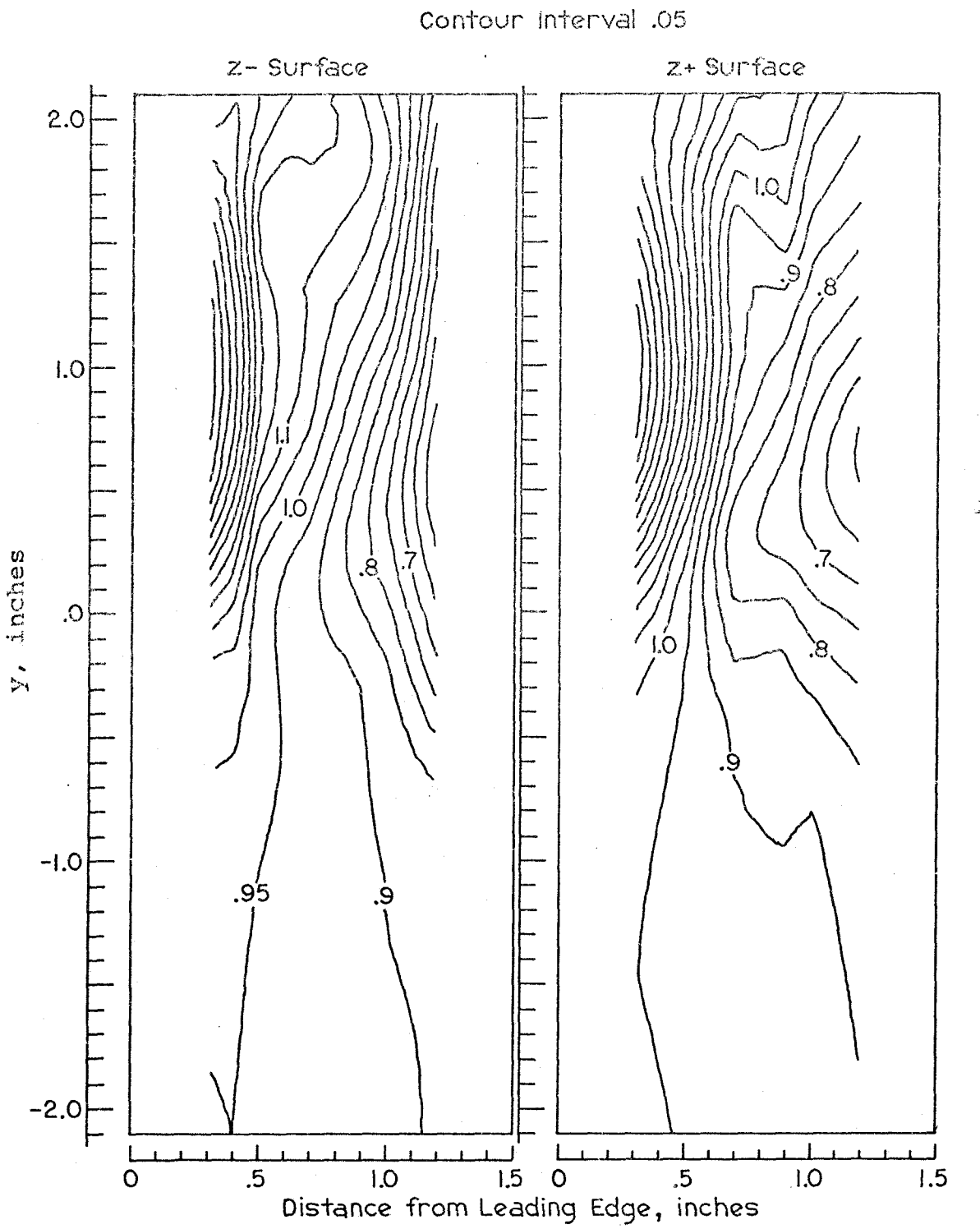

Figure 5.34: Airfoil Surface Pressure Distribution, Thick Shear Layer (Run 87, α = 0)

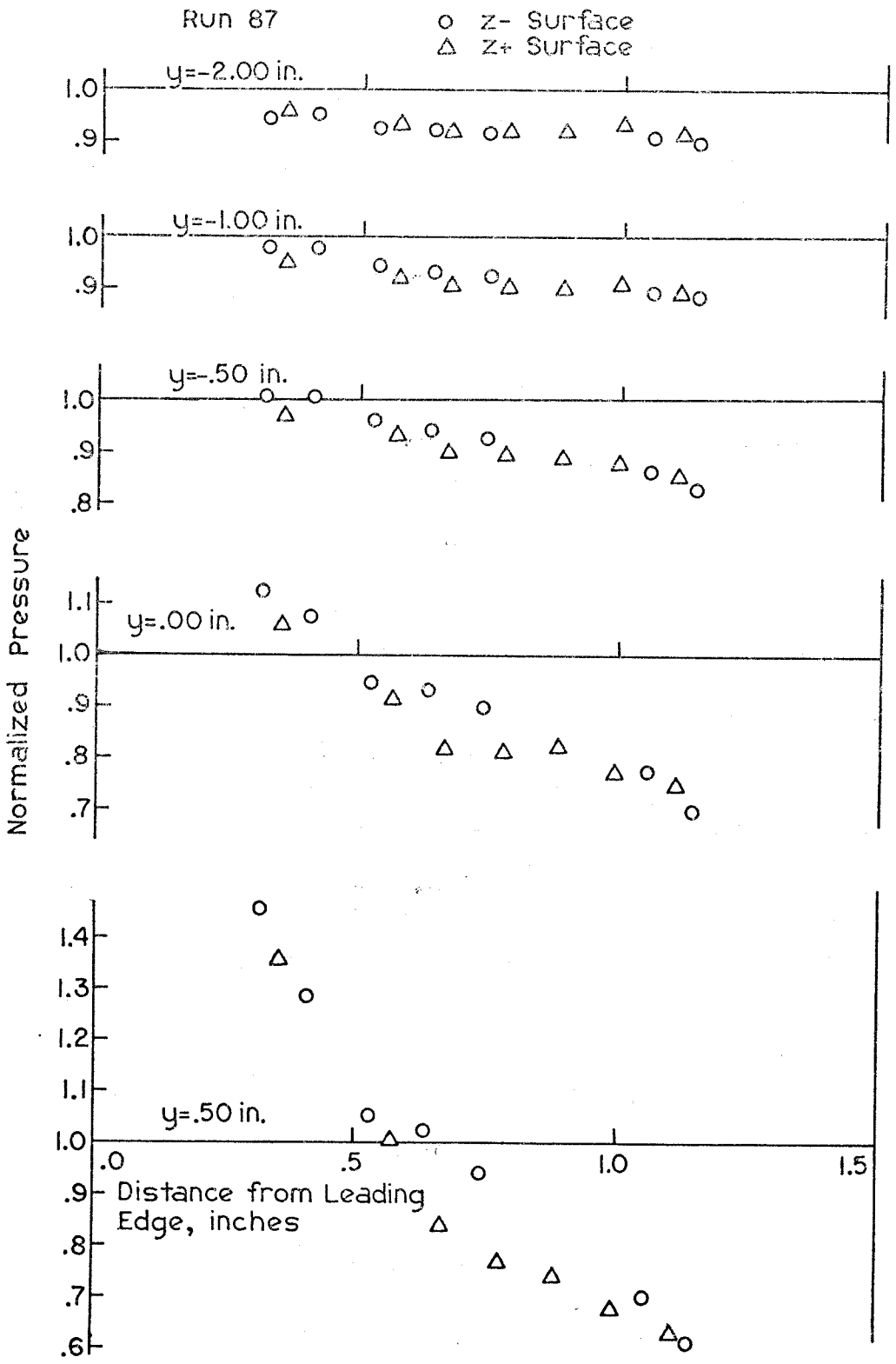

Figure 5.35: Chordwise Surface Pressure Distributions, Thick Shear Layer (Run 87, x_{LE} = 11.50 Inches, α = 0)

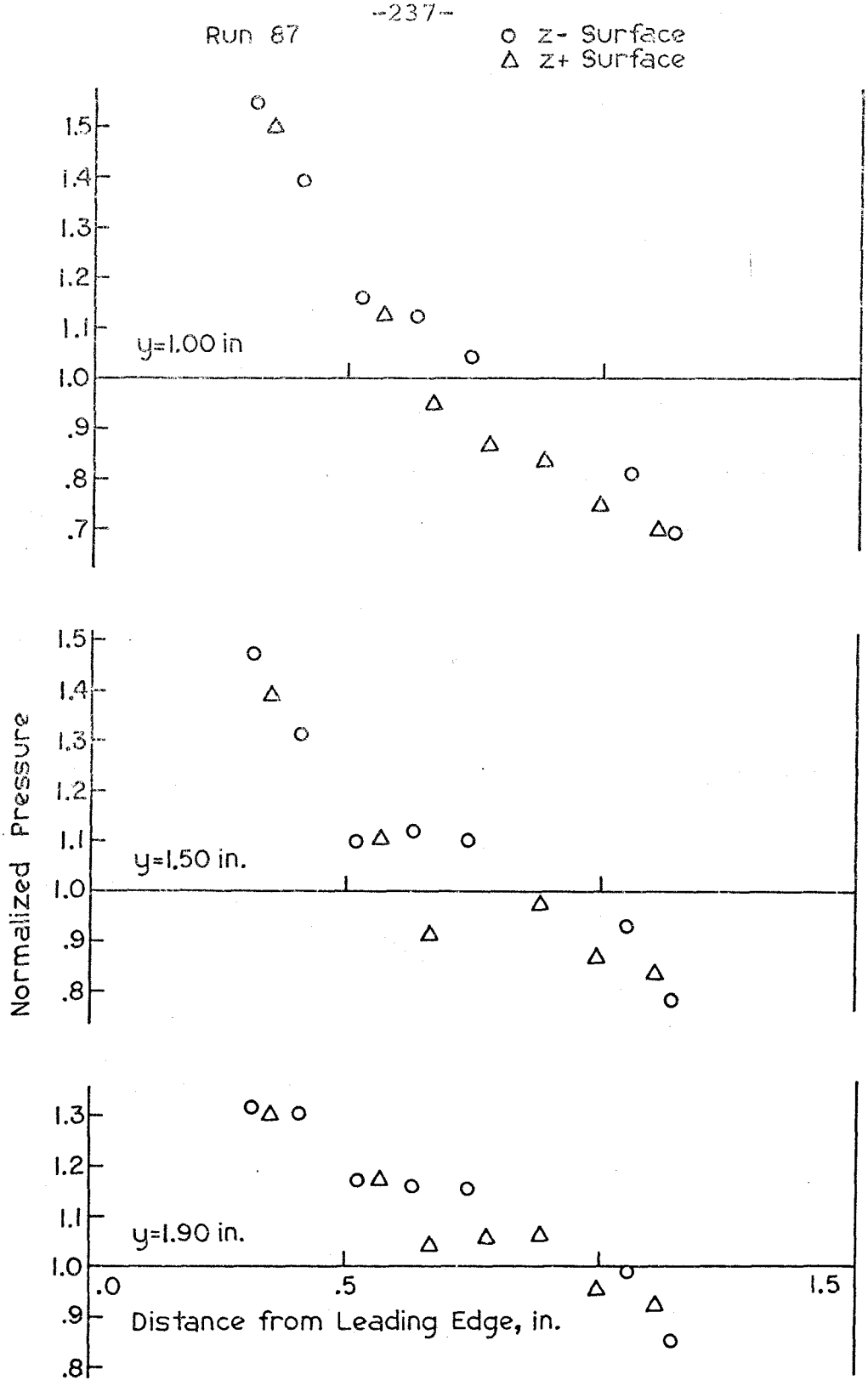

Figure 5.35, cont'd.: Chordwise Surface Pressure Distributions, Thick Shear Layer (Run 87, x_{LE} = 11.50 Inches, α = 0)

The effect of angle of attack on the blockage ratio for the blade passages is presented in Figure 5.36. As indicated by the nozzle exit Mach numbers, the range of α studied appears to have no effect on the operating point of the compressor plant. The convention has been adopted that for a positive angle of attack the leading edge of the airfoil is deflected in the z+ direction. Consequently, the z+ surface, which faces the tapped sidewall (the wall is at z = +0.985") is the suction surface. For a negative angle of attack, therefore, the z+ surface is the pressure surface of the airfoil.

The pressure in the subsonic stream is slightly elevated ahead of the pressure surface passage (higher blockage ratio) and somewhat lowered ahead of the suction surface passage (see Figure 5.37, which presents pressure data from a grid on the subsonic wall). This is also evident in Figure 5.38, which shows measured sidewall pressures in the subsonic stream. Both figures indicate this precursor begins at about x = 10.3", or about 1.2" ahead of the leading edge, and that the lateral pressure gradient in the subsonic stream increases until the leading edge is reached at x = 11.5". This gradient induces a lateral streamline curvature in the subsonic flow (see Figure 5.39) which increases somewhat the local angle of attack. This upwash ahead of the leading edge is a well-known result of subsonic potential flow over a lifting airfoil. In this case, however, it is aggravated by the area contraction in the pressure passage; flow resistance due to the contraction tends to increase the pressure ahead of the leading edge and thus divert flow into the other passage. This effect would

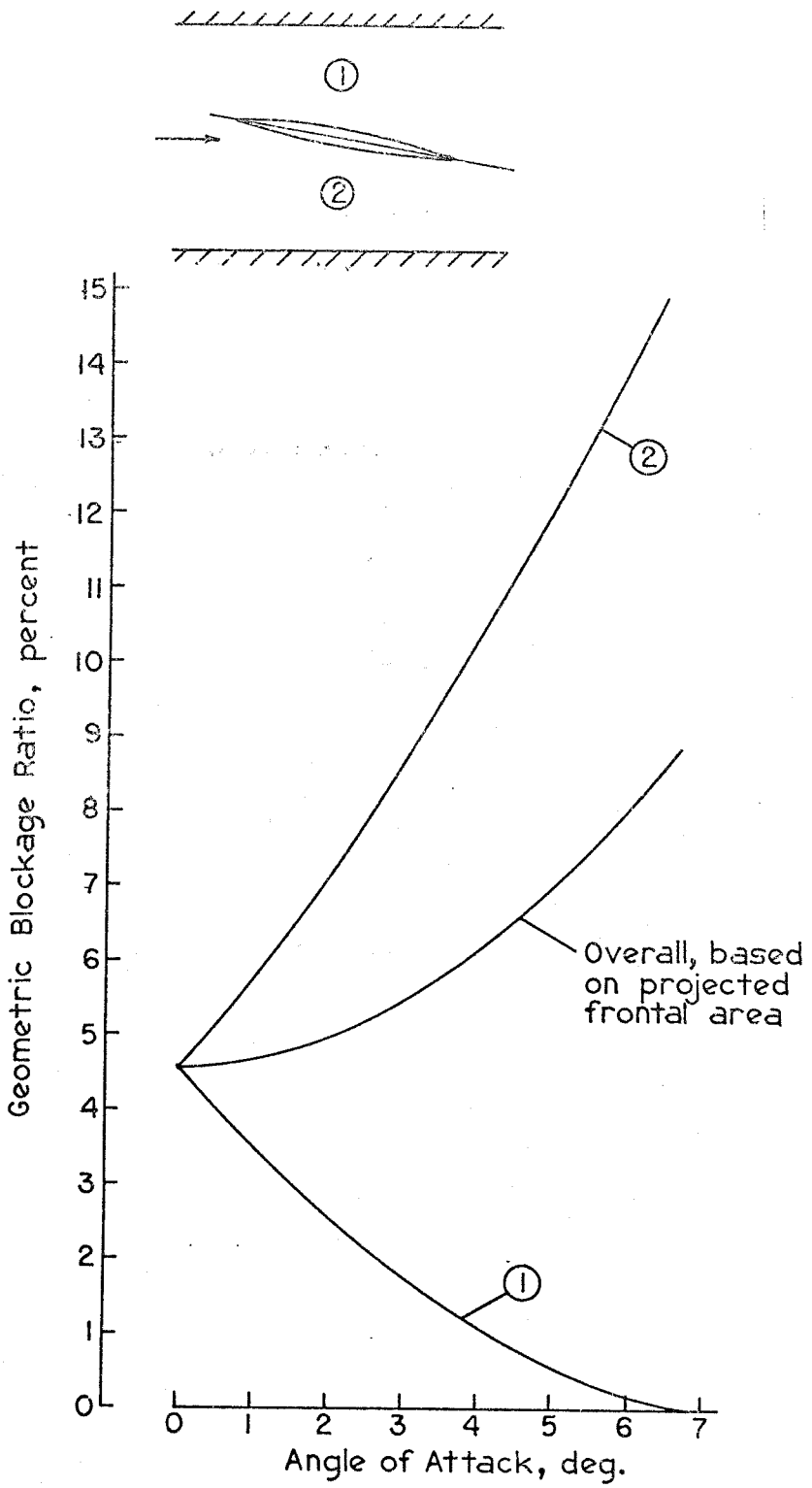

Figure 5.36: Effect of Angle of Attack on Blockage Ratio

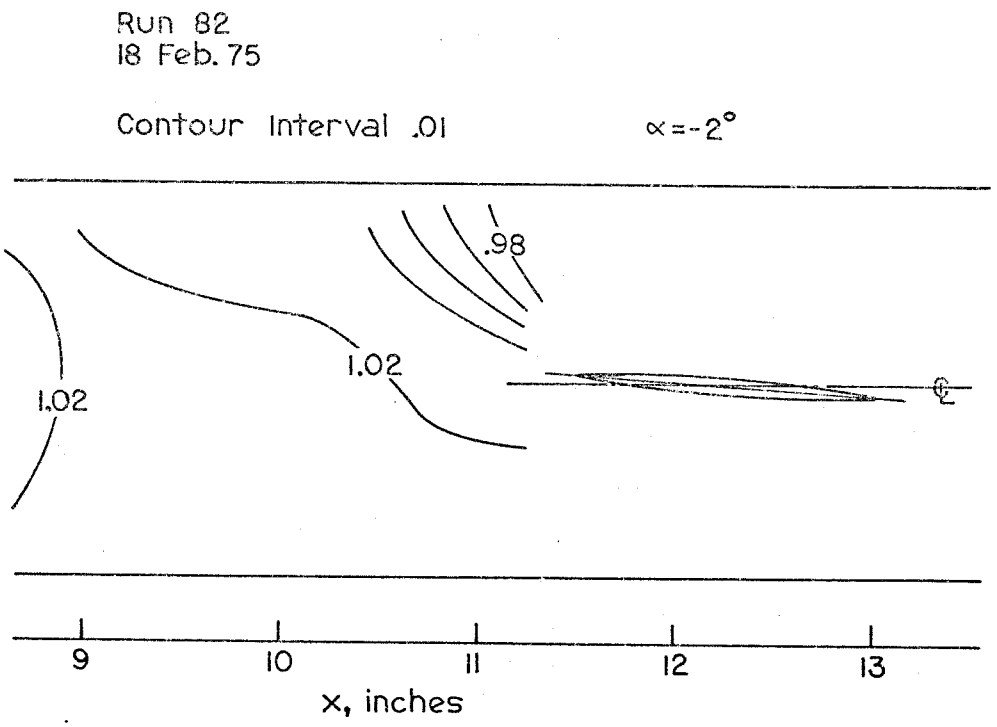

Figure 5.37: Subsonic Wall Pressure Distribution, $\alpha = 2^{o}$

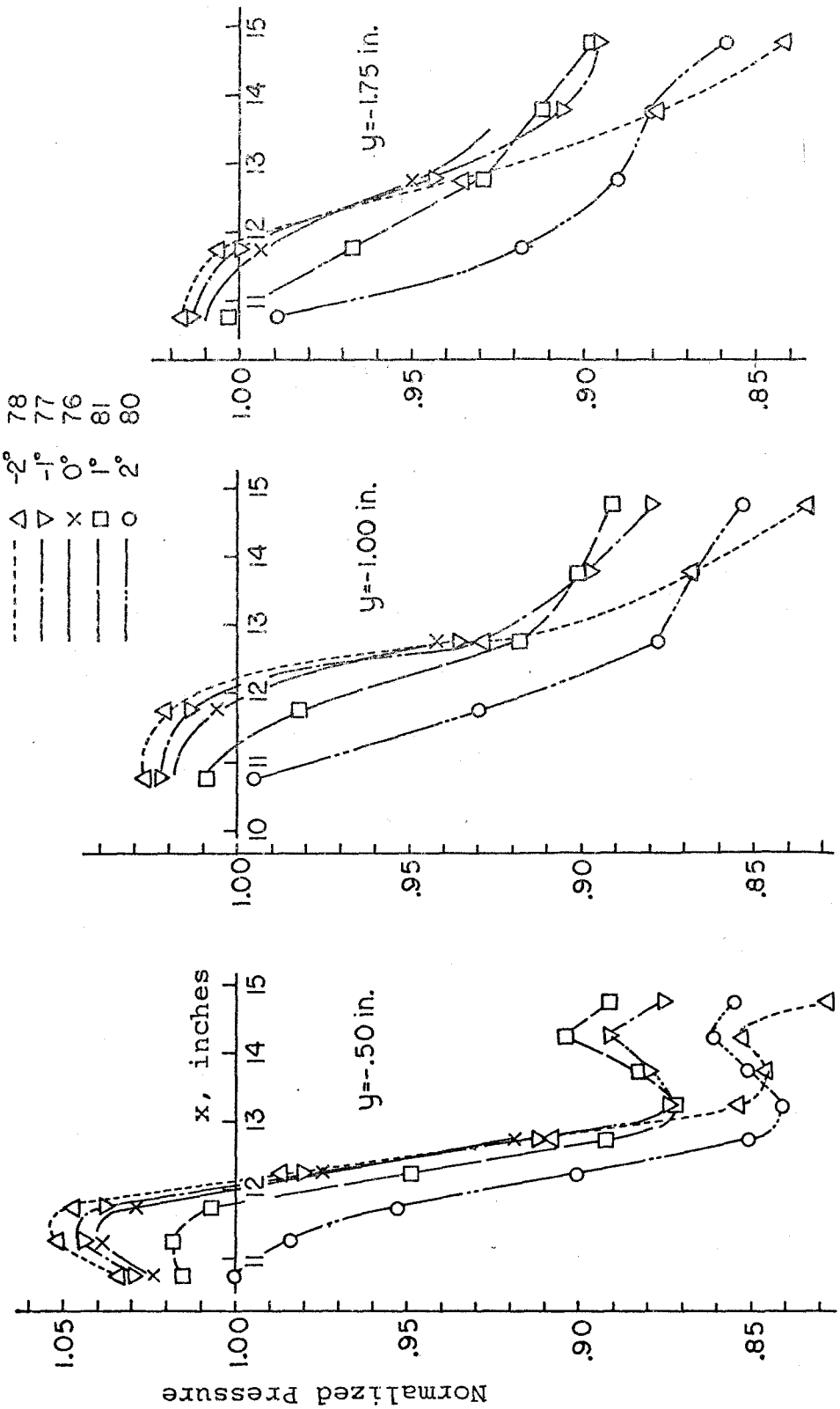

Figure 5.38: Effect of Angle of Attack on Subsonic Sidewall Pressure Distribution (airfoil L. E. at x = 11.50 inches; T. E. at x = 13.00 Inches)

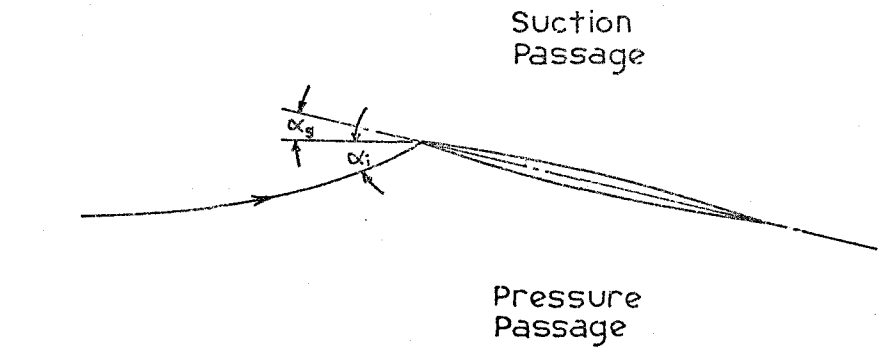

Figure 5.39: Subsonic Induced Flow near the Leading Edge (α_g = geometric angle of attack; α_i = induced angle of attack)

be less severe if the airfoil were in a cascade rather than in a rectangular channel. In the supersonic stream, except within the shear layer where the flow is influenced by pressure gradients in the subsonic stream, the inviscid flow is unperturbed until it passes the bow shock and therefore the induced angle of attack is zero.

Within the supersonic stream, the bow shock is weakened on the suction side to a deflection $\delta_o - \alpha$, where δ_o is the zero-angle-of-attack flow deflection angle, and the shock is strengthened on the pressure side to $\delta_o + \alpha$. This change affects the strength of the bow shock but not the basic geometry of the system. By comparing the sidewall pressure distributions of Figures 5.40 ($\alpha = -2^o$) and 5.41 ($\alpha = +2^o$) with that of Figure 5.19 ($\alpha = 0^o$), it can be seen that the point of maximum pressure on the supersonic sidewall always remains at about the same place, even though the peak pressure varies from 1.27 to 1.43.

This monotonic dependence of pressure on α is as expected, even though the magnitude of the dependence is considerably less than expected in uniform supersonic flow. As was seen in Section 5.4.1, the spanwise effects tend to reduce pressure extremes. The reduction in the dependence on α is proportionally about the same as the overall reduction in the extrema.

Figure 5.42 presents these and other data in a different format: the dependence of sidewall pressure on angle of attack is illustrated at a number of static pressure taps. Parts a, b, and c present data at y = 1.75, 0, and -0.50 inches, respectively, for a number of values of values of x starting upstream of the airfoil leading edge

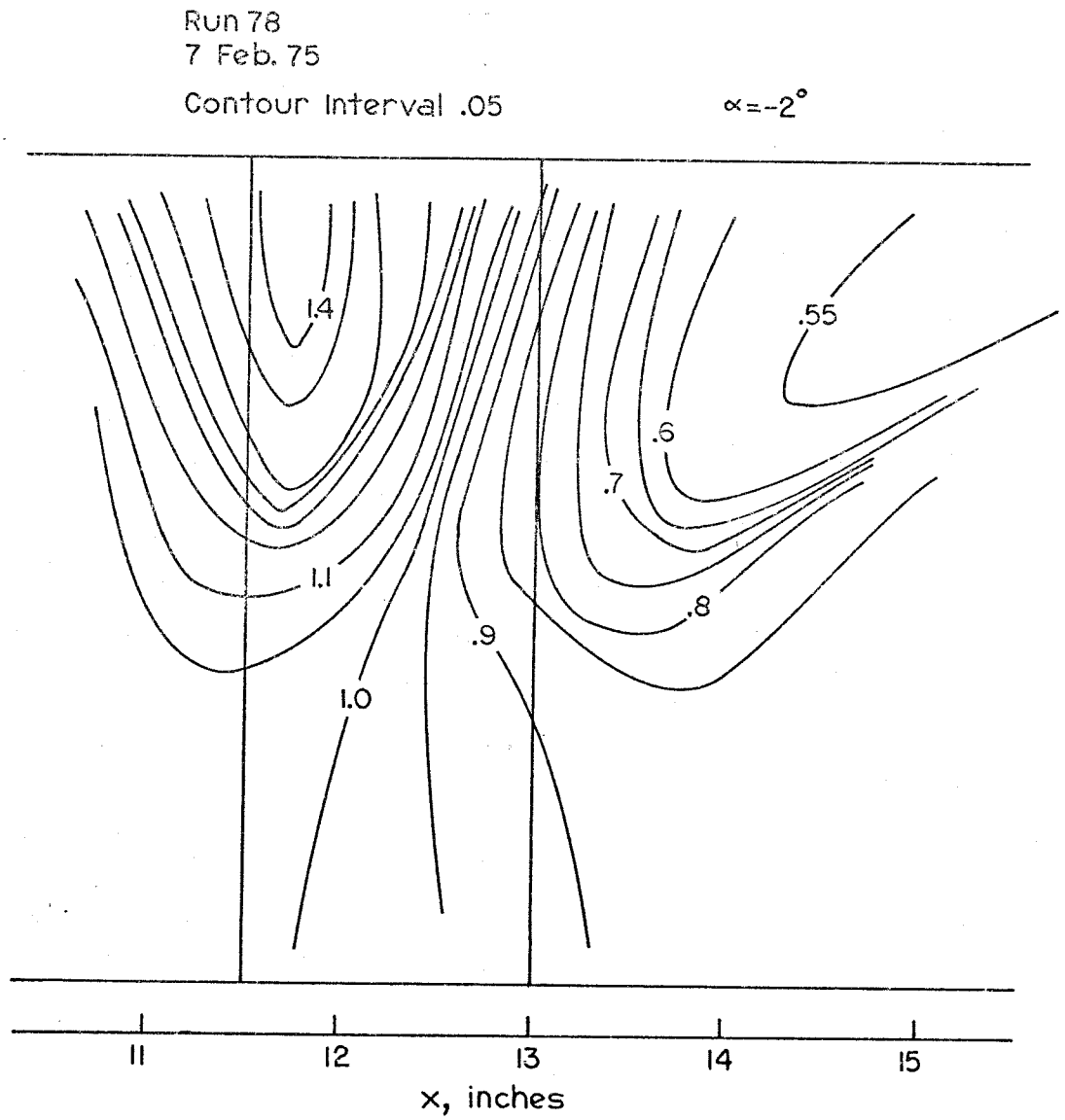

Figure 5.40: Sidewall Pressure Contours, $\alpha = -2^{o}$

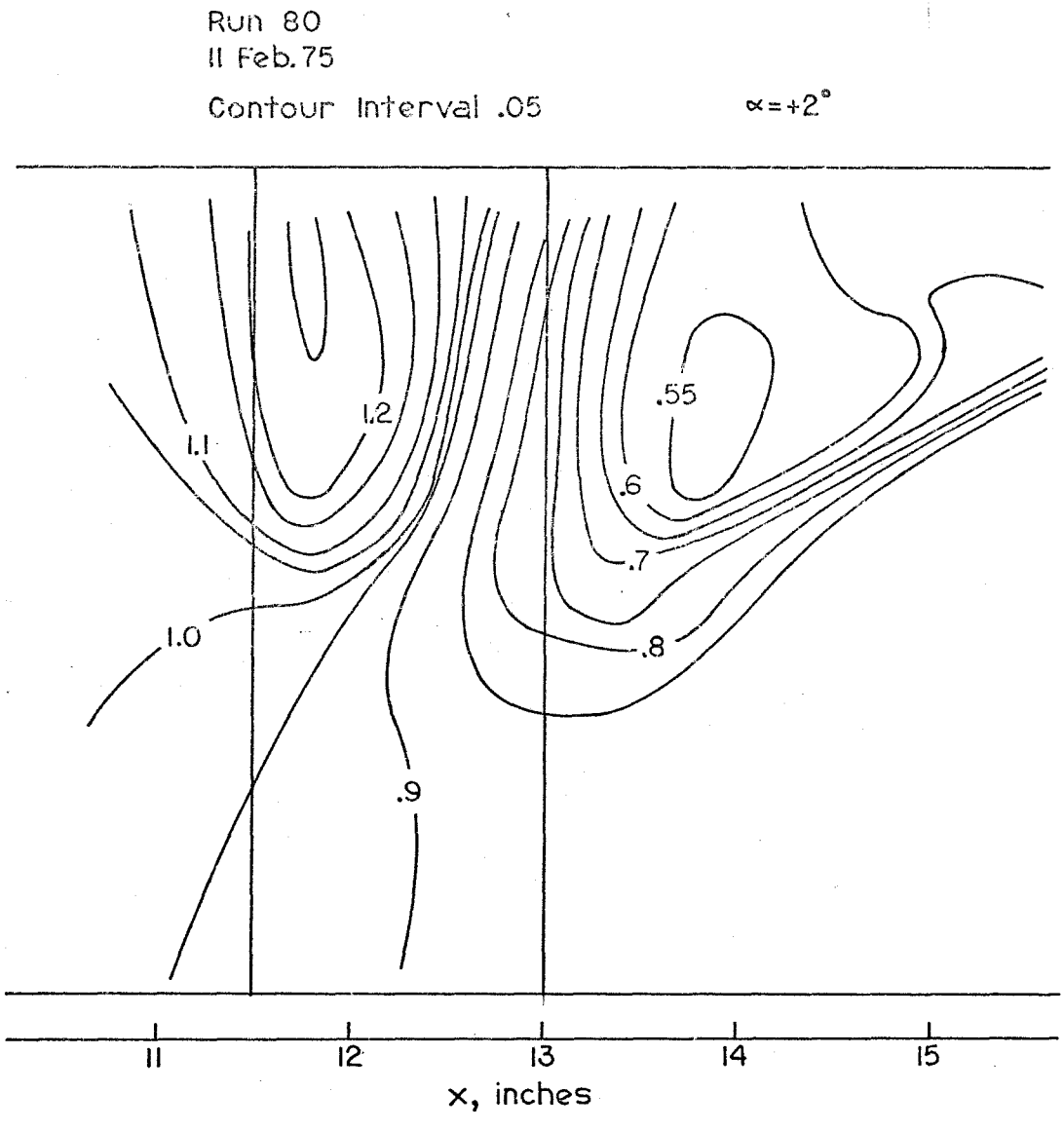

Figure 5.41: Sidewall Pressure Contours, $\alpha = +2^{\circ}$

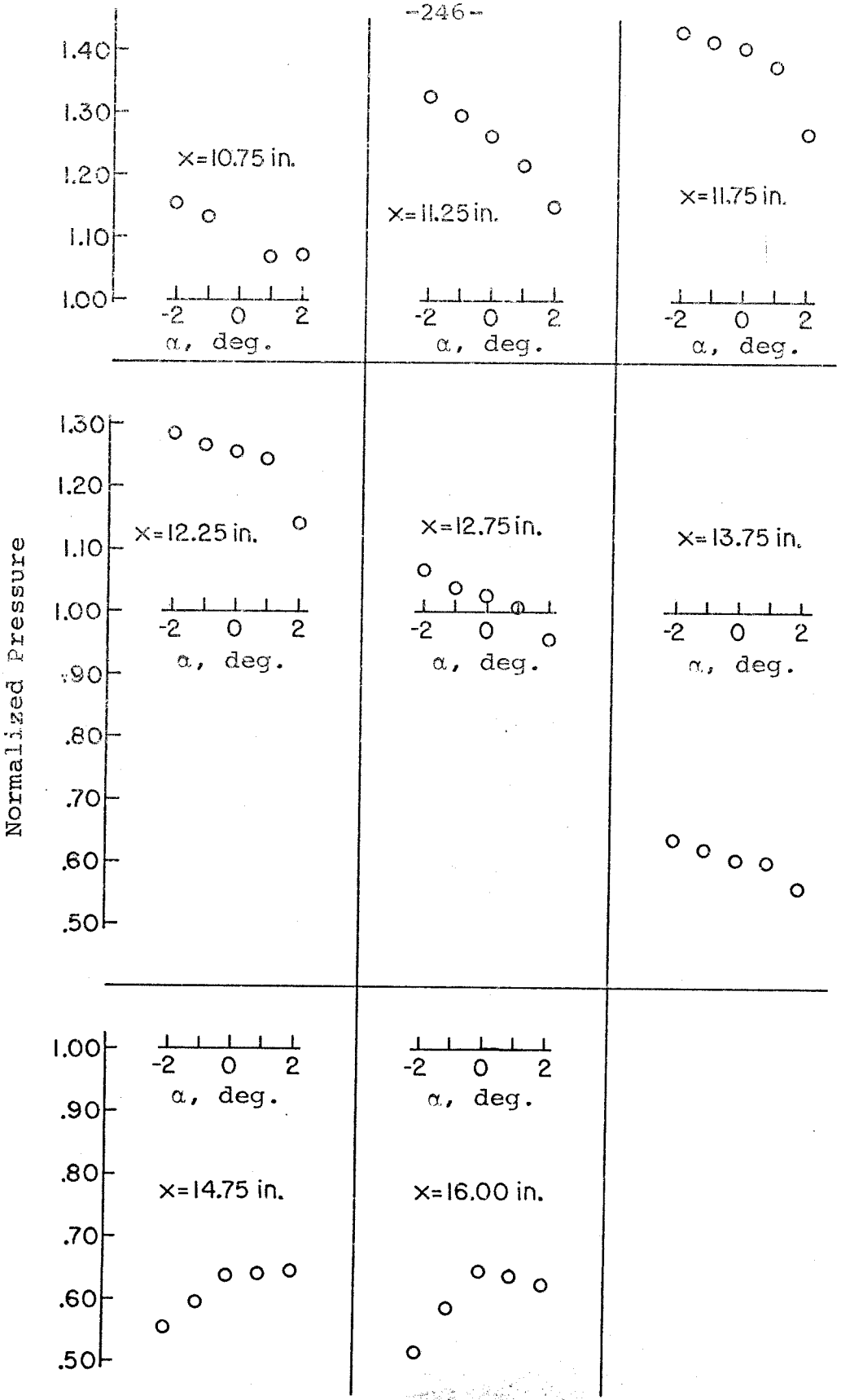

Figure 5.42a: Effect of Angle of Attack on Sidewall Pressure (y = 1.75 inches)

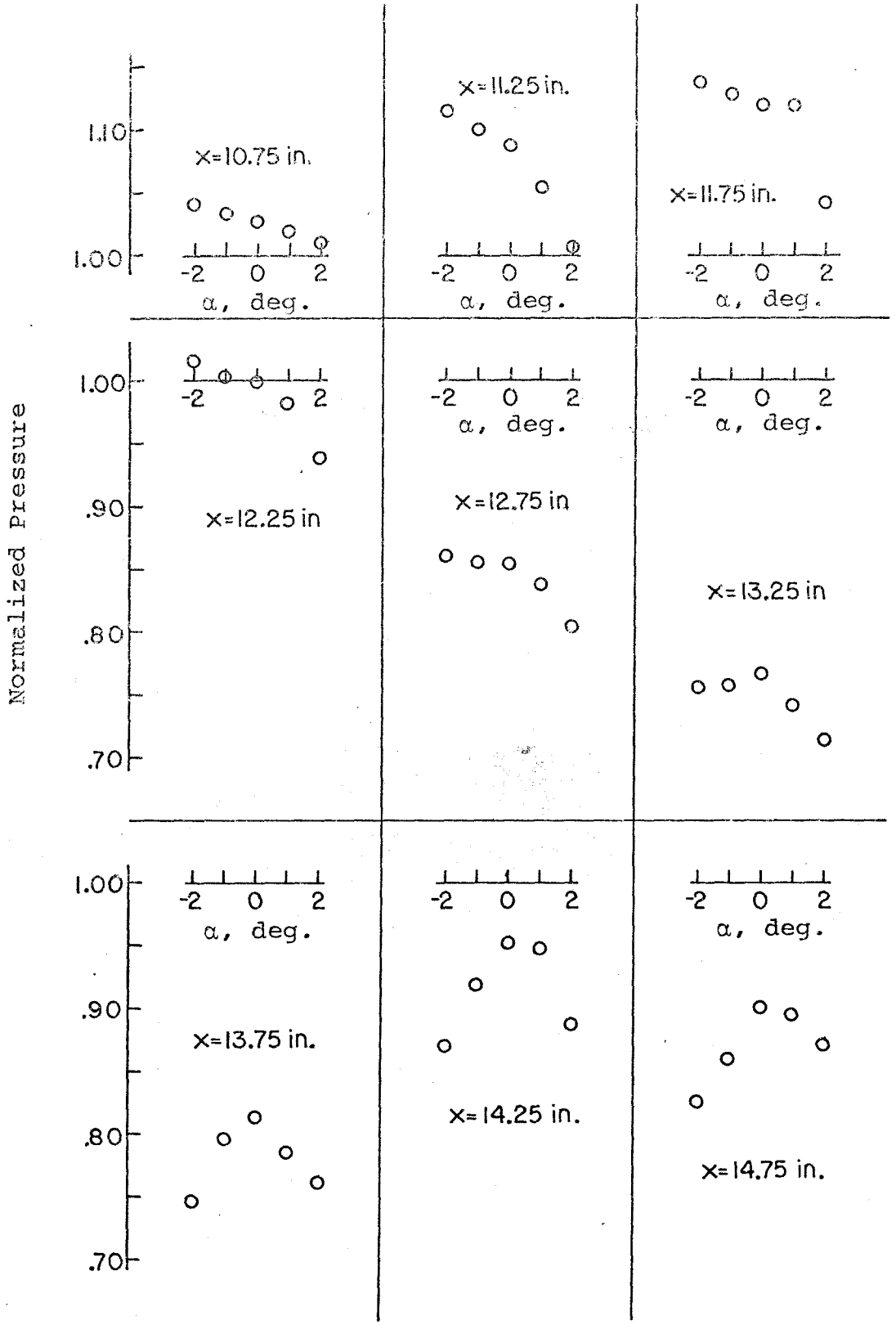

Figure 5.42b: Effect of Angle of Attack on Sidewall Pressure (y = 0)

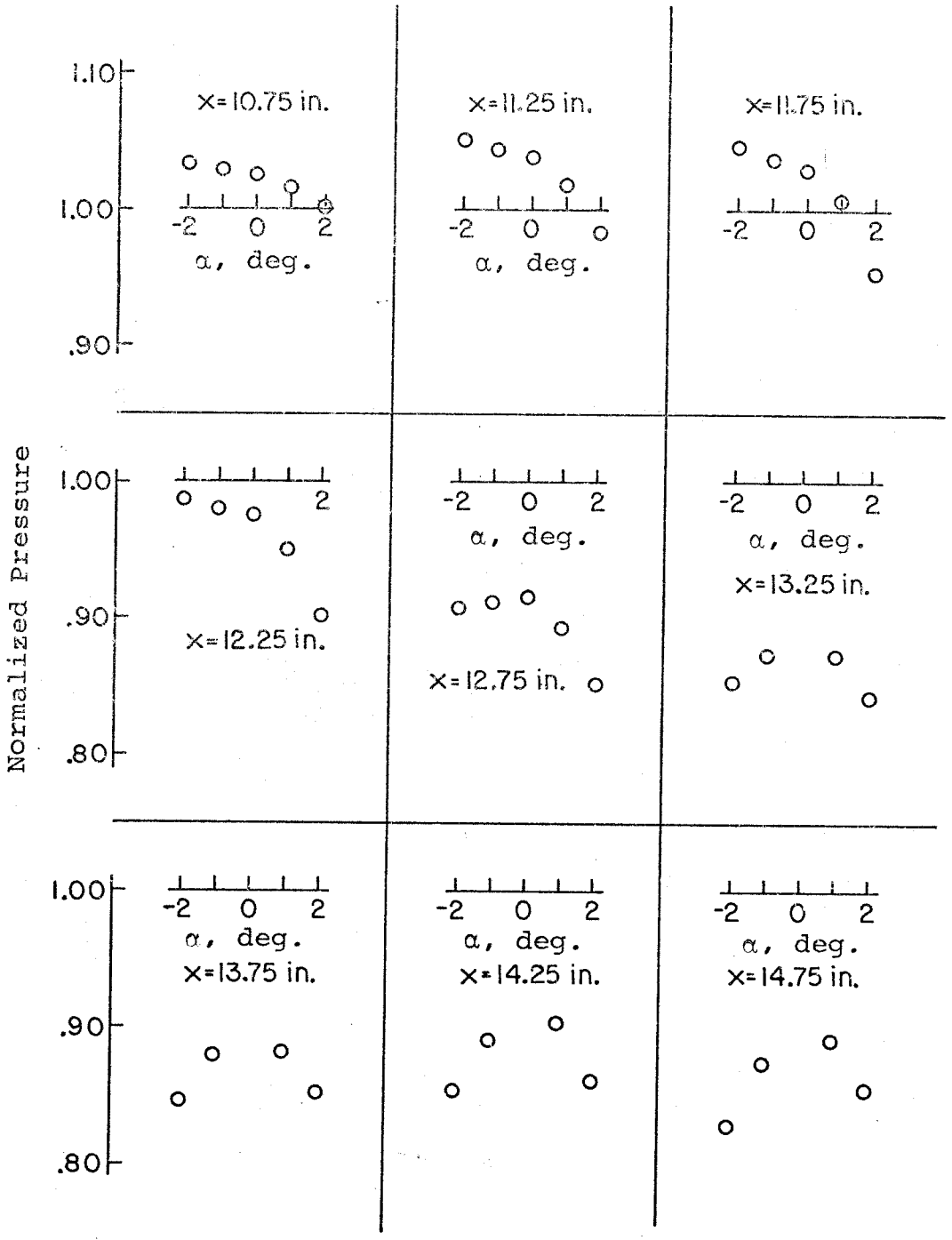

Figure 5.42c: Effect of Angle of Attack on Sidewall Pressure (y = -0.50 Inches)

and continuing to one to two chord lengths downstream of the trailing edge.

This figure shows that near and downstream of the trailing edge of the airfoil the dependence of pressure on α undergoes a basic change in character, going from a monotonic dependence on α to a dependence on $|\alpha|$. In other words, the distribution of pressure on the pressure-surface sidewall is approaching that on the suction surface sidewall. This modification can first be noticed in the subsonic stream, even somewhat upstream of the trailing edge. By $x = 12.75''$, the monotonic character is lost for $y = -.50$; the trend is visible by $x = 12.25''$ (recall that the trailing edge is at $x = 13.00''$).

Because the airfoil is mounted in and pivots about the centerline of the tunnel, at a given value of α the pressure on the tapped sidewall is the same as that on the untapped sidewall at $-\alpha$. Therefore, this tendency for the wall pressure to become symmetric in α means that the lateral pressure gradients in the subsonic stream must die out very quickly (in considerably less than one chord length) downstream of the trailing edge.

In all measurements downstream of the trailing edge, the subsonic stream pressure drops as $|\alpha|$ increases, in response to the increased deflection of the mean sonic surface into the subsonic stream. This is due to the increased loss of total pressure in the supersonic stream, with its consequent decrease in the equilibrium static pressure for the combined flow.

As is to be expected, it takes considerably longer for lateral pressure gradients at $y = 1.75''$ (as measured by the inequality in

Figure 5.42a of pressure for α and $-\alpha$) to die out. A lateral wave in the supersonic stream is only attenuated by interaction with the boundary layers and by interference between expansions and compressions of the airfoil wave system. However, the figure indicates that by x = 16.00" the modification is beginning to dominate.

Therefore, beyond about two chord lengths behind the trailing edge, the lateral and vertical waves in the supersonic stream are the only substantial waves left in the flowfield, as was seen for $\alpha = 0^{\circ}$. Figure 5.43 shows that these waves, caused by the displacements of the sonic surface within the airfoil passage, continue downstream for a considerable distance.

Figure 5.44 shows that all variations in the subsonic stream quickly become unimportant and that the stream takes on a limited homogeneous response (the stream responds as a whole, without substantial cross-flow pressure gradients) to vertically-running waves in the supersonic stream. These waves do not excite any subsonic layer response at all after the first reflection (about x = 17" to 19"), due to their dispersion in interacting with the shear layer.

5.5 Discussion and Conclusions

The previous study of airfoils in a spanwise-varying shear flow has been outlined at the beginning of Section 5.4.1.3. All these studies for compressible flow start with the linearized equation for the perturbation pressure, p:

$$[1 - M_o^2(y)] \frac{\partial^2 p}{dx^2} + \frac{\partial^2 p}{dy^2} + \frac{\partial^2 p}{dz^2} - \frac{2}{M_o(y)} \frac{dM_o}{dy} \frac{\partial p}{dy} = 0$$

or a similar equation for the perturbation velocity potential, ϕ (see

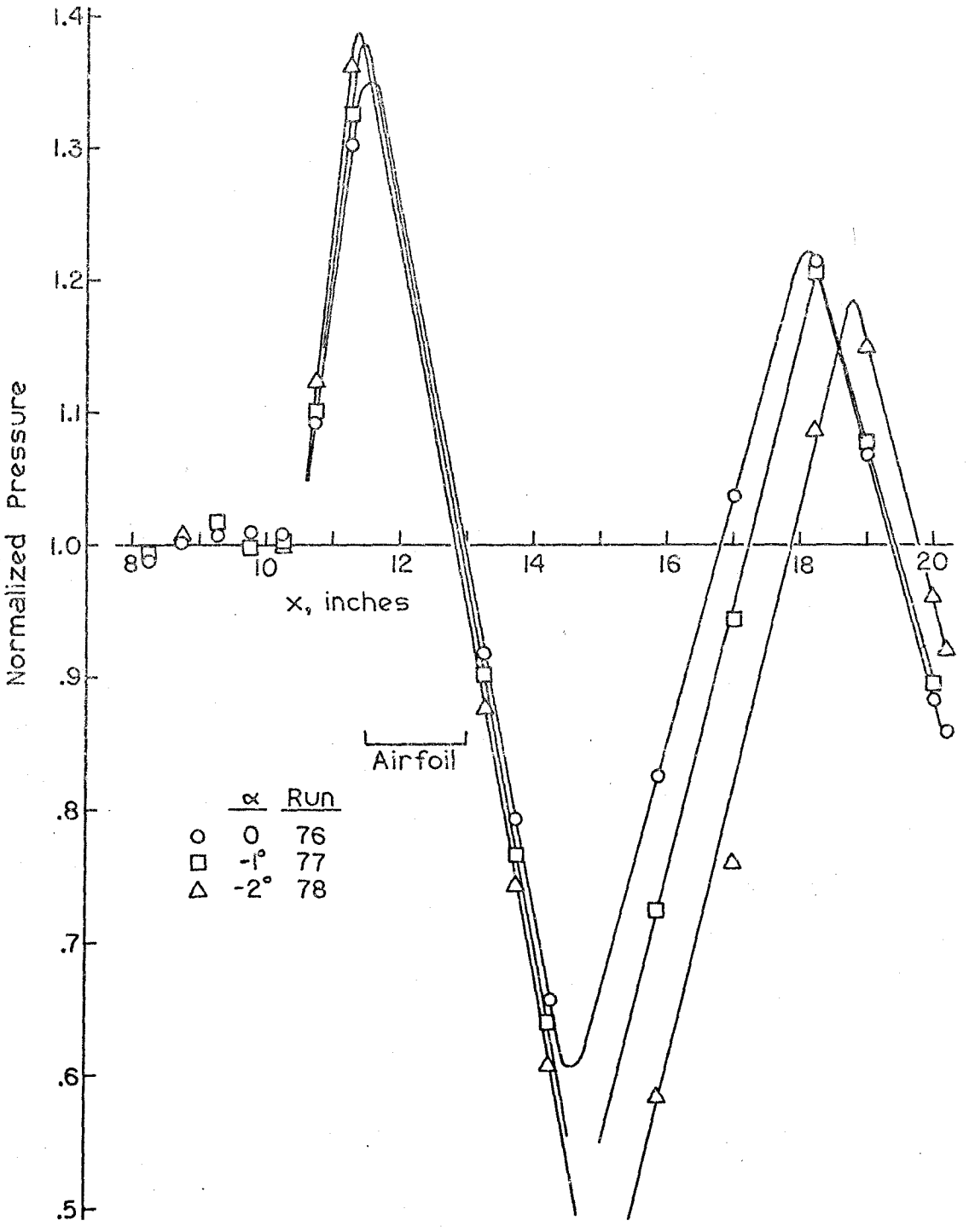

Figure 5.43: Effect of Angle of Attack on Supersonic Wall Centerline Pressure

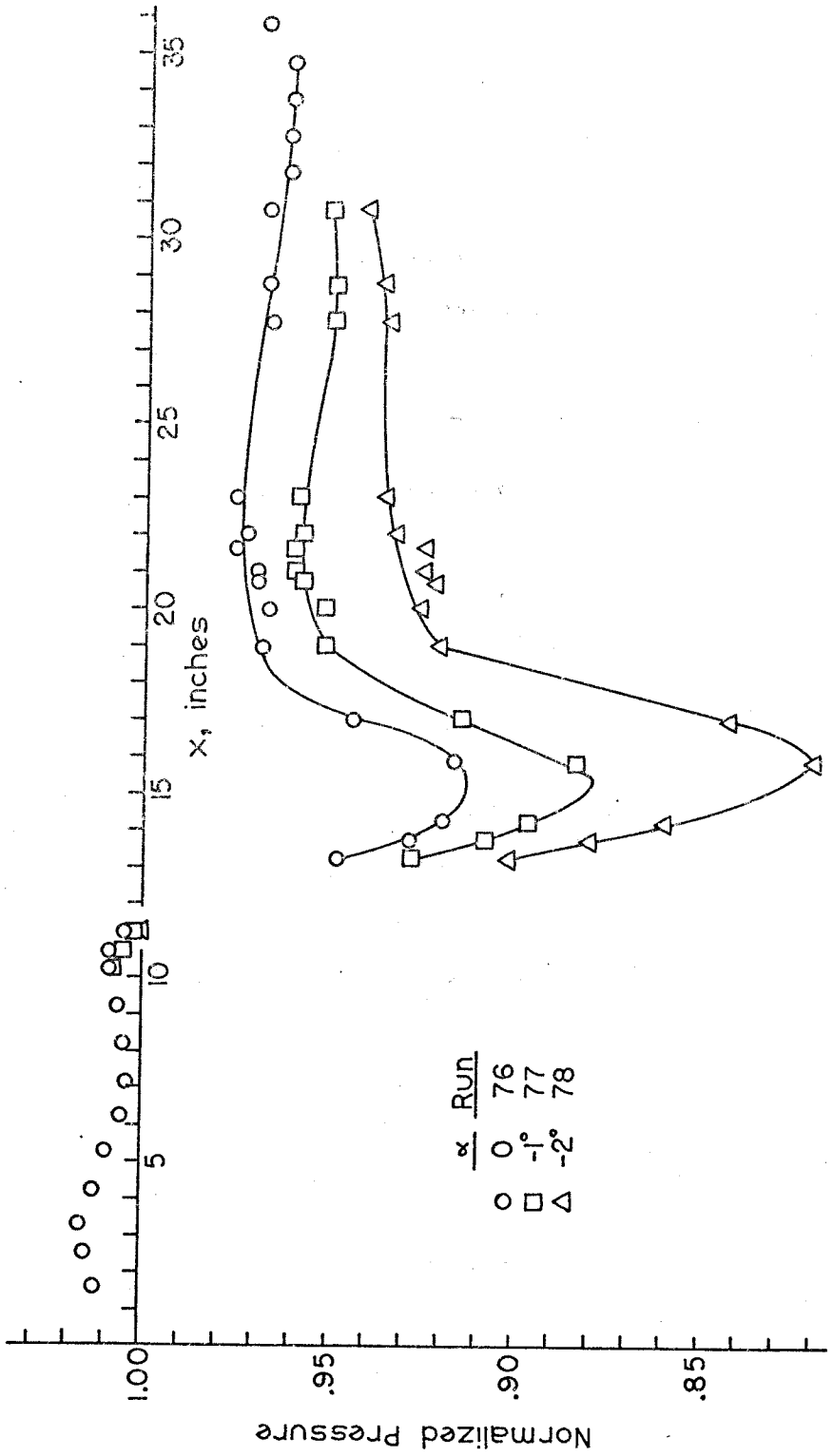

Figure 5.44: Effect of Angle of Attack on Subsonic Wall Centerline Pressure

equation 4.7a). This means the results are those of small-disturbance theory, and that spanwise displacement of stream surfaces is treated only in a grossly-simplified manner. Solutions of this problem are quite complex, and it seems nearly impossible to make physical interpretations about the nature of the flow by examining the resulting equations, which are infinite series. Rather, studies of the equations are made by comparing the numerical results of several cases, and obtaining insight into the processes in operation depends both on good fortune in selecting the specific cases to be evaluated and on the perception of the person examining the results.

Comparisons between theory and experiment for a single airfoil in incompressible shear flow were made by Kotansky[44] in 1965. While his theory was also based on a linearization, he applied a post-solution correction for the spanwise displacement of stream surfaces which improved markedly the agreement between theory and experiment.

Consideration of the effects of transonic shear about an airfoil should be made in two distinct steps: treatment of flow on and very near the surface of the airfoil (including upstream of the airfoil); and discussion of the flow sufficiently far downstream of the airfoil that the perturbations in the flow quantities about some mean value are relatively small.

Within the subsonic flow, there is an induced upwash near the leading edge of the airfoil, strongest near the subsonic wall, which adds an angle of attack (α_i) to the geometric value (α_g). This

effect has been noted in Section 5.4.2. Kotansky[44] concluded from his studies that the three-dimensional influences on the section lift coefficient are due to changes in α_i at a fixed α_g (i.e., that the pressure distribution over the airfoil in a shear flow is the same as in two-dimensional flow, though at some other angle of attack). The data he presents in support of this is persuasive.

However, theoretical studies[38, 39] and the present work (Section 5.4.2) show that α_i vanishes, as would be expected, a short distance into the supersonic stream from the sonic surface. Furthermore, at subsonic stations where compressibility is important, the basic character of the pressure distribution is changed from the two-dimensional[39, 41] in a manner not described simply by changes in the local effective angle of attack. Departures from QTD flow are the most pronounced at the lower supersonic stations[38, 39], where the gradients in the flow properties are very high and the flow is quite "stiff" in that at near-sonic conditions a stream tube is at a minimum possible area and perturbations cross it with minimal reduction in strength. Furthermore, strong and complicated interactions are set up between regions of locally supersonic and subsonic flow. These severe fluctuations are visible in the data, especially in Figure 5.13, near y = 0.

As the distance along the span from the sonic station increases (in either direction) the disturbances become more nearly two-dimensional in both theory[38, 39] and experiment[39]. This is illustrated in Figure 5.45, which compares the current chordwise pressure distributions with experimental data for a 6%-thick biconvex

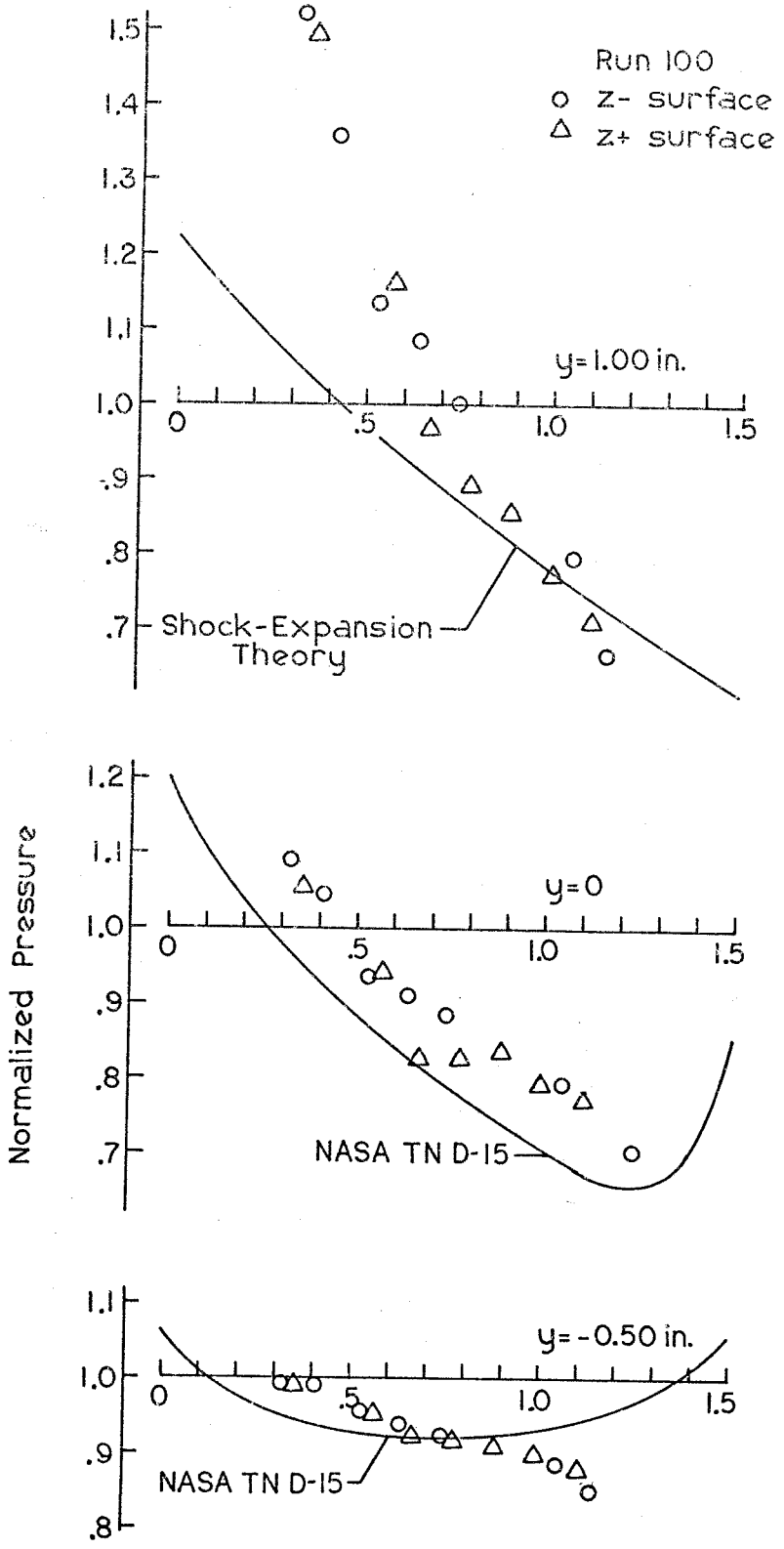

Figure 5.45: Comparison Between Chordwise Pressure Distributions in Two-Dimensional Flow and in Transonic Shear Flow (α = 0, Solid line is 2-D data)

airfoil in uniform subsonic flow[49] and with the results of shock-expansion theory at supersonic speeds. Within the subsonic stream (y = -0.50") the data show reasonable agreement over the first two-thirds of the airfoil chord. At that point, the sonic surface takes a strong downward deflection (see Section 5.4.1.3) and the comparison diverges. Near the sonic surface (y = 0) but still slightly in the subsonic flow, the two traces show similar trends, though the shear flow data has significant perturbations and the entire pressure level is elevated. In the supersonic stream (y = 1.00") agreement is very bad over the first 0.4c, probably due to the fact that the pressure is elevated because of the detached shock. The deviations from attached-shock assumptions in shock-expansion theory are substantial. It was noted that within the lower supersonic portions of the shear layer the bow shock wave was not visible. This is due to the pressure relief through the shear layer into the subsonic stream (see Section 5.4.1.2).

A consistent result of all the studies mentioned in this Section is that airfoil stations at the low-speed side of the shear layer tend to have their loading increased above the QTD levels while those on the high-speed side of the shear layer tend to have reduced loading. Presumably, therefore, the low-speed airfoil section is more prone to stall than in two-dimensional flow. This is because the magnitude of the pressure differences is naturally greater on the high-speed side: these larger pressures tend to be relieved somewhat by spanwise flow into the low-speed side. The perturbations, and thus the lift distribution, are smoothed out. Namba[39] shows that the extent

and magnitude of the unloading are most severe when the maximum Mach number is in the range of 1.0 to 1.2.

The boundary layer moves in response to the spanwise pressure gradient and by moving along a favorable gradient it is thinned out. Kotansky has demonstrated that because of this the airfoil may be more heavily loaded on the high-speed side without stalling than would be possible in two-dimensional flow. The induced drag due to non-uniform circulation along the blade is reduced, too.

The shock wave pattern presented in Figure 5.15 is strongly suggestive of a highly-loaded transonic rotor[10, 52] in the range of tip Mach number near 1.4. This resemblance is quite encouraging, especially in light of Figure 1.2 which shows that the airfoil thickness ratio of 6%, while a good mean value, is too large to be truly representative of typical blades near their tip.

Downstream of the airfoil the effect of interest is the displacement of stream surfaces, particularly the sonic surface, in the spanwise direction. It has been shown (Section 5.4.1.3) that the sonic surface displaces downward about 0.14 inch at zero angle of attack. It is believed that this displacement is governed by the redistribution of total pressure throughout the flow due to the presence of the airfoil. Therefore, this quantity (Δ) can be expected to scale with an airfoil-related parameter, such as the chord ($\Delta = 0.093\ c$) or the maximum thickness ($\Delta = 1.5\ t$). In this particular study, perhaps the thickness is to be preferred. The changes in total pressure are affected only by the drag of the airfoil, with which the thickness is most closely associated. However, in a compressor the

redistribution of total pressure is mainly affected by the lift of the blade, and the chord seems a better scaling parameter.

The lateral pressure gradients have been shown to die out very quickly, and the streamwise gradients nearly as rapidly, in the subsonic stream. This suggests that beyond two chord lengths downstream of the trailing edge the sonic surface is once again planar (except for minor perturbations).

At nonzero angle of attack, the displacement of the sonic surface into the subsonic stream is seen to increase. Even in the case of a lifting airfoil, the surface becomes planar about as quickly as before.

The mean position of the sonic surface (neglecting the presence of any three-dimensional perturbation waves) depends on the upstream flow conditions, the net flow area at a given streamwise station, and the distribution of total pressure in each stream. A successful effort was made to select the various angle of attack comparison runs so that the upstream conditions were virtually identical and the wall geometry (net flow area) was not altered between runs.

The increasing deflection of the sonic surface into the subsonic stream, as angle of attack is increased, is caused by the increasing loss of total pressure in the supersonic stream, largely because of the presence of the nearly-normal branch of the bow shock. Losses of total pressure in the subsonic stream are negligible compared to this (see Figure 5.17). The deflection of the sonic surface is somewhat greater (by about 20%) than that predicted by a linearized calculation using the measured loss of total pressure in

the supersonic stream. This difference is ascribed to nonlinear effects.

This significant displacement of the sonic surface illustrates the breakdown of QTD theory and places limits on the usefulness of linearized analytic calculations which neglect such effects. For the case in question, the QTD theory assumes that streamlines in the $y = 0$ plane downstream of the airfoil (for instance) were at the $y = 0$ plane upstream of the airfoil (0.955 Mach) when in fact they were at about $y = 0.14''$ (1.125 Mach). The shift represents differences for the streamline in its source state of 17.8% in Mach number, 18.0% in total pressure, and 38.8% in dynamic pressure.

Another conclusion of the present study is that the propagation of pressure waves upstream of the leading edge through the subsonic layer is very slight for the case studied. In a more general problem where substantial portions of the subsonic stream are still irrotational, I believe that an upper limit on this upstream propagation can be estimated through conventional potential theory. Consider the same airfoil in uniform subsonic flow at the Mach number in question. As a first approximation, this amounts to neglecting all interactions through the transonic shear layer. In this problem, a scale distance for the decay of pressure perturbations ahead of the airfoil can be determined. This is an upper bound for the scale distance of the full problem, since the inclusion of these upstream interactions causes the relief of subsonic stream overpressures and a consequent contraction of the scale distance.

As the shear layer thickens, its effect is to smooth out the pressure distribution on the airfoil. Sharp compression regions become more diffuse, as was seen in Section 5.4.1.4.

Most of the displacements of the sonic surface (and the shear layer in general) occur within the airfoil passage or within one chord length downstream of the trailing edge. Four actions affect this displacement: the disturbance ahead of the leading edge of the airfoil, which has been seen to be relatively minor; the pressure gradient through the shear layer in the airfoil passage caused by the presence of shock waves over the supersonic portions of the airfoil; the thickness distribution of the airfoil; and the redistribution of total pressure in the flow. Of these, only the total pressure effect has influence on the equilibrium location of the sonic surface for downstream.

VI. SUMMARY

6.1 Results and Conclusions

The important results of this project have already been summarized in Sections 4.7 (wedge experiments) and 5.5 (airfoil experiments).

The two-dimensional problem of a full-width wedge attached to the supersonic (top) wall of the tunnel was studied experimentally and theoretically through a first-order (linearized) calculation using Fourier analysis. Good agreement between theory and experiment was demonstrated. In particular it was interesting to note that the pressure disturbance propagation upstream in the subsonic layer caused by the shock impinging on the shear layer is limited to distances on the order of 0.6 subsonic layer thicknesses. Through parametric studies of the effect of wedge angle, afterbody thickness, and shear layer thickness, the limits of linearized theory for this problem were established.

Studies much less extensive were made of the wedge fixed to the subsonic (bottom) wall of the tunnel. The experimental data returned in this work were of low quality. The computational study indicated a strong correlation between disturbance amplitude on the subsonic wall and the unperturbed choking margin for the same geometric disturbance with varying subsonic stream source conditions.

The airfoil studies focussed on the free airfoil placed in the center of the tunnel, spanning the channel between the top and bottom walls. This airfoil was installed in a flow field consisting of uniform

supersonic and subsonic streams, with a plane shear layer separating the two. Within the shear region, shock waves are weakened considerably; outside the shear region only the bow shock is unaffected by the presence of shear in the unperturbed velocity elsewhere in the flow field. Over the aft one-third of the airfoil chord, the sonic surface takes a strong downward deflection (into the subsonic stream) on the order of 0.1c and remains at approximately this new position through the rest of the test section. This strong displacement represents a breakdown of the quasi-two-dimensional (QTD) theory by which compressor blades are designed. Increases in the geometric angle of attack promote significantly the departure from QTD results. Deviations from QTD pressure distributions on the surface of the airfoil are most significant at the lower supersonic stations.

Downstream of the airfoil, all pressure variations in the subsonic stream are quickly lost except in response to waves in the supersonic stream which are continually reflecting between the shear layer and the supersonic wall.

6.2 Recommendations for Future Research

To pursue the simulation of the compressibility effects of flow over a transonic rotor blade, it seems the next step is to construct a cascade of three or four blades of 1/2" to 3/4" chord in order to study blade-to-blade interactions. Because of the strong influence of the sidewalls, the current study conformed neither to an isolated airfoil experiment nor to a cascade study (in which the sidewall would be regarded as a plane of symmetry). A cascade study would seem particularly fruitful if a two- or three-axis pitot/static probe or a

suitable laser Doppler velocimetry system can be developed.

The three-dimensional flow field studies described here have essentially been confined to the 6%-thick biconvex airfoil. In Section 5.4.1.3 it was hinted that by moving aft on the airfoil the point of maximum thickness, the displacement of the sonic surface might be reduced. Also, it would be interesting to test an airfoil of reduced leading edge deflection angle so that the reflection of the bow shock at the sidewall would be better behaved. Thus, a comparison of the 6%-thick biconvex airfoil with symmetric 6% multiple-circular-arc sections seems desirable.

The study of the effect of angle of attack should be redone with a more sturdy airfoil in order to obtain valid surface pressure data from which the effect of shear on the distribution of section lift coefficient can be deduced. Many of the problems involved in building the instrumented airfoil used in this project could be avoided in the future through a suggestion by W. R. Hawthorne: cast the airfoil with a spar in the middle for strength; instead of using metal tubes for pressure measurements, nylon filaments (say, .015" to .020" diameter) can be strung through the mold and withdrawn after the epoxy hardens. Then it is a trivial matter to drill pressure taps into the resulting cavities.

Because the high-speed nozzle blocks are separately removable, there is an added dimension for study in that different values of M_1 and M_2 are possible. Taking advantage of this, a detailed study of the transonic mixing layer should be performed. Anatol Roshko has suggested the use of inserts on the test section sidewalls to

investigate the effect of shear layer aspect ratio on the growth rate (c. f. Section 3. 2 and the discussion of Figure 3. 6). Spark shadowgraph photographs have hinted at the existence of large-scale structure in the shear layer; a detailed study of this seems worthwhile. E. E. Zukoski has noted that injection of a different gas, such as helium, into the plenum chamber or nozzle on one side (preferably the subsonic side) of the shear layer might provide the difference in index of refraction necessary to photograph the structure with a spark shadowgraph.

It would be interesting to repeat some of the wedge experiments under conditions where the function $F(M_1, M_2, h_1/h_2)$ of equation 4. 31 is positive, so that qualitative behavior of the combined flow is supersonic rather than subsonic.

6. 3 Recommendations for Improvements to the Wind Tunnel

Several modifications to the wind tunnel to improve its operation have been suggested in Chapters III, IV, and V and in Appendix B. They mainly are concerned with reducing the empty-tunnel flow nonuniformities and with reducing the interactions between the test section and the compressor plant. All of these changes are concerned with improving the repeatability of measurements.

The splitter plate shock system should respond well to reductions in the trailing edge taper angle, which currently is 3^{o}. This should be sharpened as much as possible, and the trailing edge should not be blunted deliberately as was done before. In an effort to reduce these extraneous waves it also seems advantageous to employ wall

porosity or some other means to control the trailing edge shock at its first reflection off the supersonic wall.

The window mounting system should be completely redesigned to eliminate the beveled fittings at each end. A design using a rectangular pane of glass is much to be preferred. Care should be exercised in designing a replacement to ensure that a high-quality seal against the atmosphere is formed everywhere.

To eliminate the slow drop in static pressure through the test section, the tunnel support beams should be modified so that the divergence between the top and bottom walls can be increased slightly, say 0.2 inch at the downstream end of the test section.

As outlined in Appendix B, one of the manifestations of the tunnel/compressor plant interaction is a reduction in the system mass flow rate due to losses of total pressure within the test section. One cure, therefore, might be to compensate for test section losses by installing a second throat at the downstream end of the test section to provide better pressure recovery. The tunnel design provides for this feature but it was never installed. Alternatively, direct control of the mass flow, either by a choked orifice in the primary feedline between the compressors and the wind tunnel plenum chambers, or by the bleeding of air into the circuit somewhere between the exit diffuser and the compressor intakes, is suggested.

Oil thrown off the compressors into the gas flow severely limits the duration of a schlieren or shadowgraph run by smearing the inside surfaces of the windows. Also, silica gel from the dryer after a few runs clogs the anti-turbulence screen in the supersonic

plenum chamber so that it must be removed and cleaned. This is especially severe on the first run of the Transonic Shear Flow Wind Tunnel after one or more runs of the Hypersonic Wind Tunnel. Therefore, a separator should be installed in the main feedline, as close to the tunnel as possible.

The author feels that a three-axis traversing probe system for the tunnel is feasible if a future program should warrant its development. The primary consideration is that the blockage (in terms of projected frontal area) should be kept below 3%. This suggests a system similar to that in the GALCIT Hypersonic Wind Tunnel, where the probe runs into the test section from the downstream diffuser where streamwise translations are controlled and the pressure line is removed from the tunnel. Lateral and vertical translations could be driven through a full-span strut mounted in the test section several inches downstream of the measurement region. To obtain valid data, the measuring point of the probe should be at least two inches upstream of any obstructions such as a strut, shroud, etc. Of course, for velocity vector information the ideal approach would be a laser Doppler system.

APPENDIX A: Additional Wind Tunnel Information

This appendix is to provide the reader with supplementary information on the wind tunnel operation and on the points at which wall pressure data can be obtained.

Table A-1, presented at the end of this appendix, is a log of all runs (including those which were aborted with no data) through the completion of this project in September 1975.

A summary of the operating procedures for a typical run will be presented here. It should be understood that these procedures are guidelines only, and that modifications were not unusual. The full set of procedures is described in a manual at GALCIT prepared by this author.

To lower the dewpoint of the air in the wind tunnel circuit, a silica-gel dryer was generally operated overnight before a run. Nominally, this would be expected to lower the dewpoint to about -40°F to -60°F. Due to various problems with the drying agent, this operation was not completely reliable.

Pressure data were typically obtained by a Statham 0-15 psia strain gauge transducer, powered by a 5-volt supply built at Caltech. Before each run, this transducer was calibrated at vacuum and atmospheric pressure. The value of the ambient pressure was obtained through a barometer accurate to 0.01 inch of mercury.

To prevent damage to the wind tunnel windows should an earthquake occur while the system is idle, the windows are not rigidly sealed against the tunnel until a few minutes before the system is started. The difficulties associated with the windows have been

described previously.

When all is in readiness to start up, the system is set for operation except that valve 52 in the main feedline is closed. The motors are started and the circuit is evacuated in a no-flow condition. When the air pressure drops to about 2 psia, this valve is opened and flow is established. The valve in the subsonic feedline is adjusted to match the pressure at each nozzle exit as indicated by pressure taps in the top and bottom walls.

To shut down the tunnel, the motors are simply shut off and the circuit is vented to the atmosphere.

Pressure taps generally were installed on the top and bottom wall sections on the centerline at one-inch intervals throughout the test section. The first removable sections, spanning the distance from x = 3 inches to 15 inches, had taps at intervals of $\frac{1}{2}$-inch on the centerline. In addition, one section, which could be mounted as either the supersonic or subsonic wall, had taps at $\frac{1}{2}$-inch intervals in the streamwise direction on and $\frac{1}{2}$-inch to either side of the centerline. The distribution of taps on the sidewall is shown in Figure A. 1.

These static pressure taps were connected by vinyl tubes to toggle valve or to manually-operated Scanivalves. The transducer was then switched among the taps as desired.

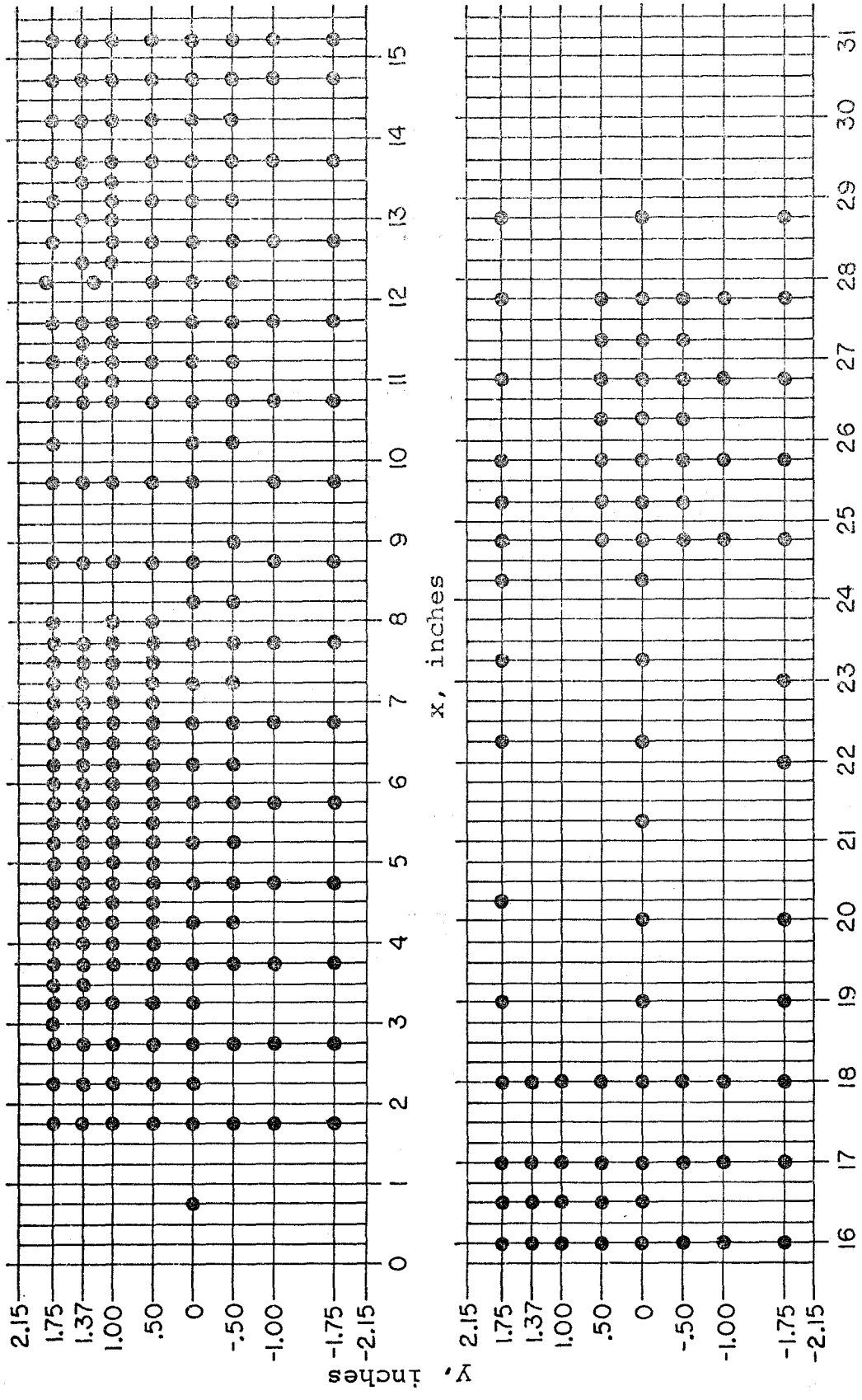

Figure A.1: Location of Sidewall Static Pressure Taps

TABLE A-1 Transonic Shear Flow Wind Tunnel Log

Run	Day	Type of Run	M_1	M_2	Match[1]	Notes
1	19 March 73	Empty				(2)
2	20 March 73	Half-Span Strut, Sta. 1				(3)
3	22 March 73	"				(3)
4	26 March 73	"				(3)
5	2 April 73	"				(3)
6	12 April 73	"				(3)
7	18 April 73	"				
8	2 July 73	"				
9	2 July 73	"				
10	3 July 73	"				
11	5 July 73	Half-Span Strut, Sta. 2				
12	16 July 73	Half-Span Strut, Sta. 3				
13	17 July 73	Half-Span Strut, Sta. 4				
14	24 July 73	"				
15	30 July 73	"				(4)
16	2 Aug. 73	"				(4, 5)
17	8 Aug. 73	"				(4, 6)
18	9 Aug. 73	"				(4)
19	15 Aug. 73	"				(6)
20	16 Aug. 73	"				(6)
21	20 Aug. 73	"				(6)

TABLE A-1 (continued)

Run	Day	Type of Run	M_1	M_2	Match[1]	Notes
22	23 Aug. 73	Half-Span Strut, Sta. 4				(6)
23	28 Aug. 73	"				(6)
24	5 Sept. 73	"				
25	8 Oct. 73	Full-Span Strut, Sta. 4	1.357	.532	.995	(3, 6)
26	10 Oct. 73	Full-Span Strut, Sta. 3	1.300	.582	1.000	(6)
27	15 Oct. 73	Full-Span Strut, Sta. 2	1.323	.568	1.000	(6)
28	17 Oct. 73	Full-Span Strut, Sta. 1	1.357	.547	1.000	(6)
29	22 Oct. 73	Full-Span Strut, Sta. 1	1.350	.555	.981	(6)
30	25 Oct. 73	Full-Span Strut, Sta. 4	1.365	.555	1.000	(6)
31A	26 Oct. 73	Empty	1.340	.597	1.000	
31B	26 Oct. 73	Empty	1.338	.613	1.012	(7)
32A	31 Oct. 73	Empty	1.379	.602	.987	
32B	31 Oct. 73	Empty	1.381	.515	.836	
32C	31 Oct. 73	"	1.383	.455	.736	
33A	2 Nov. 73	"	1.378	.643	1.056	
33B	2 Nov. 73	"	1.372	.660	1.073	
33C	2 Nov. 73	"	1.378	.597	.976	
34A	6 Nov. 73	"	1.368	.588	.961	
34B	6 Nov. 73	"	1.365	.580	.941	
34C	6 Nov. 73	"	1.368	.568	.916	
35A	19 Nov. 73	"	1.410	.630	.999	

TABLE A-1 (continued)

Run	Day	Type of Run	M_1	M_2	Match	Notes
35B	19 Nov. 73	Empty	1.410	.618	.978	
35C	19 Nov. 73	"	1.410	.607	.962	
36A	21 Nov. 73	3/32 in. Supersonic 4° Wedge, 10" L. E.	1.410	.588	1.002	(6)
36B	21 Nov. 73	"	1.412	.565	.964	
37A	5 Dec. 73	"	1.412	.588	.998	(6)
37B	5 Dec. 73	"	1.412	.578	.980	
37C	5 Dec. 73	"	1.412	.568	.961	
38A	19 March 74	"	1.415	.590	.999	
38B	19 March 74	"	1.417	.585	.981	
38C	19 March 74	"	-	-	.958	
39	4 April 74	"	1.413	.590	1.000	
40A	25 April 74	3/32 in. Supersonic 8° Wedge, 10" L. E.	1.410	.572	1.000	(6)
40B	25 April 74	"	1.408	.565	.981	
40C	25 April 74	"	1.408	.550	.960	
41	2 May 74	Full-Span Strut, Sta. 2	1.397	.531	1.001	(8)
42	9 May 74	Empty	-	-	-	(2)
43A	16 May 74	"	1.385	.610	1.000	(8)
43B	16 May 74	"	1.390	.598	.988	(8)
44A	23 May 74	"	1.415	.628	.999	
44B	23 May 74	"	1.413	.610	.961	
45A	6 June 74	3/32" Subsonic 4°Wedge, 10" L. E.	1.423	.612	1.000	

TABLE A-1 (continued)

Run	Day	Type of Run	M_1	M_2	Match	Notes
45B	6 June 74	3/32" Subsonic 4° Wedge, 10" L. E.	1.422	.593	.962	
46	18 June 74	"	1.420	.600	.999	(6)
47	26 June 74	Sidewall Airfoil	1.397	.610	1.000	
48	2 July 74	"	1.392	.635	1.001	
49	10 July 74	Full-Span Strut, Sta. 2	1.410	.575	.999	
50	10 July 74	Empty	1.390	.667	.999	
51A	16 July 74	3/32" Supersonic 8° Wedge, 10" L. E.	1.380	.588	1.000	
51B	16 July 74	"	1.380	.585	.980	
52	23 July 74	3/32" Supersonic 4° Wedge, 10" L. E.	1.435	.597	1.000	
53	23 July 74	Empty	1.410	.651	1.000	
54	30 July 74	3/32" Supersonic 2° Wedge, 10" L. E.	1.408	.631	1.000	
55	1 Aug. 74	Sidewall Airfoil	1.402	.632	1.000	
56	3 Oct. 74	Empty	1.380	.685	1.001	(9)
57	11 Oct. 74	3/32" Supersonic 2° Wedge, 17" L. E.	1.360	.654	1.000	
58	14 Oct. 74	"	1.395	.615	1.001	(6)
59	16 Oct. 74	3/64" Supersonic 4° Wedge, 10" L. E.	1.415	.636	.999	
60	16 Oct. 74	3/64" Supersonic 2° Wedge, 10" L. E.	1.400	.642	.998	
61	17 Oct. 74	3/32" Subsonic 4° Wedge, 10" L. E.	1.413	.610	1.000	
62	17 Oct. 74	3/32" Subsonic 2° Wedge, 10" L. E.	1.385	.628	1.000	
63	18 Oct. 74	3/32" Supersonic 2° Wedge, 10" L. E.	1.410	.605	1.001	(6)
64	22 Oct. 74	3/64" Supersonic 4° Wedge, 10" L. E.	1.410	.628	1.000	(6)

TABLE A-1 (continued)

Run	Day	Type of Run	M_1	M_2	Match	Notes
65	25 Oct. 74	3/64" Supersonic 4° Wedge, 17" L.E.	1.413	.618	1.000	(6)
66	12 Dec. 74	Sidewall Airfoil	1.436	.520	.999	(10)
67	8 Jan. 75	"	1.433	.530	1.001	(10)
68	13 Jan. 75	"	1.398	.612	.998	
69	15 Jan. 75	"	1.405	.598	1.000	
70	17 Jan. 75	Fixed Airfoil, $\alpha = 0^\circ$, $\chi_{LE} = 11.5"$	1.397	.590	1.000	
71	21 Jan. 75	"	1.398	.582	.999	(6)
72	24 Jan. 75	"	1.395	.586	1.000	(6)
73	27 Jan. 75	"	1.385	.592	1.000	(6)
74	30 Jan. 75	Empty	1.405	.645	1.000	
75	3 Feb. 75	Fixed Airfoil, $\alpha = 0^\circ$, $\chi_{LE} = 11.5"$	1.418	.567	1.000	
76	5 Feb. 75	"	1.425	.567	1.000	
77	6 Feb. 75	Fixed Airfoil, $\alpha = -1^\circ$, $\chi_{LE} = 11.5"$	1.420	.573	1.000	
78	7 Feb. 75	Fixed Airfoil, $\alpha = -2^\circ$, $\chi_{LE} = 11.5"$	1.420	.578	.999	
79	10 Feb. 75	Fixed Airfoil, $\alpha = +2^\circ$, $\chi_{LE} = 11.5"$	1.420	.581	.999	
80	11 Feb. 75	"	1.420	.588	.999	
81	13 Feb. 75	Fixed Airfoil, $\alpha = +1^\circ$, $\chi_{LE} = 11.5"$	1.431	.580	1.001	(10)
82	18 Feb. 75	Fixed Airfoil, $\alpha = +2^\circ$, $\chi_{LE} = 11.5"$				(6)
83	19 March 75	Free Airfoil, $\alpha = 0^\circ$, $\chi_{LE} = 11.5"$	1.379	.587	1.000	
84	27 March 75	"	1.379	.582	1.001	
85	1 April 75	"	1.385	.598	1.001	(6)
86	4 April 75	"	1.379	.610	1.001	(6, 10)

TABLE A-1 (continued)

Run	Day	Type of Run	M_1	M_2	Match	Notes
87	11 April 75	Free Airfoil, $\alpha = 0^\circ$, $\chi_{LE} = 11.5''$	1.395	.594	1.000	(10)
88	17 April 75	"	1.372	.617	1.000	
89	28 April 75	Empty	1.387	.672	.999	
90	30 April 75	"	1.410	.648	1.000	
91	2 May 75	Free Airfoil, $\alpha = 0^\circ$, $\chi_{LE} = 5.0''$	1.444	.544	.999	
92	8 May 75	"	1.429	.510	1.000	
93	13 May 75	Free Airfoil, $\alpha = 0^\circ$, $\chi_{LE} = 11.5''$, Pitot Sta. 3	1.424	.532	1.000	
94	14 May 75	Pitot Probe at Sta. 3	1.427	.571	.999	
95	15 May 75	"	1.425	.574	1.000	
96	20 May 75	Fixed Airfoil, $\alpha = 0^\circ$, $\chi_{LE} = 11.5''$, Static Probe at Sta. 3	1.417	.532	1.000	
97	27 May 75	Sidewall Airfoil				
98	5 June 75	Free Airfoil, $\alpha = -1^\circ$, $\chi_{LE} = 11.5''$				
99	17 June 75	Free Airfoil, $\alpha = 0^\circ$, $\chi_{LE} = 11.5''$	1.377	.573	.999	(11)
100	18 June 75	"	1.383	.561	1.001	(11)
101	9 July 75	"	-	-	-	(3)
102	16 July 75	"	1.396	.606	1.000	(11)

Explanation of notes on following page.

TABLE A-1 (continued)

Notes

(1) Ratio of nozzle exit pressure, subsonic to supersonic.

(2) Run aborted due to leaks.

(3) No data obtained due to instrumentation failure.

(4) Fixed pitot probe mounted in supersonic wall at Sta. 1.

(5) First use of the dryer to remove water from the air in the circuit before a run. This was done for all subsequent runs.

(6) Schlieren photographs taken.

(7) This was a shutdown of the tunnel and immediate restart to check the repeatibility of runs without additional adjustments of the controls. The results were unsatisfactory.

(8) Marginal data quality.

(9) Orifice plate was removed for this run.

(10) Oil flow study.

(11) Spark shadowgraph photos taken.

APPENDIX B. Tunnel/Compressor Plant Interactions

The schematic diagram of Figure B. 1 is proposed in an effort toward understanding the interactions between the wind tunnel and the compressor plant. In reality, the system is a closed circuit (dashed line) as is shown in Figure 2. 1, page 12, but vents are open to the atmosphere just downstream of the pumps. It is assumed that the presence of these vents fixed part of the circuit at atmospheric pressure. Neglecting any slight leakage into the circuit, in steady-state operation the net mass flow rate through these vents must be zero.

It is assumed that models in the test section affect the compressor plant by modifying the total pressure of the flow at the compressor intake. Neglecting flow losses, this pressure can be put as:

$$P_i = \frac{\dot{m}_1 P_{t1} + \dot{m}_2 P_{t2}}{\dot{m}_1 + \dot{m}_2} \quad . \tag{B. 1}$$

Because $\dot{m}_1$ is nearly three times as large as $\dot{m}_2$, and a given model causes a greater loss of total pressure in stream 1 than in stream 2, changes in P_i are dominated by losses in the total pressure of the supersonic stream. Since the supersonic stream passes through a throat with constant upstream conditions for all test section configurations (in this idealized model), $\dot{m}_1$ must remain constant.

The compressor plant operates at a constant intake volumetric flow rate. Therefore, changes in P_i must result in changes to the overall mass flow rate, thus changing $\dot{m}_2$:

$$\frac{\Delta \dot{m}_2}{\dot{m}_2} = \frac{\Delta P_i}{P_i} \tag{B. 2}$$

accurate to first order.

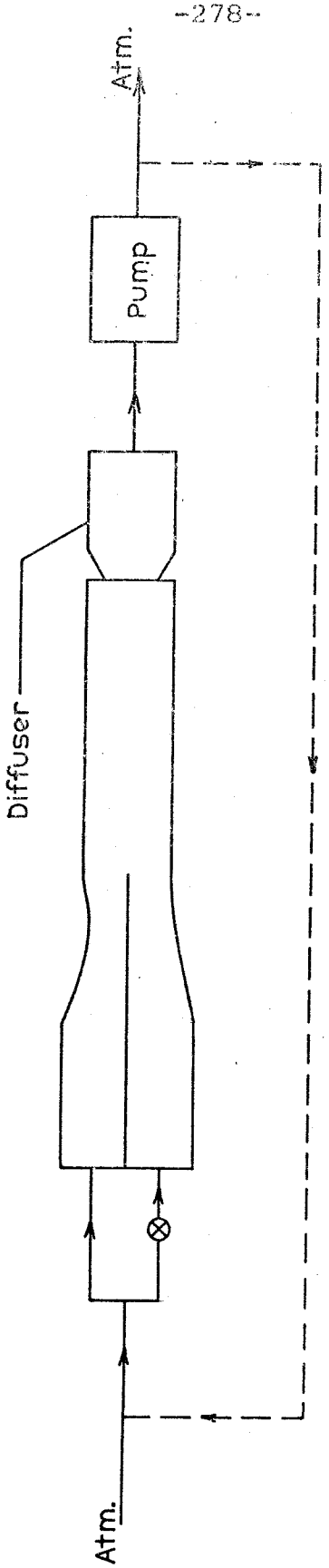

Figure B.1: Schematic Diagram of Wind Tunnel/Compressor Plant Interaction

For an aircoil of chord c in a channel of width b, the net loss of total pressure is given by

$$\frac{\Delta P_t}{P_t} = -\frac{\gamma}{2} M^2 C_D \left(\frac{c}{b}\right) , \qquad (B.3)$$

where C_D is the drag coefficient based on planform area.

Using this model with the assumption that P_{t2} is constant (i.e., pressure in the subsonic plenum chamber is unaffected by this interaction) the effect of the half-span pitot strut blockage on the nozzle exit pressure will be estimated. The results of the calculation may be compared with Figure 3.12, a portion of which is replotted as Figure B.2.

Recall that the strut enters the flow from the subsonic wall. As long as the strut is entirely confined to the subsonic stream, the losses (and thus the interaction) are assumed to be negligible, but must be considered once an appreciable portion of the strut is in the supersonic stream.

The strut is a double-wedge section with a chord of 5/16-inch and a maximum thickness of 1/16-inch (t/c = 0.2). Hoerner[51] presents data based on the transonic similarity rule which yields an estimate of $C_D = 0.219$ at Mach 1.4. The thickness ratio of the strut is larger than would normally permit the use of a similarity rule, but only a rough estimate of the effect is desired. Several phenomena, such as the flow loss through the pipes and its dependence on the mass flow rate, have been neglected which probably have a significant influence.

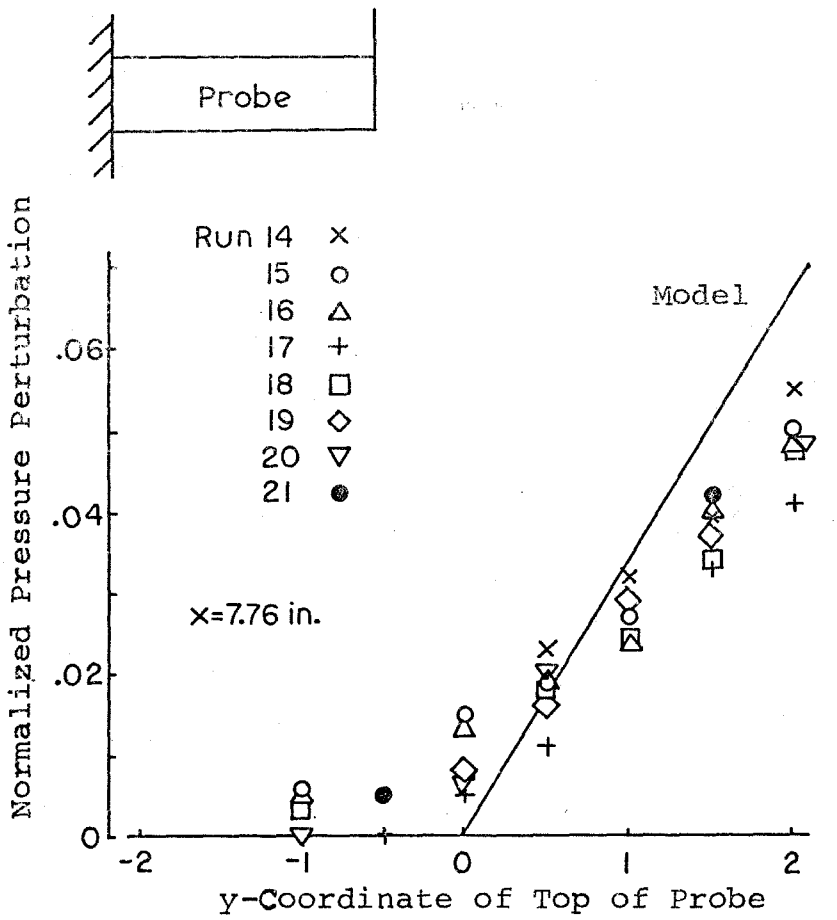

Figure B.2: Comparison of Interaction Model with Experimental Data

From this, the supersonic stream loss of total pressure can be estimated at 3.0 per cent using eq. (B.3). The decrease in $\dot{m}_2$ therefore is 11.1 per cent, and M_2 drops from 0.60 to 0.50. This causes a rise in the nozzle exit static pressure, P_2, of about 7 per cent. In Figure B.2, this estimate is seen to over-predict somewhat the actual interaction effect, which was measured in the range of 4 to 5 per cent. Considering the number of simplifying approximations made, it is felt that this represents reasonable accuracy.

The interaction takes the form of changes in the system mass flow rate due to losses of total pressure in the test section of the wind tunnel. Several means of compensation seem possible.

The first method would be to install a second throat in the exit diffuser of the wind tunnel, thus increasing the pressure recovery and offsetting test section losses. Or, perhaps the solution is to control the mass flow rate by placing a choked orifice in the primary feedline between the exit of the compressors and the wind tunnel. Another technique which suggests itself is direct control of the system mass flow rate through the bleeding of air into the circuit upstream of the compressor intakes.

APPENDIX C. Linearized Theory Program

The program described in this appendix was prepared to solve the equations derived in Section 4.3 for the supersonic and subsonic wedge problems.

Figure C.1 presents in the form of a flow chart the sequence of operations performed by the program. The main program acts as a bookkeeper and performs all input-output duties. Computations are performed in various subroutines.

Table C-1 identifies the variable names used within the program. Figures C.2 through C.12 present listings of the main program and all the subprograms. Figure C.13 is a sample of the output for the baseline supersonic and subsonic wedge cases. The following descriptions outline the duties of the subprograms.

Main Program

Sets initial data, controls output and proper sequence for calling POLES and XPHI.

Subroutine POLES

Contains logic for a modified Newton's method solution to find the zeros of function **F**, and also establishes the number of actual terms to be evaluated as corrections to the asymptotic solution.

Function F

Contains the functions of eq. (4.30), whose roots are the poles k_r and k_i.

Subroutine INPUT

Reads in the values of the system variables into the program according to the format of Table C-2.

Function XPHI

Causes the problem of a single wedge to be solved for the derivatives of ϕ at a specific point (x, y).

Function XINT

Causes calculation of a specific I_{mn}; evaluates I_{2n} and determines for all other integrals the correct half-plane contour.

Function XINT2

Evaluates all the integrals I_{mn3}; for other integrals, causes a preset number of actual terms to be summed and also causes calculation of the asymptotic solution.

Function RELTRM

Evaluates a specific term of any actual series.

Function ASYSER

Finds X, Y, a, and z for the asymptotic series so that the expression is in the form

$$\hat{I}_{mn\nu} = X\begin{pmatrix}\mathrm{Im}\\ \mathrm{Re}\end{pmatrix}\left[e^{y} \sum_{n} \frac{1}{n+a} z^{n} \right] \quad . \tag{C. 1}$$

Function CSUM

This is a buffer between ASYSER and CBSER whose purpose is to put z and a into the proper form.

Function CBSER

Given z, a, and the limits of n from the series ASYSER, this routine performs the summation

$$\sum_{n} \frac{1}{n+a} z^{n} \quad .$$

It invokes an approximation series for faster convergence if necessary depending on the magnitude of z.

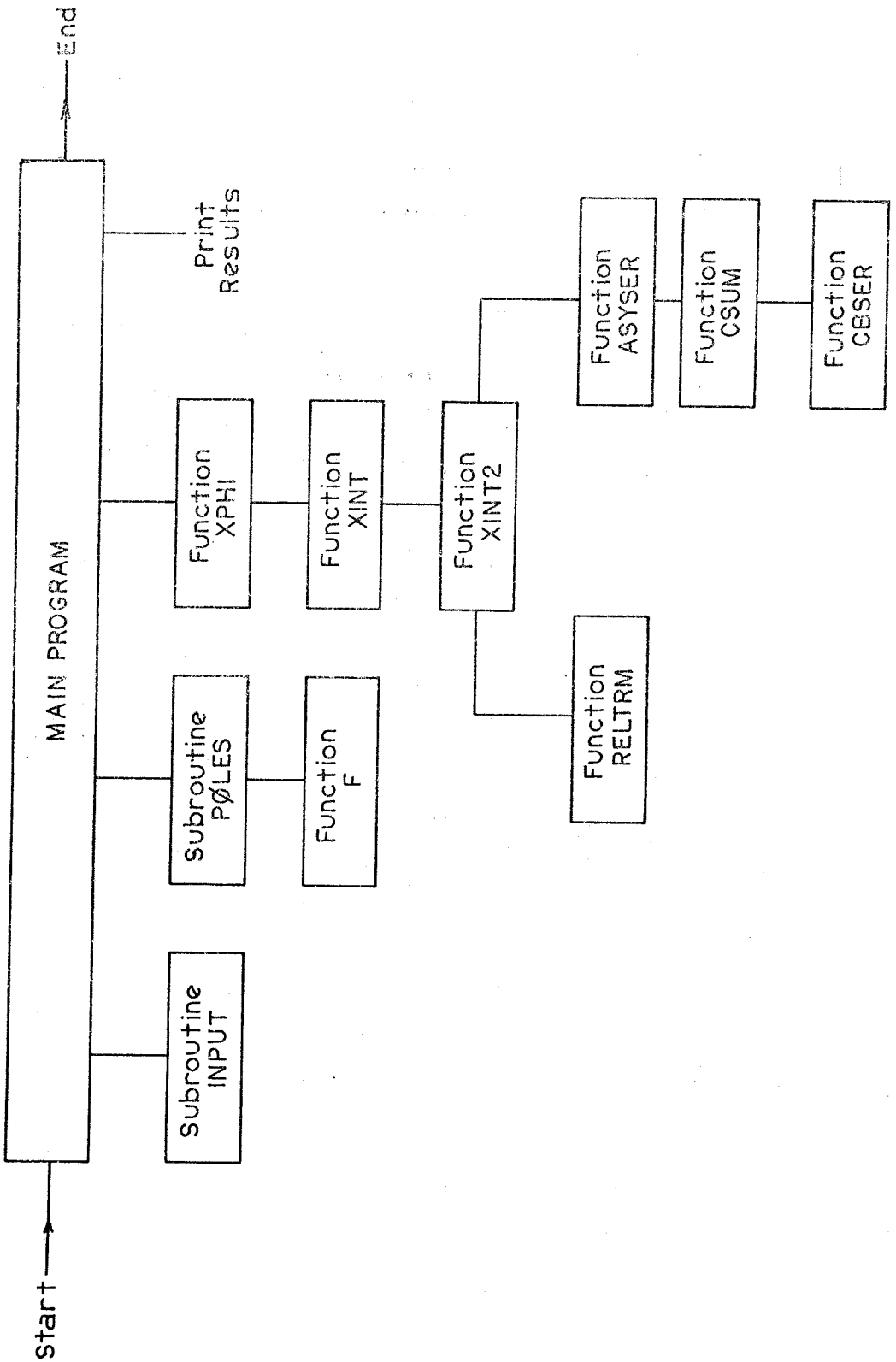

Figure C.1: Computer Program Levels of Control

TABLE C-1. Identification of Program Variables

A	$(\frac{1}{\pi}\log z)$ in the function ASYSER from the series of eq. (4.65)
AA	plus or minus 1; sets the sign of the coefficient in function ASYSER
ASYSER	function that evaluates the asymptotic series, eq. (4.65)
BETA1	$\sqrt{M_1^2 - 1}$
BETA2	$\sqrt{1 - M_2^2}$
CBSER	evaluates the hypergeometric series
CI	$\sqrt{-1}$
CSER	a dummy function, equal to CBSER. Prepares data for the asymptotic series evaluation
CSUM	adds the leading multiplicative coefficient to the hypergeometric series calculated by CBSER
EPS	ε , the wedge deflection angle (radians)
EXPMAX	a limiter to control arguments of exponentials so as to avoid overflow and underflow problems
F	a function which evaluates eq. (4.30)
GAMMA	adiabatic exponent
H1	h_1 , height of the supersonic stream (inches)
H2	h_2 , height of the subsonic stream (inches)
IDENT	parameter in Subroutine INPUT which identifies the type of variable being input
INPUT	subroutine which causes new problem conditions to be read into the program via cards
L	a logical variable which is set "true" if no more terms of the actual series can be evaluated

TABLE C-1 (continued)

LPOLE	a logical variable used in Subroutine INPUT to signal that M_1, M_2, h_1, and h_2 have been changed and that the set of poles must be recalculated
N	used in Subroutine INPUT
NN	Y(NN) is the point in the supersonic stream on the interface
NASYMX	the maximum number of terms the asymptotic series can contain for a given value of TOLASY
NBR	the subscript "ν" in the expression $I_{mn\nu}$
NCASE	identifies a case number; printed with the output as a convenience (NCASE = 0 suppresses this output)
NDER	NDER = 1 refers to $\partial\phi/\partial x$, =2 refers to $\partial\phi/\partial y$
NINT	the subscript "m" of I_{mn}
NPOLE	NPOLE = n identifies the n^{th} term of the actual series
NPOLMX	maximum number of terms in the k-series
NSWTCH	program prints a warning and stops summation if the asymptotic series has not converged by n = NSWTCH
NTYPE	= 1 for the supersonic wedge problem, = 2 for the subsonic wedge problem
NYSUBC	number of the first point in the Y-array in the subsonic stream
NYSUBW	total number of points in the Y-array (not more than 12)
P(N)	normalized pressure at the points y = Y(N)
PHI(I, J)	the array of I = NDER derivatives at the point y = Y(J) for the value of x currently under consideration
PI	π
POLES	subroutine that calculates the poles k_i and k_r

TABLE C-1 (continued)

R	$\beta_1 M_2^2 / \beta_2 M_1^2$
RELTRM	evaluates the n^{th} term of the actual series
SWITCH	negative (positive) if the contour is to be evaluated in the upper (lower) half plane
T	thickness of the wedge plate (inches)
THETAI	θ_i, defined in eq. (4.40)
THETAR	θ_r, defined in eq. (4.40)
TOLASY	evaluation of the individual terms of the asymptotic series is stopped when the magnitude of the terms is less than TOLASY
TOLXK	maximum imbalance permitted in solving eq. (4.30)
TZMIN	if the magnitude of z is less than TZMIN, the series converges so quickly that the asymptotic series need not be calculated
VALUE	parameter read in through Subroutine INPUT
X	x-coordinate under current consideration
XA	distance from the leading edge of the wedge
XEPS(N)	flow inclination (degrees) at y = Y(N)
XINT	subroutine that evaluates the series I_{mn}
XINT2	expresses all series as an asymptotic solution and a correction of real terms
XKI(N)	the array of poles k_i
XKR(N)	the array of poles k_r
XLE	the value of x at the leading edge
XMAX	stopping value of X in the calculations
XMIN	starting value of X in the calculations

TABLE C-1 (continued)

XM1	M_1
XM2	M_2
XPHI	function that calculates a specific derivative of ϕ at a specific point
XSH	x-coordinate of the shoulder of the wedge
XSTEP	the increment of X between successive evaluations
Y(N)	this array contains in non-increasing order the y-coordinates of all points to be evaluated (N not to exceed 12)
ZSWTCH	the magnitude of z above which the approximation to the asymptotic series is employed

```
      COMMON/BLOCK1/XM1,XM2,BETA1,BETA2,H1,H2,T,EPS
      COMMON/BLOCK2/NYSUBC,NYSUBK,Y(12)
      COMMON/BLOCK3/NPOLMX,THETAR,THETAI
      COMMON/BLOCK4/TOLASY,NASYMX,ABSZMX,ZSWTCH,NSWTCH,TZMIN
      COMMON/BLOCK5/NCASE,NTYPE,XMIN,XMAX,XSTEP,XLE,LPOLE
      COMMON XKA(40),XKI(40)
      DIMENSION PHI(2,12),XEPS(12),P(12)
      LOGICAL LPOLE
      TOLASY=7.0E-6
      ABSZMX=1.
      NSWTCH=250
      XN=FLOAT(NSWTCH)
      ZSWTCH=(XN*TOLASY)**(1./XN)
      XN=TOLASY**(-.25)
      NASYMX=INT(XN+1.)
      GAMMA=1.4
      PI=3.1415927
      NPOLMX=30
      TZMIN=(FLOAT(NPOLMX)*TOLASY)**(1./FLOAT(NPOLMX))
   99 CALL INPUT
      BH1=BETA1*H1
      IF (.NOT.LPOLE) GO TO 172
      X1=THETAR/PI
      X2=THETAI/PI
      WRITE (6,119) BETA1,BETA2,TOLASY,ABSZMX,NASYMX,X1,X2,ZSWTCH
  119 FORMAT (////8H BETA1 =F6.3/8H BETA2 =F6.3/23H ASYMPTOTIC TOLERANCE
     * =  1PE9.2/24H MAX Z FOR CONVERGENCE = 0PF7.4/32H MAX NUMBER OF TE
     *RMS REQUIRED IS I3/' THETAR / PI =',F5.3/' THETAI / PI =',F5.3/
     *    ' Z SWITCH AT ABS(Z) =',F7.4)
  172 XSH=XLE+T/EPS
      DO 160 NOER=1,2
      WRITE (6,109)
  109 FORMAT (1H1 4X'BISONIC WIND TUNNEL LINEARIZED FOURIER ANALYSIS')
      WRITE (6,121)
  121 FORMAT (5X,'LEADING INTERACTION ONLY')
      IF (NCASE.EQ.0) GO TO 200
      WRITE (6,201) NCASE
  201 FORMAT (5X,'CASE',I3)
  200 IF (NTYPE.EQ.1) WRITE (6,170)
      IF (NTYPE.EQ.2) WRITE (6,211)
  211 FORMAT (5X,'SUBSONIC WEDGE'/)
```

Figure C.2: Listing of the Main Program

```
170 FORMAT (5X,'SUPERSONIC WEDGE'/)
    X1=180.*ATAN(EPS)/PI
    WRITE (6,161) XLE,X1,XSH
161 FORMAT (5X'LEADING EDGE AT',F6.2,' INCHES, WEDGE ANGLE',
   *   F6.3,' DEGREES, SHOULDER AT',F6.2,' INCHES')
    WRITE (6,171) BW1
171 FORMAT (5X,'SUPERSONIC HALF-WAVELENGTH',F6.3,' INCHES')
    WRITE (6,110) XM1,XM2,H1,H2,T
110 FORMAT (//4X3HM1=F5.3,5H  M2=F5.3,5H  H1=F5.3,5H  H2=F5.3,4H  T=
   *   F4.3//)
    IF (NDER.EQ.1) WRITE (6,111)
    IF (NDER.EQ.2) WRITE (6,141)
111 FORMAT (5X,'NORMALIZED PRESSURE'/)
141 FORMAT (5X,'FLOW INCLINATION, DEGREES'/)
    WRITE (6,142) (Y(N),N=1,NYSUBW)
142 FORMAT (8X1HX3X,12F8.2)
    X=XMIN
113 XA=X-XLE
    DO 114 NY=1,NYSUBW
114 PHI(NDER,NY)=XPHI(NDER,NY,XA,NTYPE,T,EPS)
     IF (NDER.EQ.1) GO TO 144
    DO 115 NY=1,NYSUBW
115 XEPS(NY)=180.*ATAN(PHI(2,NY))/PI
    WRITE (6,145) X, (XEPS(K),K=1,NYSUBW)
145 FORMAT (5XF5.2,2X,12F8.3)
    GO TO 146
144 NN=NYSUBC-1
    DO 116 NY=1,NN
116 P(NY)=1.-GAMMA*(XM1**2)*PHI(1,NY)
    DO 117 NY=NYSUBC,NYSUBW
117 P(NY)=1.-GAMMA*(XM2**2)*PHI(1,NY)
    DO 120 K=1,NYSUBW
    IF (P(K).LT..0) P(K)=.0
120 IF (P(K).GT.9.999) P(K)=9.999
    WRITE (6,147) X, (P(K),K=1,NYSUBW)
147 FORMAT (5XF5.2,2X,12F8.4)
146 X=X+XSTEP
    IF (X.LE.XMAX) GO TO 113
160 CONTINUE
    GO TO 99
    END
```

Figure C.2, cont'd.: Listing of the Main Program

```
      SUBROUTINE INPUT
      COMMON/BLOCK1/XM1,XM2,BETA1,BETA2,H1,H2,AT,REPS
      COMMON/BLOCK2/NYSUBC,NYSUBW,Y(12)
      COMMON/BLOCK5/NCASE,NTYPE,XMIN,XMAX,XSTEP,XLE,LPOLE
      LOGICAL LPOLE
      LPOLE=.FALSE.
      PI=3.1415927
      READ (5,10) IDENT,N,VALUE
   10 FORMAT (2I2,F8.0)
      IF (IDENT.EQ.0) STOP
      GO TO 12
   11 READ (5,10) IDENT,N,VALUE
      IF (IDENT.EQ.0) GO TO 20
      IF (IDENT.LE.4) LPOLE=.TRUE.
   12 GO TO (101,102,103,104,105,106,107,108,109,110,111,112,113,
     *   114,115), IDENT
  101 XM1=VALUE
      BETA1=SQRT(XM1*XM1-1.)
      GO TO 11
  102 XM2=VALUE
      BETA2=SQRT(1.-XM2*XM2)
      GO TO 11
  103 H1=VALUE
      GO TO 11
  104 H2=VALUE
      GO TO 11
  105 AT=VALUE
      GO TO 11
  106 REPS=TAN(VALUE*PI/180.)
      GO TO 11
  107 NYSUBC=N
      GO TO 11
  108 NYSUBW=N
      GO TO 11
  109 Y(N)=VALUE
      GO TO 11
  110 NCASE=N
      GO TO 11
  111 NTYPE=N
      GO TO 11
  112 XMIN=VALUE
      GO TO 11
  113 XMAX=VALUE
      GO TO 11
  114 XSTEP=VALUE
      GO TO 11
  115 XLE=VALUE
      GO TO 11
   20 IF (LPOLE) CALL POLES
      RETURN
      END
```

Figure C.3: Listing of Subroutine INPUT

```
      SUBROUTINE POLES
C----------CALCULATE THE REAL AND IMAGINARY POLES
      COMMON/BLOCK1/XM1,XM2,BETA1,BETA2,H1,H2,AT,AEPS
      COMMON/BLOCK3/NPOLMX,THETAR,THETAI
      COMMON XKR(40), XKI(40)
      DOUBLE PRECISION XNOW,FNOW,SLOPE,F
      PI=3.1415927
      TOLXK=1.E-5
      R=(BETA1/BETA2)*(XM2/XM1)**2
      THETAR=ATAN(1./R)
      THETAI=ATAN(R)
      N=1
  132 XNOW=(THETAR+FLOAT(N-1)*PI)/(BETA1*H1)
  130 FNOW=F(1,XNOW,R)
      IF (DABS(FNOW).LT.TOLXK) GO TO 131
      SLOPE=R*BETA1*H1/(DCOS(XNOW*BETA1*H1)**2)-BETA2*H2*(1.-DTANH(XNOW
     *    *BETA2*H2)**2)
      XNOW=XNOW-FNOW/SLOPE
      GO TO 130
  131 XKR(N)=XNOW
      N=N+1
      IF (N.LE.NPOLMX) GO TO 132
      N=1
  135 XNOW=(THETAI+FLOAT(N-1)*PI)/(BETA2*H2)
  133 FNOW=F(2,XNOW,R)
      IF (DABS(FNOW).LT.TOLXK) GO TO 134
      SLOPE=BETA2*H2/(DCOS(XNOW*BETA2*H2)**2)-R*BETA1*H1*(1.-DTANH(XNOW
     *    *BETA1*H1)**2)
      XNOW=XNOW-FNOW/SLOPE
      GO TO 133
  134 XKI(N)=XNOW
      N=N+1
      IF (N.LE.NPOLMX) GO TO 135
      GO TO 105
  105 WRITE (6,106) NPOLMX, TOLXK
  106 FORMAT (20H1EIGENVALUE SUMMARY  I3,6H POLES/13H TOLERANCE =
     *    1PE9.2/3X1HN6X4HREAL3X9HIMAGINARY/)
      DO 107 N=1,NPOLMX
  107 WRITE (6,108) N, XKR(N), XKI(N)
  108 FORMAT (I3,4X,F8.4,2X,F8.4)
      RETURN
      END
```

Figure C.4: Listing of Subroutine PØLES

```
      DOUBLE PRECISION FUNCTION F (N,X,R)
C---------ROOTS OF THIS FUNCTION ARE THE POLES XKR AND XKI
C---------N=1   REAL PART
C---------N=2   IMAGINARY PART
      COMMON/BLOCK1/XM1,XM2,BETA1,BETA2,H1,H2,T,EPS
      DOUBLE PRECISION F, X
      GO TO (100,101), N
  100 F=R*DTAN(X*BETA1*H1)-DTANH(X*BETA2*H2)
      RETURN
  101 F=DTAN(X*BETA2*H2)-R*DTANH(X*BETA1*H1)
      RETURN
      END
```

Figure C.5: Listing of Function F

```
      FUNCTION XPHI (NDER,NY,XX,NTYPE,AT,AEPS)
      COMMON/BLOCK1/XM1,XM2,BETA1,BETA2,H1,H2,T,EPS
      COMMON/BLOCK2/NYSUBC,NYSUBW,YY(12)
      T=AT
      EPS=AEPS
      Y=YY(NY)
      IF (NTYPE.EQ.2) GO TO 105
      X=XX-BETA1*H1
      XPBH1=X+BETA1*H1
      ALPHA=XPBH1-T/EPS
      S=X-T/EPS
      IF (NY.GE.NYSUBC) GO TO 103
      ALPHA1=ALPHA+BETA1*(Y-H1)
      ALPHA2=ALPHA-BETA1*(Y-H1)
      ALPHA3=XPBH1+BETA1*(Y-H1)
      ALPHA4=XPBH1-BETA1*(Y-H1)
      A2=ALPHA1
      A4=ALPHA3
      IF (NDER.EQ.2) GO TO 102
      XPHI=EPS*(XINT(1,ALPHA1,Y,ALPHA1)+XINT(1,ALPHA2,Y,A2)
     *   -XINT(1,ALPHA3,Y,ALPHA3)-XINT(1,ALPHA4,Y,A4))
      RETURN
  102 XPHI=EPS*BETA1*(XINT(1,ALPHA1,Y,ALPHA1)-XINT(1,ALPHA2,Y,A2)
     *   -XINT(1,ALPHA3,Y,ALPHA3)+XINT(1,ALPHA4,Y,A4))
     *   -EPS*(XINT(2,ALPHA1,Y,ALPHA1)-XINT(2,ALPHA3,Y,ALPHA3))
      RETURN
  103 IF (NDER.EQ.2) GO TO 104
      XPHI=EPS*(XM1**2)*(XINT(3,ALPHA,Y,S)-XINT(3,XPBH1,Y,X))
      RETURN
  104 XPHI=-EPS*BETA2*(XM1**2)*(XINT(4,ALPHA,Y,S)-XINT(4,XPBH1,Y,X))
      RETURN
  105 X=XX
      IF (NY.GE.NYSUBC) GO TO 107
      A1=X+BETA1*(Y-H1)
      A2=X-BETA1*(Y-H1)
      A3=X-T/EPS+BETA1*(Y-H1)
      A4=X-T/EPS-BETA1*(Y-H1)
      S2=A2-BETA1*H1
      S4=A4-BETA1*H1
      IF (NDER.EQ.2) GO TO 106
      XPHI=EPS*(XM2**2)*(XINT(5,A1,Y,S2)+XINT(5,A2,Y,S2)-XINT(5,A3,Y,
     *   S4)-XINT(5,A4,Y,S4))
      RETURN
  106 XPHI=EPS*BETA1*(XM2**2)*(XINT(5,A1,Y,S2)-XINT(5,A2,Y,S2)
     *   -XINT(5,A3,Y,S4)+XINT(5,A4,Y,S4))
      RETURN
  107 A=X-T/EPS
      IF (NDER.EQ.2) GO TO 108
      XPHI=(EPS/BETA2)*(XINT(6,X,Y,X)-XINT(6,A,Y,A)+XINT(7,X,Y,X)
     *   -XINT(7,A,Y,A))
      RETURN
  108 XPHI=EPS*(XINT(8,X,Y,X)-XINT(8,A,Y,A)+XINT(9,X,Y,X)
     *   -XINT(9,A,Y,A))
      RETURN
      END
```

Figure C.6: Listing of Function XPHI

```
      FUNCTION XINT (NINT,ARG,Y,SWITCH)
      IF (NINT.NE.2) GO TO 103
      IF (SWITCH) 100,101,102
  100 XINT=.5
      RETURN
  101 XINT=.0
      RETURN
  102 XINT=-.5
      RETURN
  103 IF (SWITCH) 104,104,105
  104 XINT=XINT2(NINT,2,ARG,Y)
      RETURN
  105 XINT=-XINT2(NINT,1,ARG,Y)-XINT2(NINT,3,ARG,Y)-XINT2(NINT,4,ARG,Y)
      RETURN
      END
```

Figure C.7: Listing of Function XINT

```
      FUNCTION XINT2 (NINT,NBR,ARG,Y)
C         NBR=1   REAL
C         NBR=2   POSITIVE IMAGINARY
C         NBR=3   ZERO
C         NBR=4   NEGATIVE IMAGINARY
      COMMON/BLOCK1/XM1,XM2,BETA1,BETA2,H1,H2,T,EPS
      COMMON/BLOCK3/NPOLMX,THETAR,THETAI
      LOGICAL L
      JPOLMX=NPOLMX
      IF (NBR.NE.3) GO TO 105
      Q=H2*(BETA2*XM1)**2-H1*(BETA1*XM2)**2
      GO TO (100,101,103,104,107,101,108,109,110), NINT
  100 XINT2=(XM2**2)*ARG/(2.*Q)
      RETURN
  101 XINT2=.0
      RETURN
  103 XINT2=ARG/Q
      RETURN
  104 XINT2=BETA2*(Y+H2)/Q
      RETURN
  105 SUMDIF=.0
      L=.FALSE.
      DO 106 NPOLE=1,NPOLMX
      IF (L) GO TO 200
  106 SUMDIF=SUMDIF+RELTRM(NINT,NBR,ARG,Y,NPOLE,L)
      GO TO 201
  200 NPOLMX=NPOLE-1
  201 XINT2=ASYSER(NINT,NBR,ARG,Y)+SUMDIF
      NPOLMX=JPOLMX
      RETURN
  107 XINT2=-ARG/(2.*Q)
      RETURN
  108 XINT2=-BETA2*(XM1**2)*ARG/Q
      RETURN
  109 XINT2=((BETA1*XM2)**2)*H1/Q
      RETURN
  110 XINT2=((BETA2*XM1)**2)*Y/Q
      RETURN
      END
```

Figure C.8: Listing of Function XINT2

```
      FUNCTION RELTRM (NINT,NBR,ARG,Y,NPOLE,L)
C---------THIS IS A ROUTINE TO CALCULATE THE ACTUAL VALUE OF THE RESIDUE
C---------AT A SPECIFIC POLE
      COMMON/BLOCK1/XM1,XM2,BETA1,BETA2,H1,H2,T,EPS
      COMMON XKR(40),XKI(40)
      LOGICAL L
      EXPMAX=80.
      RELTRM=.0
      BH1=BETA1*H1
      BH2=BETA2*H2
      GO TO (102,109,103,108), NBR
  102 XK=XKR(NPOLE)
      IF (ABS(XK).LT..0005) RETURN
      XKBH1=XK*BH1
      XKBH2=XK*BH2
      IF (ABS(XKBH1).GT.EXPMAX) GO TO 200
      IF (ABS(XKBH2).GT.EXPMAX) GO TO 200
      IF (ABS(XK*ARG).GT.EXPMAX) GO TO 200
      THSQ=TANH(XKBH2)**2
      DENOM=H2*((BETA2*XM1)**2)*(1.-THSQ)-(H1/(XM2**2))*((BETA1**2)
     *    *(XM2**4)+(BETA2**2)*(XM1**4)*THSQ)
      GO TO (105,103,106,107,114,115,120,116,121), NINT
  105 RELTRM=((BETA1**2)*(XM2**4)+(BETA2**2)*(XM1**4)*THSQ)
     *    *SIN(XK*ARG)/(((BETA1*XM2)**2)*XK*DENOM)
  103 RETURN
  106 RELTRM=2.*COSH(XK*BETA2*(Y+H2))*SIN(XK*ARG)/(XK*COS(XKBH1)
     *    *COSH(XKBH2)*DENOM)
      RETURN
  107 RELTRM=2.*SINH(XK*BETA2*(Y+H2))*COS(XK*ARG)/(XK*COS(XKBH1)
     *    *COSH(XKBH2)*DENOM)
      RETURN
  108 XK=-XKI(NPOLE)
      GO TO 110
  109 XK=XKI(NPOLE)
  110 IF (ABS(XK).LT..0005) RETURN
      XKBH1=XK*BH1
      XKBH2=XK*BH2
      IF (ABS(XKBH1).GT.EXPMAX) GO TO 200
      IF (ABS(XKBH2).GT.EXPMAX) GO TO 200
      IF (ABS(XK*ARG).GT.EXPMAX) GO TO 200
      IF (ABS(XK*(ARG-2.*BH1)).GT.EXPMAX) GO TO 200
      THSQ=TANH(XKBH1)**2
      DENOM=(H2/(XM1**2))*((BETA2**2)*(XM1**4)+(BETA1**2)*(XM2**4)
     *    *THSQ)-H1*((BETA1*XM2)**2)*(1.-THSQ)
```

Figure C.9: Listing of Function RELTRM

```
FUNCTION RELTRM, CONT'D
      GO TO (111,103,112,113,117,118,122,119,123), NINT
  111 RELTRM=(XM2**2)*EXP(XK*ARG)*(1.-THSQ)/(2.*XK*DENOM)
      RETURN
  112 RELTRM=EXP(XK*ARG)*COS(XK*BETA2*(Y+H2))/(XK*COSH(XKBH1)
     *    *COS(XKBH2)*DENOM)
      RETURN
  113 RELTRM=EXP(XK*ARG)*SIN(XK*BETA2*(Y+H2))/(XK*COSH(XKBH1)
     *    *COS(XKBH2)*DENOM)
      RETURN
  114 RELTRM=-SIN(XK*ARG)/(XK*COS(XKBH1)*COSH(XKBH2)*DENOM)
      RETURN
  115 RELTRM=-2.*BETA2*(XM1**2)*SIN(XK*ARG)*TANH(XKBH2)*SINH(XK*BETA2*Y)
     *    /(XK*COSH(XKBH2)*DENOM)
      RETURN
  116 RELTRM=2.*BETA2*(XM1**2)*COS(XK*ARG)*COSH(XK*BETA2*Y)*TANH(XKBH2)
     *    /(XK*COSH(XKBH2)*DENOM)
      RETURN
  117 RELTRM=-.5*EXP(XK*ARG)/(XK*COSH(XKBH1)*COS(XKBH2)*DENOM)
      RETURN
  118 RELTRM=BETA1*(XM2**2)*EXP(XK*ARG)*TANH(XKBH1)*SIN(XK*BETA2*Y)
     *    /(XK*COS(XKBH2)*DENOM)
      RETURN
  119 RELTRM=BETA1*(XM2**2)*EXP(XK*ARG)*TANH(XKBH1)*COS(XK*BETA2*Y)
     *    /(XK*COS(XKBH2)*DENOM)
      RETURN
  120 RELTRM=-2.*BETA2*(XM1**2)*SIN(XK*ARG)*COSH(XK*BETA2*Y)
     *    /(XK*COSH(XKBH2)*DENOM)
      RETURN
  121 RELTRM=2.*BETA2*(XM1**2)*COS(XK*ARG)*SINH(XK*BETA2*Y)
     *    /(XK*COSH(XKBH2)*DENOM)
      RETURN
  122 RELTRM=-BETA2*(XM1**2)*EXP(XK*ARG)*COS(XK*BETA2*Y)/(XK*COS(XKBH2)
     *    *DENOM)
      RETURN
  123 RELTRM=BETA2*(XM1**2)*EXP(XK*ARG)*SIN(XK*BETA2*Y)/(XK*COS(XKBH2)
     *    *DENOM)
      RETURN
  200 L=.TRUE.
      RETURN
      END
```

Figure C.9, cont'd.: Listing of Function RELTRM

```
      FUNCTION ASYSER (NINT,NBR,ARG,Y)
C---------THIS ROUTINE PREPARES DATA FOR INPUT TO THE INFINITE
C---------SERIES ROUTINE 'CSER'
      COMMON/BLOCK1/XM1,XM2,BETA1,BETA2,H1,H2,T,EPS
      COMMON/BLOCK3/NPOLMX,THETAR,THETAI
      COMPLEX CI,A,Z,A1,A2,Z1,Z2,CSER,CSUM,CBSER
      CSER(ALPHA,Z)=CBSER(ALPHA,Z,.0)
      ASYSER=.0
      IF (NBR.EQ.3) RETURN
      IF (NINT.EQ.2) RETURN
      PI=3.1415927
      CI=(.0,1.)
      BH1=BETA1*H1
      BH2=BETA2*H2
      IF (NINT.NE.1) GO TO 100
      GO TO (108,109,99,109), NBR
  108 A=CI*ARG/BH1
      ASYSER=-AIMAG(CSUM(A,1.,0,1))/(PI*BETA1)
   99 RETURN
  100 THETA=THETAI
      IF (NBR.EQ.1) THETA=THETAR
      YR=1.+Y/H2
      SRT=SQRT((BETA1**2)*(XM2**4)+(BETA2**2)*(XM1**4))
      XX1=2./(PI*SRT)
      GO TO (101,103,99,105), NBR
  101 IF (NINT.GT.4) GO TO 111
      A1=(BETA2*Y+CI*ARG)/BH1
      A2=(-BH2*(2.+Y/H2)+CI*ARG)/BH1
      XX=-XX1
      IF (NINT.EQ.3) ASYSER=XX*AIMAG(CSUM(A1,-1.,0,0)+CSUM(A2,-1.,0,0))
      IF (NINT.EQ.4) ASYSER=XX*REAL(CSUM(A1,-1.,0,0)-CSUM(A2,-1.,0,0))
      RETURN
  103 IF (NINT.GT.4) GO TO 114
      A=(ARG-BH1)/BH2+CI*YR
      XX=2./(PI*SRT)
      IF (NINT.EQ.3) ASYSER=XX*REAL(CSUM(A,-1.,1,0))
      IF (NINT.EQ.4) ASYSER=XX*AIMAG(CSUM(A,-1.,1,0))
      RETURN
  106 ASYSER=XX*REAL(CEXP(THETA*A)*CSER(ALPHA,Z))
      RETURN
  104 ASYSER=XX*AIMAG(CEXP(THETA*A)*CSER(ALPHA,Z))
      RETURN
  105 IF (NINT.GT.4) GO TO 117
      A=-(ARG+BH1)/BH2+CI*YR
      IF (NINT.EQ.4) GO TO 207
      XX=-2./(PI*SRT)
  300 ASYSER=XX*REAL(CSUM(A,-1.,1,0))
```

Figure C.10: Listing of Function ASYSER

```
      RETURN
  207 XX=2./(PI*SRT)
      ASYSER=XX*AIMAG(CSUM(A,-1.,1.0))
      RETURN
  109 XX=2.*((XM1*XM2)**2)*BETA2/(PI*((BETA1**2)*(XM2**4)
     *    +(BETA2**2)*(XM1**4)))
      IF (NBR.EQ.4) XX=-XX
      IF (NBR.EQ.2) A=(ARG-2.*BH1)/BH2
      IF (NBR.EQ.4) A=-(ARG+2.*BH1)/BH2
      ASYSER=XX*CSUM(A,1.,1.0)
      RETURN
  111 IF (NINT.GT.5) GO TO 120
      XX=2./(PI*SRT)
      A=(-BH2+CI*ARG)/BH1
  301 ASYSER=XX*AIMAG(CSUM(A,-1.,0.0))
      RETURN
  120 XX=-2.*BETA1*BETA2*((XM1*XM2)**2)/(PI*(SRT**2))
      A=(BH2*(Y/H2-1.)+CI*ARG)/BH1
      IF (NINT.EQ.6.OR.NINT.EQ.7) ASYSER=-XX*AIMAG(CSUM(A,1.,0.0))
      IF (NINT.EQ.8.OR.NINT.EQ.9) ASYSER=XX*REAL(CSUM(A,1.,0.0))
      RETURN
  114 IF (NINT.GT.5) GO TO 116
      XX=-1./(PI*SRT)
      A=(ARG-BH1)/BH2
      GO TO 300
  116 A=ARG/BH2+CI*Y/H2
      AA=1.
  128 CONTINUE
      GO TO (99,99,99,99,99,124,125,126,127), NINT
  117 IF (NINT.GT.5) GO TO 119
      XX=1./(PI*SRT)
      A=-(ARG+BH1)/BH2
      GO TO 300
  119 AA=-1.
      A=-ARG/BH2+CI*Y/H2
      GO TO 128
  124 XX=AA*BETA1*(XM2**2)/(PI*SRT)
      ASYSER=XX*AIMAG(CSUM(A,-1.,1.0))
      RETURN
  125 XX=-AA*BETA2*(XM1**2)/(PI*SRT)
      GO TO 300
  126 XX=BETA1*(XM2**2)/(PI*SRT)
      GO TO 300
  127 XX=BETA2*(XM1**2)/(PI*SRT)
      ASYSER=XX*AIMAG(CSUM(A,-1.,1.0))
      RETURN
      END
```

Figure C.10, cont'd.: Listing of Function ASYSER

```
      COMPLEX FUNCTION CSUM (A,AA,J,K)
C---------J=0   REAL SERIES
C---------J=1   IMAGINARY SERIES
      COMMON/BLOCK3/NPOLMX,THETAR,THETAI
      COMPLEX CSUM,A,CSER,Z,CBSER
      PI=3.1415927
      IF (J.EQ.0) THETA=THETAR
      IF (J.EQ.1) THETA=THETAI
      ALPHA=THETA/PI
      Z=AA*CEXP(PI*A)
      CSUM=CEXP(THETA*A)*CBSER(ALPHA,Z,,0)
      RETURN
      END
```

Figure C.11: Listing of Function CSUM

```
      COMPLEX FUNCTION CBSER (A,CZ,ARG)
      COMPLEX CBSER,CZ,CTOT,CADD,CZ1,CZ2,XLOG,ARG
C         THIS ROUTINE IS TO EVALUATE FROM N = NPOLMX TO INFINITY
C         THE SERIES (Z**N)/(N+A)
      COMMON/BLOCK3/NPOLMX,THETAR,THETAI
      COMMON/BLOCK4/TOL,NMAX,ABSZMX,ZSWTCH,NSWTCH,TZMIN
      CTOT=.0
      CBSER=.0
      IF (CABS(CZ).LE.TZMIN) RETURN
      IF (CABS(CZ).LE.1.0001) GO TO 101
      WRITE (6,100)
  100 FORMAT (' CONVERGENCE ERROR')
      RETURN
  101 N=1
      IF (CABS(CZ).LE.ZSWTCH) GO TO 105
  102 XN=FLOAT(N)
      CADD=(CZ**N)/((XN+A)*(XN+1.)*(XN+2.)*XN)
      CTOT=CTOT+CADD
      IF (CABS(CADD).LT.TOL) GO TO 104
      N=N+1
       IF (N.LE.NMAX) GO TO 102
      WRITE (6,103) NMAX
  103 FORMAT (' FAILED TO CONVERGE AFTER',I4,' TERMS')
  104 CZ1=1./CZ
      CZ2=CZ1**2
      A1=1.-A
      A2=2.-A
      CBSER=-A+.5*A*A1*(CZ1-1.5)+(A1+A/CZ-.5*A*A1*((1.-CZ)/CZ)**2)
     *   *CLOG(1./(1.-CZ))-A*A1*A2*CTOT
      DO 108 N=2,NPOLMX
  108 CBSER=CBSER-(CZ**(N-1))/(FLOAT(N-1)+A)
      RETURN
  105 N=NPOLMX
  107 XN=FLOAT(N)
      CADD=(CZ**N)/(XN+A)
      CBSER=CBSER+CADD
      IF (CABS(CADD).LT.TOL) RETURN
      N=N+1
      IF (N.LE.NSWTCH) GO TO 107
      WRITE (6,106)
  106 FORMAT (' ALTERNATE SERIES FAILED TO CONVERGE')
      RETURN
      END
```

Figure C.12: Listing of Function CBSER

EIGENVALUE SUMMARY 30 POLES
TOLERANCE = 1.00E-05

N	REAL	IMAGINARY
1	0.6125	C.0000
2	2.1318	1.9951
3	3.8279	3.7817
4	5.1146	5.6C8
5	6.6C6C	7.4347
6	8.0973	9.2612
7	9.5687	11.0877
8	11.0CCC	12.9142
9	12.5713	14.7407
10	14.0627	16.5672
11	15.5540	18.3937
12	17.0453	20.2202
13	18.5367	22.0467
14	20.0280	23.8732
15	21.5194	25.6997
16	23.0107	27.5262
17	24.5020	29.3528
18	25.9934	31.1793
19	27.4847	33.0058
20	28.9761	34.8323
21	30.4674	36.6588
22	31.9587	38.4853
23	33.4501	40.3118
24	34.9414	42.1383
25	36.4328	43.9649
26	37.9241	45.7913
27	39.4154	47.6178
28	40.9068	49.4444
29	42.3981	51.2707
30	43.8895	53.0974

BETA1 = 0.580
BETA2 = 0.80C
ASYMPTOTIC TOLERANCE = 7.0CE-C6
MAX Z FOR CONVERGENCE = 1.0000
MAX NUMBER OF TERMS REQUIRED IS 20
THETAR / PI =0.430
THETAI / PI =C.C7C
Z SWITCH AT ABS(Z) = 0.5749

BISONIC WIND TUNNEL LINEARIZED FOURIER ANALYSIS
LEADING INTERACTION ONLY
CASE 1
SUPERSONIC WEDGE

LEADING EDGE AT 10.00 INCHES, WEDGE ANGLE 4.CCC DEGREES, SHOULDER AT 11.34 INCHES
SUPERSONIC HALF-WAVELENGTH 2.167 INCHES

M1=1.400 M2=C.600 P1=2.150 P2=2.150 T=.C94

NORMALIZED PRESSURE

X	2.15	C.0	0.0	-2.15
8.00	1.CCCC	1.C000	1.0CC0	1.C000
8.50	1.CCCC	1.C000	1.CCC0	1.C000
9.00	1.0000	1.0001	1.0001	C.9999
9.50	1.CCCC	1.CCC1	1.CCC1	C.9999
10.00	1.CCCC	1.0004	1.0004	C.9996
10.50	1.1923	1.0010	1.0010	C.9990
11.00	1.1913	1.0029	1.0029	C.9975
11.50	C.9977	1.0083	1.0083	C.9938
12.00	1.0065	1.0282	1.0421	C.9864 ✓
12.50	1.0012	1.C109	1.0015	C.9743
13.00	1.0024	C.9665	C.9586	C.9587
13.50	1.022C	C.8700	C.8623	C.9431
14.00	1.0589	C.9162	C.9078	C.9303
14.50	C.8441	C.9089	C.9106	C.9206
15.00	C.9578	C.8943	C.9083	C.9133 ✓
15.50	C.9001	C.8948	C.9033	C.9091
16.00	C.8003	C.8747	C.8676	C.9058 ✓
16.50	C.8137	C.8206	C.8290	C.9084
17.00	C.8197	C.8677	C.8745	C.9170
17.50	C.7728	C.8187	C.8279	C.9301
18.00	C.7618	C.8728	C.8770	C.9444
18.50	C.8585	C.9849	C.9691	C.9576 ✓
19.00	1.1640	C.9537	C.9731	C.9656 ✓
19.50	1.3407	C.9863	C.9734	C.9807 ✓
20.00	1.1930	C.9941	C.9815	C.9909
20.50	1.1080	1.0208	1.0209	C.9965
21.00	1.0718	1.1012	1.0659	1.0011 ✓
21.50	1.1701	1.0270	1.0418	C.9971 ✓
22.00	1.1562	C.9879	C.9805	C.9882 ✓
22.50	1.3281	C.9370	C.9803	C.9771 ✓
23.00	1.0981	C.9732	C.9732	C.9855
23.50	C.9105	C.9840	C.9926	C.9939 ✓
24.00	C.9491	C.9268	C.9693	C.9400 ✓

FLOW INCLINATION, DEGREES

X	2.15	C.0	0.0	-2.15
8.00	0.0	0.000	C.CCC	C.0
8.50	0.0	C.000	C.CCC	C.0
9.00	0.0	0.001	0.001	C.0
9.50	0.0	0.003	0.003	C.0
10.00	-2.002	0.008	C.CC8	C.0
10.50	-4.CCC	C.021	0.021	C.0
11.00	-4.CCC	C.058	C.059	C.0
11.50	C.0	0.171	0.179	C.0
12.00	0.0	0.576	C.661	0.0
12.50	0.0	-7.724	-7.749	0.0
13.00	0.0	-8.691	-8.856	C.0
13.50	C.0	-2.842	-2.C10	C.0
14.00	C.0	-1.811	-1.741	C.0
14.50	C.0	-1.746	-1.854	C.0
15.00	C.0	-2.022	-1.979	0.0
15.50	C.0	-2.148	-2.002	C.0
16.00	0.0	-3.164	-3.289	0.0
16.50	C.0	2.642	2.766	C.0
17.00	0.0	6.292	6.174	0.0
17.50	C.0	9.8C0	9.566	C.0
18.00	C.0	3.527	3.472	0.0
18.50	0.0	3.171	2.340	C.0
19.00	C.0	2.651	3.374	C.0
19.50	C.0	3.819	4.CE6	0.0
20.00	0.0	4.156	4.791	C.0
20.50	C.0	5.C56	5.613	C.0
21.00	0.0	-0.644	-C.701	C.0
21.50	C.0	-5.198	-4.548	0.0
22.00	C.0	-5.030	-5.524	C.0
22.50	C.0	-2.871	-2.854	C.0
23.00	0.0	-2.467	-3.033	0.0
23.50	C.0	-3.69C	-3.459	C.0
24.00	0.0	-4.298	-4.457	C.0

Figure C.13: Sample Computer Output

Table C-2. Data Input Format

Col. 1-2	Col. 3-4	Col. 5-12	
00	--	--	One "00" card--end of data for this case. Two consecutive "00" cards--stop execution
01	--	M_1	
02	--	M_2	
03	--	h_1	
04	--	h_2	
05	--	t	Wedge thickness
06	--	ϵ	Wedge deflection angle in degrees, taken positive into the flow
07	NYSUBC	--	
08	NYSUBW	--	
09	NN	Y(NN)	The y-array in non-decreasing order
10	NCASE	--	Case number; = 0 will suppress this printout
11	NTYPE	--	= 01, supersonic wedge = 02, subsonic wedge
12	--	XMIN	
13	--	XMAX	
14	--	XSTEP	
15	--	XLE	

APPENDIX D. The Three-Dimensional Calculation

Several approaches to the first-order calculation of the three-dimensional flow field of Figure D. 1 will be described. Methods similar to that of the wedge problem (Section 4. 3) will be employed.

Depending on whether the calculation uses as the dependent variable the pressure perturbation, p, or the perturbation velocity potential, ϕ, the governing equation is:

$$(1-M_o^2)\frac{\partial^2 p}{\partial x^2} + \frac{\partial^2 p}{\partial y^2} + \frac{\partial^2 p}{\partial z^2} - \frac{2}{M_o}\frac{dM_o}{dy}\frac{\partial p}{\partial y} = 0 \quad , \tag{D. 1a}$$

or the extension to three dimensions of eq. (4. 8a),

$$(1-M_o^2)\frac{\partial^2 \phi}{\partial x^2} + \frac{\partial^2 \phi}{\partial y^2} + \frac{\partial^2 \phi}{\partial z^2} - \frac{M_o^2}{U_o}\frac{dU_o}{dy}\frac{\partial \phi}{\partial y} = 0 \quad . \tag{D. 1b}$$

The pressure perturbation equation is used by Namba[40, 41, 50] and Honda[42, 43] in studying stationary airfoils in compressible shear flow, while the equation for perturbation velocity potential is used by McCune[4-7] for rotating systems. The choice between the two approaches should be made in view of the type of boundary conditions to be applied to the perturbation equation: a pressure condition suggests the use of eq. (D. 1a); a geometric condition is more easily implemented through eq. (D. 1b).

It should be noted that the velocity potential of eq. (D. 1b) is the traditional one:

$$\vec{u}' = \text{grad}\,\phi \, . \tag{D. 2a}$$

For the velocity potential employed in Section 4. 3,

$$\vec{u}' = U_o(y)\,\text{grad}\,\phi \quad , \tag{D. 2b}$$

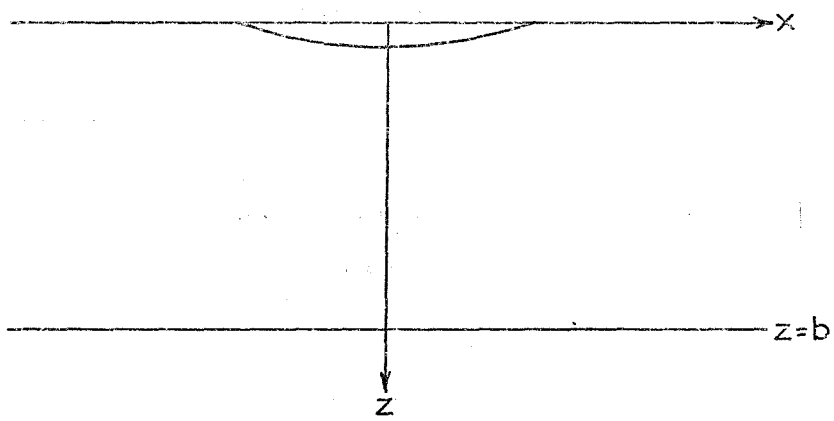

A. View from Above

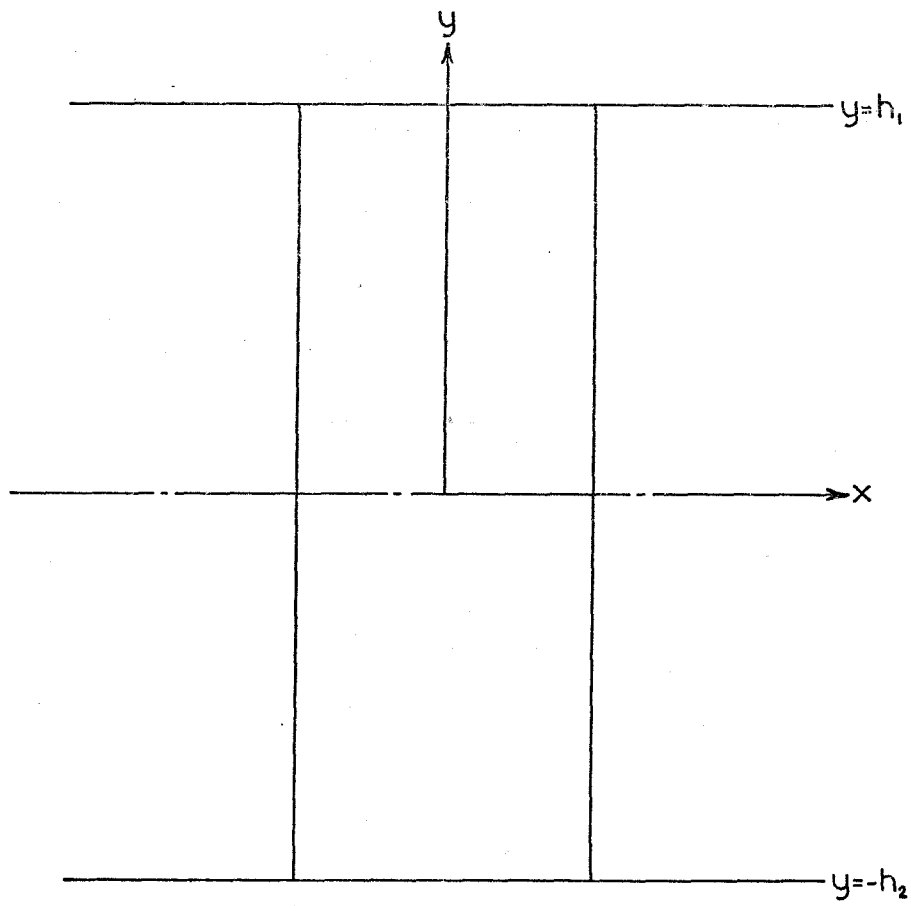

B. View from Side

Figure D.1: The Three-Dimensional Problem

the governing equation is

$$(1-M_o^2)\frac{\partial^2\phi}{\partial x^2}+\frac{\partial^2\phi}{\partial y^2}+\frac{\partial^2\phi}{\partial z^2}+(2-M_o^2)\frac{\partial\phi}{\partial y}\frac{1}{U_o}\frac{dU_o}{dy}$$

$$+\phi\left[\frac{1}{U_o}\frac{d^2U_o}{dy^2}-M_o^2\left(\frac{1}{U_o}\frac{dU_o}{dy}\right)^2\right]=0 \qquad (D.1c)$$

To each equation, apply a Fourier transform with respect to x and then use the method of separation of variables of the form

$$f(k,y,z) = Y(y;k)Z(z;k)$$

treating the Fourier variable, k, as a parameter rather than as an independent variable. Also, assume for all cases that

$$Z_n'' = -k^2\lambda_n^2 Z_n \quad . \qquad (D.3)$$

Thus, we see that this is an eigenvalue problem. The governing equation for $Y_n(y;k)$ from eq. (D.1a) is:

$$Y_n''-\frac{2}{M_o}\frac{dM_o}{dy}Y_n'-Y_nk^2(\lambda_n^2+1-M_o^2)=0 \qquad (D.4a)$$

for eq. (D.1b),

$$Y_n''-\frac{M_o^2}{U_o}\frac{dU_o}{dy}Y_n'-Y_nk^2(\lambda_n^2+1-M_o^2)=0 \qquad (D.4b)$$

and for eq. (D.1c),

$$Y_n''+(2-M_o^2)\frac{1}{U_o}\frac{dU_o}{dy}Y_n'+Y_n\left[\frac{1}{U_o}\frac{d^2U_o}{dy}-M_o\left(\frac{1}{U_o}\frac{dU_o}{dy^2}\right)^2\right.$$

$$\left.-k^2(\lambda_n^2+1-M_o^2)\right]=0 \quad . \qquad (D.4c)$$

For equations based on the perturbation velocity potential, the unperturbed distribution of total temperature must also be known (or some other function independent of M_o) to provide a link between U_o and

M_o. Two cases of interest are those of uniform unperturbed static temperature and uniform total temperature throughout the flow field.

In the case of uniform static temperature, the unperturbed sonic speed a_o is constant and eqs. (D. 4b) and (D. 4c), related respectively to the conventional and modified perturbation velocity potential, become

$$Y_n'' - M_o \frac{dM_o}{dy} Y_n' - Y_n k^2(\lambda_n^2+1-M_o^2) = 0 \quad , \tag{D.5a}$$

$$Y_n'' + \frac{2-M_o^2}{M_o} \frac{dM_o}{dy} Y_n' + Y_n \left\{ \frac{1}{M_o} \left[\frac{d^2M_o}{dy^2} - \left(\frac{dM_o}{dy} \right)^2 \right] - k^2(\lambda_n^2+1-M_o^2) \right\} \quad . \tag{D.5b}$$

For uniform total temperature, it can be seen that

$$\frac{1}{U_o} \frac{dU_o}{dy} = \frac{2}{2+(\gamma-1)M_o^2} \frac{1}{M_o} \frac{dM_o}{dy} \quad .$$

Under this substitution, eqs. (D. 4b) and (D. 4c) respectively become:

$$Y_n'' - \frac{1}{2+(\gamma-1)M_o^2} \frac{d(M_o^2)}{dy} - Y_n' - Y_n k^2(\lambda_n^2+1-M_o^2) = 0 \quad , \tag{D.5c}$$

$$Y_n'' + \frac{2-M_o^2}{2+(\gamma-1)M_o^2} \frac{1}{M_o^2} \frac{d(M_o^2)}{dy} Y_n' + Y_n \left\{ \frac{d}{dy} \left[\frac{2}{2+(\gamma-1)M_o^2} \frac{1}{M_o} \frac{dM_o}{dy} \right] \right.$$

$$\left. + (1-M_o) \left[\frac{2}{2+(\gamma-1)M_o^2} \frac{1}{M_o} \frac{dM_o}{dy} \right]^2 - k^2(\lambda_n^2+1-M_o^2) \right\} = 0 \quad . \tag{D.5d}$$

The orthogonality condition for eqns. (D. 1) under the two temperature cases of interest are provided in Table D-1. Except with the pressure perturbation equation, the additional condition is imposed that $dM_o/dy = 0$ at the top and bottom walls. In the problem of interest, the wall geometry is prescribed. Since pressure perturbations are

TABLE D-1. Orthogonality Conditions, $m \neq n$

Dependent Variable	Uniform Static Temperature	Uniform Total Temperature
perturbation pressure	$\int_{-h_2}^{h_1} \frac{Y_m Y_n}{M_o^2}\, dy = 0$	$\int_{-h_2}^{h_1} \frac{Y_m Y_n}{M_o^2}\, dy = 0$
conventional velocity potential, eq. (D.2a)	$\int_{-h_2}^{h_1} Y_m Y_n \exp\left(\frac{1-M_o^2}{2}\right) dy = 0$	$\int_{-h_2}^{h_1} \left(\frac{\rho_o}{\rho_t}\right) Y_m Y_n dy = 0$
modified velocity potential, eq. (D.2b)	$\int_{-h_2}^{h_1} M_o^2 Y_m Y_n \exp\left(\frac{1-M_o^2}{2}\right) dy = 0$	$\int_{-h_2}^{h_1} \left(\frac{p}{p_t}\right)_o M_o^2 Y_m Y_n dy = 0$

Note: subscript $(\ )_t$ refers to stagnation state, $(\ )_o$ refers to unperturbed state, $(\ )_m$ and $(\ )_n$ refer to separate eigenvalues.

not known a priori (their calculation is the goal of the computation), one of the approaches based on the perturbation velocity potential is preferred. Furthermore, a condition of the experiment is that the total temperature is uniform in each stream. For ease of applying boundary conditions, the modified perturbation velocity potential of eq. (D. 2b) is chosen. The solution is governed by eq. (D. 1c), and the separation functions by eqns. (D. 3) and (D. 5d). The orthogonality condition to be applied is

$$\int_{-h_2}^{h_1} \left(\frac{P}{P_t}\right)_o M_o^2 Y_m Y_n dy = 0 \quad . \tag{D.6}$$

Because the two streams separately are uniform, eqns. (D. 5d) and (D. 6) can be simplified to

$$Y''_{1n} + k^2(\beta_1^2 - \lambda_n^2)Y_{1n} = 0 \qquad 0 \le y \le h_1 \tag{D.7a}$$

$$Y''_{2n} - k^2(\lambda_n^2 - \beta_2^2)Y_{2n} = 0 \qquad -h_2 \le y \le 0 \tag{D.7b}$$

and the orthogonality condition is

$$\left(1+\frac{\gamma-1}{2}M_1^2\right)^{-\frac{\gamma}{\gamma-1}} \int_0^{h_1} M_1^2 Y_{1m} Y_{1n} dy + \left(1+\frac{\gamma-1}{2}M_2^2\right)^{-\frac{\gamma}{\gamma-1}} \int_{-h_2}^{0} M_2^2 Y_{2m} Y_{2n} dy = 0 \quad . \tag{D.8}$$

The solution is

$$\tilde{\phi}(k, y, z) = \sum_n A_n(k) Y_n(y;k) Z_n(z;k) \quad , \tag{D.9}$$

and the boundary conditions to be applied are

$$Y'_{1n}(h_1;k) = 0 \tag{D.10a}$$

$$Y'_{1n}(0;k) = Y'_{2n}(0;k) \tag{D.10b}$$

$$M_1^2 Y_{1n}(0;k) = M_2^2 Y_{2n}(0;k) \tag{D.10c}$$

$$Y'_{2n}(-h_2;k) = 0 \qquad \text{(D. 10d)}$$

$$Z'_n(b;k) = 0 \qquad \text{(D. 10e)}$$

$$\tilde{\phi}_{,z}(k, y, 0) = \tilde{\varepsilon}(y, k) \qquad \text{(D. 10f)}$$

where $\tilde{\varepsilon}(y, k)$ is the Fourier transform of the prescribed flow inclination angle in the $+z$ direction at the wall $z = 0$. The general forms of the solutions of eqs. (D. 3) and (D. 7) are

$$Y_{1n}(y;k) = C_{1n}(k)\cos(y-h_1)k\sqrt{\beta_1^2-\lambda_n^2} + D_{1n}(k)\sin(y-h_1)k\sqrt{\beta_1^2-\lambda_n^2}\,, \qquad \text{(D. 11a)}$$

$$Y_{2n}(y;k) = C_{2n}(k)\cosh(y+h_2)k\sqrt{\beta_2^2+\lambda_n^2} + D_{2n}(k)\sinh(y+h_2)k\sqrt{\beta_2^2+\lambda_n^2}\,, \qquad \text{(D. 11b)}$$

$$Z_n(z;k) = C_{3n}(k)\cos(z-b)k\lambda_n + D_{3n}(k)\sin(z-b)k\lambda_n\,. \qquad \text{(D. 11c)}$$

The application of eqs. (D. 10 a-e) to these general solutions yields:

$$D_{1n}(k) = D_{2n}(k) = D_{3n}(k) = 0\,, \qquad \text{(D. 12a)}$$

$$C_{2n}(k) = \frac{M_1^2}{M_2^2}\,\frac{\cos h_1 k\sqrt{\beta_1^2-\lambda_n^2}}{\cosh h_2 k\sqrt{\beta_2^2+\lambda_n^2}}\,C_{1n}(k)\,, \qquad \text{(D. 12b)}$$

$$\frac{1}{M_1^2}\sqrt{\beta_1^2-\lambda_n^2}\tan h_1 k\sqrt{\beta_1^2-\lambda_n^2} = \frac{1}{M_2^2}\sqrt{\beta_2^2+\lambda_n^2}\tanh(h_2 k\sqrt{\beta_2^2+\lambda_n^2})\,. \qquad \text{(D. 12c)}$$

Without loss of generality, we can put

$$C_{1n}(k) = \frac{1}{M_1^2\cos h_1 k\sqrt{\beta_1^2-\lambda_n^2}}\,, \qquad \text{(D. 12d)}$$

$$C_{2n}(k) = \frac{1}{M_2^2\cosh h_2 k\sqrt{\beta_2^2+\lambda_n^2}}\,, \qquad \text{(D. 12e)}$$

$$C_{3n}(k) = 1 \quad . \tag{D. 12f}$$

The final boundary condition, eq. (D. 10f), and the orthogonality condition, eq. (D. 6), enable us to solve for the coefficients $A_n(k)$:

$$A_n(k) = \frac{\int_{-h_2}^{h_1} \tilde{\epsilon}(y;k) \frac{P}{P_{t\,o}} M^2 Y_n(y;k)dy}{Z_n'(0;k) \int_{-h_2}^{h_1} \frac{P}{P_{t\,o}} M^2 Y_n^2(y;k)dy} \quad . \tag{D. 13}$$

Equation (D. 12c) defines an infinite set of eigenvalues $\{\lambda_n\}$ for a specific value of k. Substitution into the orthogonality condition of eq. (D. 8) results in a modification to eq. (D. 12c):

$$\frac{1}{M_1^2}\sqrt{\beta_1^2-\lambda_n^2}\tanh h_1 k\sqrt{\beta_1^2-\lambda_n^2} = \frac{1}{M_2^2}\sqrt{\beta_2^2+\lambda_n^2}\tanh h_2 k\sqrt{\beta_2^2+\lambda_n^2} = B(k) \quad , \tag{D. 14}$$

where the function B(k), which remains to be determined, is constant for all eigenvalues for a given k.

In the case where the shape of the airfoil (or, more generally, the geometric disturbance) is uniform in the y-direction, the function $\tilde{\epsilon}$ does not depend on y. In any event, the function $A_n(k)$ shows a very complex dependence on k, $\lambda_n(k)$, and B(k). No criterion for establishing B(k) has been found. This function, $A_n(k)$, must be substituted into the full solution of eq. (D. 9), and the resulting infinite series is to be evaluated by the inverse Fourier transform, given in eq. (4. 11b). The resulting expression is

$$\phi(x, y) = \frac{1}{\sqrt{2\pi}} \int_{-\infty}^{\infty} \sum_n A_n(k) Y_n(y;k) Z_n(z;k) e^{-ikx} dk \quad . \tag{D. 15}$$

Also, there is an infinity of solutions of eq. (D. 12c), each of which

(except for singular cases) is at a different value of B(k), defined by eq. (D. 14). To proceed with a solution, it is necessary to find the poles of the integrand. The poles of the function $A_n(k)$ are: $\lambda_n = 0$, which reduces to the two-dimensional wedge problem expression (dependence on Z vanishes); $B(k) = 0$, which is only satisfied for discrete combinations of (k, λ_n); $\sin \lambda_n kb = 0$; and whatever additional poles are contained in the boundary condition function $\tilde{\epsilon}(y;k)$. It appears that the solution of eq. (D. 15) is several double infinite series, summed over n and over all values of k for which there are poles in the integrand at a specific n.

APPENDIX E. Airfoil Casting Procedure

This appendix describes the casting of the solid and tapped airfoils used in the experimental studies of Chapter V. The method is from Collins[23] and several discussions were held with him to refine the technique in view of the special requirement that the maximum thickness be kept below 0.098 inch.

The airfoil was chosen to be a biconvex section, and a thickness ratio of 6 per cent was selected as representative (cf. Figure 1.2). A chord length of 1.5 inches, giving a maximum thickness of 0.090 inch, was chosen.

A pilot model, the "solid" airfoil, was first cast (see Figure 5.11 for a section view of the airfoils). A spar was machined of phosphor bronze to run down the middle of the mold, around which the epoxy would be cast, to give strength to the finished airfoil. A usable airfoil resulted on the third attempt using the compound Epoxylite 4141-44. The first attempt failed due to improper mixing of the epoxy. The components were mixed in the ratio of 10:1 by volume, when it should have been done by weight. In the second attempt, the epoxy was prepared correctly and hardened to a glass-like finish but suffered from some voids in the finished casting.

On the third attempt, care was taken during the mixing of the epoxy resins to entrain as little air as possible. In addition, after mixing the epoxy was placed in a near-vacuum. The mixture frothed up quite strongly, quadrupling its volume within about 30 seconds. At this point, the vacuum jar was vented and the mixture rapidly collapsed to its original size. Vacuum was re-applied, and the frothing

repeated with apparently the same vigor. It was decided that perhaps volatile components of the epoxy were vaporizing, and that further time in a vacuum might do more harm than good. The total time under vacuum was estimated at 3 minutes.

The other problem with the second attempt was that the central spar (12 inches long, .063 inch thick) was supported within the 10-inch long mold only at the ends, and apparently had been in contact with the inner surface of the mold in places. In the vicinity of these reduced-clearance places, the epoxy was unable to flow and left voids and exposed sections of spar in the final casting. This was remedied by using a thinner spar (.045 inch) and putting a few drops of solder on each side, filed down to hold the body of the spar at least .018 inch away from the mold. After seeing the finished casting, it was felt that .012 inch would have been sufficient.

Both of these solutions worked: the final casting was free of voids and exposed sections of spar. Immediately after the injection of epoxy was completed, the vacuum jar was vented to atmospheric pressure and the epoxy was allowed to harden. A test sample was poured out of the same batch so that the rate of hardening could be monitored. To facilitate opening the mold, all interior surfaces were given a thin coating of silicone grease before the injection to prevent adhesion of the epoxy, while the central spar was cleaned with first acetone, then methanol (to remove a slight residue left by the acetone).

The airfoil casting was about 10 inches long, with about 1 inch of the spar protruding at each end. The best 4.3 inches of airfoil were chosen to be preserved, and the remainder of the eopxy was cut

away using a Dremel hand-held tool. Care should be taken during this process to avoid damaging the leading and trailing edges of the airfoil.

The finished airfoil had a thickness of .086 ± .002 inch, and was sufficiently faithful to the mold that the minute scratches left in the mold by the scraper during construction of the mold were visible in the finished airfoil. The epoxy was strong enough that erosion of the material while in the wind tunnel was not the problem that was feared. However, it would have been prudent nevertheless to have given the leading edge a coat of a light lacquer for protection.

Considerably more problems were encountered in the casting of the instrumented airfoil. The idea was to place as many pressure taps as possible at separate chordwise locations, and by translating the airfoil in the spanwise direction while the tunnel was in operation, continuous pressure distributions at each tap could be obtained.

As the mold used for the previous casting was still in good condition, it was used for the instrumented casting as well. The central spar of the airfoil was made of 19 hollow tubes in line, the central 13 having .049-inch diameter, and the outer 3 tubes at each end were of .033-inch diameter. The tubes were attached together by epoxy at several spanwise locations.

The casting process was performed in the same manner as before using a slightly different compound, Epoxylite 4141-65, which is colored red rather than the blue of the previous castings. The red compound cast equally well as the blue, but hardened into a glossier finish with a tougher, finer structure. Consequently, use of this red compound is recommended for future work.

The material was sufficiently hard for handling in eight hours, though it retained some plasticity for an additional twelve hours. After the airfoil was removed from the mold and had finished hardening, all casting flares were removed and the fit of the airfoil in the mounting assembly was checked.

Translation of the airfoil was to be driven by the same unit which had previously been used for the pitot probe. An assembly which attached to the wind tunnel walls at each end of the airfoil was constructed to permit the translation and reading of the static pressure taps while sealing against the atmosphere. Also, the assembly permitted setting the airfoil at angles of attack up to $\pm 5^{o}$. The airfoil was put in tension by attaching it to the drive unit at its upper end while hanging 40 pounds of weight from its lower end.

At first, the airfoil did not fit through the seal assembly near either end of its span; only the center 5 inches (where fortunately the taps had to be placed anyway) were within tolerance. On inspection, it was found that at each end the airfoil was .010 inch too thick. This additional thickness was filed off. It is testimony to the hardness of the epoxy that this task required 4 hours' work! Certainly this work resulted in deviations from the nominal airfoil contour, but it was felt that as this area was about two chord lengths of span away from the static pressure taps, the effect on the pressure data would be negligible.

As has already been mentioned, provision was made for 19 taps in the airfoil. The taps were to be drilled to alternating surfaces (see Figure 5.11). Substantial problems were encountered in doing this,

which required three weeks to overcome. These were due to the basic concept used in installing the taps, which was to drill through the surface of the airfoil into the metal tubes after the epoxy had hardened. In practice, the epoxy was not rigid enough to prevent the drill from wandering around the edge of the tube rather than cutting into it. This problem was solved by cutting a channel .042 inch wide into the surface of the airfoil deep enough that a flat was put into the surface of each tube in the desired location. Holes of .020 inch diameter were drilled into the tubes through the flats and were then plugged with greased half-inch long wires. The channel was refilled with epoxy, and after hardening the filler was cut off flush with the original surface. This method was very tedious, and the results were not always satisfactory; the use of 5 of the 19 taps was never regained. A slightly different method of installing taps in a cast airfoil was suggested by W. R. Hawthorne and is described in Section 6.2.

APPENDIX F. Correction to the Calculation of Tsien and Finston

This appendix presents the derivation of the correction to the calculation of Tsien and Finston[18] for the problem of the wedge attached to the subsonic wall. When this modification is inserted in their calculation, the results are in good agreement with the limiting case of the present calculation as presented in Section 4.4.

Tsien and Finston impose as a boundary condition the flow inclination angle $\epsilon(x)$ at the subsonic wall:

$$\epsilon(x) = 0 \qquad x < 0$$

$$\epsilon(x) = e^{-\beta x} \qquad x > 0 \qquad (\beta > 0)$$

In the limit as β vanishes, the perturbation is that of an infinite wedge.

The conventional relation between perturbation velocity components and the gradient of the velocity potential is employed, namely:

$$u = \partial\phi/\partial x \ , \tag{F.1a}$$

$$v = \partial\phi/\partial y \ . \tag{F.1b}$$

The change in static pressure is given by

$$\Delta P = -\rho U u' \quad . \tag{F.2}$$

A parameter θ is defined as

$$\cos\frac{\theta}{2} = \left(\frac{M_2^2}{M_1^2}\right) \Bigg/ \sqrt{\left(\frac{M_2^2}{M_1^2}\right)^2 + \frac{\beta_2^2}{\beta_1^2}} \quad , \quad 0 < \theta < \pi \ . \tag{F.3}$$

Expect where specifically stated, the notation adopted in Chapter IV will be employed in this appendix. The general expression for the subsonic stream perturbation velocity potential is found to be (ref. 18, eq. 46):

$$\phi_2 = U_2\left\{\frac{\epsilon}{\pi\beta_2}\int_{-\infty}^{\infty}\frac{\sinh\lambda\beta_2(y+h_2)}{\lambda(\beta^2+\lambda^2)}[\beta\cos\lambda x+\lambda\sin\lambda x]d\lambda\right.$$

$$\left.+\int_0^{\infty}\cosh\lambda\beta_2(y+h_2)[a_2(\lambda)\sin\lambda x+b_2(\lambda)\cos\lambda x]d\lambda\right\} \quad . \quad (F.4)$$

Application of the boundary conditions yields the expressions for the Fourier coefficients, $a_2(\lambda)$ and $b_2(\lambda)$, presented as equations (52) and (53) in Tsien and Finston's paper:

$$\left[\cos^2\frac{\theta}{2}\cosh^2\lambda h_2\beta_2+\sin^2\frac{\theta}{2}\sinh^2\lambda h_2\beta_2\right]a_2(\lambda) =$$

$$-\frac{\epsilon}{\pi\beta_1(\beta^2+\lambda^2)}\left[\frac{\beta}{\lambda}\frac{M_1^2}{M_2^2}\cos^2\frac{\theta}{2}+\frac{1}{2}\frac{\beta_1}{\beta_2}\sinh 2\lambda h_2\beta_2\right] \quad , \quad (F.5a)$$

$$\left[\cos^2\frac{\theta}{2}\cosh^2\lambda h_2\beta_2+\sin^2\frac{\theta}{2}\sinh^2\lambda h_2\beta_2\right]b_2(\lambda) =$$

$$-\frac{\epsilon}{\pi\beta_1(\beta^2+\lambda^2)}\left[-\frac{M_1^2}{M_2^2}\cos^2\frac{\theta}{2}+\frac{1}{2}\left(\frac{\beta}{\lambda}\right)\frac{\beta_1}{\beta_2}\sinh 2\lambda h_2\beta_2\right] \quad . \quad (F.5b)$$

The factor which was omitted by Tsien and Finston is the quantity (β/λ) on the right-hand side of eq. (F.5b). The work of Tsien and Finston up to the point where eq. (53) is obtained from eqs. (48), (49), (50), and (51) is correct. The evaluations will be carried out in the limit where β tends toward zero; thus, inclusion of this factor will eventually result in a considerable simplification.

The integration variable λ and the space coordinate x are redefined as dimensionless quantities:

$$S = 2h_2\lambda\beta_2 \quad , \quad (F.6)$$

$$\xi = \frac{\pi x}{2h_2\beta_2} \quad . \tag{F.7}$$

Note that all the integrands in eq. (F.4) are even functions of λ. If $f(\lambda)$ is even, then

$$\int_0^\infty f(\lambda)d\lambda = \frac{1}{2}\int_{-\infty}^{\infty} f(\lambda)d\lambda \quad .$$

The integrands will be evaluated by the same technique as was employed in Chapter IV, and then the limit of the expressions will be taken as β vanishes. First-order poles exist at the points

$$\lambda = \pm i\beta \tag{F.8a}$$

and

$$S = i\pi(2n+1 \pm \theta/\pi) \tag{F.8b}$$

$$S = -i\pi(2n+1 \pm \theta/\pi) \quad . \tag{F.8c}$$

The solution for the pressure perturbation at the interface is

$$\frac{\Delta P}{(\frac{1}{2}\rho_1 U_1^2)(\frac{2\epsilon}{\beta_1})} = 2\cos\frac{\theta}{2} F_4(\xi;\theta) \qquad \xi < 0 \tag{F.9a}$$

$$= 1 - 2\cos\frac{\theta}{2} F_3(\xi;\theta) \qquad \xi > 0 \tag{F.9b}$$

where, in the notation of Tsien and Finston,

$$F_3(\xi;\theta) = \frac{1}{\pi}\sum_{n=0}^{\infty}(-1)^n \frac{e^{-(2n+1+\theta/\pi)|\xi|}}{2n+1+\theta/\pi} \quad , \tag{F.10a}$$

$$F_4(\xi;\theta) = \frac{1}{\pi}\sum_{n=0}^{\infty}(-1)^n \frac{e^{-(2n+1-\theta/\pi)|\xi|}}{2n+1-\theta/\pi} \quad . \tag{F.10b}$$

The equations (F.9) should replace equations (54) and (55) in ref. 18. All other work in that paper has been verified.

References

1. Johnsen, I. A., and Bullock, R. O., "Aerodynamic Design of Axial-Flow Compressors," NASA SP-36, 1965.

2. Bullock, R. O., "Critical High Lights in the Development of the Transonic Compressor," Transactions of the ASME: Journal of Engineering for Power, vol. 83, series A, pp. 243 - 257, July 1961.

3. Marble, F. E., "Three-Dimensional Flow in Turbomachines," in Aerodynamics of Turbines and Compressors, W. R. Hawthorne, ed., Princeton Series on High Speed Aerodynamics and Jet Propulsion, vol. X, Princeton University Press, Princeton, N. J., 1964.

4. McCune, J. E., "A Three-Dimensional Theory of Axial-Compressor Blade Rows--Application in Subsonic and Supersonic Flows," JAS, vol. 25, no. 9, pp. 544 - 560, Sept. 1958.

5. McCune, J. E., "The Transonic Flow Field of an Axial Compressor Blade Row," JAS, vol. 25, no. 10, pp. 616 - 626, Oct. 1958.

6. Okurounmu, O., and McCune, J. E., "Three-Dimensional Vortex Theory of Axial Compressor Blade Rows at Subsonic and Transonic Speeds," AIAA J., vol. 8, no. 7, pp. 1275 - 1283, July 1970.

7. Okurounmu, O., and McCune, J. E., "Lifting Surface Theory of Axial Compressor Blade Rows: Part I--Subsonic Compressors; Part II--Transonic Compressors," AIAA J., vol. 12, no. 10, pp. 1363 - 1380, Oct. 1974.

8. Hesse, W. J., and Mumford, N. V. S., Jr., Jet Propulsion for Aerospace Applications, 2nd ed., Pitman, New York, 1964.

9. Lieblien, S., and Johnsen, I. A., "Résumé of Transonic-Compressor Research at NACA Lewis Laboratory," Transactions of the ASME: Journal of Engineering for Power, vol. 83, series A, pp. 219 - 234, July 1961.

10. Benser, W. A., Bailey, E. E., and Gelder, T. F., "Holographic Studies of Shock Waves Within Transonic Fan Rotors," ASME Paper 74-GT-46, 1974.

11. Dolait, J. P., "Transonic Wind Tunnel for Investigation of Turbomachinery Blades," Aeronautical Engineer Thesis, California Institute of Technology, Pasadena, Calif., 1971.

12. Reid, L., and Urasek, D. C., "Effects of Increased Leading-Edge Thickness on Performance of a Transonic Rotor Blade," NASA TN D-7489, Nov. 1973.

13. Brown, G. L., and Roshko, A., "On Density Effects and Large Structure in Turbulent Mixing Layers," JFM, vol. 64, part 4, pp. 775 - 816, 1974.

14. Maydew, R. C., and Reed, J. F., "Turbulent Mixing of Compressible Free Jets," AIAA J., vol. 1, no. 6, pp. 1143 - 1144, June 1963.

15. Sirieix, M., and Sloignac, J. L., "Contribution à l'Etude Expérimentale de la Couche de Melange Turbulent Isobare d'un Ecoulement Supersonique," Symposium on Separated Flow, AGARD Conference Proceedings No. 4, pp. 241 - 270, 1966.

16. Eggers, J., "Velocity Profiles and Eddy Viscosity Distributions Downstream of a Mach 2.22 Nozzle Exhausting to Quiescent Air," NASA TN D-3601, Sept. 1966.

17. Ikawa, H., "Turbulent Mixing Layer Experiment in Supersonic Flow," Ph.D. Thesis, California Institute of Technology, Pasadena, Calif., 1973.

18. Tsien, H. S., and Finston, M., "Interaction Between Parallel Streams of Subsonic and Supersonic Velocities," JAS, vol. 16, no. 9, pp. 515 - 528, Sept. 1949.

19. Holder, D. W., Chinneck, A., and Gadd, G. E., "An Experimental Investigation of the Interaction of a Shock Wave with a Subsonic Stream Bounded by a Wall," A. R. C. Tech. Report 16,559, Rept. No. F. M. 2025, Feb. 1954.

20. Liepmann, H. W., Roshko, A., and Dhawan, S., "On Reflection of Shock Waves from Boundary Layers," NACA Report 1100, 1952.

21. Ackert, J., Feldmann, F., and Rott, N., "Investigations of Compression Shocks and Boundary Layers in Gases Moving at High Speed," NACA TM 1113, Jan. 1947.

22. McCabe, A., "The Three-Dimensional Interaction of a Shock Wave with a Turbulent Boundary Layer," Aero. Quart., vol. 17, pt. 3, pp. 231 - 252, Aug. 1966.

23. Collins, D. J., "An Inexpensive Technique for the Fabrication of Two-Dimensional Wind Tunnel Models," Rev. Sci. Instrum., vol. 44, no. 7, July 1973.

24. Kim, C. S., "Experimental Studies of Supersonic Flow past a Circular Cylinder," Journal of the Physical Society of Japan, vol. 11, no. 4, pp. 439 - 445, April 1956.

25. Ames Research Staff, "Equations, Tables, and Charts for Compressible Flow," NACA Report 1135, 1953.

26. Sternberg, J., "Triple-Shock-Wave Intersections," Phys. Fluids, vol. 2, no. 2, pp. 179 - 206, March-April 1959.

27. Fage, A., and Sargent, R. F., "Shock-Wave and Boundary-Layer Phenomena Near a Flat Surface," Proc. Roy. Soc. A190, pp. 1-20, June 1947.

28. Shapiro, A. H., The Dynamics and Thermodynamics of Compressible Fluid Flow, Ronald Press, New York, 1954.

29. Neumann, E. P., and Lustwerk, F., "Supersonic Diffusers for Wind Tunnels," Journal of Applied Mechanics, vol. 16, no. 2, pp. 195-202, June 1949.

30. Uchida, S., and Yasuhara, M., "The Rotational Field Behind a Curved Shock Wave Calculated by the Method of Flux Analysis," JAS, vol. 23, no. 9, pp. 830-845, Sept. 1956.

31. Moeckel, W. E., "Approximate Method for Predicting Form and Location of Detached Shock Waves Ahead of Plane or Axially Symmetric Bodies," NACA TN 1921, July 1949.

32. Alperin, M., "Experimental Information on Two-Dimensional Detached Shock Waves," Progress Report 4-44, Jet Propulsion Laboratory, California Institute of Technology, Pasadena, Calif., May 1950.

33. Hurley, F. X., "Measured Three-Dimensional Effects in Transonic Airfoil Testing," AIAA J., vol. 13, no. 2, pp. 250-252, Feb. 1975.

34. Moulden, T. H., "A Discussion of the Shock-Wave in Mixed Flow," AIAA Paper 69-43, presented at the AIAA 7th Aerospace Sciences Meeting, New York, Jan. 20-22, 1969.

35. Liepmann, H. W., "The Interaction Between Boundary Layer and Shock Waves in Transonic Flow," JAS, vol. 13, no. 12, pp. 623-637, Dec. 1946.

36. Alber, I. E., Bacon, J. W., Masson, B. S., and Collins, D. J., "An Experimental Investigation of Turbulent Transonic Viscous-Inviscid Interactions," AIAA J., vol. 11, no. 5, pp. 620-627, May 1973.

37. Collins, D. J., and Krupp, J. A., "Experimental and Theoretical Investigations in Two-Dimensional Transonic Flow," AIAA Paper 73-659, 1973.

38. Namba, M., "Theory of Transonic Shear Flow Past a Thin Airfoil," JFM, vol. 36, pt. 4, pp. 759-783, 1969.

39. Namba, M., "Transonic Shear Flow Past a Symmetric Airfoil," Memoirs of the Faculty of Engineering, Kyushu University, vol. 30, no. 2, pp. 51-67, Nov. 1970.

40. Namba, M., "Lifting Surface Theory for a Rotating Subsonic or Transonic Blade Row," A. R. C. R. and M. No. 3740, 1974.

41. Namba, M., and Asanuma, T., "Theory of Lifting-Lines for Cascade of Blades in Subsonic Shear Flow," Bulletin of JSME, vol. 10, no. 42, pp. 920-938, 1967.

42. Honda, M., "Theory of Thin Wings in a Shear Flow," Proc. Roy. Soc. A254, pp. 372-394, 1960.

43. Honda, M., "Theory of Shear Flow Through a Cascade," Proc. Roy. Soc. A265, pp. 46-70, 1961.

44. Kotansky, D. R., "Thin Airfoils in Rotational Flow," Sc.D. Thesis, Massachusetts Institute of Technology, Cambridge, Mass., 1965.

45. Hawthorne, W. R., "The Applicability of Secondary Flow Analyses to the Solution of Internal Flow Problems," in Fluid Mechanics of Internal Flow, Symposium on the Fluid Mechanics of Internal Flow, General Motors Research Labs, Warren, Mich., 1965; G. Sovran, ed., Elsevier, New York, 1967.

46. Hawthorne, W. R., "On the Theory of Shear Flow," Gas Turbine Laboratory Report No. 88, Massachusetts Institute of Technology, Cambridge, Mass., Oct. 1966.

47. Hawthorne, W. R., "On the Theory of Shear Flow: Supplement and Corrigenda to Gas Turbine Laboratory Report No. 88," G. T. L. Report No. 93, Massachusetts Institute of Technology, Cambridge, Mass., March 1968.

48. Oliver, D. A., and Sparis, P., "A Computational Study of Three-Dimensional Transonic Shear Flow in Turbomachine Cascades," AIAA Paper 71-83, presented at the AIAA 9th Aerospace Sciences Meeting, New York, Jan. 25-27, 1971.

49. Knechtel, E. D., "Experimental Investigation at Transonic Speeds of Pressure Distributions over Wedge and Circular-Arc Airfoil Sections and Evaluation of Perforated-Wall Interference," NASA TN D-15, Aug. 1959.

50. Namba, M., "Lifting-Surface Theory for Cascade of Blades in Subsonic Shear Flow," JFM, vol. 36, pt. 4, pp. 735-757, 1969.

51. Hoerner, S. F., Fluid-Dynamic Drag, published by the author, Midland Park, N. J., 1965.

52. Miller, G. R., and Bailey, E. E., "Static Pressure Contours in the Blade Passage at the Tip of Several High Mach Number Rotors," NASA TM X-2170, Feb. 1971.